Conference Proceedings of the Society for Experimental Mechanics Series

Evro Wee Sit *Editor*

Sensors and Instrumentation, Volume 5

Proceedings of the 34th IMAC, A Conference and Exposition on Structural Dynamics 2016

SEM

Springer

Conference Proceedings of the Society for Experimental Mechanics Series

Series Editor
Kristin B. Zimmerman, Ph.D.
Society for Experimental Mechanics, Inc.,
Bethel, CT, USA

More information about this series at http://www.springer.com/series/8922

Evro Wee Sit
Editor

Sensors and Instrumentation, Volume 5

Proceedings of the 34th IMAC, A Conference and Exposition on Structural Dynamics 2016

Springer

Editor
Evro Wee Sit
SVcommunity.com
Hermosa Beach, CA, USA

ISSN 2191-5644 ISSN 2191-5652 (electronic)
Conference Proceedings of the Society for Experimental Mechanics Series
ISBN 978-3-319-29858-0 ISBN 978-3-319-29859-7 (eBook)
DOI 10.1007/978-3-319-29859-7

Library of Congress Control Number: 2016940977

Printed on acid-free paper

This Springer imprint is published by Springer Nature
The registered company is Springer International Publishing AG Switzerland

Preface

Sensors and Instrumentation represents one of ten volumes of technical papers presented at the 34th IMAC, A Conference and Exposition on Structural Dynamics, organized by the Society for Experimental Mechanics, and held in Orlando, Florida, on January 25–28, 2016. The full proceedings also include volumes on Nonlinear Dynamics; Dynamics of Civil Structures; Model Validation and Uncertainty Quantification; Dynamics of Coupled Structures; Special Topics in Structural Dynamics; Structural Health Monitoring, Damage Detection & Mechatronics; Rotating Machinery, Hybrid Test Methods, Vibro-Acoustics and Laser Vibrometry; Shock & Vibration, Aircraft/Aerospace, Energy Harvesting, Acoustics & Optics; and Topics in Modal Analysis & Testing.

Each collection presents early findings from experimental and computational investigations on an important area within Sensors and Instrumentation. Topics represent papers on calibration, smart sensors, rotational effects, stress sensing, and tracking of dynamics.

The organizers would like to thank the authors, presenters, session organizers, and session chairs for their participation in this track.

Hermosa Beach, CA, USA — Evro Wee Sit

Contents

Chapter 1
Phase Control of RF Cavities

Brian Page, Orlando Murray, Patricia Tan, Alexandria N. Marchi, Alexander Scheinker, Daniel Rees, and Charles Farrar

Abstract Particle accelerators use superconducting radio frequency (RF) cavities that create extremely large electromagnetic fields to accelerate charged particles. The latest accelerators require an unprecedented level of precision in terms of particle energy, which translates into accelerating field amplitude and phase within error bounds of 0.01 % and 0.01°, respectively. To save money, it is possible to split the output of one high power controlled RF source to multiple cavities. However, in practice, all cavities are slightly different and experience different disturbances in operation. Because of an inability to quickly modulate the phase and amplitude of the individual split high power RF signals, the fields of an entire multi-cavity system are averaged and treated as one entity on which feedback control is performed at the low power input to the high power RF amplifier. The issue is compounded by the severe electrical loading that the RF cavity experiences during operation. Radiation pressure causes Lorentz force detuning, which shifts each cavity's resonance peak, amplitude, and phase of its accelerating field in a unique way. Piezo tuners have been used to counteract Lorentz force detuning of individual cavities. This paper studies RF cavity phase control via piezo tuners. The controller designed is capable of quickly modifying the natural frequency of a cavity as a tool for modulating the phase of an RF signal. The approach is validated in hardware with a Niobium coated single-cell copper TESLA-type RF cavity.

Keywords Particle accelerator • RF resonator • Resonance control • Lorenz force detuning • Phase shifting

1.1 Introduction

Radio frequency (RF) cavities are used in particle accelerators to generate acceleration gradients on the order of 20 MV/m. RF cavities operate by resonating electromagnetic fields at very high frequencies ranging from high MHz to low GHz. In an effort to lower costs, new accelerators are being designed with many clustered RF cavities that are fed by single high power klystrons, as shown in Fig. 1.1. Legacy control methods focus on averaging the phases and amplitudes of the entire bank of cavities and controlling the klystron output as well as using piezo tuners to counteract the dynamic Lorentz force detuning that occurs within each cavity at operational voltages [1–5]. For example, the Matter-Radiation Interactions in Extremes (MaRIE) experimental facility at Los Alamos National Laboratory plans to employ resonance cavities operating at approximately 1.3 GHz and 20 MV/m average acceleration gradient with 8–24 cavities driven by a single klystron. Each MaRIE accelerating cavity must be tuned to account for manufacturing variability and dynamic detuning during operation with an unprecedented degree of accuracy, i.e., amplitude and phase error bounds within 0.01 % and 0.01°, respectively.

B. Page
Department of Mechanical Engineering-Engineering Mechanics, Michigan Technological University, Houghton, MI 49931, USA

O. Murray
Department of Electrical and Computer Engineering, University of Florida, Gainesville, FL 32611, USA

P. Tan
Department of Structural Engineering, University of California, San Diego, La Jolla, CA 92093, USA

A.N. Marchi (✉) • C. Farrar
Los Alamos National Laboratory, Engineering Institute, MS T001, P.O. Box 1663, Los Alamos, NM 87545, USA
e-mail: amarchi@lanl.gov

A. Scheinker • D. Rees
Los Alamos National Laboratory, RF Engineering, MS T001, P.O. Box 1663, Los Alamos, NM 87545, USA

E. Wee Sit (ed.), *Sensors and Instrumentation, Volume 5*, Conference Proceedings of the Society for Experimental Mechanics Series, DOI 10.1007/978-3-319-29859-7_1

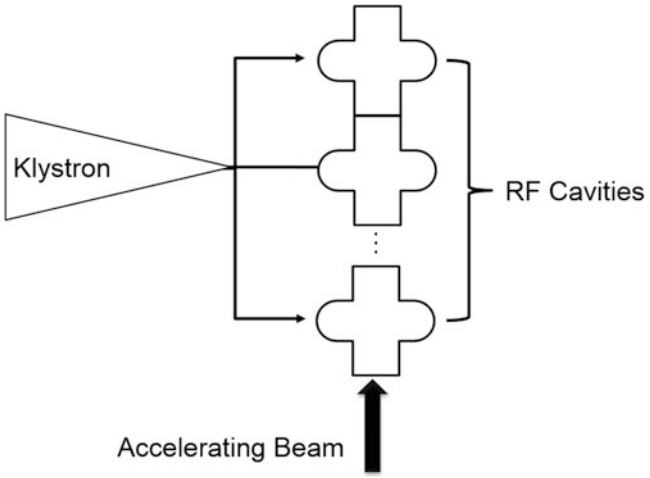

Fig. 1.1 Diagram of current accelerator layout

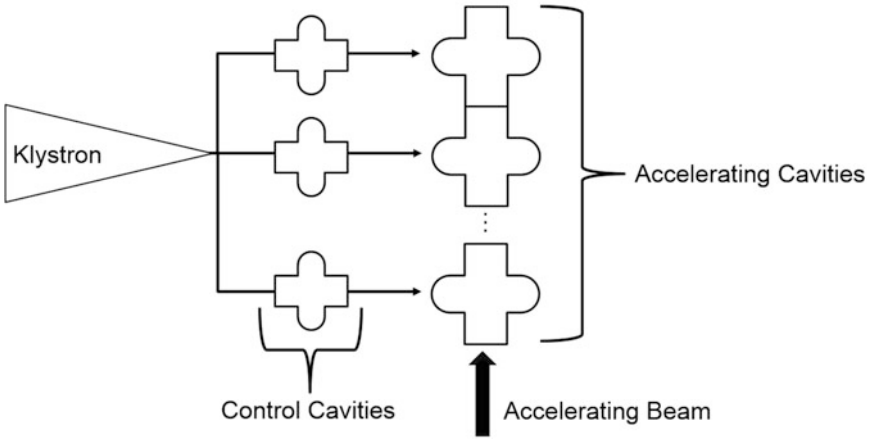

Fig. 1.2 Proposed accelerator with control cavities

This paper studies a new method for modulating high power RF signals. By placing additional RF cavities between the klystron and the accelerating cavities and using high power piezo-tuners the input phases and amplitudes of the RF fields entering each accelerating cavity may be modulated independently as shown in Fig. 1.2.

This method focuses on using multiple piezo tuners and individual feedback control loops for each control cavity. Through this method, it is possible to individually control the resonant frequency of each cavity in a bank of cavities through a relatively wide band of adjustments depending on the Q factor of the cavity and the piezo actuation. The control loop is a multilevel controller built around a low level PID feedback loop, and a high level synchronizer that ensures all the cavities operate together with the correct phase shift between cavities.

The designed low level PID loop operates on the IQ model of RF cavities in Eqs. (1.1) and (1.2). The IQ model separates the RF cavity into inphase (V_i) and quadrature (V_r) components of cavity voltage effectively separating the quickly oscillating RF signal from the relatively slow amplitude and phase shifting that occurs during operation. By using the IQ model, the control loop is able to operate at a much lower frequency and still effectively control the RF field.

$$\frac{dV_i}{dt} + \omega_{1/2} V_i - \Delta\omega V_r = \omega_{1/2} R_L I_i \tag{1.1}$$

$$\frac{dV_r}{dt} + \omega_{1/2} V_r - \Delta\omega V_i = \omega_{1/2} R_L I_r \tag{1.2}$$

In the IQ model, $\omega_{1/2}$ is the cavity bandwidth, $\Delta\omega$ is the difference between resonance frequency and input RF frequency, R_L is the cavity's resistance, and I is the driving current in both inphase and quadrature components.

1.2 Experimental Setup

Controller design is completed in both simulation and hardware. Simulations focus on the development of an IQ model of an RF cavity in Simulink while hardware validation is completed with LabVIEW on a Niobium coated single-cell copper TESLA-type RF cavity operating at approximately 1.3 GHz, shown in Fig. 1.3. Attached to the RF cavity are four piezo tuners, which are capable of modifying the length of the cavity and thus adjusting resonance. The cavity/piezo tuner assembly is mounted into a rigid frame. An RF antenna fed from a signal generator is used as the RF source for the cavity and another RF antenna acts as the receiver for the controller. The RF signal coming from the cavity is fed through a custom signal demodulator that converts the RF signal into amplitudes and phases that are relative to the input signal that results in steady state phase error bounds of $\pm 0.075°$. The cavity is used in non-superconducting mode but conclusions can be transferred to superconducting cavities.

Simulink modelling of the IQ model of an RF cavity is shown in Fig. 1.4. The model is built around the state space representation of the IQ model of RF cavities described in [6]. This model is capable of simulating both superconducting and non-superconducting through choice of the Q and R_L factors. In the model implemented Q was chosen to be 45,000 and R_L of 5 corresponding to a normal conducting cavity. The generic cavity model simulated allows for simulation of various controller and filtering strategies quickly.

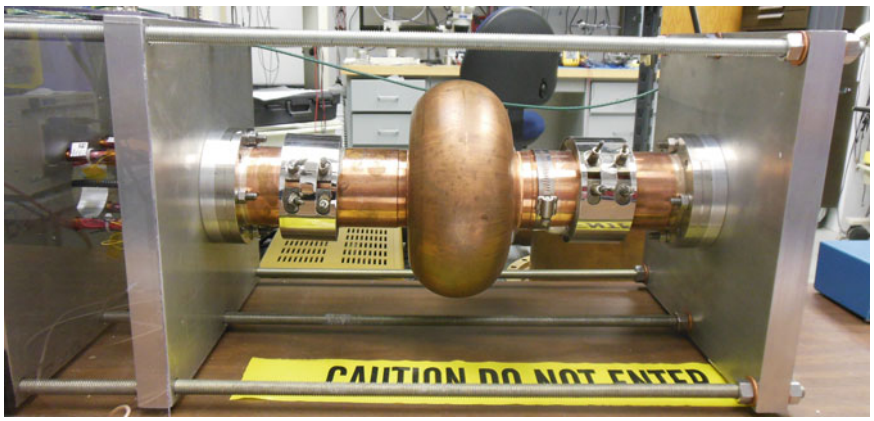

Fig. 1.3 TESLA-type RF cavity setup

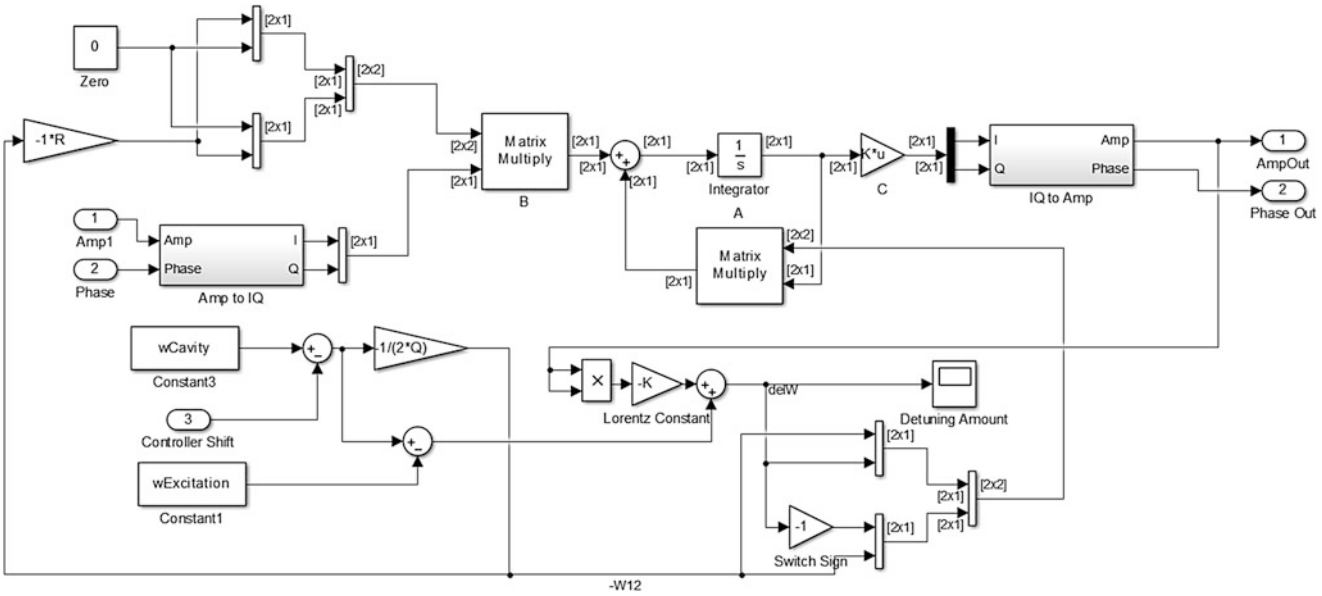

Fig. 1.4 State space model of RF cavity

Hardware validation of controller design is completed with National Instruments LabVIEW and a TESLA cavity. A closed loop control system is designed to guarantee performance of the cavity through the various detuning factors and across multiple cavities. Control tests focus around four possible use cases: (1) constant input frequency-constant target phase, (2) moving input frequency-constant target phase, (3) constant input frequency-moving target phase, and (4) moving input frequency-moving target phase.

1.3 Simulation Results

Controller development focuses on implementing a feedback system to control phase of the cavity output signal. Each RF cavity in a multi-cavity system is modeled as shown in Fig. 1.4, while the entire system is modeled together in Fig. 1.5. In the multi-cavity model, a standard PID controller is implemented based on the average of the output amplitudes in a similar fashion to legacy tuning methods. Phase is controlled by setting a constant target phase for the klystron and then using the control cavities (Red in Fig. 1.5) to dynamically shift the phase towards the target. This phase shifting is accomplished with PID control of the piezo actuation on the cavity walls. In simulation the control cavities are capable of shifting the phase $\pm 15°$in 160 ± 10 μs with a controller updating at 1 MHz. Provided powerful enough hardware, the fast phase shifting capabilities of RF cavities could be harnessed to shift phase within individual pulses or to maintain a constant phase in extremely noisy conditions.

1.4 Hardware Results

Hardware validation of simulation results is completed on a Niobium coated single-cell copper TESLA-type RF cavity using LabVIEW.

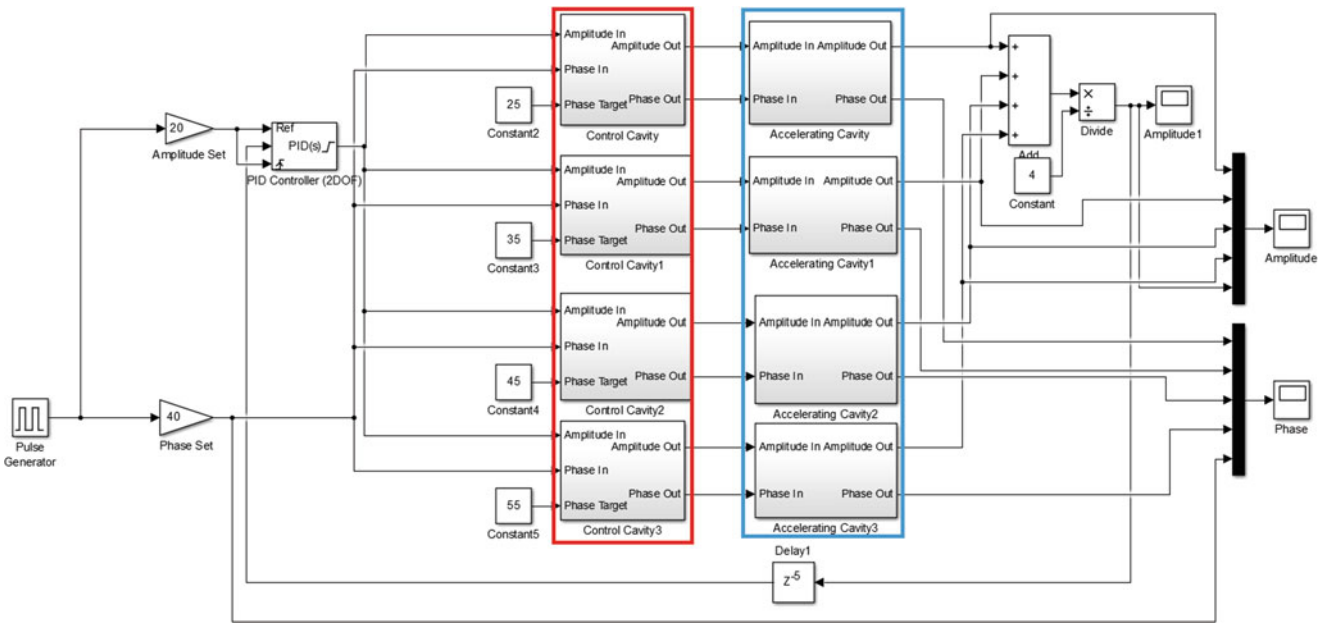

Fig. 1.5 Multicavity model of RF system

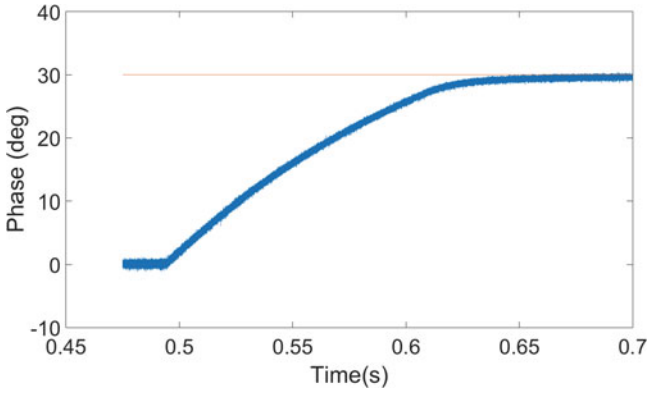

Fig. 1.6 Upper limit phase modulation

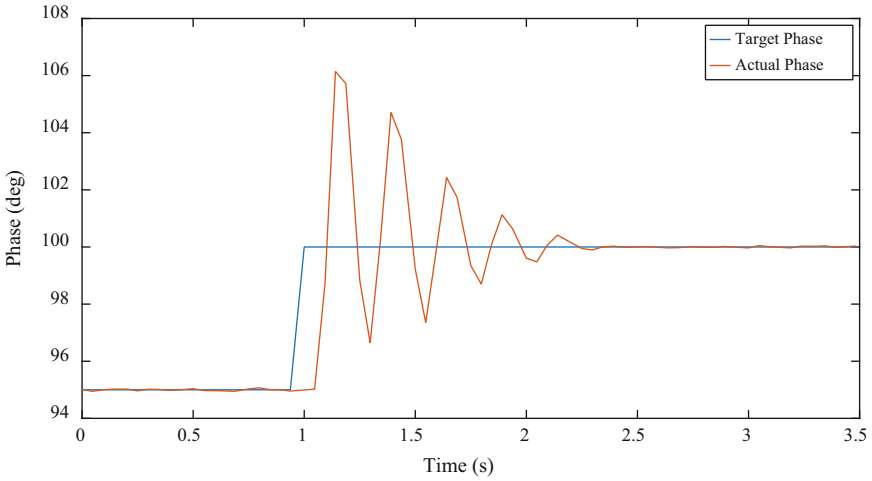

Fig. 1.7 Constant input frequency-constant target phase

1.4.1 Hardware Limitations

The piezo tuner/amplifier system is capable of shifting the resonance peak by approximately 200 kHz, which corresponds to a 30° phase swing in 0.15 s, shown in Fig. 1.6. This upper limit on phase swing and rate is determined by the capabilities of our amplifier. The 1 W amplifier reaches its current limit while charging the piezos, using a commercially available amplifier with 1 kW of output power, the 30° phase shift could be achieved in 150 μs.

A PID controller is developed in LabVIEW to control the piezo actuation against the phase error. The controller is able to operate at 20 Hz. This very slow control frequency could be improved to the point of functionality within the accelerator environment by using dedicated hardware, such as an FPGA. Four tests are completed to characterize the controller performance. These tests are (1) constant input frequency-constant target phase, (2) moving input frequency-constant target phase, (3) constant input frequency-moving target phase, and (4) moving input frequency-moving target phase.

1.4.2 Constant Input Frequency-Constant Target Phase

The constant input frequency-constant target phase test is the most likely use case in accelerator applications. This test involves inputting a constant frequency near the cavity resonance and tracking a step input for target phase as shown in Fig. 1.7. Shown here is a step input jumping from 95 to 100° phase shift. The controller is able to settle out this phase shift in 1.5 s to within 0.1° of the phase target. The signal demodulator accounts for much of the remaining phase error. After accounting for the demodulator error, the controller is accurate to within ±0.025° in this use case. With a faster control loop, settling time would be greatly reduced and accuracy improved.

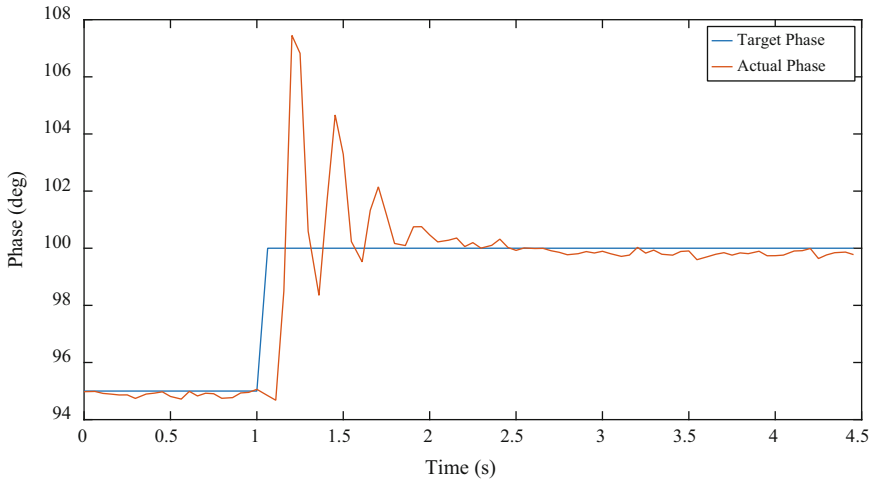

Fig. 1.8 Moving input frequency-constant target phase

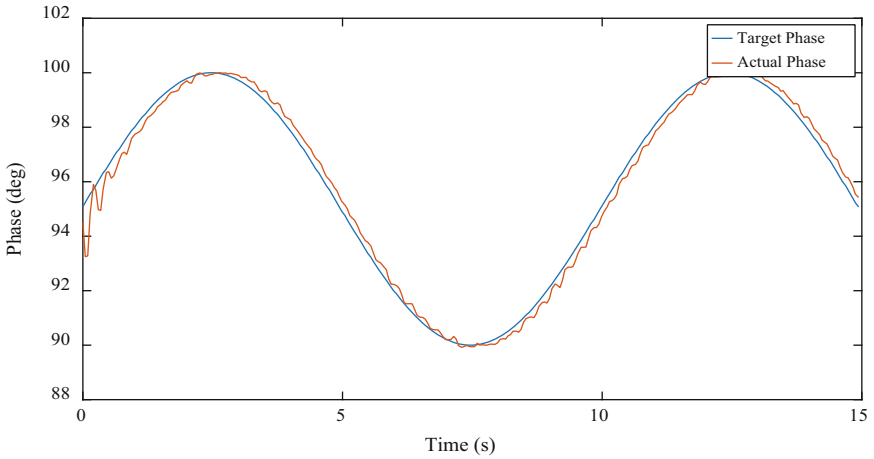

Fig. 1.9 Constant input frequency-moving target phase 0.1 Hz

1.4.3 Moving Input Frequency-Constant Target Phase

Tracking a constant target phase with a moving input frequency is the second case in Fig. 1.8. In this test, the input frequency is modulated at 20 Hz. The input phase is then down sampled to 0.02 Hz oscillation. With the moving input, the controller is capable of settling the RF cavity to the new desired phase in 2 s within 0.3° of the target. The errors are slightly larger with the moving input frequency as the controller has to compensate for the slowly shifting input phase.

1.4.4 Constant Input Frequency-Moving Target Phase

Tracking a moving target with a constant input frequency is shown in Fig. 1.9. In this test the target phase modulates at varying frequencies between 90 and 100° while the input frequency remains constant. With this test the actual phase lags behind the target phase due to the nature of a feedback only controller. A feed forward controller or a controller that operates significantly faster than the phase oscillation could compensate for the phase lag between target and actual phase.

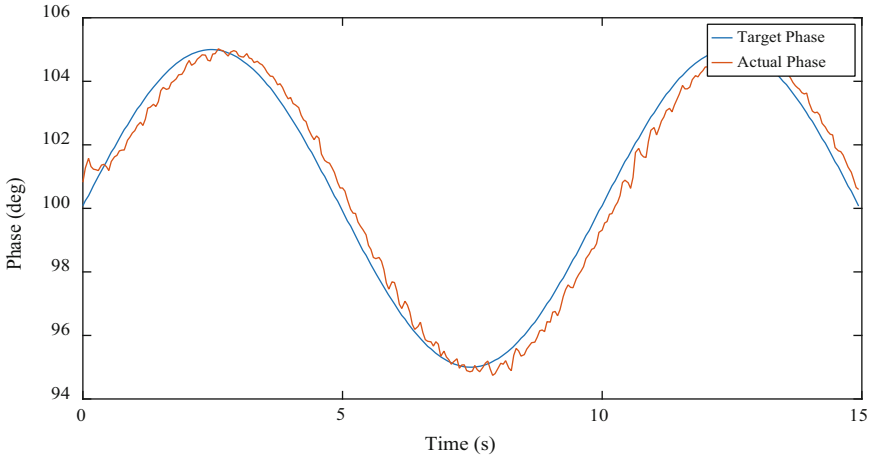

Fig. 1.10 Moving input frequency-moving target phase 0.1 Hz

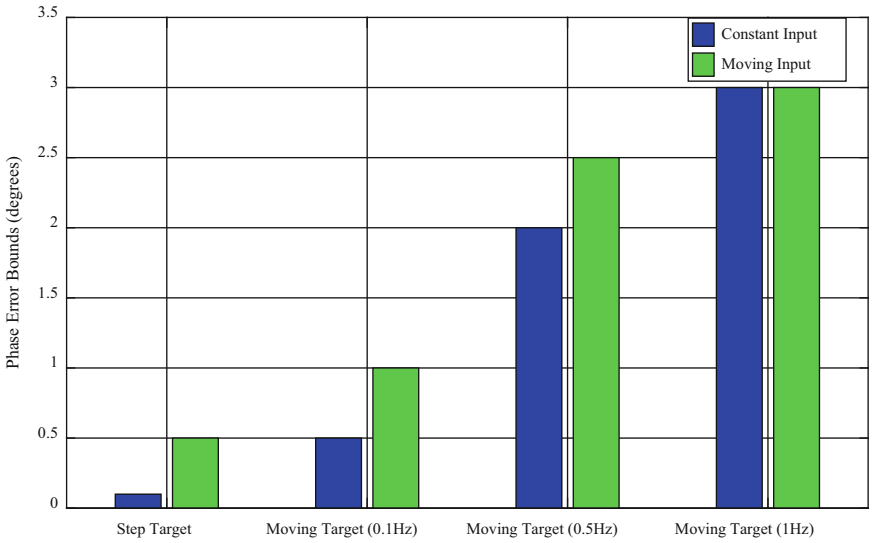

Fig. 1.11 Steady state phase error bounds

1.4.5 Moving Input Frequency-Moving Target Phase

Tracking a moving target phase while having a moving input frequency is the worst case scenario for RF cavity operation. In Fig. 1.10, the target phase oscillates between 90 and 100° at 0.1Hz and the input frequency also modulates. Even through this worst case scenario, the error bounds are $\pm 1°$ of the target largely due to system lag.

1.4.6 Steady State Error Comparison

Steady state error for the different test cases is shown in Fig. 1.11. As expected the fastest oscillating moving target causes the largest phase error, while the constant target cases result in the smallest. After accounting for demodulator error bounds, the constant target-constant input case is nearly within the desired error bounds for accelerator operation with a controller only operating at 20 Hz. A faster controller and higher quality demodulator would improve the response characteristics. The controller described is capable of tracking a moving target with reasonable fidelity as long as the moving target is not oscillating quickly.

1.5 Conclusions

Fast phase shifting of RF signals is possible using RF cavities as phase modulating devices. These cavities shift the phase of the incoming RF signal by modifying the resonance frequency of the cavity with respect to the input frequency. The shift in frequency is accomplished through piezo actuation of the cavity walls. A possible limitation of this approach, is the large losses experienced when coupling through an RF cavity. By controlling the input phase into each accelerating cavity in a bank individually, the overall efficiency of the accelerator can be increased yielding higher particle energies. Individual phase control will enable next generation particle accelerators like the MaRIE at Los Alamos National Lab to achieve unprecedented acceleration gradients and energy efficiency.

Acknowledgements The authors would like to thank Tsuyoshi Tajima for lending the RF cavity and Mark Prokop for lending the RF measurement equipment used for this study. We would also like to thank Lawrence Castellano and Phil Torrez for their help in setting up the RF experiment.

References

1. Ayvazyan, V., Simrock, S.: Dynamic Lorentz force detuning studies in Tesla cavities. In: Proceedings of European particle accelerator conference, Lucerne (2004)
2. Grecki, M., Andryszczak, J., Pozniak, T., Przygoda, K., Sekalski, P.: Compensation of Lorentz force detuning. In: Proceedings of EPAC08, Genoa (2008)
3. Kumar, A., Jana, A., Kumar, V.: A study of dynamic Lorentz force detuning of 650 MHz $\beta g{=}0.9$ superconducting radiofrequency cavity. Nucl. Instrum. Methods Phys. Res. Sect. A **750**, 69–77 (2014)
4. Liepe, M., Moeller, W., Simrock, S.: Dynamic Lorentz force compensation with a fast piezoelectric tuner. In: Proceedings of the 2001 Particle Accelerator Conference, Chicago (2001)
5. Simrock, S.: Lorentz force compensation of pulsed SRF cavities. In: Proceedings of LINAC2002, Gyeongju (2002)
6. Basak, S., Pandey, H., Chakrabarti, A.: Simulation analysis of analog IQ based LLRF control of RF cavity. In: Proceedings of PCaPAC2012, Kolkata (2012)

Chapter 2
Smart Setup and Accelerometer Mounting Check for Vibration Measurements

Bin Liu, Dmitri Tcherniak, Niels-Jørgen Jacobsen, and Martin Qvist Olsen

Abstract This paper describes some of the challenges experienced by many experimentalists and presents new ways of overcoming these. The Smart Setup can dramatically reduce the time required for the test setup and the presented Accelerometer Mounting Check procedure can check the transducer's health and the integrity of the whole measurement channel. The goal is to get the data right first time and in the shortest possible time.

Keywords Vibration measurement • Smart setup • System verification • Transducer mounting

2.1 Introduction

Performing vibration measurements can be quite time-consuming. In particular, proper mounting of transducers on the test structure, connecting them to the measurement hardware and checking everything is working as expected can be a significant part of the total test time. In addition, this often has to be done under extreme time constraints.

Obviously, not only large scale testing like modal surveys with hundreds of channels, but also smaller scaled tests, can benefit greatly from efficient measurement setup and system verification tools. Ensuring the integrity of each measurement channel becomes even more critical and difficult when transducers are located in remote areas or areas with limited or no access.

This paper first presents the technical background and the implementation of the patented technology called Accelerometer Mounting Check that can secure the health of all channels before and during measurements. Then Smart Setup, the patent-pending technology that can reduce measurement setup time, is introduced. A vibration measurement setup is used to illustrate the entire workflow.

2.2 Technical Background

Typical designs of piezoelectric accelerometer are shown in Fig. 2.1. They all have a similar mechanical principal: the active part of such an accelerometer is one or several piezoelectric elements that together, act as a spring connecting the base of the accelerometer to the seismic mass. When the base is mounted on a test object, its vibrations are transmitted via the accelerometer mount to the base and further to the seismic mass. The force acting on the piezoelectric elements produces a charge proportional to the force acting on it and hence, the acceleration of the seismic mass. Over the operational frequency range, the seismic mass vibrates with the same magnitude and phase as the accelerometer base and the surface on which the accelerometer is mounted [1], and the charge output of the accelerometer correctly reflects the acceleration of the test object.

The direct piezoelectric effect utilized in the accelerometers is a reversible process, that is, the same piezoelectric material exhibits the reverse effect: responding to the applied electrical field, it generates an internal mechanical strain. Applied to the mechanical scheme implemented in the accelerometer, the reverse effect means that subjecting the piezoelectric element with an alternating electric field, one will generate an alternating force acting on the seismic mass and the base. This force will be transmitted via the accelerometer structure and the accelerometer mount to the test object.

B. Liu (✉) • D. Tcherniak • N.-J. Jacobsen • M.Q. Olsen
Brüel & Kjær Sound & Vibration Measurement A/S, Skodsborgvej 307, Nærum 2850, Denmark
e-mail: bin.liu@bksv.com; dmitri.tcherniak@bksv.com; niels-jorgen.jacobsen@bksv.com; martinqvist.olsen@bksv.com

E. Wee Sit (ed.), *Sensors and Instrumentation, Volume 5*, Conference Proceedings of the Society for Experimental Mechanics Series, DOI 10.1007/978-3-319-29859-7_2

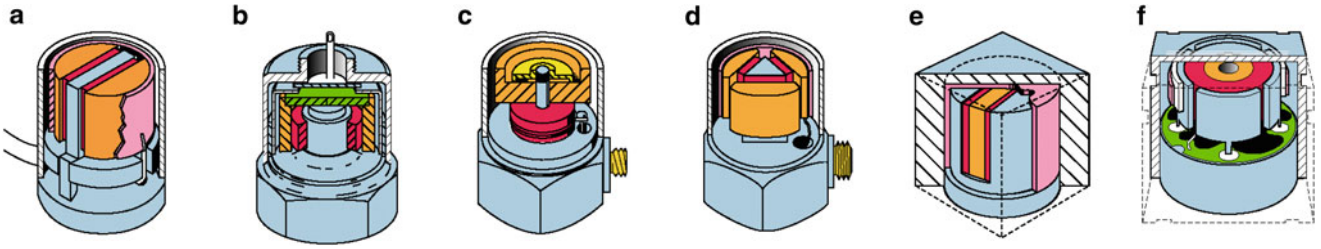

Fig. 2.1 Different designs of piezoelectric accelerometers: (**a**) PlanarShear; (**b**) annular shear; (**c**) centre-mounted compression; (**d**) DELTASHEAR®; (**e**) THETASHEAR®; (**f**) ORTHOSHEAR®

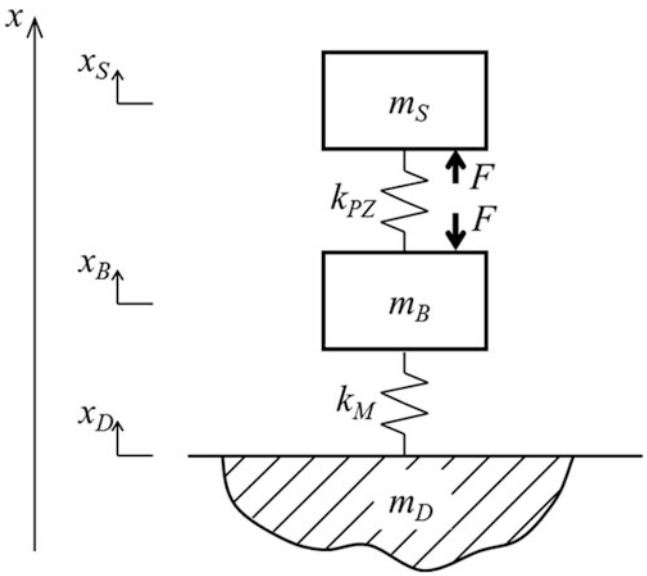

Fig. 2.2 Mechanical system representing the parts of the accelerometer and its mounting

If the accelerometer's output is measured simultaneously with applying the excitation voltage, one can notice that the readings are sensitive to the implementation of the accelerometer mount. This sensitivity is utilized in the Accelerometer Mounting Check technology.

Let us demonstrate the mechanical concept behind the Mounting Check on a simple model. The mechanical parts of the accelerometer, the mount and the test object are modelled as a three degree-of-freedom system (Fig. 2.2). The seismic mass and the accelerometer body, represented by masses m_S and m_B respectively, are connected by the piezoelectric element represented by a spring with linear stiffness k_{PZ}. The mount is modelled as the second linear spring with stiffness k_M, attached to the test object. Mass m_D models the part of the structure, which is involved in the local mechanical vibration of the accelerometer-structure assembly. The forces caused by applying the electric excitation to the piezoelectric element are denoted as F. By varying the parameters, one can observe how the accelerometer mounting (or the absence of mounting) affects the output of the accelerometer.

The equations of motion can be readily set

$$\begin{pmatrix} m_S & 0 & 0 \\ 0 & m_B & 0 \\ 0 & 0 & m_D \end{pmatrix} \begin{pmatrix} \ddot{x}_S \\ \ddot{x}_B \\ \ddot{x}_D \end{pmatrix} + \begin{pmatrix} k_{PZ} & -k_{PZ} & 0 \\ -k_{PZ} & k_{PZ}+k_M & -k_M \\ 0 & -k_M & k_M \end{pmatrix} \begin{pmatrix} x_S \\ x_B \\ x_D \end{pmatrix} = \begin{pmatrix} F \\ -F \\ 0 \end{pmatrix} \tag{2.1}$$

Assuming harmonic excitation $F = F_0 e^{i\omega t}$ and steady state of the system, the equations of motion can be solved. The electric output of the accelerometer is proportional to the forces acting on the piezoelectric element, which are proportional to its deformation $s = x_S - x_B$. The latter can be presented in the form $s(t) = s_0(\omega) e^{i\omega t}$, $s_0 \in \mathbb{C}$, and the expression for the frequency response function (FRF) $H(\omega) = s_0(\omega)/F_0$ can be found analytically or evaluated numerically.

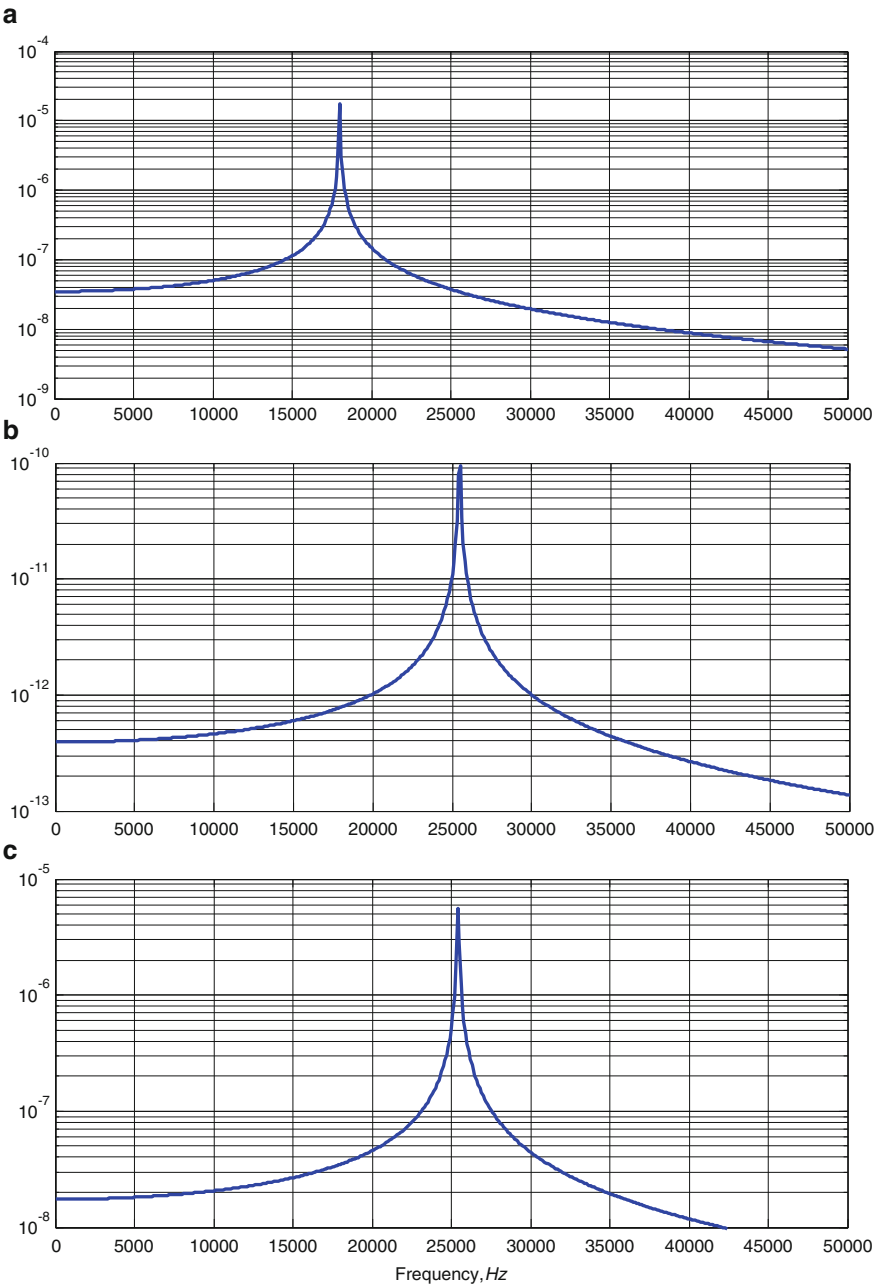

Fig. 2.3 Typical FRF $H(\omega) = s_0(\omega)/F_0$ for (**a**) perfectly mounted on an infinitely heavy object; (**b**) free hanging position; (**c**) mounted on a light structure

Figure 2.3. shows typical FRFs for three limit cases: the accelerometer is perfectly mounted on infinitely heavy structure ($k_M \to \infty,\ m_D \to \infty$), the accelerometer is freely hanging $k_M = 0$ and the accelerometer is perfectly mounted on a very light structure ($k_M \to \infty,\ m_D \to 0$). The other parameters are set to the values typical to miniature Brüel & Kjær accelerometer Type 4507-C.

From the equation of motion (2.1), one can also obtain the values for the resonance frequencies. For the limit cases, they can be obtained from simple expressions [1]: For the accelerometer perfectly mounted on an infinite mass, the value of the *mounted resonance frequency* is

$$\omega_{MR}^2 = \frac{k_{PZ}}{m_S} \tag{2.2}$$

and in *free hanging position*, the resonance frequency is

$$\omega_{FH}^2 = k_{PZ}\left(\frac{1}{m_S} + \frac{1}{m_B}\right) \tag{2.3}$$

These values coincide with the frequency of the peaks in Fig. 2.3a, b respectively. For a typical case when $m_S \approx m_B$, the resonance frequency in free hanging position is about 40 % higher than the mounted resonance frequency: $\omega_{FH} \approx \sqrt{2}\,\omega_{MR}$.

The above mentioned considerations demonstrate that it is possible to evaluate the state of accelerometer mounting based on the FRF estimated in the range between the mounted resonance frequency and the resonance frequency in free hanging position. Thus, if one could measure the FRF in this frequency range, it would be possible to judge if the accelerometer is properly mounted on the structure or if it would fall off.

2.3 Implementation

In brief, Accelerometer Mounting Check technology means sending an electrical excitation signal to accelerometer's piezoelectric element combined with simultaneous measurement of its response.[1] The practical implementation of the technology in industrial products involves a tight interaction between the data acquisition hardware and post-processing software. Let's take Brüel & Kjær LAN-XI modules and PULSE Reflex® software as an example.

2.3.1 FRF Measurement

In practice, the FRF measurement consists of a number of steps:

1. PULSE Reflex® sends the connected LAN-XI data acquisition module(s) a command to start the Accelerometer Mounting Check test.
2. The LAN-XI module, using the built-in signal generator, generates a number of sine sweeps and sends them to the accelerometer; the sine sweeps are generated around the resonance frequency in free hanging position.
3. Simultaneously, the module measures the accelerometer response and sends the digitized data accompanied with the "sweep start" trigger events to PULSE Reflex®.
4. Knowing the chirp characteristics (the start and stop frequencies and the sweep rate), the software reconstructs the sine sweep signals that were employed for exciting the accelerometer. Using the reconstructed signal and the measured response, it calculates the FRF and coherence functions. The noise is attenuated by means of averaging.
5. PULSE Reflex® sends the LAN-XI module a command to end the Mounting Check test.
6. The resulting FRF and coherence function are used as a *characteristic* of the current mounting state.

The FRFs show in Fig. 2.3 are based on analytical expression and a simplified accelerometer-mount-structure model. In reality, the construction of the accelerometer is much more advanced (Fig. 2.1), and the test object and the accelerometer mount cannot be generally represented as a simple mass-string system. Therefore, the real FRF corresponding to the perfectly mounted accelerometer may significantly differ from the analytical one shown in Fig. 2.3a. Examples of the measured FRFs corresponding to different structures and mounting schemes are shown in Fig. 2.4.

2.3.2 Detection of Faulty Mounts

The algorithm behind the Accelerometer Mounting Check technology will say whether the accelerometer is properly mounted on the structure or not, with a simple Yes or No. In *Machine learning* [2], such class of algorithms is called *Classification* or *Decision making*. In broad terms, the Machine learning suggests two ways of implementation: *unsupervised learning* and *supervised learning.*

[1] Patented technology.

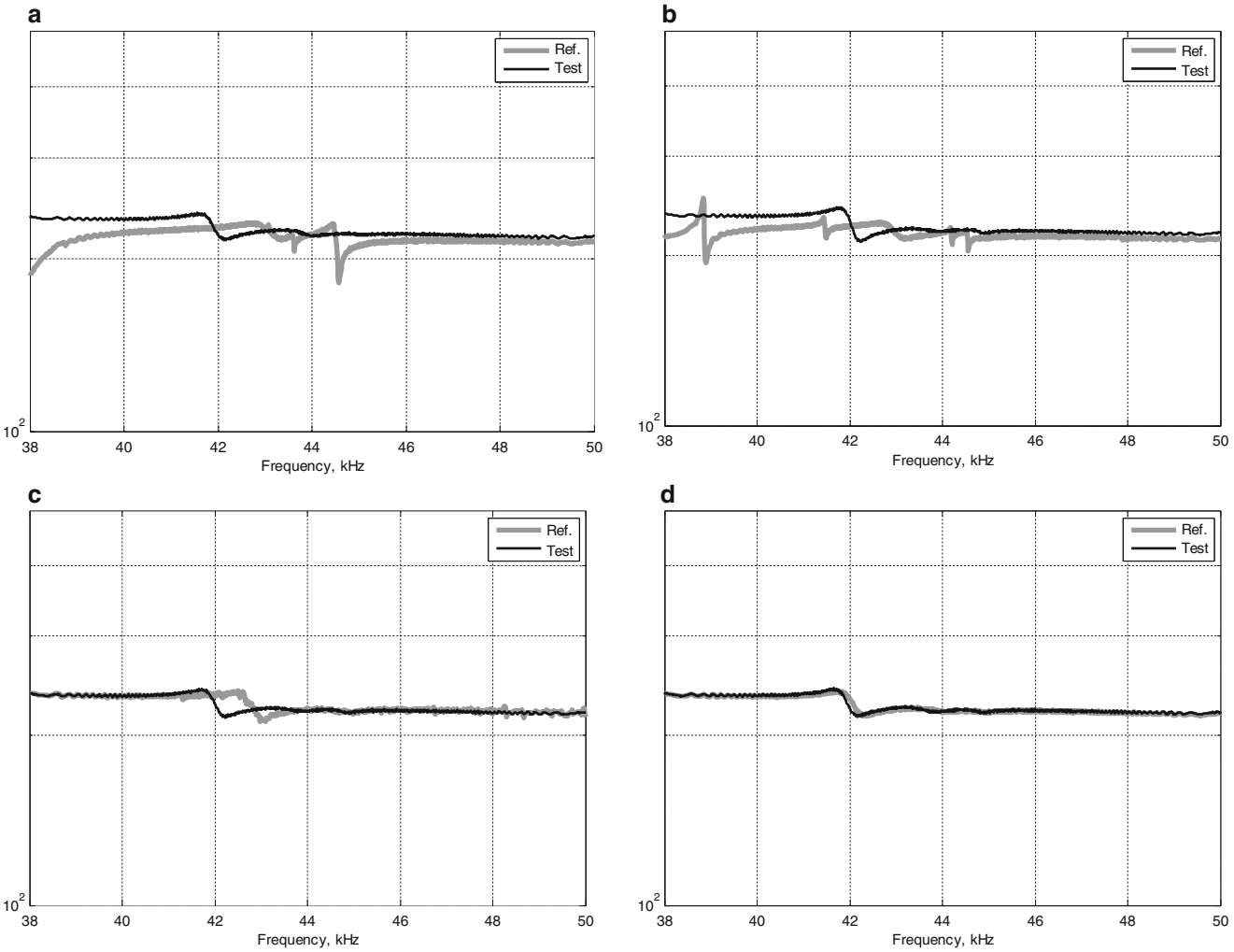

Fig. 2.4 FRFs. Thick grey: proper mount; thin black: the accelerometer falls off the structure. (**a**) heavy steel block, steel stub; (**b**) heavy steel block, beeswax; (**c**) 1.5 mm steel plate, beeswax; (**d**) composite structure (thickness 20 mm), beeswax

The *unsupervised learning* may involve some parametric modelling of the FRF corresponding to the proper mounting (for example, using modal parameters). Then the classification will compare the model of the current state with the reference model of the proper mounting state. The deviations will indicate that the accelerometer is not properly mounted. The implementation of this approach might be difficult since the FRFs corresponding to the proper mounting state may significantly differ, depending on the test object and the mounting techniques (for example, compare the thick curves on Fig. 2.4). Then the opposite approach can be taken: comparing the thin curves in Fig. 2.4, one can notice that the FRFs corresponding to the improper mounting are very similar, and thus, using the improper state as the reference can be more sensible. Then, if the current state is different from the reference state, the mounting is good, and if the current state is close to the reference state, the mounting is bad.

In the case of the *supervised learning*, every time we mount the accelerometer on the structure, we measure and store the reference state. During the measurement campaign, we measure the current state and compare it with the reference state. The difference in the states indicates that something has happened with the mounting and it needs to be checked.

The present Accelerometer Mounting Check implementation utilizes the supervised learning. For the user of the system, it involves the following steps:

1. The user mounts the accelerometers on the test object and connects them to the data acquisition modules.
2. When the process is completed, the user makes sure that all accelerometers are mounted correctly.
3. The Mounting Check "Create reference" procedure is started via PULSE Reflex® GUI. Internally, this procedure involves the number of steps described in Sect. 3.1 but it is initiated by a single command (mouse-click). Then the "reference state" (consisting of the FRF and coherence curves), reflecting the correctly mounted accelerometers, is stored.

4. The user starts the measurements. Once in a while, between the tests, the user initiates the "Check mounting" procedure, which is called via PULSE Reflex® GUI. This procedure involves exactly the same steps as described above (see Sect. 3.1).
5. The FRF and coherence curves generated in the last step are compared with those of the reference state. If the current and reference states differ significantly, the software informs the user about the potential problem with the accelerometer mounting, providing the information where the accelerometer is mounted (for example, its DOF or its location in setup geometry, if available). If the current state does not differ from the reference state, the system informs the user that all accelerometers are mounted correctly.

2.3.3 *Classification Algorithm*

As mentioned earlier, Accelerometer Mounting Check is implemented via a classification algorithm with supervised leaning. Depending on the mounting state, the classifier puts the samples into two classes: (1) "Proper mounting" and (2) "Improper mounting." The classifier uses *features*, which is a reduced set of relevant parameters characterizing the class. To make the algorithm more robust to noise, we use two features. The first feature characterizes the difference between the reference FRF and the current FRF; this is a normalized scalar product of two FRFs' magnitude weighted by the corresponding coherence values:

$$f_1 = \frac{\sum_{\omega_1}^{\omega_2} \gamma_R^2(\omega)\,\gamma_C^2(\omega)\,|H_R(\omega)|\,|H_C(\omega)|}{\sum_{\omega_1}^{\omega_2} |H_R(\omega)| \sum_{\omega_1}^{\omega_2} |H_C(\omega)|} \tag{2.4}$$

where the subscripts R and C denote the reference and current states respectively, $\gamma^2(\omega)$ is the coherence function and $[\omega_1;\ \omega_2]$ is the frequency range of interest. The second feature is the coherence index:

$$f_2 = \frac{1}{N} \sum_{\omega=\omega_1}^{\omega_2} \gamma_C^2(\omega) \tag{2.5}$$

where N is the number of frequency lines in the $[\omega_1;\ \omega_2]$ range. As one can notice, $f_1, f_2 \in [0; 1]$.

Each state of the system can be presented as a point in the features space. For the two features' classification problem, the state is a point with coordinates f_1 and f_2 (Fig. 2.5) on the (f_1, f_2) coordinate plane. Collecting several points representing the proper and improper mounting states, two clusters will be formed, in Fig. 2.5 they are colored green and red respectively.

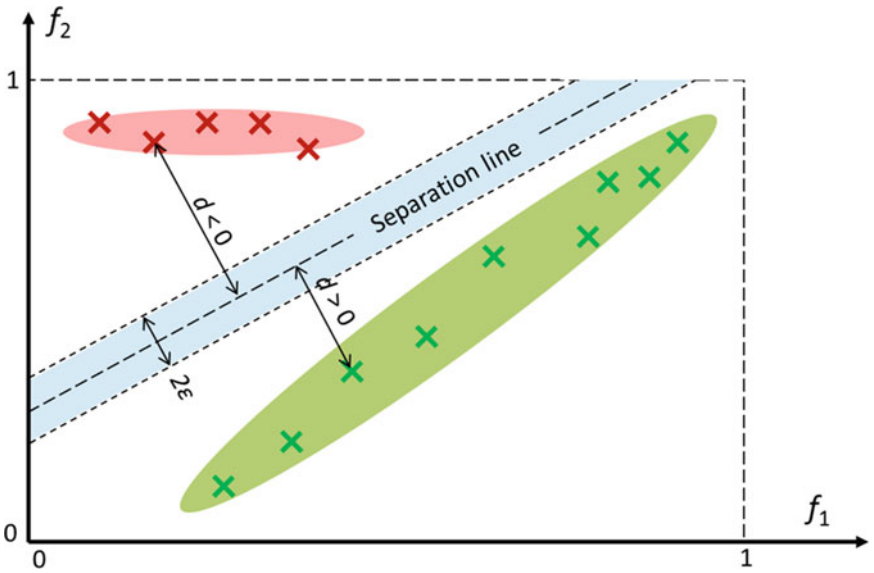

Fig. 2.5 Schematic view of the two features' space. Green crosses: the states representing the proper mounting, red crosses correspond to the states with improper mounting. Linear classification is represented by the separation line

A linear classifier can be presented as a line separating the clusters; the equation of the line on the (f_1, f_2) coordinate plane is $w_1 f_1 + w_2 f_2 + w_3 = 0$. The coefficients $w_1 \ldots w_3$ can be found experimentally, and they are invariant to the type of accelerometer, the mounting method and the test structure. The distance d between the point with coordinates (f_1, f_2) and the line is calculated as $d = w_1 f_1 + w_2 f_2 + w_3$. If $d > 0$, the point is below the separation line and represents the proper mounting. In contrast, the points with $d < 0$ are classified as belonging to the "Improper mounting" class. If the point is too close to the separation line, $|d| < \epsilon$, it can be classified as uncertain.

2.4 Smart Setup

When making measurements, it is often a challenge to align the degrees of freedom (DOF) information (Component ID, Node ID and DOF Direction) for transducer placement on the test object with the measurement software. Entering type numbers, serial numbers and transducer placement information manually into the measurement software is time-consuming and error prone.

The smart transducer setup scans the Data Matrix Code engraved on the transducer using the Transducer Smart Setup app available for iOS devices (iPhone, iPad and iPod touch) on iTunes (Fig. 2.6). This helps eliminate the time-consuming manual processes to mount transducers. It also keeps track of the mounted transducers in the data acquisition process.

Data Matrix Codes use Reed-Solomon error correction codes for reliable reading, regardless of scratching or denting from regular use of the accelerometer. The matrix codes can be generated to be used to encode DOF information (location and ID number) for the test setup.

The Transducer Smart Setup app helps register the DOF information correctly and enriches this with transducer metadata. The information can be loaded into PULSE Reflex to simplify setting up the data acquisition and analysis tasks. The Smart Setup smartphone app has a patented algorithm that automatically detects the orientation of an accelerometer by scanning the code, making sure that the transducer is synchronized with PULSE Reflex for faster setup and easier measuring.

Even without the app, one can scan the data matrix code with any 2D barcode scanner and get immediate access to detailed transducer information, including calibration data.

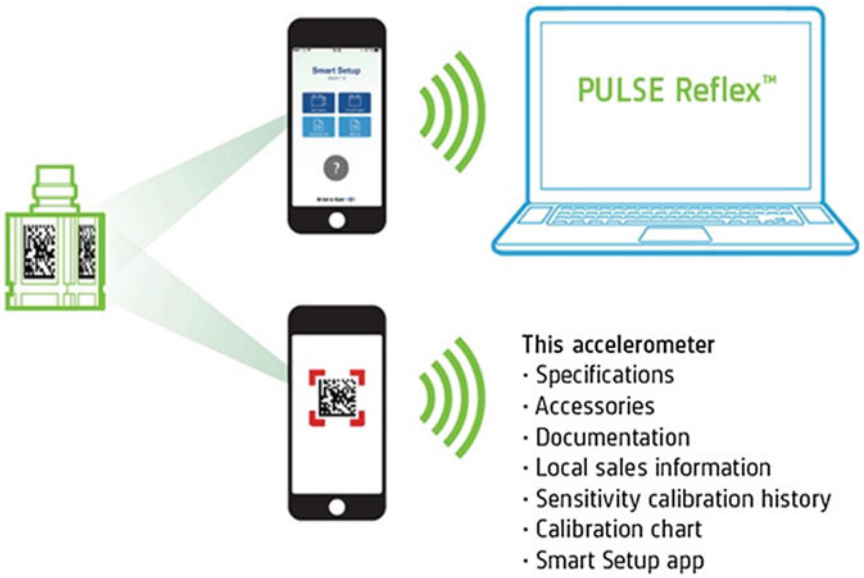

Fig. 2.6 Illustration of Smart Setup workflow

2.5 Vibration Measurements

For every vibration measurement, proper mounting of transducers on the test structure, connecting them to the measurement hardware and checking that everything is working as expected, is time-consuming. When measuring on a big structure requiring a multichannel test system, it is even more crucial to do the above steps properly because the correct data must be acquired first time.

The test object with mounted accelerometers is shown in Fig. 2.7. In total, 25 triaxial CCLD accelerometers are used. A triaxial accelerometer, engraved with Data Matrix code on three surfaces, is shown in Fig. 2.8a. The codes engraved on the different surfaces are different, and each code indicates the measurement direction. The data matrix code printed on the sticker contains DOF information including location and node number, which are predefined by the user. Figure 2.8b shows the scanning of the code using a mobile phone.

When the transducers are mounted with the help of Smart Setup, Accelerometer Mounting Check can help to ensure that the mounted accelerometers are mounted correctly following the procedure described in Sect. 3.2.

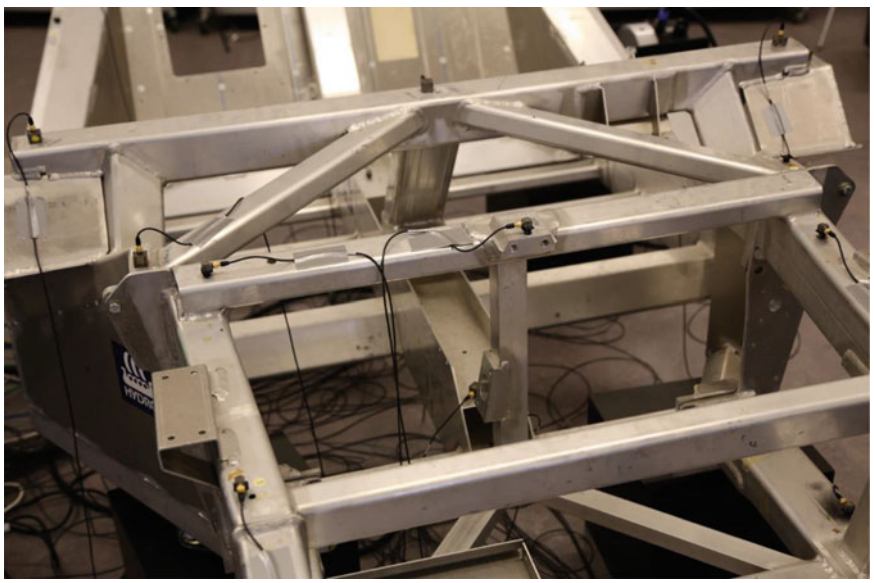

Fig. 2.7 Test object with accelerometers mounted

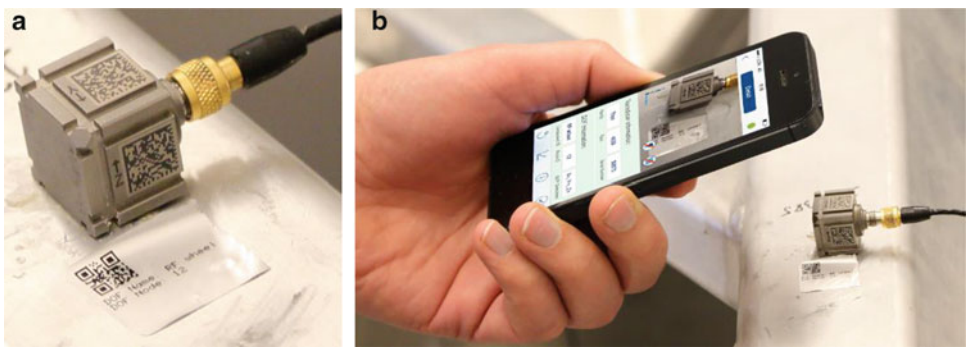

Fig. 2.8 (**a**) Accelerometer with engraved Data Matrix Code; (**b**) Scanning the Data Matrix Code using the Transducer Smart Setup app

2.6 Conclusion

The paper presents two innovative methods of efficiently conducting vibration measurements. Smart Setup, using the Data Matrix Code and an easily selected measurement coordinate system, reduces the setup time. Accelerometer Mounting Check ensures the health of all channels before and during measurements.

References

1. Serridge, M., Licht, T.R.: Piezoelectric accelerometers and vibration preamplifier handbook. K. Larsen & Søn A/S, Glostrup, Denmark (1987)
2. Bishop, C.M.: Pattern recognition and machine learning. Springer, New York, USA (2006)

Chapter 3
NVH Development at Achates Power

Hasan G. Pasha, Dnyanesh Sapkal, and John Koszewnik

Abstract Achates Power, Inc (API) has developed radically improved internal combustion engines that increase fuel efficiency, reduce greenhouse gas emissions and cost less than conventional engines. Achates Power has perfected the opposed-piston engine that enables to achieve the world's most stringent current and future fuel efficiency, and emissions standards. The opposed-piston engine presents unique challenges in terms of structural design due to its construction. A sophisticated design process that encompasses advance modeling, simulation and testing facilities is necessary to deliver best-in-class NVH characteristics. Achates Power's engine development is driven by a well-defined and efficient process to provide excellent noise, vibration and harshness (NVH) characteristics. This paper discusses the process followed and the infrastructure available at Achates Power to guide the NVH development.

Keywords Opposed piston engine • A48-3 • NVH • Verification and validation • Modal testing • Multi-body systems

Notation

API	Achates Power, Inc
CAD/CAE	Computer Aided Design/Computer Aided Engineering
FEA	Finite Element Analysis
FRAC	Frequency Response Assurance Criteria
MAC	Modal Assurance Criteria
MBS	Multi-Body System
MPRR	Maximum Pressure Raise Rate
NVH	Noise, Vibration and Harshness
OP2E	Opposed Piston Two-Stroke Engine
PCI	Peripheral Component Interconnect
PXI	PCI eXtensions for Instrumentation
SPL	Sound Pressure Level
V & V	Verification and Validation

3.1 Introduction

One of the most crucial automobile design requirements is good noise, vibration and harshness (NVH) characteristics as they impact ride comfort and customer perception. In addition, good NVH characteristics are necessary to satisfy stringent environmental standards. Moreover, excessive vibration can cause durability issues.

Fundamental to any good NVH development process is understanding the noise and vibration sources and applying NVH design and material selection guidelines upfront. Most commonly observed NVH issues in the powertrain are related to combustion noise, torsional vibration of the powertrain components, geartrain rattle/excitation, excitation resulting from engine imbalance, poorly designed engine mounts, structural vibration/transmission of powertrain components, air handling system, accessory noise sources, etc.

H.G. Pasha (✉) • D. Sapkal • J. Koszewnik
Achates Power, Inc., San Diego, CA, USA
e-mail: pasha@achatespower.com

E. Wee Sit (ed.), *Sensors and Instrumentation, Volume 5*, Conference Proceedings of the Society for Experimental Mechanics Series, DOI 10.1007/978-3-319-29859-7_3

In the subsequent sections, background on the Achates Power A48-3 engine is provided and the NVH development process adopted at Achates Power is described.

3.2 Achates Power Opposed-Piston Two-Stroke A48-3 Engine

In an opposed-piston engine, two pistons facing each other come together at the top dead center in a single cylinder. The piston crowns form the combustion chamber and they move apart under combustion (Fig. 3.2). Opposed-piston two-stroke diesel engines have a great cost and weight advantage over conventional diesel engines because of their low complexity (no cylinder head, no valve train, etc.). Reference [4] provides a general treatise on history and evolution of opposed piston engines.

Achates Power, Inc (API) has developed radically improved internal combustion engines that increase fuel efficiency, reduce greenhouse gas emissions and cost less than conventional engines. Achates Power has perfected the opposed-piston two-stroke engine (OP2E) that enables to achieve the world's most stringent current and future fuel efficiency, and emissions standards [5]. Achates Power's A48-3 three-cylinder OP2E is shown in Fig. 3.1 and the technical specifications are listed in Table 3.1.

Truck engines have to last more than a million miles. In addition to the combustion process, major emphasis is placed on durability and dynamics of the powertrain at Achates Power.

Fig. 3.1 Achates Power A48-3 opposed piston two-stroke engine

Table 3.1 A48-3 engine technical specifications [5]

Engine type	Opposed piston two-stroke engine
Maximum power	53 kW/cylinder @ 2160 rpm
Maximum torque	334 Nm/cylinder @ 1390 rpm
Number of cylinders	Three
Displaced volume	1.64 L/cylinder
Stroke	215.9 mm
Bore	98.425 mm
Maximum BMEP	12.8 bar
Trapped compression ratio	15.6:1

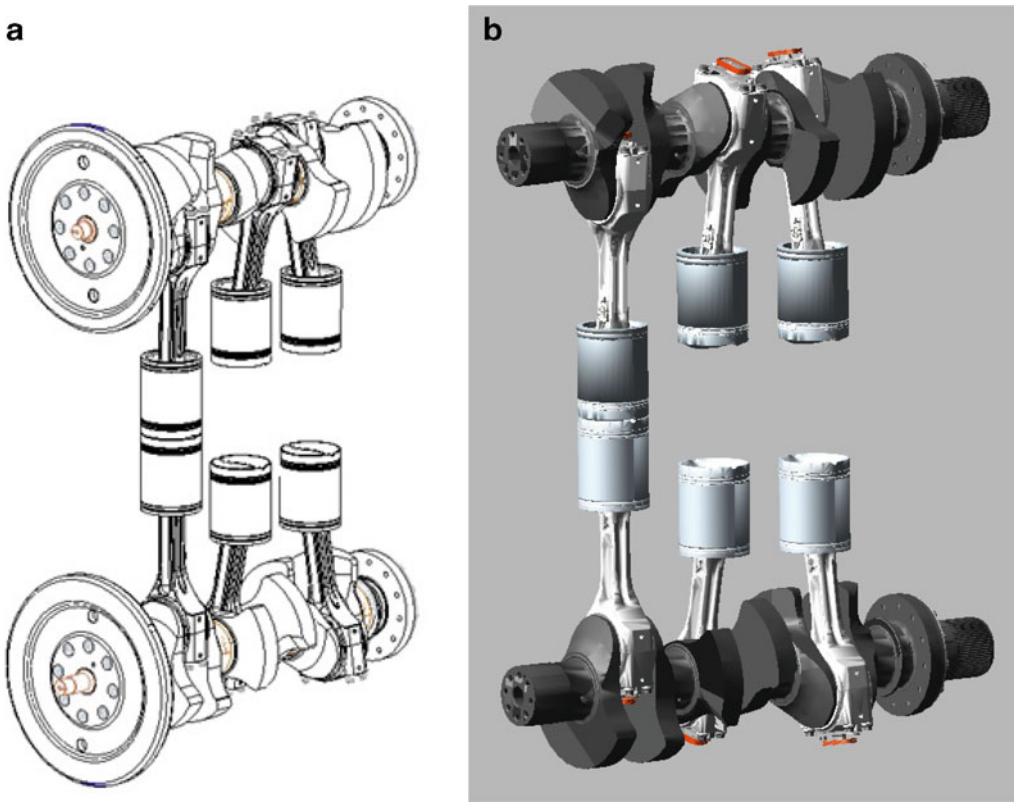

Fig. 3.2 Cranktrain of the A48-3 engine (**a**) CAD (**b**) MBS Model

3.3 Powertrain Related NVH Sources

Development of a well refined vehicle requires the understanding and controlling various noise and vibration sources. The major noise and vibration sources in powertrains are discussed below.

(1) *Combustion noise:* The combustion process in an engine causes a rapid rise in the pressure. This pressure rise rate is one of the main factors known to affect the combustion noise. The maximum pressure rise rate (MPRR) is directly proportional to the sound pressure level (SPL) [7]. Inherently, an opposed-piston engine can expand volume at a faster rate than a conventional four-stroke engine for a specified MPRR. Achates Power has laid the engine design guidelines to limit the MPRR to less than 3 bar/crank angle degree on passenger car applications and less than 10 bar/crank angle degree on commercial truck applications.

(2) *Torsional vibration of crankshaft:* Periodic combustion impulses cause torque pulsations and rotational speed fluctuations of the crankshaft, which result in crankshaft torsional vibrations [1]. All structures are flexible to a certain degree. Though crankshafts are designed to be very stiff, they can twist due to excitation. The nature and degree of twisting depends on the excitation and the crankshaft design. Understanding and controlling torsional vibration is important in the powertrain NVH development.

(3) *Geartrain rattle/excitation:* The torsional vibration due to the fluctuations of torque causes gears to become periodically unloaded, which can produce a high noise level [9]. Geartrain rattle affects not only noise but also engine performance and durability [2]. In the A48-3 engine, the intake and exhaust crankshafts are connected using a geartrain with typically five gears, one on each crankshaft, two idler gears and a power takeoff gear. Various concepts have been designed for good NVH characteristics. Currently, these concepts are being tested at Achates Power's engine test cells. More details and results will be forthcoming.
(4) *Excitation resulting from engine imbalance and engine mounts:* Unbalanced forces and moments generated by engine operation result in noise radiation from engine surfaces and structure-borne noise [6]. The shaking forces of the A48-3 engine are significantly less compared to a four-stroke 90° V8 diesel engine of comparable power (in which the first order moments are completely balanced). The pitch moment of the A48-3 engine is comparable to that of a much smaller passenger car engine with outstanding NVH characteristics. The yaw moment of the A48-3 engine is insignificant in comparison. The unbalanced moments and shaking forces can be easily managed with the appropriate engine mount strategy.
(5) *Valvetrain related engine imbalance effects:* The imbalance effects in the valvetrain of four-stroke engines can cause NVH issues. The valvetrain unbalanced moments can be nearly as large as the cranktrain unbalance [8]. Due to the unique opposed-piston architecture, there are no valvetrains, camshafts, pushrods, rocker arms, valves, valve springs, valve keeps and other parts used in conventional powertrains [5]. This offers benefits in terms of NVH, durability and cost.
(6) *Structural vibration and transmission from powertrain components:* On a three-cylinder two-stroke engine, the predominant frequencies of interest will be:

- First order—primarily from the cranktrain inertia, which can be offset by crankshaft counterweights
- Third order—due to the firing frequency

The structural components should be designed to be stiff in the engine operating range. At Achates Power, design guidelines have been laid down to insure these conditions.

In addition, NVH issues are also caused by accessories (manifolds/air handling system, front-end accessory drive, fuel pump, turbocharger, supercharger, water pump and oil pump) and mechanical sources (piston slap and injector tick).

3.4 Achates Power's NVH Development Process

The opposed-piston engine presents unique challenges in terms of structural design due to its construction. A sophisticated design process that encompasses advance modeling, simulation and testing facilities is necessary to deliver best-in-class NVH characteristics. Achates Power's engine development is driven by a well-defined and efficient process based on a V-Model shown in Fig. 3.3, in order to insure excellent noise, vibration and harshness (NVH) characteristics.

The process starts with overall engine NVH targets that are set based on the actual engine, the environment where it will operate and the noise related regulations. These are cascaded down to quantitative requirements for individual components. Upfront target setting and cascading of these targets guides CAD/CAE to achieve the desired goals in the early stages of a program, avoiding delays and rework. In addition, the components that affect the NVH bottom line are identified early thereby increasing the efficiency of the design process.

3.5 Design, Modeling and Simulation

Validated models can reduce model uncertainties and potentially lead to reduction of empirical margin requirements and designs with improved performance, improved durability and reduced weight. In addition, improved model accuracy can reduce the potential for re-design and re-test, thereby saving time and money.

At Achates Power, a lot of emphasis is placed on modeling and simulation using the verification and validation (V&V) framework. Components are designed using NVH guidelines. Finite element (FE) models are developed to perform static and dynamic structural analyses. Currently, ANSYS Workbench® software is used for finite element analysis (FEA).

At the subsystem and system level, multi-body system (MBS) dynamic simulations are performed for validating and guiding design decisions aimed to reduce noise and vibration associated with the OP engines. Currently, MSC Adams®

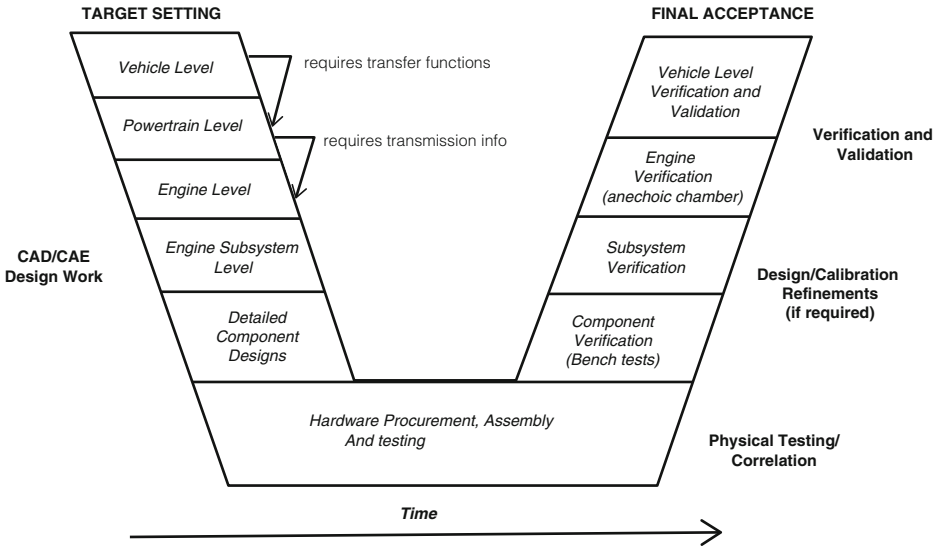

Fig. 3.3 NVH development process

software is used for performing MBS modeling and simulation. The MBS simulation helps in identifying modes and natural frequencies. It also assists in performing forced vibration response and estimating the dynamic loads acting on various components. The MBS results feed in to durability and acoustic analyses. At Achates Power, validated MBS models have been employed to perform design sensitivity studies, for example to understand the effect changing flywheel inertia on the torsional behavior of the cranktrain, etc.

3.6 Testing Facilities

Achates Power has two engine test cells and a third test cell is currently under development. These engine test cells are equipped with dynamometers and have state-of-the-art data acquisition systems. The Test Cell 2 driveline is shown in Fig. 3.4. The test cells have a capacity to acquire 40 channels of data using a PXI based NI system that can be configured for acquisition in the time or the crank angle domain (Fig. 3.5). A wide array of sensors including accelerometers, pressure sensors, torque sensors, and shaft, are used to acquire data on the engine at various loading conditions.

In addition to the dynamometer test cells, API has a component testing lab equipped with an NI PCI-6143 16-channel data acquisition system. Additional data acquisition hardware, sensors and equipment to facilitate engine NVH development was recently procured. This includes an impact hammer, additional accelerometers, microphones and signal conditioners. NI LabVIEW® and SDRL X-Modal® software packages are being used for data acquisition and data processing. With this infrastructure, modal testing and acoustic data acquisition can be performed at Achates Power's test cells.

3.7 Testing

3.7.1 Bench Testing

At the component level, modal testing is performed for calibrating and validating FE models. Analysis of experimental data is performed with a focus on estimating natural frequencies, damping factors, modal vectors and modal scaling. Calibration and validation is performed by correlating the modal parameters obtained from the FE and test models. The percentage difference in modal frequencies, cross-Modal Assurance Criteria (MAC), Frequency Response Assurance Criteria (FRAC), etc. are used as validation metrics.

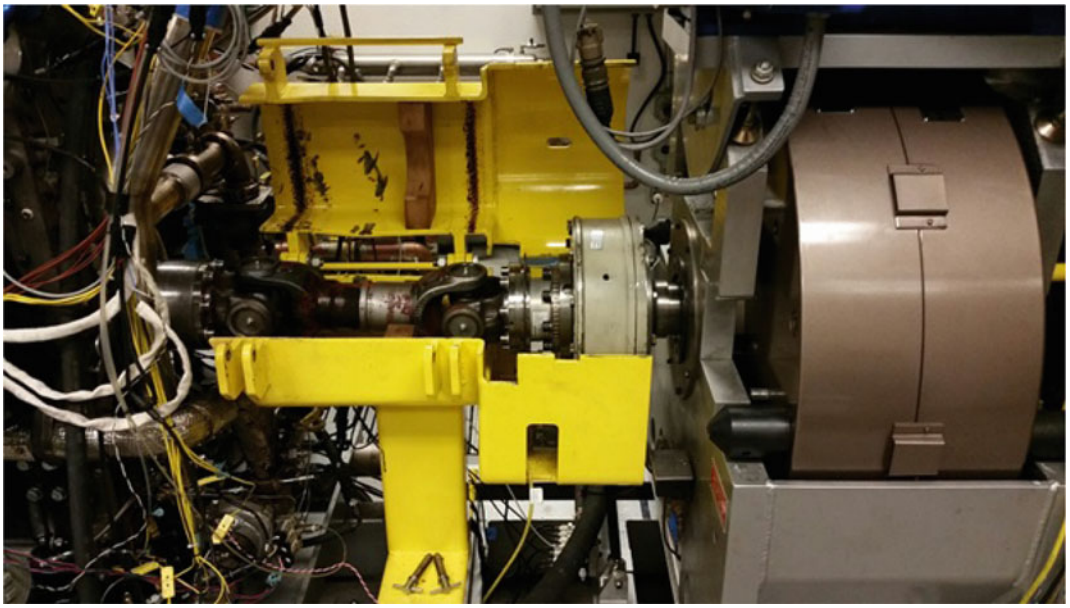

Fig. 3.4 Achates Power Test Cell 2 driveline

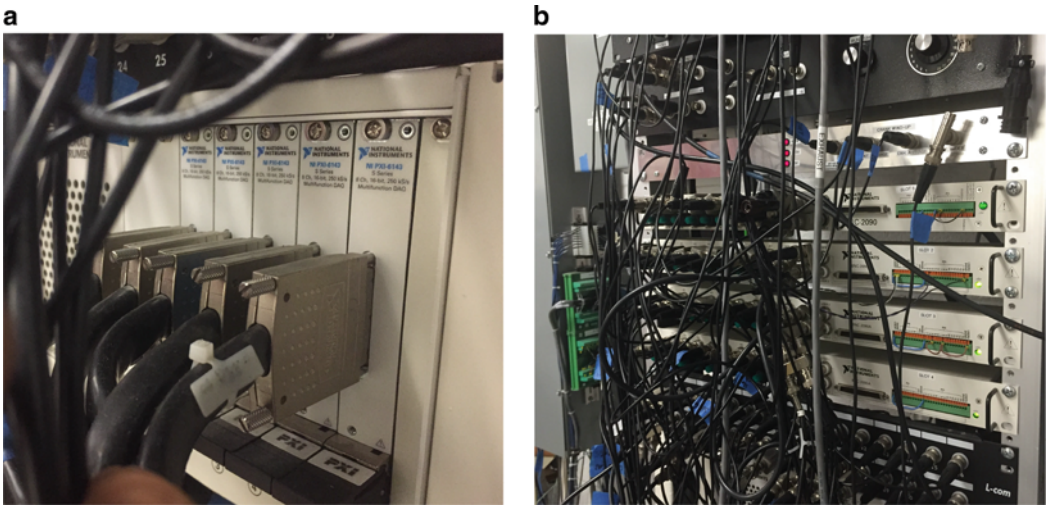

Fig. 3.5 PXI based NI system at Achates Power's test cell

3.7.2 Torsional Vibration Measurement

Physical testing under various operating load conditions is conducted using the dynamometer in the engine test cells to identify modes, frequencies and acoustic hotspots. The acquired data is used to correlate and validate the MBS and vibro-acoustic model predictions.

The torsional vibration in the engine is characterized by the angular position of the rotating components—crankshafts or gears. The crank angle encoder provides the basis for all crank-angle-related measurements of the engine. The encoder used at Achates Power consists of an optical angle encoder, a signal conditioner and a line terminator. It generates two transistor-transistor logic (TTL) rectangular-pulse signals [3]. Encoders are mounted on both crankshafts. The intake crankshaft triggers the acquisition of crank-angle-related data. A single block of the acquired data consists of data for 24 engine cycles captured at $\frac{1}{2}^{\circ}$ crank angle resolution (17,280 samples). Crankshaft wind-up is a measure of one crankshaft's position relative to the other. The output from the encoders on the crankshafts is processed to provide the crankshaft wind-up. The time histories of windup and loads from the MBS simulations and the test data are used to perform correlation.

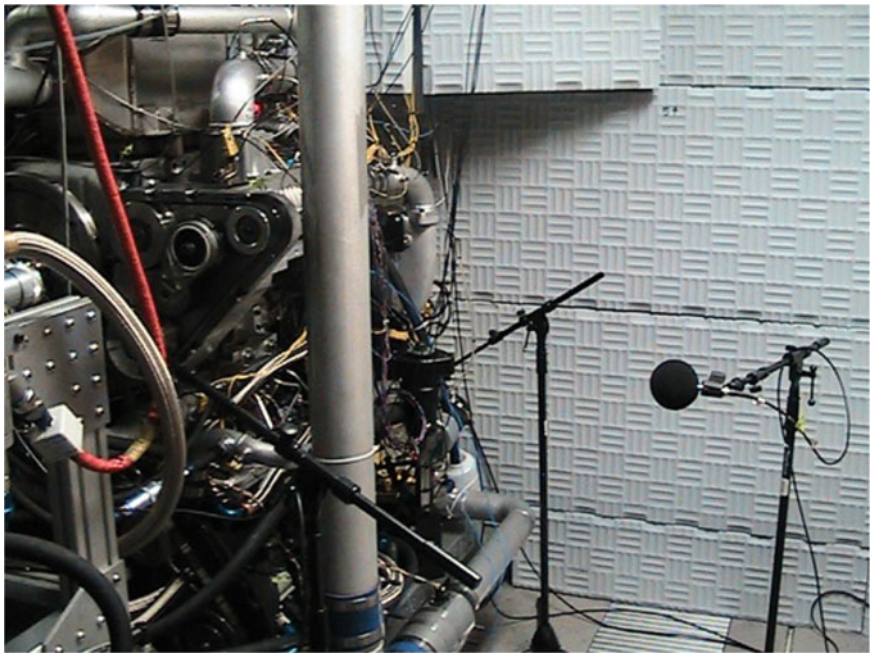

Fig. 3.6 Vibro-acoustic testing conducted on the A48-3 engine

3.7.3 Vibro-Acoustic Testing

Vibro-acoustic testing to compare the NVH characteristics of two different gearboxes has been conducted. The test setup is shown in Fig. 3.6. As part of these tests, acoustic array mapping of sound power hotspots and accelerometer mapping of structural vibration was performed. The results from the tests were helpful in discerning the benefits of the design concepts and contrasting the two gearboxes on their NVH performance.

3.8 Summary and Conclusions

Achates Power, Inc (API) has developed radically improved internal combustion engines that increase fuel efficiency, reduce greenhouse gas emissions and cost less than conventional engines. Various noise and vibration sources can present NVH related challenges during a typical powertrain development and integration process. The opposed-piston engine presents unique challenges in terms of structural design and NVH due to its construction. An integrated simulation and test based design process, in which NVH related targets are cascaded down to the component level is necessary to deliver good NVH characteristics. Achates Power's engine development is driven by a well-defined and efficient process that encompasses advance modeling, simulation and testing facilities to provide best-in-class noise, vibration and harshness (NVH) characteristics.

Acknowledgements The authors would like to acknowledge the contributions and support from Chris Pesko of Achates Power and Siemens LMS Engineering Services.

References

1. Adamson, S.: Improved Approaches to the Measurement and Analysis of Torsional Vibration. SAE Technical Paper 2004-01-1723 (2004)
2. Derk, J.R.: Effects of compliant geartrains on engine noise and performance. Sound Vib. Mag. (2005)
3. Kistler: Product Specifications for Kistler 2614B Crank Angle Encoder. Kistler Instruments (2015)
4. Pirault, J.P., Flint, M.: Opposed Piston Engines: Evolution, Use, and Future Applications. SAE International, Warrendale, PA (2010)

5. Regner, G., Fromm, L., Johnson, D., Koszewnik, J., Dion, E., Redon, F.: Modernizing the Opposed Piston, Two Stroke Engine for Clean, Efficient Transportation. SAE Technical Paper 2013-26-0114 (2013)
6. Reinhart, T.E.: NVH Considerations in Engine Development, Encyclopedia of Automotive Engineering. Wiley, New York (2014)
7. Selim, M.: Effect of exhaust gas recirculation on some combustion characteristics of dual fuel engine. Energy Convers. Manag. 44, 707–721 (2003)
8. Stout, J.: Valvetrain Unbalance and Its Effects on Powertrain NVH. SAE Technical Paper 971993 (1997)
9. Vance, J.M., Zeidan, F., Murphy, B.: Machinery Vibration and Rotordynamics. Wiley, Hoboken, NJ (2010)

Chapter 4
35 Years with Structural Measurements at Brüel & Kjær

Svend Gade and Henrik Herlufsen

Abstract Both Gade & Herlufsen started working for Brüel and Kjær Company, when the modern era of structural measurements began in the early 1980s. In (Brown and Allemang, Sound Vib Mag 19–25, January 2007), it is even argued that the modern era of Experimental Modal Analysis already started one or maybe two decades earlier. In 1982 we participated at IMAC I, the first international modal analysis conference at Hyatt Orlando, USA—the time considered when modal analysis changed from being a pure scientific concept to be a practical engineering tool. Many tests were at that time limited to Single Input/Single Output, SISO measurements. In 1983, we were involved in the release of Brüel and Kjær's first Dual Channel Signal analyzer. Today Dual channel FFT analysis is the established method of performing Frequency Response Function measurements used for what we might call classical mobility based modal testing and analysis. Over the years, we have seen progress and development in all fields of the measurement chain from the input vibration transducers via the signal conditioning to the analog to digital conversion, real time- and post-processing of functions followed by modal parameter estimation and applications of the modal model. This paper will deal with what we see (and we both have been involved with from a Brüel & Kjær perspective) as some of the most important/biggest steps achieved in this progress. Today it is not unusual that modal analysis is performed using several hundreds of high dynamic range measurement channels connected to dedicated smart modal accelerometers (with build-in Transducer Electronic Data Sheets (TEDS)) doing Multiple Input Multiple Output measurements with automated modal parameters estimation and model correlation with large Finite Element models.

Keywords History • Modal analysis • Hardware • Software • Accelerometers

4.1 Background

We were both employed during the first half of 1980 as application engineers at the B&K sales department/headquarters in Denmark. Some of our first responsibilities were to run Frequency Analysis and Digital Signal Analysis courses both internally as well as for customers. Our reference books were Frequency Analysis written by Bob Randall [1], who was also our colleague back then, as well as a Fourier analysis book written by Oran Brigham [2]. From these sources and our colleague/mentor Niels Thrane, we learned what we initially needed to know about analog and digital frequency analysis. Using digital techniques was rather new to many of our customers and colleagues so there was really a need for training people in topics like Fast Fourier Transform (FFT), sampling, aliasing, convolution, weighting functions, uncertain principle, units/scaling etc. and also to operate and demonstrate the new and more complex digital instrumentation. At that time our digital analyzers were single channel instruments basically measuring auto spectra either by Digital Filtering (1/n octaves—acoustics) or FFT (narrowband—vibration) techniques, but Brüel and Kjær were in progress of development of Dual Channel Signal Analyzer Type 2032, including preparing the largest release activity at that time. We were heavily involved with testing the functionality, learning about and understanding dual channel concept, including reading/studying a newly released and very inspiring book of Bendat & Piersol [3], and much more. In addition, we were writing application notes, sales training notes and even one of the manuals for the dual channel analyzer. April 1, 1983 several application/sales engineers in groups of two went on a worldwide tour introducing the Type 2032 analyzer, which became an instant success for the B&K company, see Chap. 19, "Training for Success" in Ref. [4]. Herlufsen & Gade started their tour in UK by having to rush in a Volvo station wagon from Copenhagen to Harwich in order to reach the ferry from Esbjerg to Harwich just in time carrying two brand new 2032 instruments with last minute updates. We carried transducers (including a newly developed modal

S. Gade (✉) • H. Herlufsen
Brüel & Kjær Sound & Vibration Measurement A/S, Skodsborgvej 307, Nærum, 2850 Denmark
e-mail: sgade@bksv.com

E. Wee Sit (ed.), *Sensors and Instrumentation, Volume 5*, Conference Proceedings of the Society for Experimental Mechanics Series, DOI 10.1007/978-3-319-29859-7_4

impact hammer) and we were on the road for quite some time covering several countries. Probably the most important new application we introduced and demonstrated was hammer based mobility measurements and just informing about the easy extension from dual channel FRF measurements to modal analysis.

4.2 Cross-Spectrum Signal Analyzers

Besides a very large display, Dual Channel Signal Analyzer Type 2032 was unique in several ways. It was the first analyzer on the market that used the concept of measuring at any time what we called "total documentation" namely the two auto-spectra and the complex cross-spectrum (and the last block of the two input time signals). All other functions were just derived/post-processed (in real time) from these fundamental three spectra. The list of function were long (actually 34) including Frequency Response Function (FRF), Coherence, Impulse Response Function, Auto- and Cross-correlation, Cepstra and Sound Intensity just to mention a few. Type 2032 was using in parallel three processors that worked independent of each other, ensuring same high real-time speed of 6 kHz (in dual channel mode) no matter what kind of function was displayed during measurements. A measurement processor controlled by a measurement setup was processing the three basic spectra, a display processor controlled by display setup parameters made further processing of the three basic spectra ensuring a reasonable high update live display performance of the desired functions and finally a zoom processor was used for decimation (including low-pass filtering and zooming) of data.

In contrast to other companies on the market, we decided to use the terminology Frequency Response Function (frequency domain) rather than Transfer Function (Laplace domain), since at least in modal analysis application it is important to clearly distinguish between these two domains. Most other companies called their similar instruments for Transfer Function Analyzers, TFA. Furthermore, it was the first analyzer on the market that offered several different FRF estimators, H1, H2 and H3 in order to handle noise at either input or output. A 2034 version with reduced real-time speed was available for embargo reasons.

We knew there was a need for more than just two channels in modal applications, but it was not until 1991 before Multichannel Analysis System Type 3550 (Type 2035 Signal Analyzer Unit in Dual Channel configuration) was ready for release. Type 3550 was based upon same principles and quite similar hardware as Type 2032, but visually extended with a floppy disk drive, see Fig. 4.1. 3550 featured a number of advanced options such as order tracking analysis, 100 kHz frequency range, multichannel option etc. The maximum number of channels was 16 and 3550 was able to do Multiple Input Multiple output (MIMO) measurement. In practical situations MIMO was basically limited to two inputs (two shakers, see Fig. 4.2) in order to limit the number of cross-spectra calculations and for not reducing the number of FFT lines from the "standard" 800 lines.

In the meanwhile, personal computers entered the market and Type 3550 was based on older technology. Thus, we developed the so-called PULSE analysis system, which we introduced in 1996. It was unique in several ways. It was the first multichannel (up to max. 32 channels at release) real-time analysis system on the market that was PC and MS Windows (Windows NT ver. 3.51) based and being able to do multi-analysis, i.e. the possibility of doing various analysis tasks simultaneously including direct reporting in MS Office. Number of FFT lines were selectable in binary steps from 50 to 6400, thus nearly eliminated the need for zoom measurements. First release was based on the 3550 input modules, but today PULSE is using its 5th generation of hardware, see Fig. 4.3. Some of the major hardware improvements over the years are listed in the following. First extending the original 32-channel limit several times, todays LAN-XI system architecture has in principle no channel limitations, any limit resides in the PC configuration. Real-time systems with up to hundreds of measurement channels have been tested and delivered to users. Other improvements are in terms of dynamic range going from 16bit ADCs to 24bit and finally in 2005 to 2x24bit—called Dyn-X (Dynamics Extremes) technology [4] that efficiently offers 160 dB dynamic range in narrow band analysis. For the user it means that there is no attenuator setting to worry about, one range covers it all, so no need to make preliminary measurements as long as transducers with a proper sensitivity has been chosen for the actual application.

Typically, one system has been used for measuring the basic FRF data (e.g. PULSE LabShop signal analysis software) and another system (modal analysis software) is used for modal parameter estimation although both systems may be running in the same PC just exchanging data using export/import facilities. The PULSE Reflex Structural Measurement (released 2015) is fully integrated system (hardware as well as software) performing all tasks (measurement/analysis/post-processing/automated reporting) of Modal Testing. That includes MIMO measurements ("unlimited" number of channels), modal parameter estimation, validating modal model, correlating test model with Finite Element Models to finally creating automated reports (Word, PowerPoint or Excel).

Fig. 4.1 Multichannel Analysis System Type 3550 with a typical dual channel mobility shaker setup

The latest LAN-XI Hardware Frames Types 3660-C/D-100 (2014) supports synchronous measurement via the Global Positioning Synchronization (GPS) clock due to built-in GPS receivers, see Fig. 4.3. This is useful when performing modal test on large structures, especially for Operational Modal Analysis, OMA applications. A number of completely independent (unconnected) PULSE data acquisition systems can make data recordings being in synchronism with each other. For example, using an independent measurement system on each floor of a large building to make phase synchronous data recordings that can be used for cross-spectra (FRF) calculations between any channel from any frame and finally perform modal parameter estimation in Reflex Modal.

The PULSE Reflex software platform has recently changed from being a 32-bit to a 64-bit version (year 2015). This ensures use of more memory capacity and supports larger data sets, especially when correlating and comparing large finite element models against test models.

4.3 Modal Analysis Software

When Brüel & Kjær released the Dual Channel Signal Analyzer Type 2032, the company was entirely focusing on developing hardware products, so there was a need for working with modal software vendors in order to offer complete solutions. In 1980, we had one HP9825 computer and one programmer in the sales department, thus he could demonstrate to customers that it was possible to program and control our digital analyzers via the IEEE 488 interface! Our first partner was Structural Measurement System, SMS, a company founded by Mark Richardson, Ken Ramsey, Don Kientzy and Dave Formenti in 1979. The SMS people had great experience from development the first MODAL Analysis software for Hewlett Packard Type HP5423A Structural Dynamics Analyzer released in 1979. The first SMS modal software Structural Testing & Analysis System, STAS was running in HP computers, where you had to load the Basic 2.0 operating and programming software followed by loading the STAS software using 5¼ inch floppy disks [5] before any work could take place, no built-in HDD or SSD (of course) were available at that time. Communication between analyzer and HP computer took place over the IEEE 488 cable and interface. STAS was command driven, so you had to learn all necessary commands and parameters by heart or you had to have the manual open next to you at all times. Not very user friendly according to today's standard but the state of the art at that time.

Fig. 4.2 MIMO based on a 16 channel Type 3550/3551 system

Fig. 4.3 Type LAN-XI 3660-D-100 frame (GSP support) with removable LAN-XI modules

SMS created the first Windows based Modal software (STAR Modal—Structural Analysis and Reporting System) in 1985 (but had to wait until 1987 for IMAC-V for the first official release). This became a very popular platform due to its intuitive user interface and sold by B&K to many users worldwide. The STAR software is today a product of Spectral Dynamics.

When we entered the multichannel market around 1990, B&K and Leuven Measurement System, LMS started cooperating on multichannel systems. B&K delivered multichannel hardware (3550 based frontend system called 3551) and LMS the necessary software, the UNIX based CADA-X. For smaller system (e.g. dual channel), B&K delivered Type 3550 analyzer

together with a LMS Windows based modal software called CADA-PC Modal. One important issue was that B&K was constantly behind the market with respect to number of measurement channels in the early 1990s due to long development times. When the market needed 16 channels B&K offered two channels, then we made 16 channels but now there was a need for 32 channels. When the 32 channel front end was ready, the market needed 64 channels but a 32 channel front end was the last system we offered on that platform although then again there was a need for 128 channels—we were told. Finally, the cooperation with LMS ended since LMS was regarded to be a competitor rather than a partner. B&K introduced its next generation multichannel hardware, Intelligent Data Acquisition (IDA) in 1995 to be used by the PULSE LabShop system from 1999. IDA multichannel systems offered a considerable cost reduction per measurement channel compared to the 3550/3551 hardware solutions.

After the LMS adventure B&K went back again to cooperate with Mark Richardson, who had sold the STAR Modal software to Spectral Dynamic and founded a new company Vibrant Technology, Inc. in 1991. Their main product was the modal software ME'scope (later ME'scopeVES). For many years, ME'scope became the preferred modal software supporting our Type 3550 and PULSE systems.

In 2001, we released first version of a new analysis technique called "output only" modal analysis, also known as Ambient Modal or Operational Modal Analysis, OMA for in-situ measurements, see Ref [6]. The software was developed by Structural Vibration Solutions A/S, SVS (Palle Andersen) in cooperation with and support by Brüel & Kjær (Product Manager Niels-Jørgen Jacobsen) and is today the preferred "output only" software on the market with many users worldwide. SVS calls the product ARTeMIS, Ambient Response Testing and Modal Identification Software. The primary use was for extracting modal parameters of civil engineering structures and soon for mechanical structures under operating condition too. The advantage of the method is that no artificial excitation needs to be applied to the structure or force signals to be measured. The parameter estimation is based upon response signals only, thereby minimizing the work of preparation for the test. Two very different estimation techniques are included: a non-parametric (and patented) Frequency Domain Decomposition (FDD) technique, and a parametric data driven Stochastic Subspace Identification (SSI) algorithm. Instantly the FDD became a popular method because it was fast, easy to use, and easy to understand. The SSI method was difficult to understand and required in the beginning extensive computer calculations, (typically an analysis of even a small test required calculations for several hours). There has been many improvements over the years, so today the parameter estimation is fully automated making the SSI method as fast as, and as well accepted/understood as the FDD method. Modal parameter estimation using current pc-technology takes just a few seconds even for large scale testing.

Brüel & Kjær took over the Test for I-deas product portfolio in 2006 after MTS Corporation's Noise and Vibration Division had closed down. Structural Dynamics Research Corporation, SDRC, originally developed test for I-deas. In course of time, it was decided to move this modal product from UNIX platform to the Windows platform and is presently supported on maintenance contracts. PULSE Reflex Modal software was first released in 2009. Today Reflex Structural Analysis solution is a mature product and comprises Modal Analysis (including Structural Measurements), Model Correlation, Operating Deflection Shapes (ODS) and Shock Response Analysis. Reflex Modal and Correlation softwares are offered in exchange today free of charge on a one to one basis for Test for I-deas users on maintenance contracts.

No need to mention that, of course, there has been a tremendous improvement in modal parameter estimation (earlier called curve fitting) algorithms, but it is outside the scope of this paper to go into details. We have seen the market moving from simple manually controlled local mono-reference SDOF curve fitters to advanced fully automated global poly-reference MDOF parameter estimation methods. See, for example, Ref. [7] as well as the reference list in that paper.

4.4 Modal Test Software

One of the first dedicated applications on the PULSE LabShop Platform was Modal Test Consultant (MTC) released in 1999. This has also been one of the most popular PULSE application over the years. MTC is an application on top of the PULSE measurement platform and guides the user through a complete modal test. Typical steps include selecting hardware and transducers, creating geometry, defining degrees of freedom (DOFs) and measurement sequence. Then predefined setups are chosen for hammer or shaker testing including ratio calibration, for performing geometry driven measurement. Finally measurement validation is carried out e.g. FRF based geometry animation and exporting the data (measurements, DOFs and geometry) to a user selected modal software or to disk in, for example, the widely accepted Universal File Format (UFF). MTC has dedicated measurement templates for hammer, shaker (including MIMO), ODS and OMA tests.

Fig. 4.4 Impact Hammer Type 8208

4.5 Modal Test Transducers

Besides introduction of a wide range of modal hammers (example in Fig. 4.4) and shakers (example in Fig. 4.5) for the past 35 years especially many advances have taken place in the design of modal response transducers, i.e. accelerometers and their conditioning. Actually B&K introduced their first accelerometer as early as 1943, Ref. [8]. Typical accelerometers were charge accelerometers in the early 1980s connecting to the analyzer inputs via a charge conditioning preamplifier, for example, the widely used B&K Charge Amplifier Type 2635. This offered high quality measurements with a wide frequency range, high and low pass filters, adjustable gain etc, but expensive solution per measurement channel. The introduction of accelerometers with built-in charge to voltage converter reduced the price per measurement channel considerably without compromise on accuracy for modal analysis, which is a typical low to mid frequency range application. This technological development allowed the accelerometer to operate on a two wire, low impedance cable, significantly simplifying and reducing cabling problems (and cost as mentioned) as well as the calibration sensitivity that comes with long cables. Kistler already introduced the principle as early as 1965. These types of vibration transducers has a variety of names depending on the manufacturer. Names like Piezotron™, ICP® (Integrated Circuit Piezoelectric), DeltaTron®, CCLD (Constant Current Line Drive), IEPE (Integrated electronic piezoelectric) are often seen. B&K was late on the market with CCLD because B&K had developed a slightly different principle called CVLD (Constant Voltage Line Drive), but it was the CCLD principle that became the de facto standard.

In 1999 smart accelerometers were introduced by Brüel & Kjær. These are transducers with a small built-in chip containing transducer information such as manufacturer, type, serial number, sensitivity, calibration, polarity and resonance frequency. The user may also type in information like measurement position ID (DOF information) using an editing program. The information is then automatically identified/read by a smart transducer compatible measurement system. The benefits for the user are less setup time, less mistakes and significantly more confidence in measured data, especially for a high channel count. Smart transducers are also called TEDS (Transducer Electronic Data Sheet) transducers and the information in the

Fig. 4.5 Modal Exciter Type 4826

Fig. 4.6 Tri-axial accelerometer Type 4506 mounted on a swivel base

chip is designed according to the accepted IEEE 1451.4 TEDS standard that was finalized in 2004. Brüel & Kjær developed the template-based protocol structure that is used in TEDS.

Modern dedicated modal accelerometers are of cubic design giving the possibility of mounting the accelerometer on any of the five measurement surfaces, making it easier to align an accelerometer according to a global rectangular coordinate system, for example, by use of a swivel base, a mounting clip and a spirit level, see Fig. 4.6. Typical size and weight are 1 cm × 1 cm × 1 cm and 5 g. There is a wide variety of cubic modal accelerometers with different sensitivities, different cable mounting and there are uni- and tri-axial versions, see Figs. 4.7 and 4.8. Brüel & Kjær introduced their first cubic modal accelerometers in 1997. See also Refs. [8, 9] for review of accelerometer history.

Fig. 4.7 Mono-axial accelerometer Type 4507 with mounting slots

Fig. 4.8 Tri-axial accelerometer Type 4524 with mounting slots

4.6 IMAC Conference

Brüel & Kjær has joined all IMAC conferences from the very beginning (1982) and both Gade and Herlufsen have most of the years been participating with various activities. We normally have one of the largest exhibition booth, and we offer a hospitality event for our customers on (typically) Wednesday evening. Every year B&K presents a couple of conference papers (with quite a few given by Gade & Herlufsen during the years). At the first many IMACs B&K supported the classical Modal Analysis pre-course (run in the past by modal society celebrities such as Dr. David L. Brown, Dr. Randall J. Allemang, Dr. Peter Avitabile and Dr. David Ewins, see Ref. [10]) with hands on at afternoon sessions. We offered the participants hands on exercises using four complete modal analysis test (both hammer and shaker) and analysis systems, i.e. using quite a large amount of B&K instrumentation, see Fig. 4.1 as well as highly qualified instructors (Thrane, Døssing, Herlufsen & Gade). Since 2007 Svend Gade together with professor Dr. Carlos Ventura (University of British Columbia, Canada) have been running an IMAC pre-course called Operational Modal Analysis, Background, Theory & Practice. B&K is also involved in the "Basics of Modal Analysis for the New/Young Engineer" sessions organized by Mike Mains. IMAC homepage is located at https://sem.org/.

4.7 IOMAC Conference

After the OMA techniques became mature enough, we decided to exchange and share our knowledge more efficiently by introducing a new international conference with the name International Operational Modal Analysis Conference, IOMAC. About 150 participants have attended each of these conferences. The driving forces behind the two first conferences were the two companies SVS (by Rune Brincker) and B&K (by Nis B. Møller). The conference is held in Europe at odd years (The other European modal conference ISMA, "International Conference on Noise and Vibration Engineering" is held at even years in Leuven, Belgium). The IOMAC locations have been Copenhagen, Denmark 2005 and 2007, Portonovo, Italy 2009, Istanbul, Turkey 2011, Guimarães, Portugal 2013, Gijón, Spain 2015 and the next IOMAC will be held at Ingolstadt, Germany 8^{th}–12^{th} May 2017. Brüel & Kjær (at present represented by S. Gade) is member of the permanent IOMAC Committee. Prior to all these conferences S. Gade and C. Ventura have been running an OMA pre-course. IOMAC homepage is located at http://www.iomac.eu/.

4.8 Modal Seminars

In the early 1980s, there was a need for B&K to offer a Modal Analysis seminar covering all aspects of modal topics as for example found in Ref. [11]. The contents of a generic three day modal seminar were developed by Niels Thrane, Ole Døssing, Henrik Herlufsen and Svend Gade and the high quality lecture material was produced by the B&K literature department, initially as overhead transparencies and later transferred into PowerPoint presentations (see Chap. 19 in Ref. [3]). The seminar is still on the agenda and held twice every year in Nærum in Denmark by Gade & Herlufsen (on request at other locations). Day one introduces mechanical mobility measurements (FFT principles, Input/Output Analysis, Excitation Techniques and Mobility etc.) and day two introduces Modal Analysis (SDOF & MDOF models, MIMO and Parameter estimation etc.). Only day three which is about model scaling, validation and the use of modal model has seen major changes over the years. Today the focus is on modal model correlation and updating finite element models as well as more elaborate validation techniques have been developed and included. Ole Døssing made two Brüel & Kjær primers that covers the topics from day one and day two of the course [12, 13]; these can be found on B&Ks homepage http://bksv.com/.

4.9 Computers

It should not be forgotten that huge amount of the progress for all scientific disciplines is heavily impacted by the continuous development of better and faster computers. For history and time line of UNIX workstations see Ref. [14]. The introduction of PC is considered to be in 1981 with the birth of the IBM PC [15] and MS DOS, Disk Operating System by Microsoft, but we had to wait another four years until 1985 before we saw the release of the MS Windows ver. 1.0 operating system [16]. IMAC V, 1987 at Imperial College, London was the first time B&K brought Windows operated PCs for our Modal Exhibition and for the afternoon hands on modal exercises. According to the legendary Moore's law [17] from 1965, the increase of processing speed (original no. of transistors in circuit boards) is predicted to be a doubling every 18 months. A prediction that was still reasonable accurate after the first 10 years in 1975, when Moore's law was re-introduced. This means that the speed of PCs (according to Moore's law) may have been doubled about 25 times for the last 35 years. Two raised to the power of 25 is more than 30 million times!!!

4.10 Summary/Conclusions

Both Gade and Herlufsen have now been working for more than 35 years as application specialists at the Brüel & Kjær Company. We have both been involved in a very wide range of applications within the world of sound and vibration, but especially we have had a focus and interest in modal analysis over the years. Thus, we thought it was time to review the activities we have been involved in for this application area. Even though the basic principles of modal analysis is nearly unchanged, there have been significant advances in theories and practical implementation as well as in instrumentation of modal testing. A great amount of our achieved knowledge we have tried to preserve in a number of B&K Technical Reviews (a few relevant examples see Refs. [18–20]) as well as technical in papers at conferences, in magazines and in our seminar material.

References

1. Randall, R.B.: Application of B&K equipment to frequency analysis. Brüel & Kjær Book, Naerum, Denmark (1977)
2. Brigham, E.O.: The fast Fourier transform. Prentice-Hall, Inc., Englewood Cliffs, NJ (1974)
3. Mowry, J., Borring, G.: Journey to greatness. Acoustical Publications, Inc., Bay Village, OH (2012)
4. Andersen, O.T., Jacobsen, N.J., Gade, S.: Practically obtainable dynamic ranges of data acquisition systems based on 24-bit technology. Inter-Noise Proceedings (2005).
5. Wikipedia. History of the floppy disk. https://en.wikipedia.org/wiki/History_of_the_floppy_disk.
6. Brincker, R., Ventura, C.: Introduction to operational modal analysis. Wiley Book (2015).
7. Allemang, R.J., Phillips, A.W.: The unified matrix polynomial approach to understanding modal parameter estimation: an update. Proceedings of ISMA 2004.
8. Licht, T.R.: Five decades of accelerometer development at Brüel & Kjær. 67'th Shock & Vibration Symposium, Monterey, CA, USA (1996)
9. Walter, P.L.: The History of the accelerometer. 1920s-1996—prologue and epilogue, 2006. Sound Vib Mag (2007).
10. Brown, D.L., Allemang, R.J.: The modern era of experimental modal analysis, one historical perspective. Sound Vib Mag 19–25 (2007).
11. Ewins, D.J.: Modal testing: theory and practice, Research Studies Press., Ltd, Brüel & Kjær Book, 1st ed. (1984), 2nd ed. (2000).
12. Døssing, O.: Structural testing, part 1, mechanical mobility measurements. Brüel & Kjær Primer (1988).
13. Døssing, O.: Structural testing, part 2, modal analysis and simulation. Brüel & Kjær Primer, (1988).
14. UNIX Workstation—History and Time Line. http://www.unix.org/what_is_unix/history_timeline.html.
15. The birth of the IBM PC https://www-03.ibm.com/ibm/history/exhibits/pc25/pc25_birth.html.
16. Microsoft. A history of windows. http://windows.microsoft.com/en-us/windows/history#T1=era1.
17. Moore, G.E.: Moore's law. Electro Mag. (1965).
18. Herlufsen, H.: Dual channel FFT analysis (part I and part II). Brüel & Kjær Technical Review No. 1 & 2 (1984).
19. Gade, S., Herlufsen, H.: Windows to FFT analysis (part I and part II). Brüel & Kjær Technical Review No. 3 & 4 (1987).
20. Gade, S., Herlufsen, H.: Damping measurement (part I and part II), Brüel & Kjær Technical Review No. 1 & 2 (1994).
21. Bendat, J.S., Piersol, A.G.: Engineering applications of correlation and spectral analysis. Wiley Interscience, New York (1980)

Chapter 5
Measuring Violin Bow Force During Performance

Rodrigo Sarlo, David Ehrlich, and Pablo A. Tarazaga

Abstract Violin bowing is a complex skill and controls a majority of the sound produced by the instrument. Yet despite significant interest in the modal analysis of violins, comparatively little work has been done to study the complexities of this "input." In this work, we have used fiber optic strain sensors, a modern strain sensing technology, to test a novel method for measuring bowing force during violin performance. Gaining greater insight into how violinists vary bowing force to create sound could not only lead to better violin excitation methods for modal analysis but might also key in discovering indicators of violin quality and musician preferences. Live performance testing was performed by a professional violinist on two violins of differing quality and at different volume levels. The results showed a log-linear relation between bowing force and volume. In addition, a bowing gesture named the "average down-up stroke" was found by averaging several similar gestures. Its duration was observably longer for a high quality violin compared to a fair quality sibling. Such a measure could be adapted for various gestures and styles and subsequently be explored as a potential indicator of violin quality or player preference.

Keywords Violin • Bow • Force • Strain • Instrumentation

5.1 Introduction

Bowing is arguably the most complex skill a violinist must master and the primary contributor to a violin's sound [1]. In fact, a player's bowing technique can greatly influence sound quality perceived by an audience. Yet a majority of literature on violin modal analysis uses simple excitation methods. Hammer impact excitation on the violin bridge has historically been the most common [2–4] although some experiments by Jansson et al. have used an electromagnetic shaker at the foot of the bridge [5, 6]. While these methods do excite the natural dynamics of the violin body, they are not representative of how the violin is excited to produce sound during a performance. Perhaps the most realistic excitation method was undertaken in separate experiments by Meinel [7], Saunders [8] and Gren [9], who used a similar "bowing machine". It consisted of a rosined celluloid disk, controlled by a motor, with a counter weight to control the contact force. The machines were able to excite the violins in a realistic way but would need to be expanded for extensive study of all the bowing parameters that violinists use to control volume and tone: bow velocity, bow force, and distance from the bridge. Furthermore, while these parameters are recognized in literature, there is little work on understanding and quantifying their effects on sound and tone production. In short, detailed studies on the relationships among bowing "inputs" would foster more realistic and informative excitation methods for modal analysis.

A significant portion of violin modal analysis research has been aimed at discovering quantitative indicators of violin quality. Some proposed indicators include the frequency and/or input mobility levels of specific body modes [3, 10]. In particular, strong body resonance in the range of 2–3 kHz has been associated with high quality violins by various authors [6, 11]. In an extensive modal analysis of over 34 violin modes, Marshall also hypothesized that the lower order bending modes may contribute to how the instrument "feels", despite the fact that these modes radiate very little sound. Overall, the results of these quality indicators have been far from conclusive. Finding reliable measures of quality is difficult primarily because violin responses are very unique and no clear, observable patterns exist, even among violins of the same maker. The whole discussion assumes that some objective measure of violin quality exists, but violinist opinion and preference tends to vary widely and depends on tastes and playing styles [12]. This indicates that there is no clear criteria, and that quality

R. Sarlo (✉) • D. Ehrlich • P.A. Tarazaga
Vibrations, Adaptive Structures and Testing (VAST) Laboratory, Department of Mechanical Engineering, Virginia Tech, 635 Prices Fork Road, Blacksburg, VA 24060, USA
e-mail: sarlo@vt.edu; rodri.sarlo@gmail.com

E. Wee Sit (ed.), *Sensors and Instrumentation, Volume 5*, Conference Proceedings of the Society for Experimental Mechanics Series, DOI 10.1007/978-3-319-29859-7_5

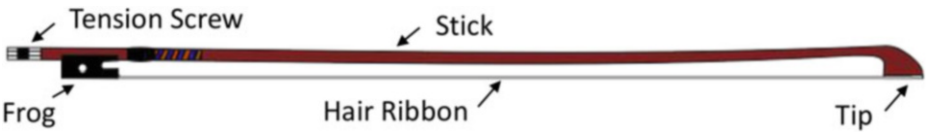

Fig. 5.1 Parts of the violin bow

is to a great extent subjective. Thus, since quality is relative to a player, might the judgment be biased toward how a violin "feels" under his/her bow? And vice versa, may a violin that feels "good" to a player sound better because of this very fact? In the end, we cannot separate the violin response from a player and so must try to understand the complexities of bowing technique. It may shed light on how a player's style relates to the sound produced and why certain violins are preferred.

Several instrumentation strategies have already been implemented to measure the three key bowing parameter: bow force, bow velocity and distance from the bridge. To aid in this discussion, a labeled diagram of the relevant parts of the violin bow is shown in Fig. 5.1. Young, of the MIT media lab, developed the "Hyperbow," which used accelerometers and an electromagnetic field sensor to track bow motion and a single strain gauge bonded to the middle of the bow stick to measure bowing force. All sensor data was transmitted wirelessly through a radio transmitter also mounted to the bow. The system was used to successfully classify different bowing techniques, but few details were given on the force sensor, aside from the results of a simple calibration procedure [13, 14]. Demoucron outfitted a bow with a small cantilevered metal strip which pushed against the string ribbon. The strip would deform when the bow hairs were tensioned by a bowing gesture and this was measured by strain gauges. Demoucron found the strain gauge measurement to be a function of both bowing force and contact point. Thus, to accurately measure force, he needed to track the bow position as well. He did this through a six camera motion tracking system, tracking all six degrees of freedom of the bow motion [15]. The system was used to measure bowing parameters during a performance, but mostly to validate the functionality of the system. No analysis was done to understand how the sensor data correlates to player behavior or intentions. In another study, Askenfelt used thin bronze strips as extensions of the hair ribbon (the hair was glued to the strips) which were fastened at the frog and the tip, in place of the hair. Four strain gauges, at the top and bottom of each strip, were wired in a wheatstone bridge configuration. Balancing the strain gauge bridge against a load cell showed an approximate linear relationship to force, however, the signal tended to over estimate forces near the violin tip. A wheatstone bridge was also used for position measurements. A resistance wire placed along the hair ribbon made electrical contact with the steel strings and changes in resistance due to the changing contact length were used to calculate position. Askenfelt subjected his system to extensive live testing, including various bowing articulations, dynamic variations (crescendo/diminuendo), and even changes in style and mood. In general, he observed that bowing force and velocity ranged from 0.5–2 N and 0–0.4 m/s, respectively [16].

In the bow instrumentation systems mentioned above, the challenge of position measurement has been resolved to a satisfactory extent using tracking systems, either optical or electromagnetic. Even if they might be a bit cumbersome to implement, they provide good accuracy and operate wirelessly, which is beneficial to avoid hindering the violinist. Force measurement, on the other hand, seems to be a more difficult problem, since strain on the bow can depend on wide range of factors: bow tension, bow position, bow angle and others [15, 16]. In addition, the force measurement methods of Demoucron and Askenfel restrict areas of the hair ribbon near the tip and frog, shortening the bowing length available to a player. And while these instrumentation systems have been tested in various performance scenarios, systematic study on the relationships between violin input (bowing parameters) and output (sound/tone/volume) are still lacking. Is it possible to link bowing parameters to a periodic input to the violin? How do bowing parameters vary from player to player, and from violin to violin?

In this work we explore a modern fiber optic strain sensor from Luna, Inc. as an alternative to previous force sensing methods. Two different configurations of the sensing fiber are tested. They show clear transduction capability but, like some of the previous sensors, are sensitive to the position of the bow. Nevertheless. they require minimal installation and due to their small size, introduce virtually no changes to the weight, feel and playability of the bow. The results help to correlate violinist pressure to the intended volume. We also compare bowing behavior between two violins of different quality to see if any differences in style arise.

5.2 Methods

The bow force sensing method took advantage of strain sensing fibers that can measure strain along their length. One of the goals of testing was to find the most favorable sensor configuration for realistic playing conditions. These conditions included various violins, dynamics (volumes), and bowing patterns. The strain on the bow, however, depends on various factors (e.g. bow contact position) and thus systematic tests were used to determine their effects. We first describe the instrumentation components and installation, followed by descriptions of the calibration and live playing setups.

5.2.1 Bow and Violin Instrumentation

The bowing force was measured through optical distributed strain sensors (Luna Inc.). These are fiber optic strain sensors manufactured from off the shelf, telecommunication grade optical fiber, with a germanium doped fused silica core, fused silica cladding, and an outer Polyimide coating. Strain measurements are achieved without the use of gratings by measuring the low amplitude signal of reflected light referred to as Rayleigh backscatter. This is an inherent phenomenon in fiber that Luna's interrogator (ODiSI Platform[1]) utilizes to measure strain continuously along the entire length of the fiber optic cable with very high spatial density [17]. In this test, strain was reported every 2.5 mm along the optical fiber. The strain sensing fibers were installed in two arrangements on separate violin bows. In the first, the fiber was permanently bonded to the wood along the top of the bow stick, as seen at the bottom of Fig. 5.2. The sensor measured the local strain in the wood and was about one meter in length. We will refer to this configuration as the "bow sensor." The second configuration had a fiber specially mounted along the bow strings as shown at the top of Fig. 5.2. This configuration was meant to be modular, and thus was not bonded to the violin bow directly. Instead, custom mounts were fastened to the frog and bow tip. With the bow untensioned, a two meter fiber (twice the length of the bow) was bonded to the frog mount, looped around an extension of the tip mount and bonded once to the other side of the frog mount. With sensor in place, the bow was tensioned to normal playing condition, stretching the fiber to hold it in place. The fiber ran close to each edge of the hair ribbon with about two millimeters of vertical separation. This arrangement was designed to measure more directly the changes in tension of the hair ribbon caused by the bow's force on a string. We will refer to this configuration as the "hair sensor." For both sensors, the interrogation end of the fiber was bound to the player's arm for stability then connected to the ODiSI measurement system.

In addition to the strain sensor, each bow was instrumented with a small accelerometer (PCB Piezotronics Inc., 352C22) on the frog to measure acceleration of the bow in the lengthwise axis (i.e. the bowing direction). The bottom of Fig. 5.2 shows the precise location. The sensor was used as an indicator of bow movement. Finally, a piezoelectric contact microphone (Korg, CM-200) was clipped to the bridge of the violin to measure the sound produced by the instrument.

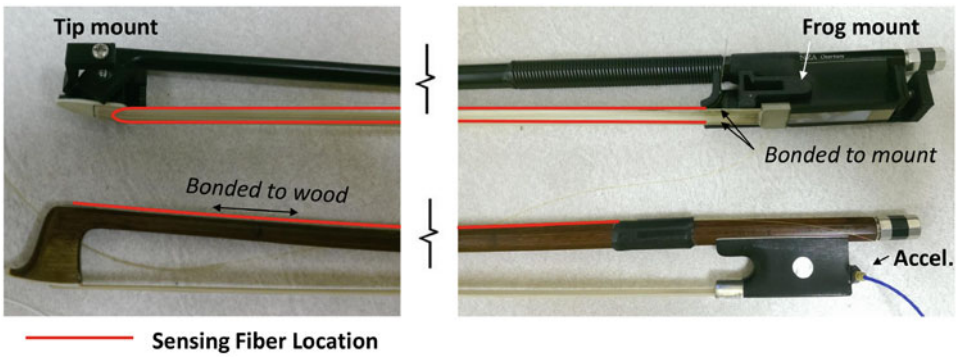

Fig. 5.2 Two different configurations of the strain sensing fiber. *Bottom*: bonded to the wood along the top of the bow (bow sensor). *Top*: stretched between two custom fixtures to run along hair ribbon (hair sensor)

[1] http://lunainc.com/odisi.

5.2.2 Angle and Position Calibration

The fiber optic sensors measure strain and not the violinist's applied force directly. The strain and tension of the bow was found by the author and others [18] to depend on several factors:

1. Violinist's bowing force
2. Pre-tension in the violin bow (chosen by the performer)
3. Bow tilt (roll axis)
4. String contact along the length (frog to tip)
5. Bow angle (pitch axis)

The first factor is what we hope to measure. The second can be assumed to be constant for short playing periods and can be tared at the beginning of a test. The third is also assumed to be constant since violinists vary the tilt of the bow only small amounts during a performance. The last two factors (longitudinal contact and bow angle), however, can affect the measured strain significantly. In the case of the latter, the bow's self weight is comparable to the forces applied by the violinist, thus the angle at which it's played can influence the string normal force due to gravity. In the case of the former, the string's contact point influences the moment arm on the bow. A force near the tip will result in greater strains than the same force near the frog. Thus, we first conducted an experiment to assess these effects on the strain measurement.

A bow with each sensor configuration was cantilevered at the frog, to simulate a violinist's grip. To test the effects of the bow angle, the bow was rotated counter-clockwise 0–180° from horizontal while measuring strain. To measure the effects of string contact location, the hair ribbon was oriented upwards (180° in the previous test) and masses were hung at 15, 30, 45 and 60 cm from the frog as shown in Fig. 5.3. The masses (20, 40, 50 and 70 g) simulated the normal force of the violin string due to the violinist's pressure. The mass weights approximately cover the lower range of bowing forces that a violinist typically applies, about 0.2–0.7 N. Violinists have been observed to apply up to 2 N [16]. Each combination of mass and weight position was tested. The strain effects due to the bow's self weight were zeroed with no weight applied. In this way, we treat the weight as the combined force of bow weight and player pressure.

5.2.3 Play Test

The principal test was to measure force during performance. For this purpose, we asked a professional violinist to play two different violins with each bow-sensor configuration. The violins were of fair and good quality in the violinist's own opinion. We will refer to the former as the "Euro Model" and the latter as the "Shan Model." For each bow-violin combination, the violinist was asked to play a chromatic scale over the full range of the instrument. He was also asked to play each of the open strings with a downbow-upbow pattern for four dynamic (volume) levels: *piano* (soft), *mezzo piano* (medium soft), *mezzo forte* (medium loud), *forte* (loud).

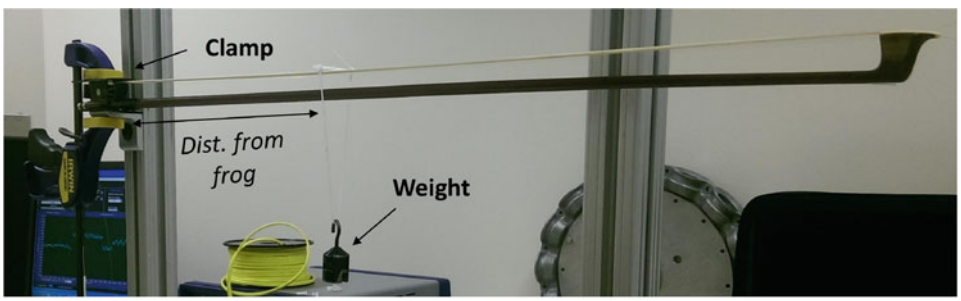

Fig. 5.3 Cantilevered bow setup to observe effects of string contact position

5.3 Results

The following results first explore the effects of bow contact point and angle on the measured strain. These were gathered from the calibration tests outlined in Sect. 5.2.2. For the live performance tests, we explore the correlation between what the violinist hears and what he plays. Based on the results, we evaluate the relative merits of each configuration.

5.3.1 Effects of Bow Contact Position

A cantilevered bow was tested for several applied forces (via weights) at various distances from the frog. The resulting strain profiles are shown in Fig. 5.4 for both the bow sensor and hair sensor configurations. For clarity, not all combinations are shown in the figures. Notice that for a force against the string ribbon, the bow sensor (Fig. 5.4a) measures compression around the base of the bow and tension near the tip. This is attributed to the combination of bending moment on the bow, which compresses the top fibers, and the tension from the hair ribbon, which stretches them. It is interesting to note that the point of transition (zero strain) is independent of the loading location. Greater moment and/or force seem only to positively scale the measured strain. The hair sensor (Fig. 5.4b), on the other hand, measures constant strain along its length. This is intuitive, since the sensor is in contact with the bow only at two points, and thus registers changes in overall tension. As in the bow sensor case, the strain increases with both moment and force.

Since we observe that both bow contact position and force have comparable effects on the measured strain, we analyze whether these effects can be separated based on the measured sensor data. We use principal component analysis (PCA) [19, 20], to project the sensor profile measurements from Fig. 5.4 into a new orthogonal basis. Each basis "principal component" explains the maximum possible variance in descending order. The correlation, or loading, between a component and the measurement data shows what percentage of the data variance is explained by that component. Data with redundant measurements will have only a few components with large loadings. PCA was carried out for three combinations of data: bow sensor, hair sensor, and both sensors combined. The results are shown in Table 5.1.

In all cases, an overwhelming majority of the data is explained by the first principal component. This means that the strain profiles of each sensor are determined primarily by a single degree of freedom, some combined effect of the weight and the

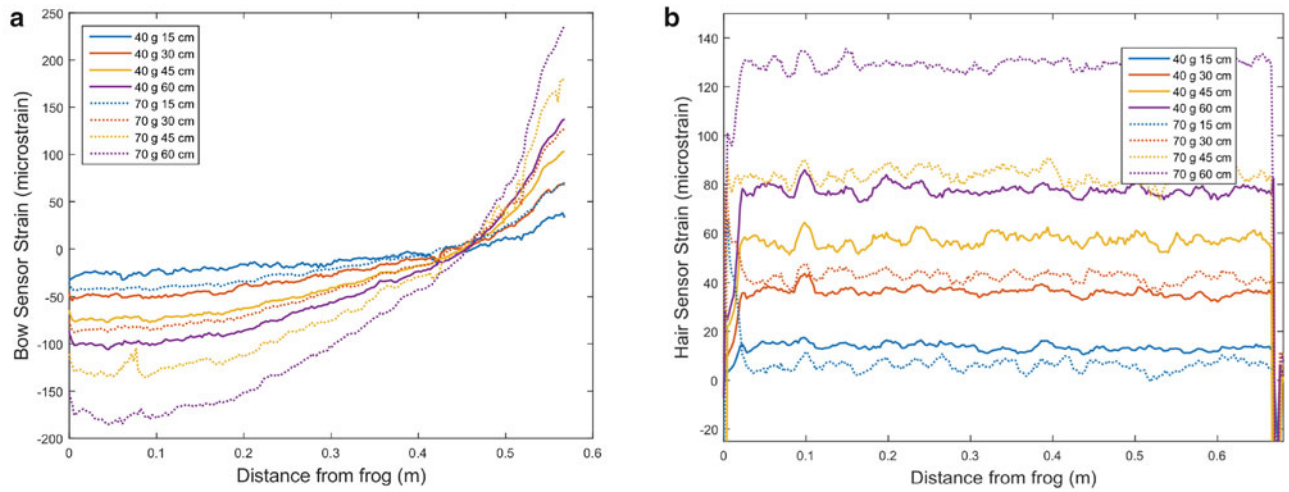

Fig. 5.4 Strain profile along the sensor length for various combinations of weight and position (contact point). (**a**) Bow sensor, (**b**) hair sensor

Table 5.1 Principal component analysis (PCA) of both strain sensor profiles individually and combined

	Bow sensor Variance explained (%)	Hair sensor Variance explained (%)	Combined Variance explained (%)
Principal component 1	99.5	99.4	97.8
Principal component 2	0.30	0.40	2.00

Addition principal components were very low (<0.2 %) and are not included

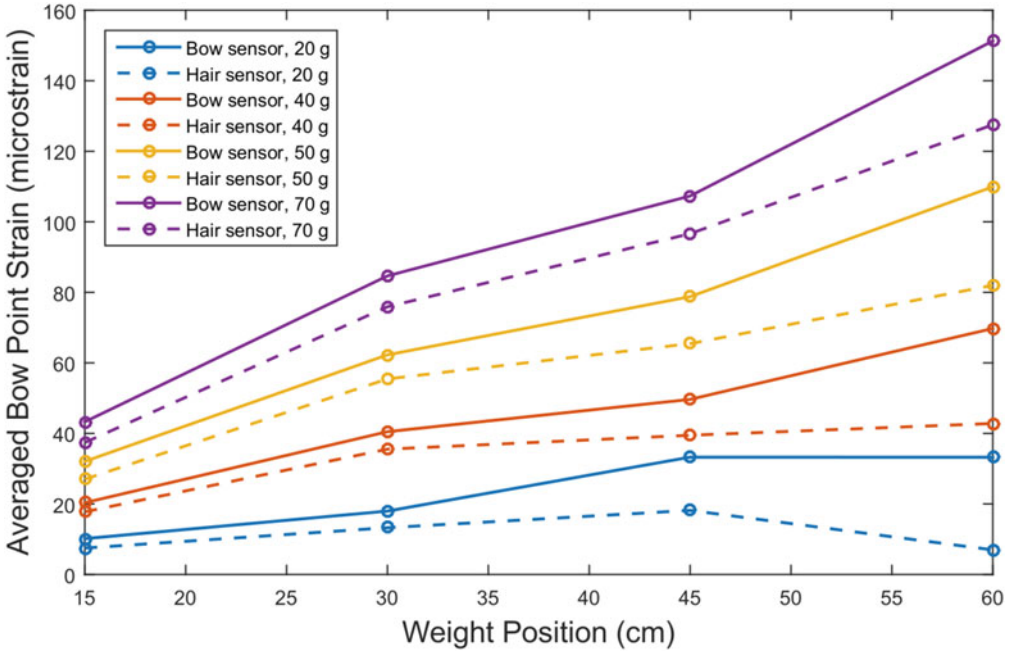

Fig. 5.5 Measured point strain magnitude with respect to weight position. Each line is a constant weight. Bow sensor (*solid lines*), measuring at 0.2 m from the frog. Hair sensor (*dashed lines*), lengthwise average

weight position. Therefore, without much loss in information we can describe each sensor output by a single point, rather than by the entire profile. For the bow sensor, we chose a point at 0.2 m from the frog, since it is far from the point of zero strain and shows a good signal to noise ratio. For the hair sensor, we averaged the measurements point across the entire length. Figure 5.5 shows the full results of the weight-position test in terms of these single point measurements. Note that the graphs display the strain *magnitude*, since the bow and hair sensors are in compression and tension, respectively. This shows the increase in measured strain with respect to force position for each of the tested weights. The relationship is somewhat linear, although the slope tends to decrease near the middle. Both sensing configurations show very similar behavior and magnitudes overall. However, the hair sensor seems to be slightly less sensitive to weights near the tip of the bow, as can be seen by the increased difference in measured strain at 60 cm. This may be the reason for the slightly higher variance explained by the second principal component for the combined case (2 %).

Fundamentally, the results show that the strain profiles of each sensor are largely determined by a single combined effect of the weight and the weight position. Independently, each of these factors follows a roughly linear trend. Consequently, we cannot use the strain data alone to distinguish between bowing position and force. In the playing test, however, we do have additional information about the bow's position based on accelerometer data and understanding of the bowing technique. This is helpful in assessing the strain measurements.

5.3.2 Effects of Bow Angle

The strain reading versus bow angle, using the same single-point measurements described in the preceding section, are shown in Fig. 5.6. The bow was clamped at the frog and rotated, as explained in Sect. 5.2.2. The sensor was zeroed at 90° from horizontal, the position with no transverse force on the bow. The strain values are normalized to the direction of the force on the bow; a force pushing on the hairs (positive moment on the bow) is shown as positive strain, a force pulling on the hairs (negative moment) is shown as negative. In a playing context, the second case would mean the violinist is applying a moment to lift the bow's full weight form the strings. As seen in the figure, this is the case for less than 90°, where the moment at the frog is "lifting" the bow. The opposite effect is true when the angle is greater than 90°. The unusual measurement of the hair sensor at 180° is due to higher-than-usual noise at that point. Aside from this point, the sensors are in quite good agreement, again suggesting that both are signals are driven by the same phenomenon. Despite being close to the hair ribbon, the hair sensor is not activated solely by deflection of the hair ribbon (as was originally intended) but rather by changes in its tension caused by deflection of the stick.

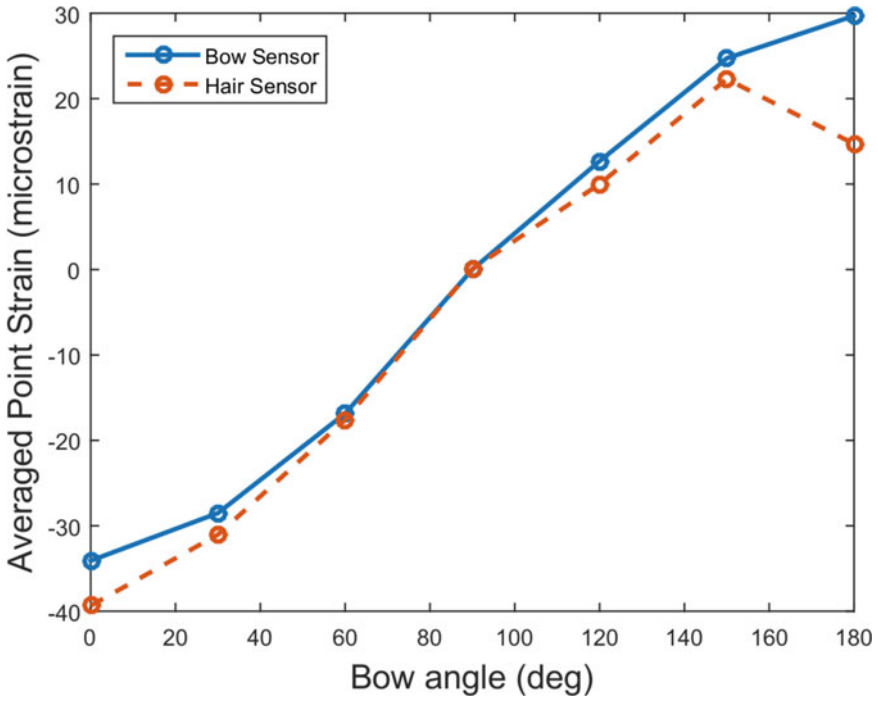

Fig. 5.6 Measured point strain magnitude with respect to bow angle. Bow sensor (*solid line*), measuring at 0.2 m from the frog. Hair sensor (*dashed line*), lengthwise average

The strain magnitudes due to bow angle (-40 to $+30$ microstrain) are of comparable magnitude to those due to string normal forces (0 to $+140$ microstrain). This means that the effects of bow angle and gravity cannot be neglected. However, angle effects can be seen as beneficial and not detrimental to the force sensing endeavor. If we construe a change in bow angle as a change in the normal force of the string, then by varying the angle the violinist is, in fact, changing his bowing force, a change which the sensors will register. We can then consider the bow at 0° resting on the strings as the point of no applied bowing force and use it to shift the data accordingly. We utilize this zeroing method for the live performance measurements.

5.3.3 Live Performance

In the first live performance test, we asked the violinist to play an downbow-upbow stroke combination on each of the four open strings in order (G, D, A, E). The stroke begins with string contact near the frog and moves towards the tip (downbow) and the reverses (upbow). Figure 5.7 shows data acquired from a bow strain sensor, bow accelerometer and bridge microphone for one such test. For the microphone output, we notice the distinct vibration envelope for each stroke, where each downbow-upbow motion counts as two. The strain shows a gradual increase during the downbow motion as the contact point nears the tip of the bow. The behavior is symmetric for the upbow portion as the contact moves towards the frog. This agrees with our analysis on contact point effects, since the strain sensitivity increases near the tip. The strain shows a sharp peak at the transition and consistency across strings. The accelerometer was the most difficult sensor to interpret, since the playing motions involved changes in bow angle. This caused changing gravitational effects on the sensor output. As a consequence, integrating the signal resulted in too much drift to be particularly useful for measuring velocity. Thus, only approximate conclusions about the bowing velocity can be drawn from the acceleration measurements. For example, we notice that the acceleration remains close to zero during the bowing motion, which implies constant velocity bowing. There are sharp snaps at the bow transitions, which are consistent with the flick that violinists traditionally use when changing bow direction. Unfortunately, because we cannot measure the bow position with certainty, it is impossible to use the calibration data from the preceding section to estimate the true magnitude of the bowing force.

To get a better idea of general player behavior, we treat each downbow-upbow combination as a unit and average them for particular conditions. We will refer to this average unit as the "average down-up stroke." For this study, we focus on how the average down-up stroke changes for dynamics (volume) and the type of violin played. For each case, we compare the average stroke for each sensor arrangement to evaluate their merits and disadvantages.

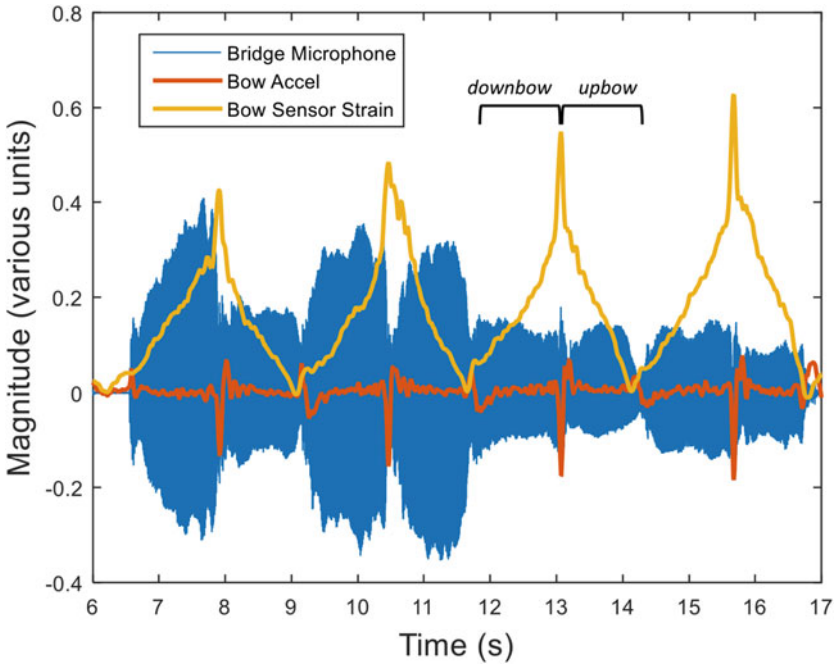

Fig. 5.7 Outputs of the bridge microphone (*blue*), the bow accelerometer (*red*), and the bow strain sensor (*yellow*) while performing an downbow-upbow stroke on each open string. Note: signals are different units

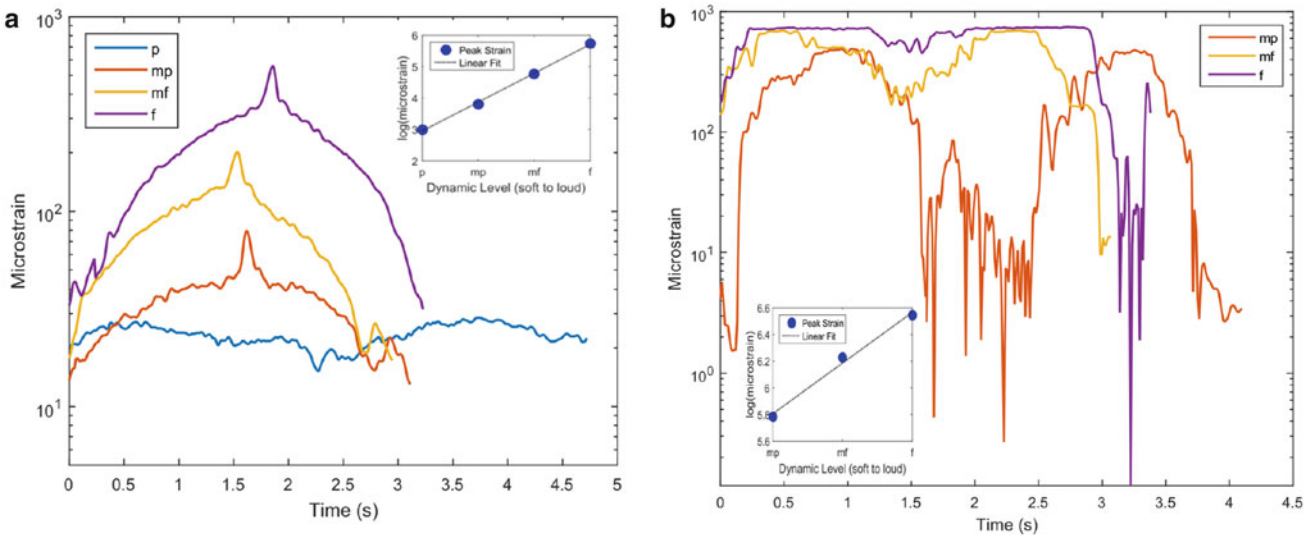

Fig. 5.8 Average down-up stroke for different dynamics. (**a**) Bow sensor, (**b**) hair sensor. Picture inlay shows the peak magnitude as a function of volume and a corresponding linear fit

Figure 5.8a and b show the average strokes for the bow and hair strain, respectively, and their change with respect to a dynamic (volume level). The violinist was asked only to play at *piano* (p), *mezzo piano* (mp), *mezzo forte* (mf), and *forte* (f). While these dynamics should be experienced by the listener as increasing volume from "soft" to "loud" at equal intervals, the precise bowing force and velocity used to achieve these levels was left up to the violinist to determine, based on his own experience, training and ear. In general, we observe that the average stroke strain increases with increasing volume. We also observe that average stroke duration differs depending on the dynamic. This correlates directly with the bowing velocity. For *piano* (p), for example, the bow is moved slowly with light pressure. The duration decreases for mp and mf dynamics, yet surprisingly increases slightly for *forte* (f). Because bowing pressure and velocity are loosely coupled in the generation of string vibration [21], higher velocity should correlate to higher pressures. The exception to this phenomenon at *forte* is not yet understood.

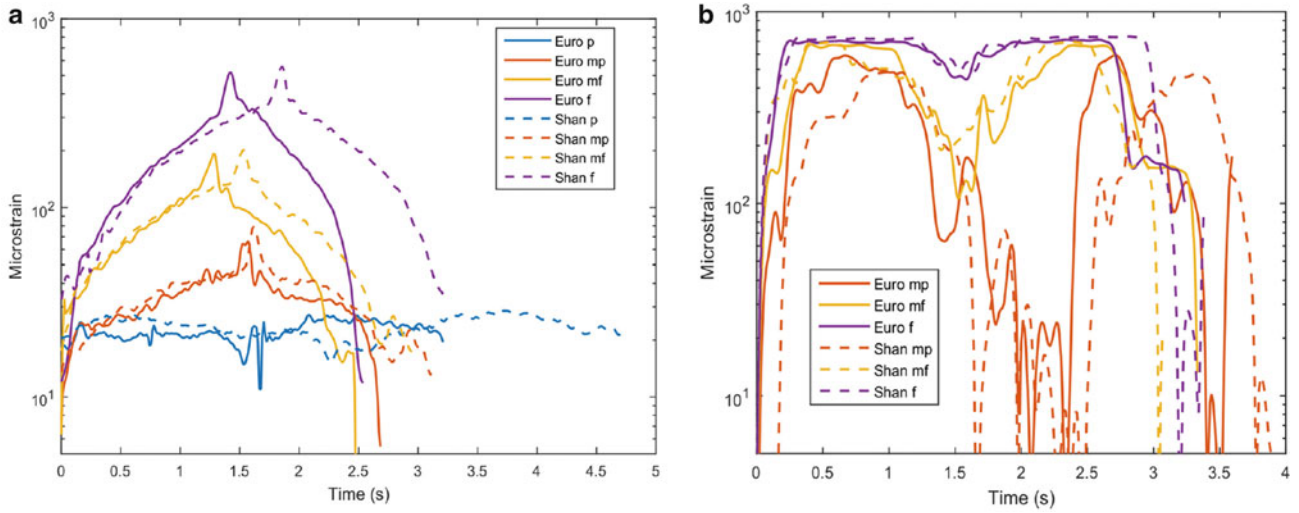

Fig. 5.9 Average down-up stroke for different dynamics on two different violins (Euro model and Shan model). (**a**) Bow sensor, (**b**) hair sensor

In comparison, the hair sensor is observed to be much noisier that the bow sensor. The strain measurement at *piano* (p), in fact, could not be distinguished from the noise floor and thus is not presented in Fig. 5.8b. This is a consequence of the sensor fibers themselves, which are sensitive to vibrations. The hair sensor signal tended to have a higher noise floor due to its proximity to the vibrating string. The hair sensor is, however, much more constant with respect to position, which could make it a better candidate for sensing the bow force. It also indicates a dip in strain in the transition from downbow to upbow, in contradiction with the peak in the bow sensor data. It is difficult to reconcile these differing observations with the results from Sect. 5.3.1, which suggested identical behavior. One possibility is that the combination of positions and forces in bowing technique cannot be explained through a simple static weight experiment.

The graph inlays in Fig. 5.8 show the how the logarithm of peak magnitude for each sensor changes with volume. Peak magnitude was used as an indicator of overall bowing force. Both sensors show a strong log-linear behavior with volume (bow sensor: $R^2 = 0.998$, hair sensor: $R^2 = 0.991$), as is illustrated by the corresponding fits. This behavior is quite intuitive when we consider the log-linear relationship of sound pressure level and perceived volume in humans. The data indicates that the bow pressure is directly proportional to the sound pressure level produced by the violin, since the dynamics are intended by the violinist to increase in a linear fashion.

We also analyzed how the average down-up stroke changes depending on the violin model used. Figure 5.9 shows a strain signal comparison of the Euro (solid lines) and Shan (dashed lines) violins played at the various dynamic levels. We notice that for both sensors, the strain *magnitudes* are almost identical. Yet, the stroke periods are noticeably longer for the Shan violin, the one of higher quality. This is observed in both separate bow experiments, indicating that a faster bowing velocity on the Euro violin is required to match the volume of the Shan model. Could this be an indicator of quality? Bow length management is an important consideration in bowing technique and certain choices in this regard can affect the performance of a piece. Because each test was performed only once, one cannot reject the possibility that this difference is due to the random variation of the player. However, this is an interesting avenue for future work.

5.4 Conclusions

In this work we have used fiber optic strain sensors, a modern strain sensing technology, to test an alternative method for measuring bowing force during violin performance. Gaining greater insight into how violinists vary bowing force to create sound could not only lead to better violin excitation methods for modal analysis but might also key in discovering indicators of violin quality and musician preferences. Two different sensor configurations were used: one bonded to the bow stick (the bow sensor) and one stretched between the frog and the tip, close to the hair ribbon (the hair sensor). In a simple static calibration procedure, PCA analysis of the sensor output showed both configurations exhibited the same behavior, namely a dependence on both force and contact point. Surprisingly, their behavior was quite different during live playing tests. This may be due to considerably different magnitudes of force applied during playing, or the use of a different bow for

each configuration. Overall, it is difficult to obtain reliable bowing force estimates without an accurate measurement of bow position. Suitable solutions to this problem, however, have already been implemented in literature using wireless tracking [13, 15, 18].

The results of the sensing method are promising. We demonstrate a log-linear relation between bowing force and dynamic level (volume), which should be also log-linear in the sound pressure levels produced by the violin. In addition, we were able to measure a bowing gesture we call the "average down-up stroke" and found that its duration was observably longer for a high quality violin compared to a fair quality sibling. Such a measure could be adapted for various gestures and styles and subsequently be explored as a potential indicator of violin quality or player preference. Future work should incorporate bow tracking and study variations in bowing parameters among several players and violins.

Acknowledgements The authors would like the Virginia Tech Institute for Creativity, Arts and Technology (ICAT) for funding this work through the SEAD mini grant. They would like to thank Luna, Inc. in Blacksburg, VA for providing the strain sensing equipment and access to their facilities. Special thanks in particular to Aida Rahim and Naman Garg for their tremendously useful assistance and interest in the project.

References

1. Beament, J.: The Violin Explained: Components, Mechanism, and Sound. Oxford University Press, New York (1997)
2. Marshall, K.D.: Modal analysis of a violin. J. Acoust. Soc. Am. **77**(2), 695–709 (1985)
3. Bissinger, G.: Structural acoustics of good and bad violins. J. Acoust. Soc. Am. **124**(3), 1764–1773 (2008)
4. Skrodzka, E.B., Linde, B.B., Krupa, A.: Modal parameters of two violins with different varnish layers and subjective evaluation of their sound quality. Arch. Acoust. **38**(1), 75–81 (2013)
5. Jansson, E.V.: Admittance measurements of 25 high quality violins. Acta Acust. United Acust. **83**(2), 337–341 (1997)
6. Jansson, E.V.: Violin frequency response—bridge mobility and bridge feet distance. Appl. Acoust. **65**(12), 1197–1205 (2004)
7. Meinel, H.: Regarding the sound quality of violins and a scientific basis for violin construction. J. Acoust. Soc. Am. **29**(817), (1957)
8. Saunders, F.: The mechanical action of violins. J. Acoust. Soc. Am. **9**(2), 81–98 (1937)
9. Gren, P., Tatar, K., Granström, J., Molin, N., Jansson, E.V.: Laser vibrometry measurements of vibration and sound fields of a bowed violin. Meas. Sci. Technol. **17**(4), 635 (2006)
10. Alonso Moral, J., Jansson, E.: Input admittance, eigenmodes and quality of violins. Report STL-QPSR, pp. 2–3 (1982)
11. Woodhouse, J.: On the bridge hill of the violin. Acta Acust. United Acust. **91**, 155–165 (2005)
12. Fritz, C., Curtin, J., Poitevineau, J., Morrel-Samuels, P., Tao, F.-C.: Player preferences among new and old violins. Proc. Natl. Acad. Sci. **109**(3), 760–763 (2012)
13. Young, D.: Wireless sensor system for measurement of violin bowing parameters. In: Stockholm Music Acoustics Conference, pp. 111–114 (2003)
14. Young, D.: Classification of common violin bowing techniques using gesture data from a playable measurement system. In: Proceedings of the NIME, vol. 2008, Citeseer (2008)
15. Demoucron, M.: On the control of virtual violins—Physical modelling and control of bowed string instruments. Ph.D. thesis, Université Pierre et Marie Curie-Paris VI. Royal Institute of Technology, Stockholm (2008)
16. Askenfelt, A.: Measurement of bow motion and bow force in violin playing. J. Acoust. Soc. Am. **80**(4), 1007–1015 (1986)
17. Kreger, S.T., Gifford, D.K., Froggatt, M.E., Soller, B.J., Wolfe, M.S.: High resolution distributed strain or temperature measurements in single- and multi-mode fiber using swept-wavelength interferometry. In: Optical Fiber Sensors, p. ThE42. Optical Society of America (2006)
18. Guaus, E., Bonada, J., Maestre, E., Pérez, A., Blaauw, M.: Calibration Method to Measure Accurate Bow Force for Real Violin Performances. MPublishing, University of Michigan Library, Ann Arbor, MI (2009)
19. Jolliffe, I.: Principal Component Analysis. John Wiley & Sons, Ltd. (2002)
20. Abdi, H., Williams, L.J.: Principal component analysis. Wiley Interdiscip. Rev.: Comput. Stat. **2**(4), 433–459 (2010)
21. Cremer, L., Allen, J.S.: The Physics of the Violin. MIT Press, Cambridge (1984)

Chapter 6
Synthesizing Uncorrelated Drive Files for MIMO Transmissibility Measurements on Road Simulators

Shounak S. Deshmukh, Randall J. Allemang, and Allyn W. Phillips

Abstract Traditionally, road simulators have been used for durability and NVH testing of automobiles which involve estimation of simulated road inputs. The responses (ride files) are measured during actual road testing at a number of locations over different terrains which lead to the generation of the simulated road inputs by utilizing an iterative process. The process generally involves an inverse calculation so that the response measured in the actual road test of the vehicle for a given type of terrain can be replicated very closely by estimating the inputs to the four axes of the road simulator. The numerical estimation procedure of the inputs is based upon the characteristics and limitations of the specific four axis road simulator being used but it does not constrain these inputs (drive files) to the individual hydraulic actuators to be uncorrelated. The drive files to the four axis road simulators more often than not are significantly correlated which is a big hindrance to MIMO transmissibility measurements. Thus synthesis of uncorrelated drive files using the estimated correlated drive files by the way of a MATLAB® based interface is the focus of this research. The analysis shows that the auto power spectra is equivalent for the synthesized uncorrelated drive files compared to the original correlated drive files. These results are further corroborated by the experimental results obtained from the measurements done on the MTS four axis road simulator at UC-SDRL. These same methods should also be useful in estimating FRFs from drive files if the input forces can be measured.

Keywords Drive files • Synthesized drive files • Uncorrelated drive files • Four axis road simulator • MIMO transmissibility

Nomenclature

F_{EQ}	Equivalent or driving force
R	Actual input (reference)
F_T	Transmitted force
X	Actual output
F_{max}	Maximum frequency that can be observed in a Spectrum
T_{pq}	Transmissibility function of output p with respect to reference q
F_{samp}	Sampling frequency of the DSA
$[G_{XX}]$	Output output cross spectra matrix
$\widehat{X}_p$	Spectrum of p-th output, measured
$[G_{XR}]$	Output reference cross spectra matrix
$\widehat{R}_q$	Spectrum of q-th reference, measured
$[G_{RR}]$	Reference reference cross spectra matrix
v_q	Spectrum of noise portion of reference
η_p	Spectrum of noise portion of output

S.S. Deshmukh (✉) • R.J. Allemang • A.W. Phillips
Structural Dynamics Research Laboratory, Department of Mechanical and Materials Engineering, University of Cincinnati, Cincinnati, OH 45221, USA
e-mail: deshmusk@mail.uc.edu

E. Wee Sit (ed.), *Sensors and Instrumentation, Volume 5*, Conference Proceedings of the Society for Experimental Mechanics Series, DOI 10.1007/978-3-319-29859-7_6

6.1 Introduction

The automobile market today is highly competitive with a number of vehicles available to the customer, each having its own unique selling points. Amongst them, ride comfort is and always will be a major criteria for a customer buying a vehicle. Thus a lot of automotive research has been dedicated to reducing cabin noise and vibrations in vehicles. Modal analysis and frequency response functions (FRFs) have been traditionally used to quantify these vibrations in a laboratory setting. Road tests done on various road surfaces recreated using a four axis road simulator are ride focussed tests that begin to take into account non-linearities. Both these provide for accurate results for further analysis but are limited to a single vehicle and thus to compare similar vehicles with different configurations and structural sizes becomes difficult.

Thus to compare with different vehicles and attain benchmark levels, simulation of vehicle road tests has been of huge interest to researchers. Recreating the responses on the vehicles to be the same as that obtained during the actual road test is the objective of the simulation. Creating custom input signals to get desired responses in frequency or time domain is an added capability so that different vehicles can be tested with the same reference. Four axis road simulators are used for different quality considerations but mostly for durability and noise, vibration and harshness (NVH) concerns. Traditionally, these road simulators make use of LVDTs (linear variable displacement transducers) which quantifies input to vehicles in terms of displacement. Having vehicle response measured to this kind of input motion is quite convenient. FRF estimation requires input forces be measured which can be realized by using load cells at the four axes. But this instrument set up is uncommon, very expensive and not currently available at the University of Cincinnati, Structural Dynamics Research Lab (UC-SDRL).

The transmissibility concept is therefore useful here. The ratio of the force transmitted to the foundation (F_T) referenced to the equivalent or driving force (F_{EQ}) is defined as transmissibility [1]. Transmissibility can also be described as the ratio of structure displacement to the base displacement if the base is of moving type. This concept is particularly applicable to four axis road simulation where the road inputs (displacements) are controlled. Traditionally transmissibility is defined as a single input, single output, single degree of freedom (SDOF) concept, but a multiple input, multiple output (MIMO) approach, involving multiple degree of freedoms (MDOF) has to be used for a four axis road simulator owing to the inputs at four axes.

By utilizing the displacements measured from the LVDTs at the four shakers the transmissibility can be estimated by taking responses at various locations on the vehicle with respect to the four inputs. Similar to MIMO FRF estimation, the four inputs have to be conditioned to allow for numerical estimation of MIMO transmissibility. With the inputs being simulated to recreate the responses obtained in the actual road test, the conditioning for the four inputs more often than not becomes poor and thus numerical estimation of MIMO transmissibility is not possible. So inputs have to be synthesized such that condition improves and the synthesized inputs are still equivalent to the estimated inputs used to recreate the responses.

6.2 Theory and Background

The numerical estimation procedure for simulated input signals or drive files has been discussed at length in MS thesis by U N Godbole [2] developed specifically for the road simulator at UC-SDRL. The iterative process is also specified by OEMs for their specific road simulators in SAE papers by Cryer et al [3] and Kim et al [4] to be used for different quality testing. Since the estimation uses response data from actual road test data, most of the times the drive files are correlated. This is discussed further in Section 3 by using examples. It is also critical to understand why having correlated inputs cannot be used to estimate MIMO transmissibility. The MIMO transmissibility as a concept has been developed as a parallel to the MIMO FRF estimation algorithms [5–8, 12, 13]. The following schematic (Fig. 6.1) is representative of the multi-reference transmissibility as a general case.

The following equation represents the transmissibility measurement case involving multiple references and a single output. This linear equation is simply replicated for each additional output.

$$\widehat{X}_p - \eta_p = \sum_{q=1}^{4} T_{pq} \times \left(\widehat{R}_q - \nu_q \right) \tag{6.1}$$

The following nomenclature was used to define the MIMO transmissibility measurement case for the least squares estimation of transmissibility, exactly paralleling the least squares estimation of MIMO frequency response functions [7].

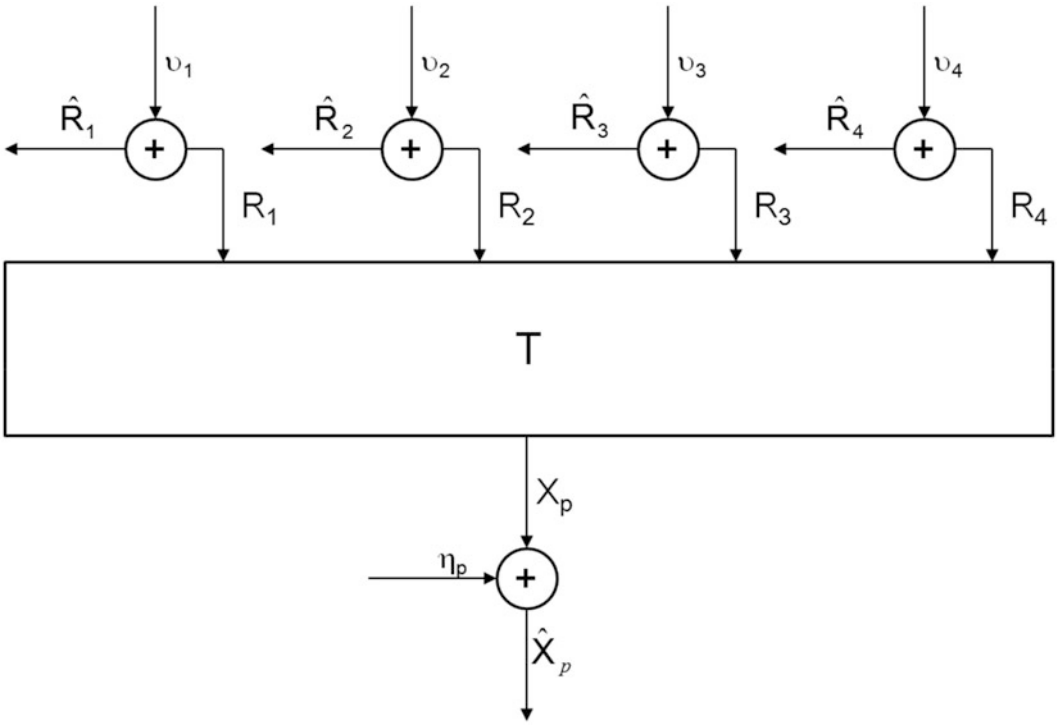

Fig. 6.1 Multiple input transmissibility measurement model

$[G_{XR}] = \{X\}\{R\}^H$—Output Reference Cross-Spectra Matrix.

$$[G_{XR}] = \begin{Bmatrix} X_1 \\ X_2 \\ . \\ . \\ X_{N_o} \end{Bmatrix} \begin{bmatrix} R_1^* & R_2^* & . & . & R_{N_r}^* \end{bmatrix} \tag{6.2}$$

$$[G_{XR}] = \begin{bmatrix} G_{XR_{11}} & . & G_{XR_{1N_r}} \\ . & . & . \\ G_{XR_{N_01}} & . & G_{XR_{N_oN_r}} \end{bmatrix}$$

R^*—Complex Conjugate.
$[G_{XX}] = \{X\}\{X\}^H$—Output Output Cross-Spectra Matrix.

$$[G_{XX}] = \begin{Bmatrix} X_1 \\ X_2 \\ . \\ . \\ X_{N_o} \end{Bmatrix} \begin{bmatrix} X_1^* & X_2^* & . & . & X_{N_o}^* \end{bmatrix}$$

$$[G_{XX}] = \begin{bmatrix} G_{XX_{11}} & . & G_{XX_{1N_o}} \\ . & . & . \\ G_{XX_{N_01}} & . & G_{XX_{N_oN_o}} \end{bmatrix} \tag{6.3}$$

$G_{XX_{ik}} = G_{XX_{ik}}^*$—Hermitian Matrix.

$[G_{RR}] = \{R\}\{R\}^H$—Reference Reference Cross-Spectra Matrix.

$$[G_{RR}] = \begin{Bmatrix} R_1 \\ R_2 \\ . \\ . \\ R_{N_r} \end{Bmatrix} \begin{bmatrix} R_1^* & R_2^* & . & . & R_{N_r}^* \end{bmatrix} \tag{6.4}$$

$$[G_{RR}] = \begin{bmatrix} G_{RR_{11}} & . & G_{RR_{1N_r}} \\ . & . & . \\ G_{RR_{N_r1}} & . & G_{RR_{N_rN_r}} \end{bmatrix}$$

$G_{RR_{ik}} = G^*_{RR_{ik}}$—Hermitian Matrix.

Note that the subscript "R" in the matrices above refers to "reference" and is not to be confused with "response". Outputs (responses) are denoted with subscript "X". The G_{RR} matrix is analogous to the G_{FF} matrix in FRF estimation. As with the G_{FF} matrix, the G_{RR} matrix must be well conditioned (invertible) for the transmissibility to be computed for the MIMO case. Highly correlated inputs causes ill-conditioning of the G_{RR} matrix. The computation of this correlation parallels the principal force (virtual force) computation for MIMO FRF estimation and is used in the same way. For the case of four input transmissibility, this is referred to as principal reference (or virtual reference) analysis [9]. For two or more references, a principal response analysis using singular value or eigenvalue decomposition of the G_{RR} matrix is needed to determine that the inputs are not highly correlated [10, 11].

The MIMO transmissibility estimation process parallels the MIMO, least squares, FRF estimation process. The notations are same as the least squares FRF estimation techniques namely H_1, H_2, H_v [7, 8] and are denoted as T_1, T_2 and T_v [12, 13]. In general, for all three techniques, the four inputs (references) used in the four axis road simulator must not be highly correlated. This means that the actual measured motions at the four hydraulic actuators can be partially correlated but must not be completely correlated at any frequency in the analysis band. This evaluation is done using singular value decomposition of the G_{RR} matrix, in the form of virtual references, in the analytical as well experimental chapters of this research.

6.3 Analytical Results

All the data was provided by UC-SDRL from their information data archive. The data primarily was response files generated during actual four axis road simulation tests for different surfaces on a number of vehicles. Data was consolidated for four different type of vehicles over four different types of road surfaces. Due to the proprietary nature of the data, the vehicles are denoted as Vehicle A, B, C and D. Similarly the road surfaces are designated as NVH 1, NVH 2, NVH 3 and NVH 4. Drive files for these 16 cases were generated using the MATLAB® based SimTest® software and was provided by the information data archive. These 16 drive files are the original drive files and are then utilized for further analysis and synthesis of uncorrelated drive files using a custom MATLAB® script. The custom MATLAB® interface can be utilized from the MS thesis by S S Deshmukh on the same topic as this research paper [14]. Only one example will be illustrated in this paper but discussion of all the other 15 cases can be found in the MS thesis referred to above.

The approach is therefore to randomize the four inputs of the original drive files in some way so that the data is uncorrelated and can be utilized in a MIMO estimation procedure for transmissibility or possibly FRF estimation. The approach also needs to achieve the goal of maintaining the same level of motion as a function of frequency. Essentially that means the auto power of the synthesized drive files is equivalent to the original drive files.

The illustrated example of the original drive files estimated from response or ride files are as follows. These have been generated using the iterative process to recreate the responses of the actual road test. These have been generated using collocated responses at the axle closest to the wheels. Ride files having four responses were used to create these drive files. These drive files are the base for all the further analysis done. The illustrated example is for Car D on road surface NVH 4 (Fig. 6.2).

Upon close inspection of the time domain data it can be seen clearly that the rear wheels lags the front wheels by a constant amount of time. This is expected as the drive files are numerically estimated from actual road test response or ride files. After the front wheels move over a particular road surface irregularity the rear wheel will also be subjected to that irregularity, most of the times leading to the constant time lag and subsequently the correlation of the inputs estimated. The following

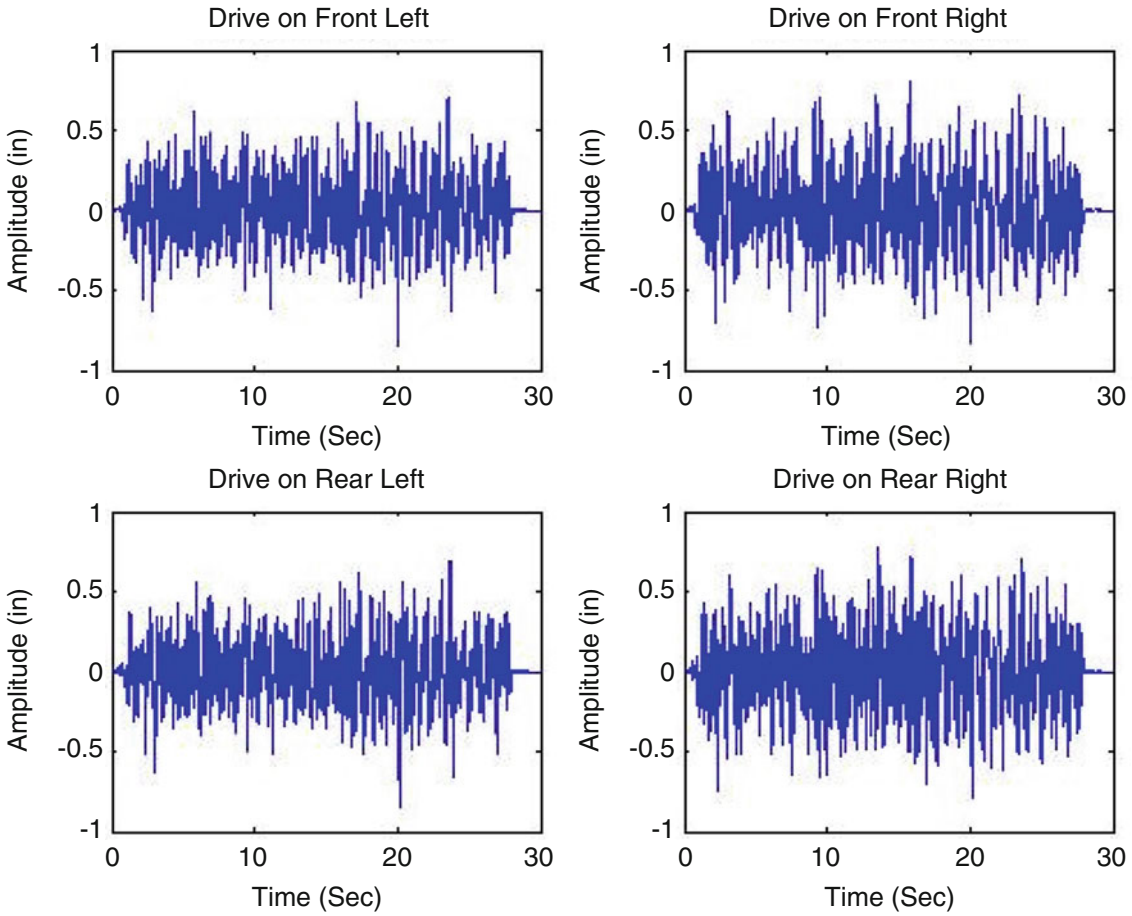

Fig. 6.2 Original drive file

figures illustrate the time lag between the front and rear wheels. Specific time intervals have been zoomed in to clearly show the illustration. The time lag is measured to be 0.1367 s. The overlap explains how the front and rear wheels line up almost perfectly after the time lag has been removed thus resulting in correlation of input references (Fig. 6.3).

The use of principal component analysis (PCA) using the singular value decomposition (SVD) function in MATLAB® further corroborates the high correlation of the input drive signals. The digital signal processing (DSP) parameters used for this analysis were:

- Sampling frequency-204.8 Hz.
- Window-Hanning.
- Averaging-50 % Overlap.
- Block Size-1024.

The original drive files generated from the SimTest® software were bandpass filtered from 4 to 40 Hz using a Butterworth filter. The filtering capability is built into the software. The limits are selected taking into consideration that the discomfort in the cabin is generally caused by road surface inputs in between these frequencies. The example of principal or virtual references of the original drive files is as follows.

The principal or virtual reference analysis involves the singular value decomposition of the G_{RR} matrix (Eq. 6.4) at each frequency of the power spectra of the references. Since the singular vectors of such a decomposition are unitary, the singular values should all be of approximately the same size if each of the inputs or references is contributing to the excitation of the structure equally. If one of the singular values is much smaller at a particular frequency, it can be concluded that one of the inputs is not present or one of the inputs is correlated with the other input(s) at that frequency. As clearly seen from the Fig. 6.4, inputs are correlated as the singular values of two inputs are much smaller than the remaining inputs at almost all the frequencies.

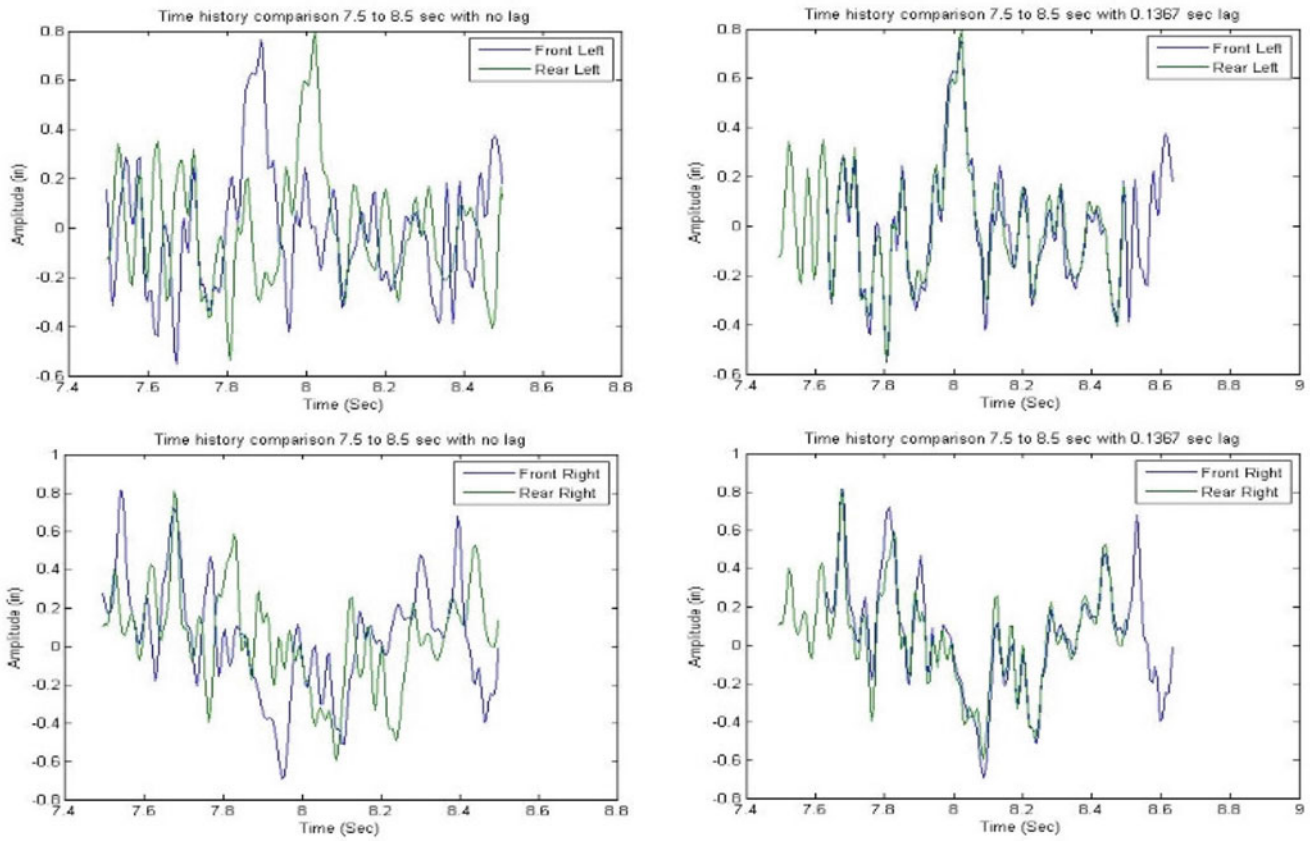

Fig. 6.3 Time interval 7.5–8.5 s zoomed in from original drive file to illustrate constant time lag

Synthesizing drive files was done using a custom made script in MATLAB®. Since the synthesized files needed to be comparable to the simulated original input files, different randomizations were applied to the simulated drive files. Physically that would correspond to the wheels moving independently relative to each other leading to removal of correlation between the inputs. The singular values plot (i.e. the virtual references) for synthesized drive files will show that at all the frequencies the singular values for all the inputs are comparable.

First, a randomization technique was applied, shifting time by a fixed duration for all the four wheel inputs. But as expected, the data was still correlated as the time lag was still constant between the wheels. The example for this randomization technique is below. The virtual references plot is also included (Fig. 6.5).

The second technique applied was essentially moving the input to the wheels by random time durations to get over the constant time lag that the rear wheels have with respect to the front wheels. The random time durations were applied to all wheels with them either moving forward or backward relative to each other. This technique helped in removal of the correlation between the inputs. The following is the example (Fig. 6.6).

The next technique applied was flipping the complete time history for the rear wheels as they are the ones with the constant time lag. This helps in keeping the front wheel inputs the same as the simulated original drive files and removing the correlation between the inputs. The example is as below with the virtual references also included (Fig. 6.7).

One final technique used was a variation of the flipped technique used earlier. In this technique, only half of the time data for the rear wheels was flipped. This helps in keeping half of the rear wheel inputs same as the simulated original drive files. The front wheel drive files are same as the original drive files. Thus one more technique which helps in removing correlation between the inputs (Fig. 6.8).

The synthesized drive files and original drive files were extended for using on the four axis road simulator. It was done to get a bigger time stream of data for a better analysis and to have enough confidence on the data acquired. The original drive files were extended end to end by 20 times the original length of the time data. The synthesized drive files were created using a conjunction of the three randomizing techniques discussed earlier which leads to uncorrelated inputs. Each of the 20 streams of original time data was divided into quarters and with each quarter having one of the techniques applied to it. They were then added end to end to get the big time stream of synthesized data. Even the selection of which technique was applied

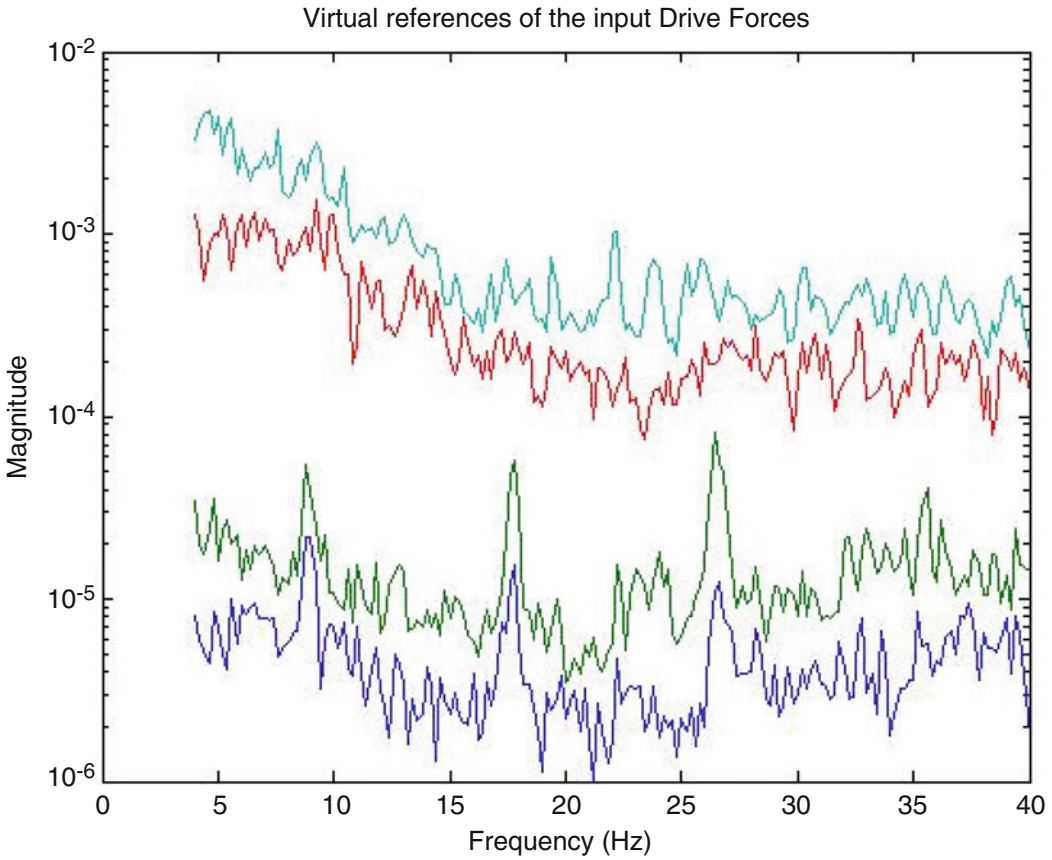

Fig. 6.4 Virtual references of original drive file

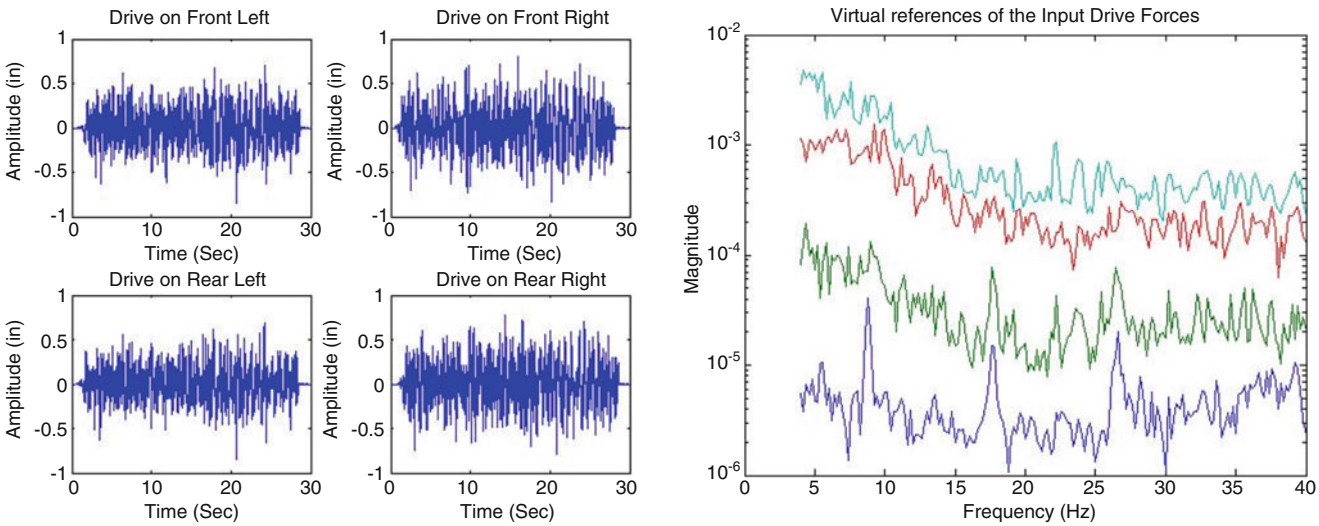

Fig. 6.5 Fixed shifted synthesized inputs with virtual references

to one time stream was chosen randomly. This resulted in drive files which even though extended are effectively the same as the original drive files and the synthesized drive files in its properties. The example of the extended drive file is given below along with the virtual references (Fig. 6.9).

The synthesized data was then checked for their auto power spectra. This was done to compare the energy content between the synthesized drive files with the original simulated drive files. It was imperative that they are similar so that it can safely

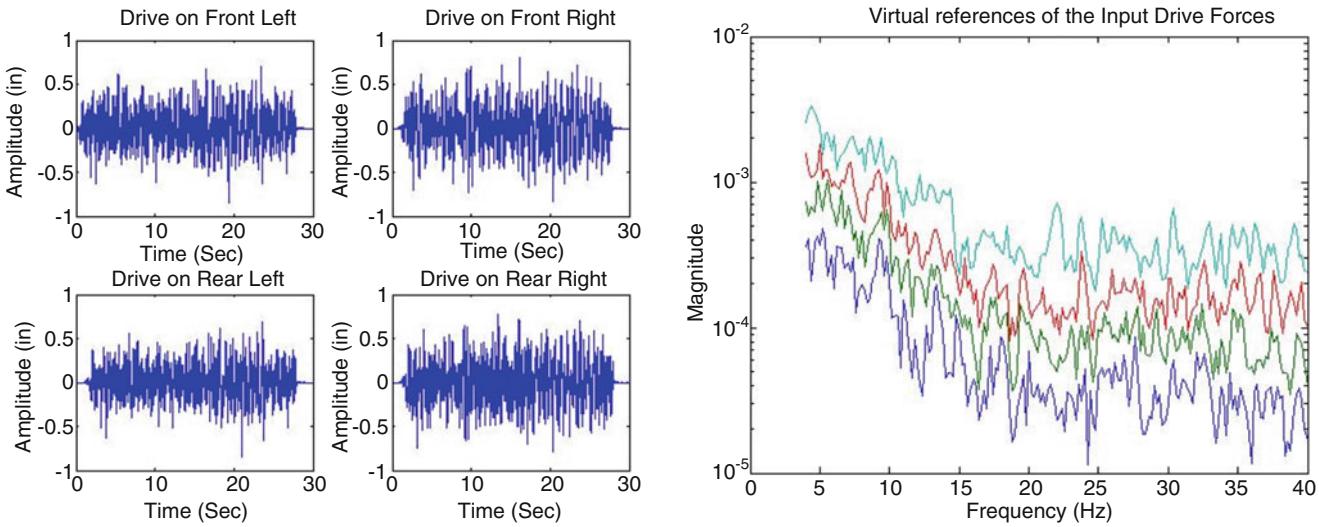

Fig. 6.6 Random shifted synthesized inputs with virtual references

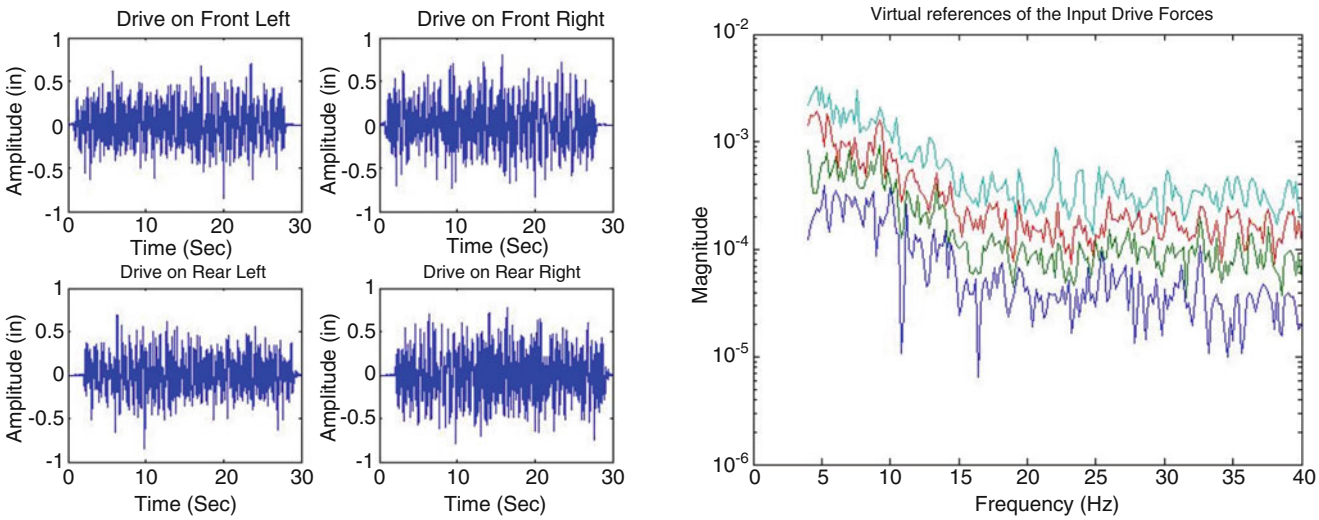

Fig. 6.7 Flipped synthesized inputs with virtual references

be assumed that the synthesized drive files excite the vehicle quite similar to the original simulated drive files. The following example shows how they are equivalent and form the basis for further experimentation on the four axis road simulator using the analytical data (Fig. 6.10).

6.4 Experimental Results

A readily available pick-up truck frame was used for testing on the four axis road simulator. Responses were measured at the axle closest to wheel hub connection for all the four wheels to simulate collocated response measurements. The inputs were given to the actuators using a combination of softwares. X-Modal, an internally developed software used by the UC-SDRL, allows the user to input a drive file using a commercially available PC. The drive files need to be in the MATLAB® ".mat" format. The X-Modal software interfaced with a VXI Mainframe having four VXI VT1435 8 channel cards. Each card had one input interfaced with the MTS 320 road simulator controller. The FlexTest II software interfaces with the MTS 320 controller to enable the user to control the four axis road simulator using a commercially available PC (Figs. 6.11 and 6.12).

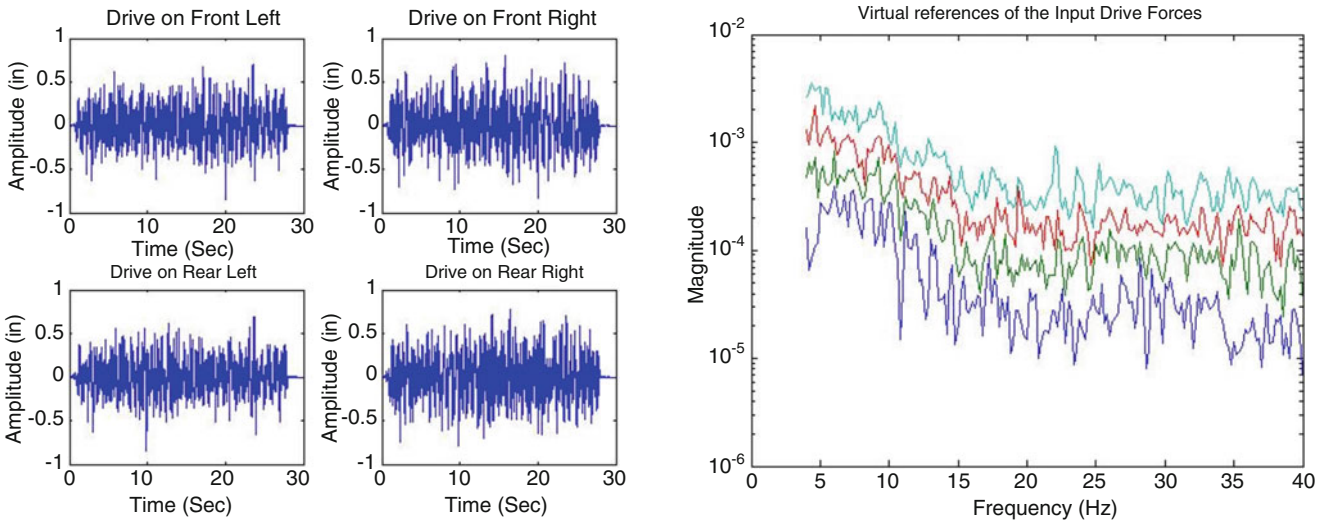

Fig. 6.8 Half flipped synthesized inputs with virtual references

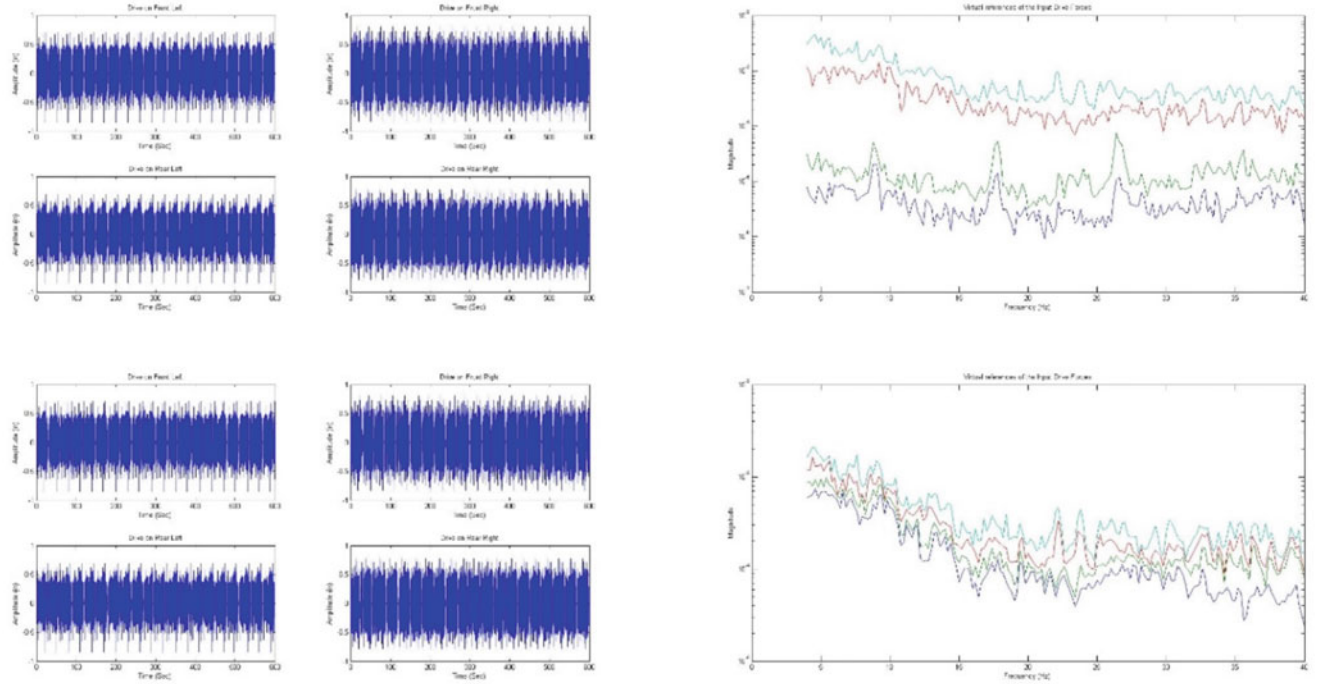

Fig. 6.9 Extended original and synthesized drive files with virtual references

The data acquisition was done using X-Modal software interfaced with one of the four VXI VT1435 8 channel cards. Four channels on the card were used to measure the actual input to the pick-up truck frame by using the measurements from the LVDT fitted in the actuators. The other four channels were used to measure response from the PCB tear drop accelerometers attached on the axle of the frame. The sampling frequency for the analytical results was 204.8 Hz which was governed by the F_{samp} of the response data in the information data archive at UC-SDRL. X-Modal has the capability to resample this input data to match the F_{samp} available for data acquisition. The digital signal processing (DSP) parameters used for data acquisition are as follows:

- F_{samp}-256 Hz, F_{max}-100 Hz, frequency lines-500.
- Window-Hanning.
- 75 Ensembles, each 5 s.

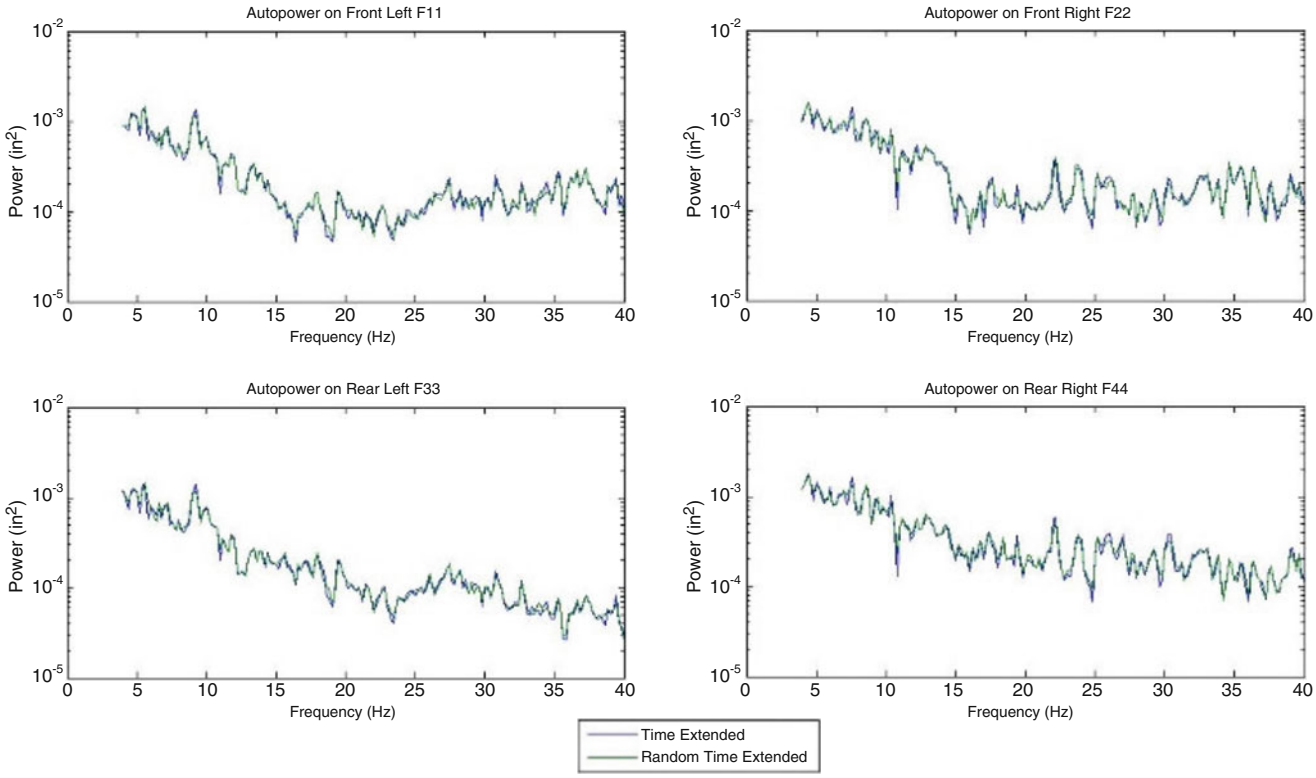

Fig. 6.10 Auto power comparison

Fig. 6.11 Experimental test setup using pick-up truck frame

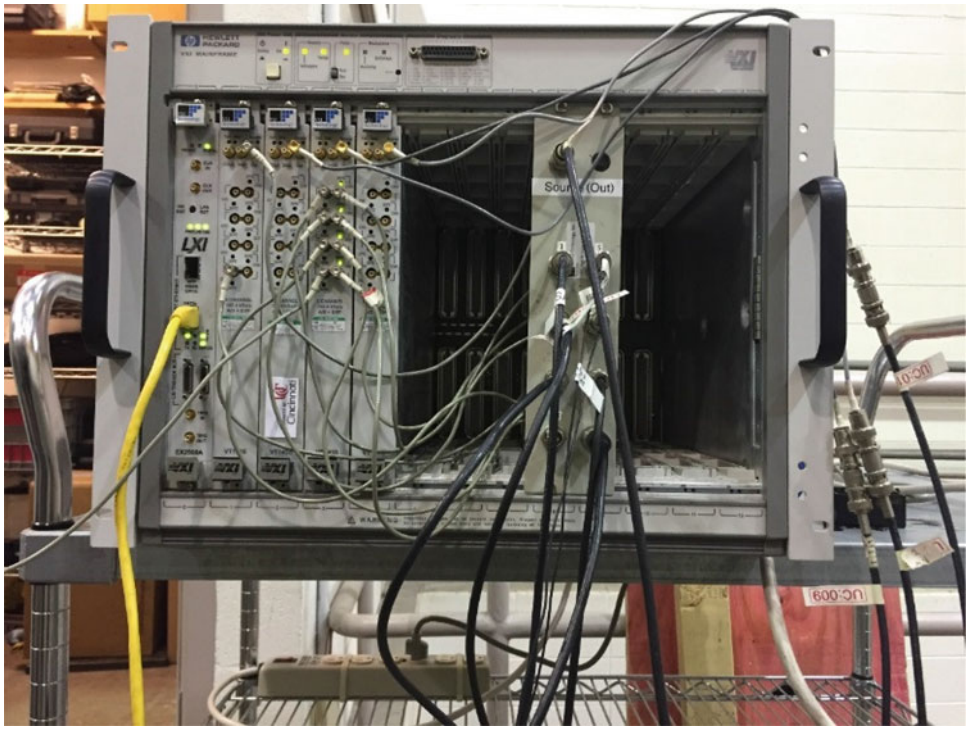

Fig. 6.12 HP mainframe with four VXI VT1435 8 channel cards with one input each

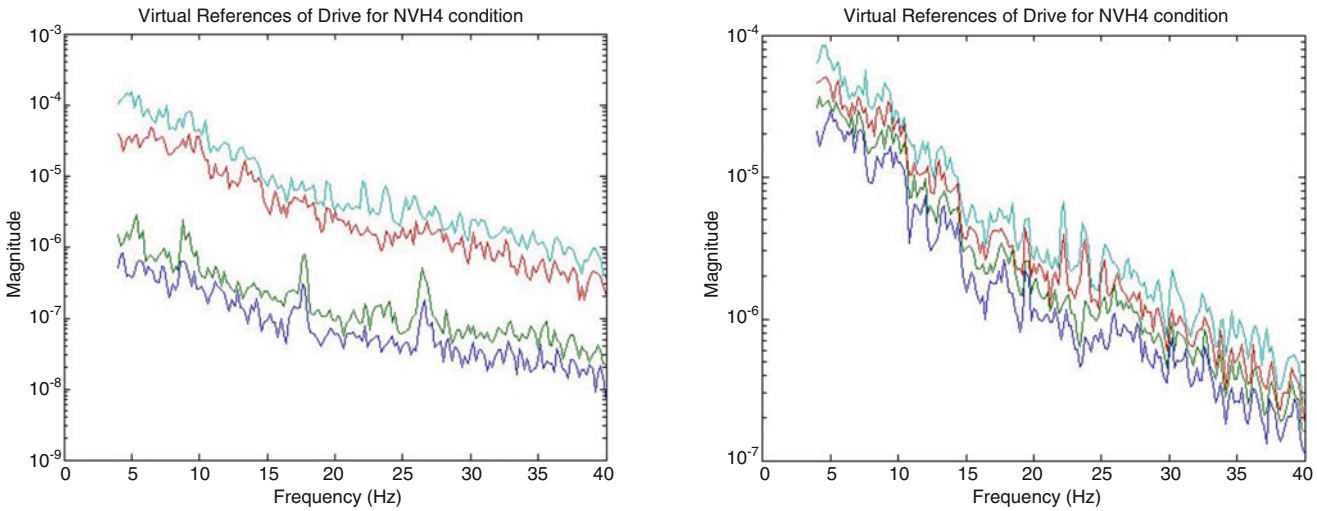

Fig. 6.13 Virtual references of measured data using original drive file and synthesized drive file

- Accelerometer calibration data: FL-98.4, FR-100.6, RL-99.4 & RR-103.2 mV/g.
- LVDT calibration data: All actuators-3.34 V/in.

The extended drive files were used as an input to the actuators with the data acquisition system in place. The data acquired was auto power and cross power data for the reference and response channels. A MATLAB® based script was used to analyse these measurements. The virtual references of the original drive files and synthesized drive files showed expected results. The original drive files were still correlated as can be seen in the virtual references plot, where the singular values for two inputs are consistently much lower than the other two inputs. The synthesized drive files had no correlation of inputs as the singular values of all the inputs are comparable. The example of the virtual references of the measured data from the four axis road simulator is as below (Fig. 6.13).

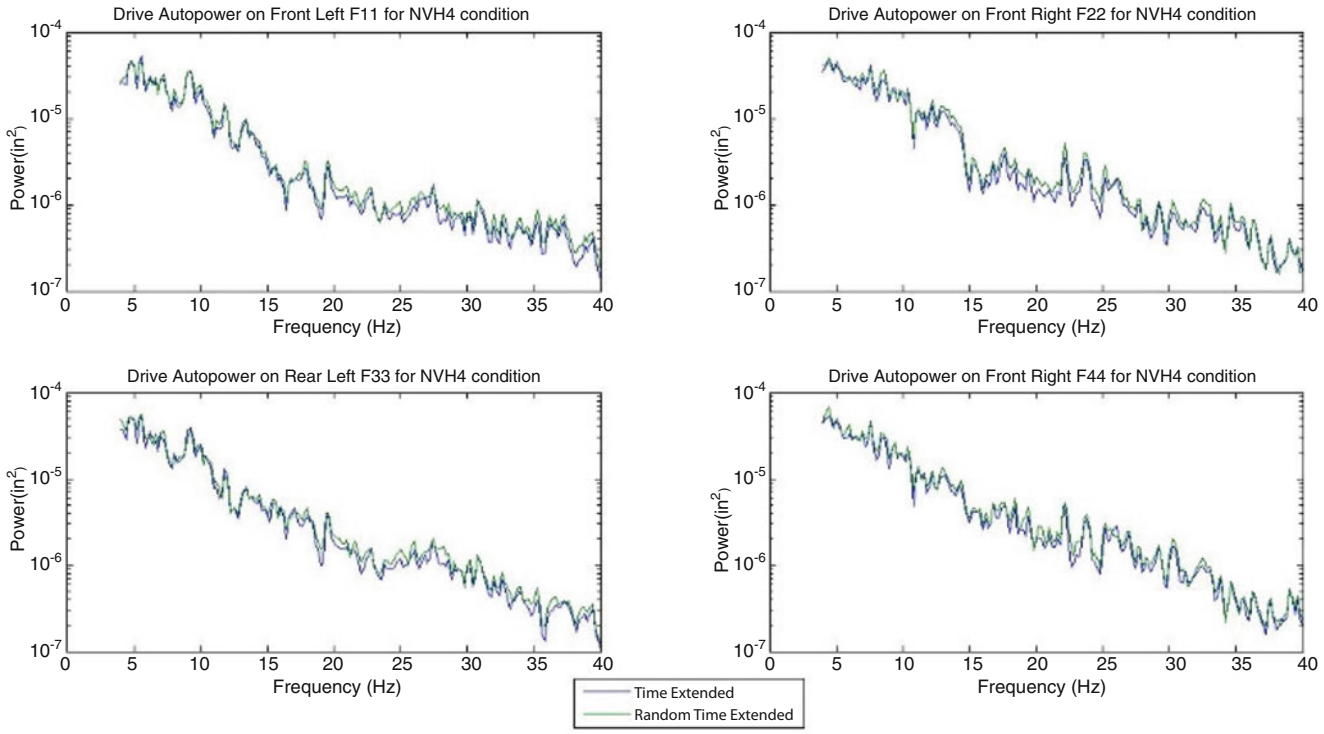

Fig. 6.14 Auto power comparison of measured data

Again it was important to have equivalent auto power from the synthesized drive files compared to the original drive files as measured from the actuators of the four axis road simulator with the pick-up truck frame over it. The energy content exciting the frame should be quite similar so that any subsequent NVH or durability analysis provides results which are equivalent to what are expected from an actual road test. Since the original drive files are simulated from actual road test responses. The example provided below clearly shows that the auto power of the measured data, both for original drive files and synthesized drive files is equivalent (Fig. 6.14).

6.5 Conclusions

More often than not and as seen from the analytical results, the drive files are correlated. There is a constant time lag between rear and front wheels of a vehicle moving over a particular surface during an actual road test. The simulated inputs are generated using the actual road test responses which have the constant time lag effect. This translates to correlation between the simulated inputs.

The MATLAB™ based interface which has been developed helps to synthesize drive files using different randomization techniques leading to removal of correlation of these input signals. The randomization techniques are mostly aimed at removing the time lag effect. They effectively make the wheels move differently relative to each other such that a particular irregularity of a surface which was acting on the wheels with a constant time lag now acts on the wheel without the constant time lag.

The randomization techniques used in conjunction with each other results in synthesized drive files which now are uncorrelated. The uncorrelation between the inputs was corroborated by the experimental results. Furthermore these signals carry the equivalent energy as the original drive files as seen from the analytical as well as experimental results. These signals can now be directly used for analysis as the condition of uncorrelation has been met and it will excite a structure with an equivalent energy content as the original drive files.

References

1. Tse, F.S., Morse, I.E., Hinkle, R.T.: Mechanical vibrations theory and applications. Allyn and Bacon, Inc, Boston, MA (1963)
2. Godbole, U.N.: Vehicle road test simulation, University of Cincinnati, MS Thesis (2005).
3. Cryer, B.W., Nawrocki, P.E., Lund, R.A.: A road simulation system for heavy duty vehicles, SAE Technical Paper 760361 (1976).
4. Kim, M.G., Kim, K.S., Yoo, W.S.: Modified road profile generation using road-wheel FRF and simulation of dynamic load transfer in vehicle suspension. In: SAE International Congress and Exposition, Detroit (1999).
5. Bendat, J.S., Piersol, A.G.: Random data: analysis and measurement procedures. Wiley, New York (1971)
6. Allemang, R.J.: Investigation of some multiple input/output frequency response function experimental modal analysis techniques, University of Cincinnati, PhD Dissertation (1980).
7. Allemang, R.J.: Vibrations: experimental modal analysis, University of Cincinnati, UC-SDRL-CN-20-263-663/664 (2007).
8. Rost, R.W.: Investigation of mulitple input frequency response function estimation techniques for experimental modal analysis, University of Cincinnati, PhD Dissertation (1985).
9. Allemang, R.J., Phillips, A.W., Allemang, M.R.: Application of principal compenent analysis methods to experimental structural dynamics. In: Proceedings of the International Modal Analysis Conference-XXVIII, Jacksonville (2010).
10. Strang, G.: Linear algebra and its applications, Thomson Brooks/Cole (2006).
11. UC-SDRL.: Singular value decomposition concepts, University of Cincinnati, Course Notes, (2008).
12. Yee, A.K.; Using group transmissibility concepts to compare dissimilar vehicle platforms, University of Cincinnati, MS Thesis (2009).
13. Allemang, M.R.: Comparison of automotive structures using transmissibility functions and principal component analysis, University of Cincinnati, MS Thesis (2013).
14. Deshmukh, S.S.: Synthesizing uncorrelated drive files for MIMO transmissibility measurements on road simulators, University of Cincinnati, MS Thesis (2015).

Chapter 7
Calibration Techniques for Non-contacting Force Excitation Part 1: Frequency Domain Methods

Patrick Logan and Peter Avitabile

Abstract Experimental characterization of the higher frequency modes of a structure presents challenges due to the frequency limitations of traditional excitation techniques. Non-contact excitation via low power ultrasonic transducer presents the possibility of exciting higher frequencies not currently possible with shakers or impact hammers. However, quantification of the actual force applied by the ultrasonic transducer requires that a relationship between the ultrasonic pressure field and the voltage driving the transducer be established.

In part 1 of this paper, calibration techniques shall be explored using spectral domain techniques with conventional instrumentation before extending the techniques to the ultrasonic transducer. Frequency response functions generated from uncalibrated excitation transducers shall be compared with those generated from calibrated equipment to determine an appropriate sensitivity for the uncalibrated transducers. Reciprocal measurements shall also be examined as a means of calibrating transducers. Time domain techniques for calibration shall be examined in part 2 of this paper.

Keywords Non-contact excitation • High frequency excitation • Non-intrusive excitation • Ultrasonic transducer • Calibration methods

7.1 Introduction

Use of ultrasonic waves is being explored as a means by which higher frequency modes of a test article may be characterized without the need for direct contact. Traditional excitation via impact hammers and shakers permits measurement of the force applied to a test article by measuring the voltage output from a force gage, but no analogous mechanism exists for the ultrasonic transducer, which produces an ultrasonic pressure field that is dependent upon the voltage driving the transducer. While some ultrasonic transducers produce an ultrasonic field which acts over a wide area, certain transducers focus the ultrasonic pressure field over an area small enough to be approximated as a discrete point. The question then arises as to how the effective force acting at the focal point can be related to the voltage driving the ultrasonic transducer.

To determine a meaningful calibration value for the ultrasonic transducer, frequency response functions obtained using traditional calibrated instruments may be used to establish a scale for uncalibrated measurements made with the same input and output locations. When experimental conditions arise which prevent the acquisition of measurements with the same input and output locations, reciprocal measurements may also be used for calibration. The technique and validation using traditional excitation equipment shall be presented within this paper.

7.2 Theoretical Background

7.2.1 Comparison of Calibrated and Uncalibrated Frequency Response Functions

For any linear system, the input force acting at any location j, $F_j(j\omega)$, and the response at any location i, $X_i(j\omega)$, may be related at any frequency, $j\omega$, by the frequency response function, $H_{ij}(j\omega)$, as shown by

P. Logan (✉) • P. Avitabile
Structural Dynamics and Acoustic Systems Laboratory, University of Massachusetts Lowell, One University Avenue, Lowell, MA 01854, USA
e-mail: patrick_logan@student.uml.edu

E. Wee Sit (ed.), *Sensors and Instrumentation, Volume 5*, Conference Proceedings of the Society for Experimental Mechanics Series, DOI 10.1007/978-3-319-29859-7_7

$$\frac{X_i(j\omega)}{F_j(j\omega)} = H_{ij}(j\omega) \tag{7.1}$$

The frequency response functions (FRFs) of a particular system result from the system mass, damping, stiffness and boundary conditions. In considering the experimental assessment of a particular FRF, where the input location and response location are fixed, the measurements should, in theory, provide the same FRF, despite that the excitation and response spectra may differ with each measurement.

As a simplification to the treatment of this material, experimental measurements of force and response are idealized such that they are interchangeable with the actual quantities measured. Use of calibrated equipment to measure the input allows that the actual force input may be expressed as the product of the output voltage, V, and the instrument calibration value, α, as described by

$$F_j(j\omega) = \alpha \cdot V_j(j\omega) \tag{7.2}$$

Substitution of (7.2) into (7.1) yields an expression for the FRF, as related to the input measurement in terms of raw voltage and the calibration value, as shown by

$$\frac{X_i(j\omega)}{\alpha \cdot V_j(j\omega)} = H_{ij}(j\omega) \tag{7.3}$$

Forming the FRF with calibrated measurements of the response and the uncalibrated measurements of the input yields an uncalibrated FRF. The uncalibrated FRF, denoted by an asterisk, describes response per unit measured voltage as shown by

$$\frac{X_i(j\omega)}{V_j(j\omega)} = H^*_{ij}(j\omega) \tag{7.4}$$

Dividing the expression for the uncalibrated FRF by the expression for the calibrated FRF yields the calibration value of the uncalibrated instrument, as shown by

$$\frac{H^*_{ij}(j\omega)}{H_{ij}(j\omega)} = \alpha \tag{7.5}$$

With (7.5), the unknown calibration value of the instrumentation can be obtained by dividing the uncalibrated FRF by the calibrated FRF. Although this treatment of the material presents idealized measurements, unaffected by noise and other problems which plague measurement systems, real measurements present additional challenges. In lieu of comparing experimentally obtained FRFs over the entire frequency band for which they were acquired, consideration may be limited to the peaks, where the response may be assumed to be well measured.

7.2.2 Calibration via Reciprocal Measurements

Equations 7.1–7.5 describe the determination of an instrument's calibration value by normalizing an uncalibrated FRF by the calibrated FRF obtained using the same input location and output location. Some instrumentation may preclude use of the same set of input and output locations. For example, a system will exhibit differences in dynamic behavior when a shaker is attached as opposed to when no shaker is attached. However, maintaining the shaker attachment through subsequent measurements prevents access to the attachment location for force input from a different instrument. When the same set of input and output locations are not available for both the calibrated and uncalibrated FRFs, reciprocal measurements may be used for comparison [1].

The principle of reciprocity arises from the square-symmetric nature of a discrete system's mass, damping and stiffness matrices. Reciprocity holds that, for any frequency response function obtained from some input location j and some response location i, the frequency response function obtained by switching the input and output locations will be the same. A fundamental expression of reciprocity is given by

$$H_{ij}(j\omega) = H_{ji}(j\omega) \tag{7.6}$$

Because reciprocal measurements should yield the same frequency response function, an uncalibrated measurement may also be normalized by its calibrated reciprocal measurement, and vice-versa, to obtain a calibration value.

7.2.3 Calibration via Newton's Second Law

As a comparison, instrument calibration can be performed in the time domain by use of a pendulous mass instrumented with an accelerometer [2]. By impacting the mass and measuring the peak voltage from the impact hammer with the peak response from the accelerometer, the instrument sensitivity can be obtained via Newton's Second Law of Motion. The calibration value can be expressed with respect to the peak voltage of the hammer, V_P, the peak acceleration response, a_p, and the mass, m, of the pendulum, as shown by

$$\alpha = \frac{m \cdot a_p}{V_p} \tag{7.7}$$

7.3 Structure Description

The structure used for testing consists of a quarter inch aluminum plate bolted into a block with a significantly larger mass, shown in Fig. 7.1. The plate measures 2 in. wide and 5 in. in height above the base.

7.4 Testing Performed

Calibrated frequency response functions were obtained with a miniature impact hammer, PCB model 086D80 and the Polytec PSV-400 laser [3]. Data acquisition and processing was performed with LMS Test Lab [4]. The miniature impact hammer, typically used for higher frequency measurements on small structures, was affixed to a tabletop tripod via plastic straw to permit better repeatability of impacts. The miniature impact hammer is shown with the calibration structure in Fig. 7.2. The nominal calibration value of the hammer is 10 lbf/V, or 44.482 N/V.

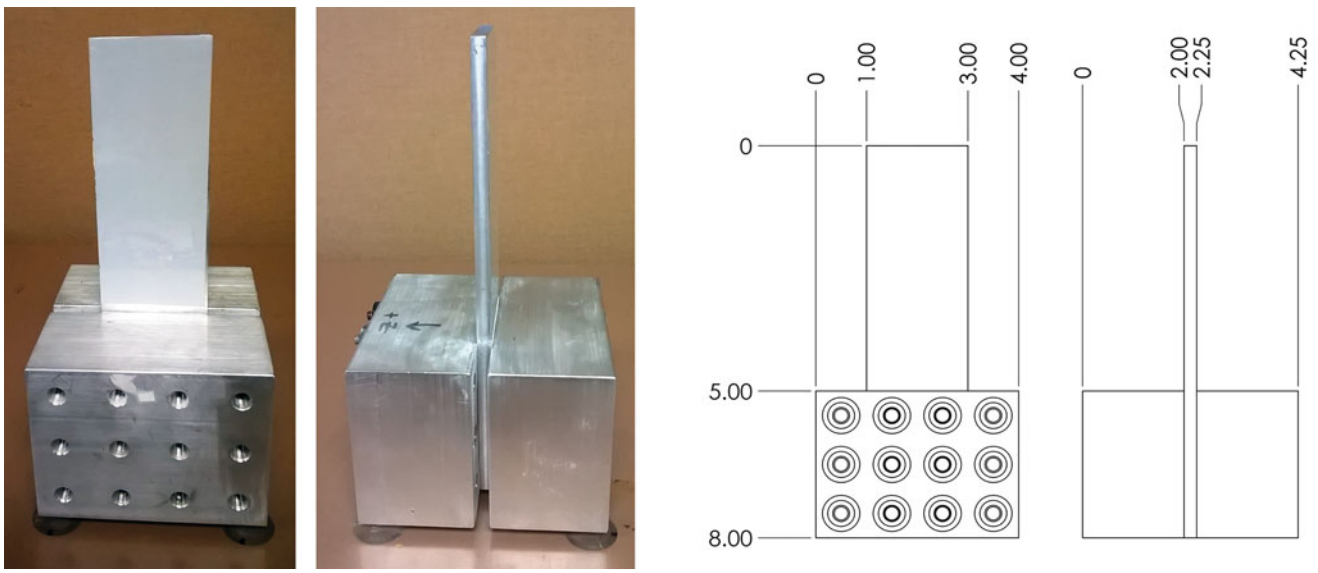

Fig. 7.1 Quarter inch aluminum plate, used as calibration structure, pictured from front and side (*left*), and drawn with dimensions provided in inches (*right*)

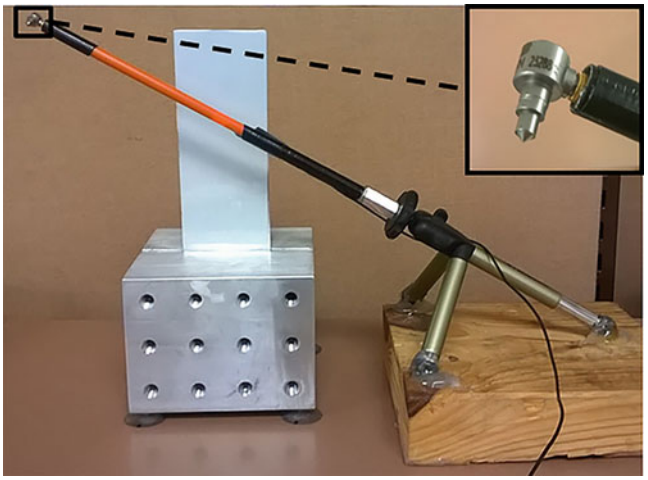

Fig. 7.2 Calibration structure and miniature impact hammer, with hammer head shown *top right*

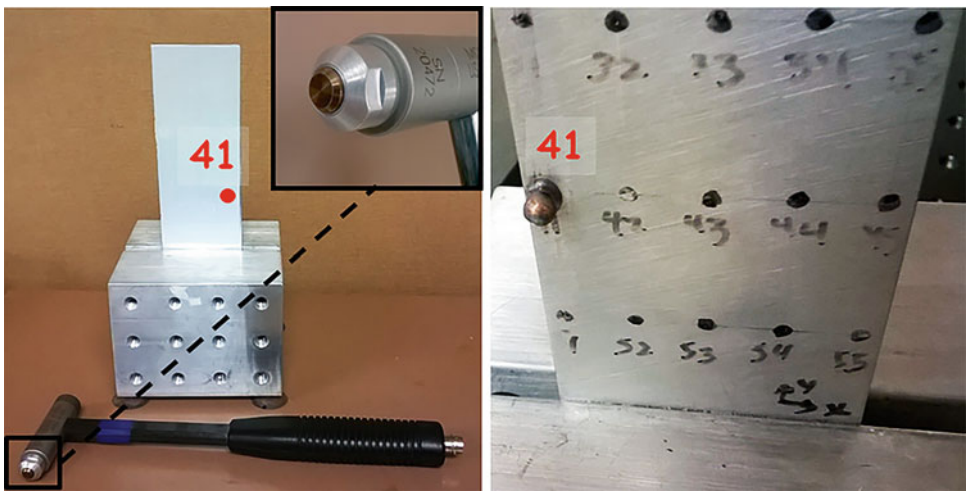

Fig. 7.3 General purpose impact hammer employed as an uncalibrated input, with location of drive point on front of structure (*left*), and ball bearing glued to back of structure, at impact point (*right*)

7.4.1 Calibration via Drive Point FRF

As an examination of the capability of the technique to provide a meaningful calibration value for a different model of impact hammer, a larger, general purpose, impact hammer was used as an uncalibrated input. The hammer's calibration value of 502.51 N/V was not used: a calibration value of 1 V/V was applied. A metal tip was used to excite as wide of a frequency band as possible. The top corners of the plate had been initially considered for use as input locations, but the high responsiveness to and interaction with the general purpose hammer caused significant drops in the input spectrum at certain frequencies of interest, making difficult the assessment of the input force at those locations. Impact and response were measured at point 41, which was determined from finite element modeling and prior testing to exhibit medium to high levels of response over the modes of interest. A ball bearing was glued to the structure at the drive point, for better repeatability of impact with the general purpose hammer. An extender mass was attached to the mini impact hammer to increase the lower frequency components of the input force and decrease the higher frequency components. Five spectral domain averages were taken at the drive point, over a bandwidth of 6.4 kHz. The drive point measurement was repeated with the calibrated mini-impact hammer. The uncalibrated hammer and drive point location are shown in Fig. 7.3. The FRFs from the calibrated and uncalibrated hammers are shown in Fig. 7.4, with coherence and input spectra.

Peak magnitudes for the flexible modes were compared from both the calibrated and uncalibrated measurements. The peak magnitudes of the uncalibrated frequency response function were plotted against those of the calibrated function. A line was fit to the data points via least squares error minimization to establish the ratio of the uncalibrated FRF to the calibrated FRF.

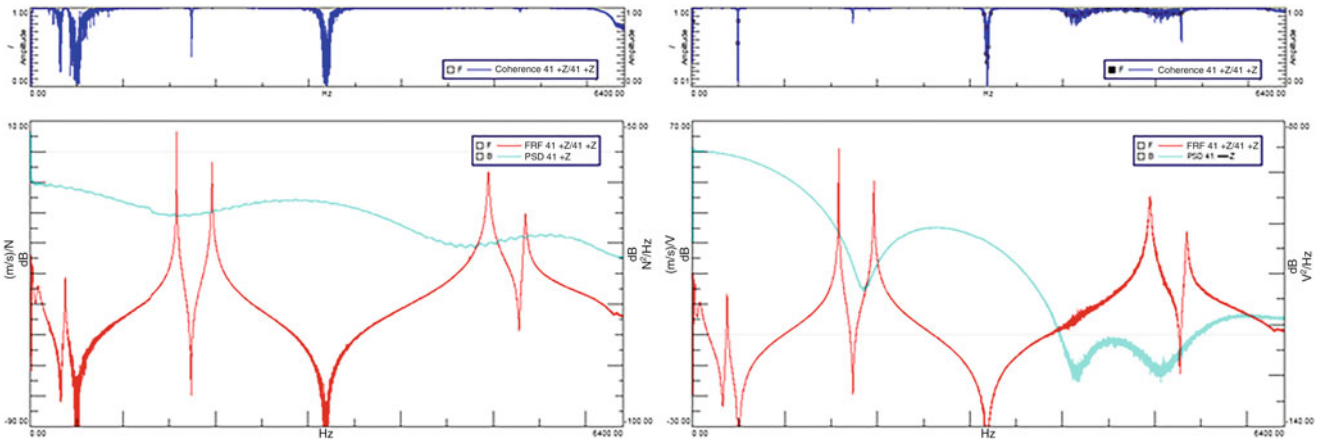

Fig. 7.4 Drive Point FRFs, input spectra and coherences for the calibrated mini hammer (*left*) and the uncalibrated general purpose hammer (*right*)

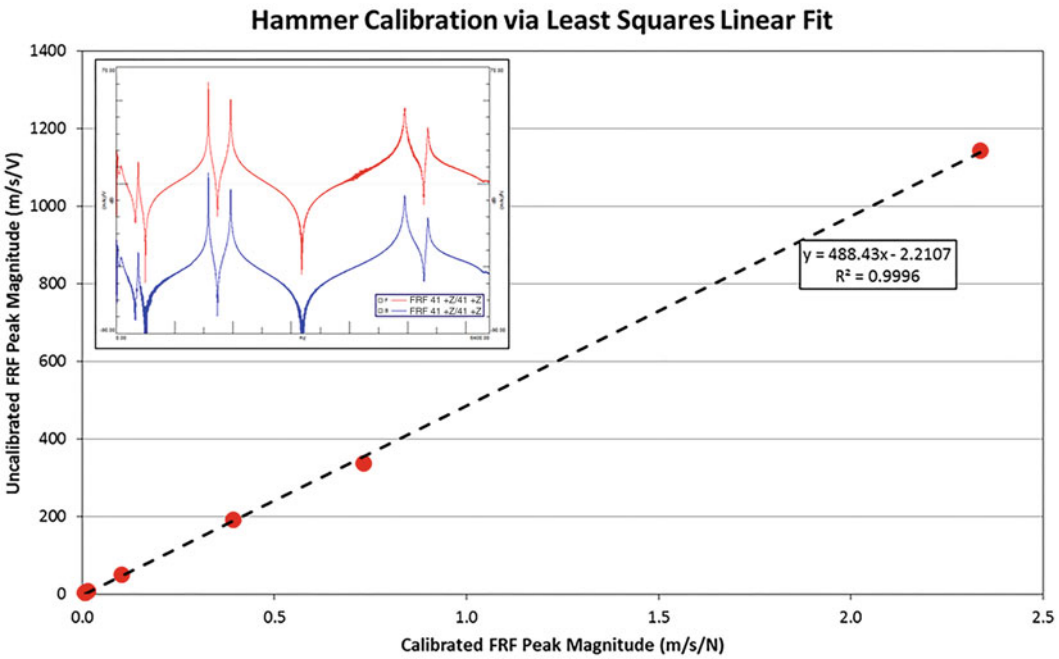

Fig. 7.5 Determination of calibration value from comparison of drive point FRF peaks at point 41, with calibrated (*blue*) and uncalibrated (*red*) FRFs shown *upper left*

Figure 7.5 compares the peak magnitudes of the calibrated and uncalibrated FRFs, represented by the points on the plot, and provides a calibration value via least squares linear fit, represented by the dashed line. Figure 7.5 provides a calibration value of 488.4 N/V, approximately 2.8 % less than the stated calibration value.

7.4.2 Calibration via Reciprocal Measurements

Points 1 and 2, shown in Fig. 7.6, were selected for impact on the calibration structure. The mini impact hammer was used to make a calibrated measurement by impacting at point 1 and measuring response at point 2 over a frequency span of 25.6 kHz. The same mini impact hammer was then used to make an uncalibrated measurement by impacting at point 2 and measuring

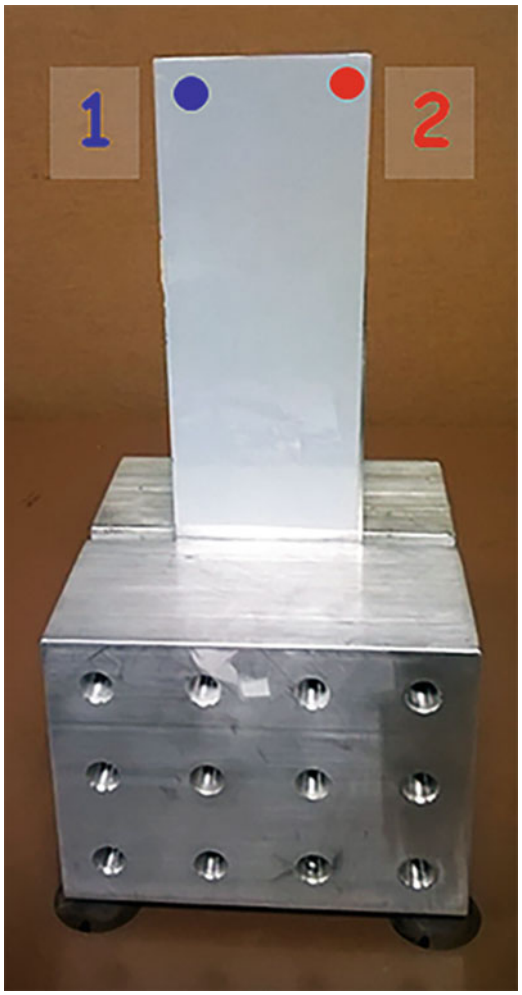

Fig. 7.6 Impact points for reciprocal measurements

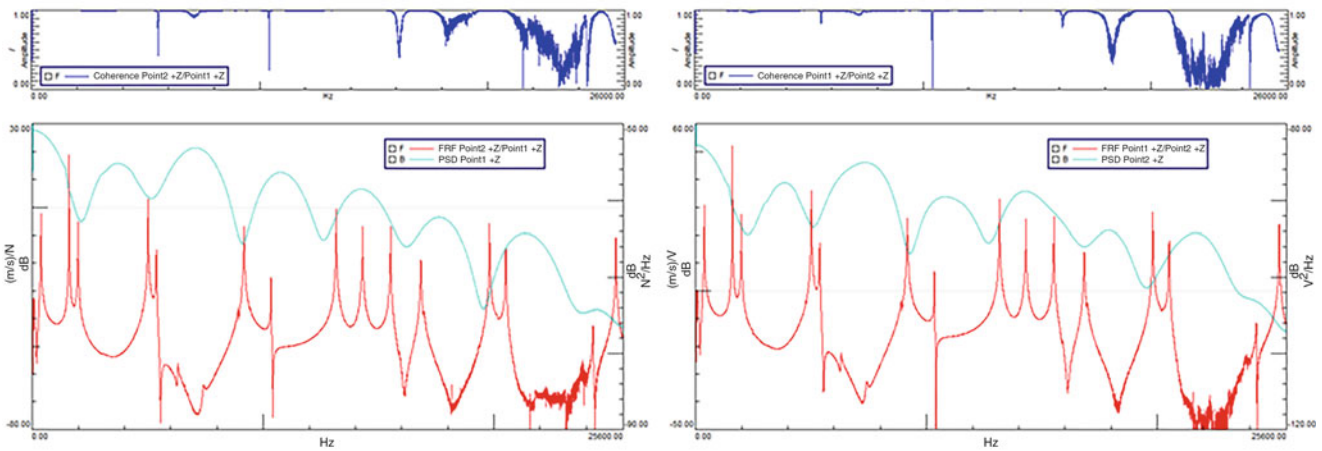

Fig. 7.7 Reciprocal FRFs, input spectra and coherences for the calibrated (*left*) and uncalibrated (*right*) mini-hammer

response at point 1. Figure 7.7 shows the calibrated and uncalibrated measurements side-by-side, with coherence and input spectra. Only the flexible modes below 22 kHz were considered for the calibration. Figure 7.8 compares the peak magnitudes of the thirteen modes of interest of the calibrated and uncalibrated FRFs, and provides a calibration value via least squares linear fit of the data.

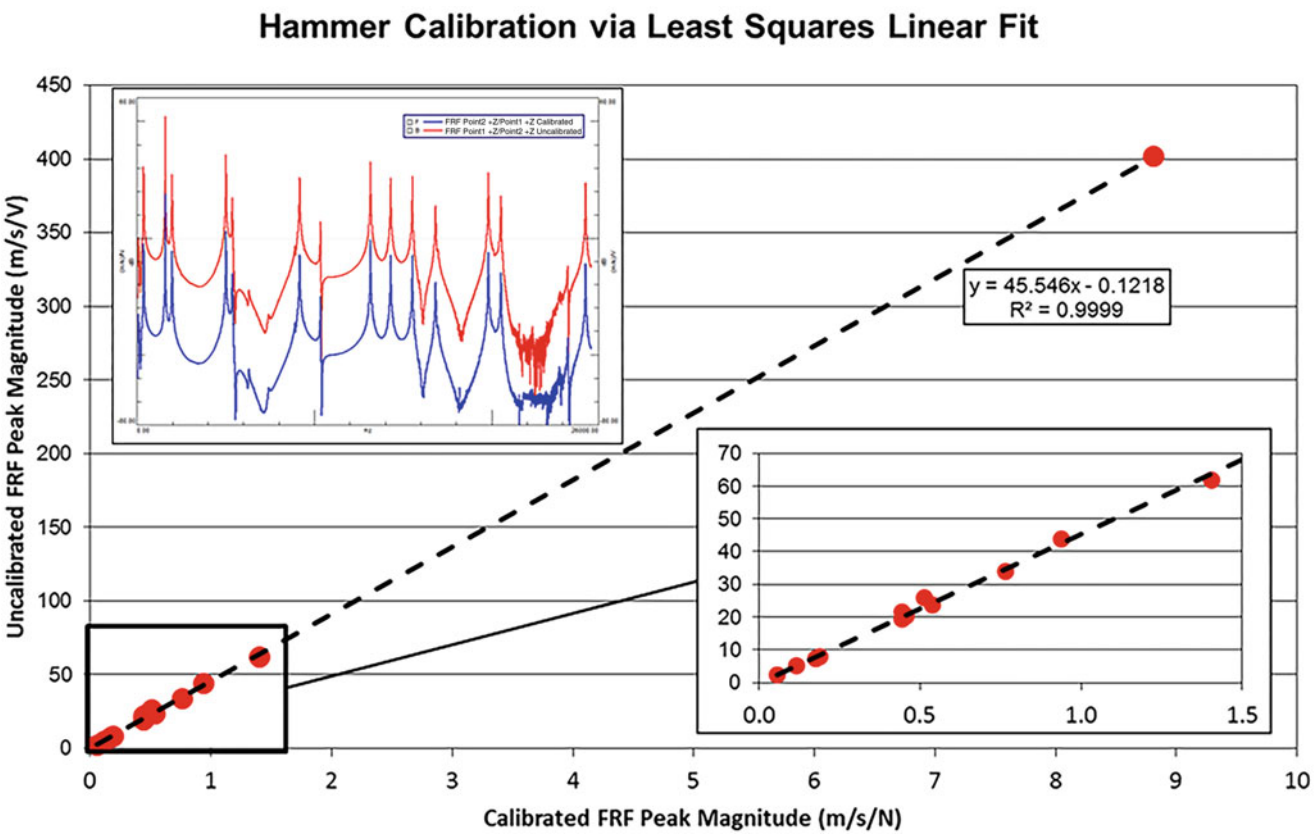

Fig. 7.8 Determination of calibration value from comparison of peaks from reciprocal FRFs, with calibrated (*blue*) and uncalibrated (*red*) FRFs shown *upper left* and magnified view of lower magnitude peaks shown *bottom right*

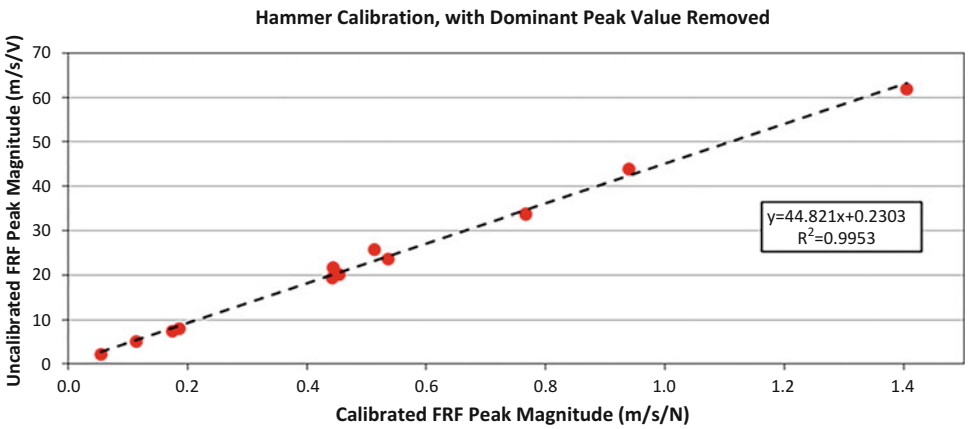

Fig. 7.9 Determination of calibration value from comparison of peaks from reciprocal FRFs, after removal of outlier

Figure 7.8 provides a calibration value of 45.546 N/V, 2.4 % higher than the nominal. Examination of the data shows that all but one point have calibrated peak magnitudes of less than 1.5 m/s/N. A single peak lies far outside this region, and appears to be dominating the linear fit. The fit was reconsidered after excluding the high magnitude peak. Figure 7.9 shows the fit after exclusion of the outlier. Figure 7.9 provides a calibration value of 44.821 N/V, 0.76 % greater than the nominal value.

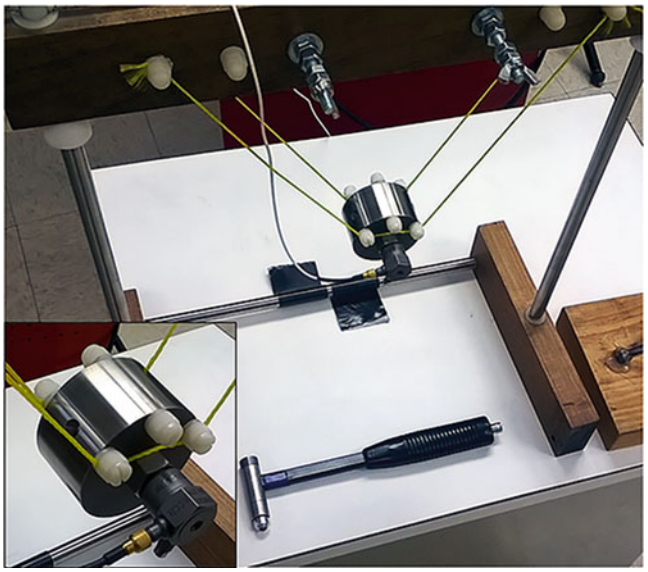

Fig. 7.10 Pendulous mass instrumented with accelerometer, with alternate view of the mass shown at *lower left*

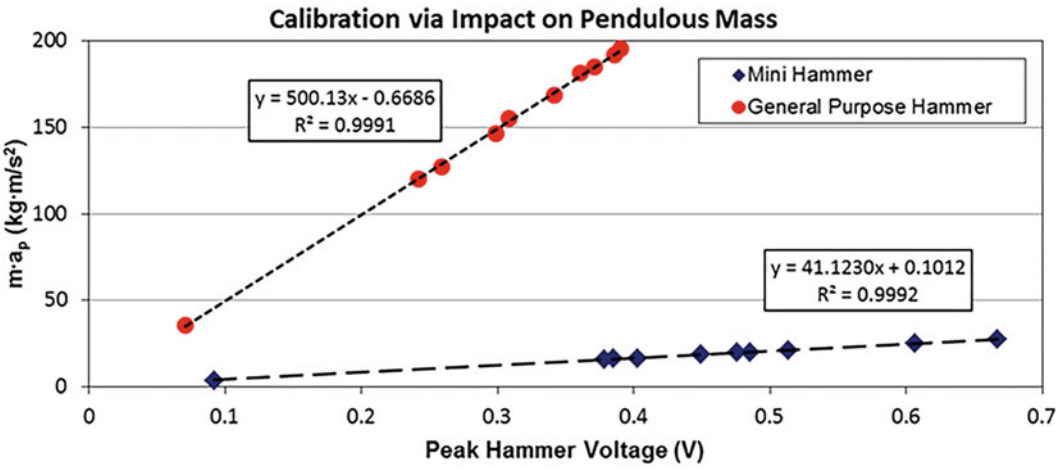

Fig. 7.11 Calibration values obtained from comparison of peak pendulum accelerations with peak hammer output voltage

7.4.3 Calibration via Impact on a Pendulous Mass

Additional calibration of the two impact hammers was performed by use of a pendulous mass, shown in Fig. 7.10. An impedance head was attached to the mass via stud: the impedance head accelerometer was used to obtain the peak acceleration of the mass. The total mass of the pendulum, without considering the support twine or the instrument cabling, was 0.5106 kg. Ten impacts were performed with the general purpose impact hammer, and the mini impact hammer with extender mass. Peak acceleration values and peak hammer output voltages were obtained from time domain measurements. The peak acceleration values, multiplied by the mass, were plotted against the peak voltages from the impact hammers, and linear fits were used to obtain calibration values for both hammers, as shown in Fig. 7.11. The calibration value for the mini impact hammer, 41.123 N/V, differs from the nominal, which does not include the effects of the extender mass, by approximately 7 %. The calibration value obtained for the mini impact hammer was used to provide the scale for the calibrated drive point FRF at point 41. The calibration value obtained for the general purpose hammer, 500.13 N/V, is within 0.5 % of the stated calibration and 2.4 % of the value obtained via drive point FRF comparison.

7.5 Observations

While the calibration between instruments and the calibration with reciprocity provided results very close to the expected values, the process was found to be very sensitive to the quality of the measurements. In prior testing with the general purpose impact hammer, impact directly on the structure without the added ball bearing did not assure good repeatability of the impact, and resulted in greater than 5% difference in calibration. The responsiveness of a measurement location is also worthy of consideration. Earlier testing with the general purpose hammer was performed at a location intended to maximize the measured response. However, at the frequencies of interest, the input spectrum was poorly measured because the structure was too compliant: significant drops in the input spectrum were observed at the frequencies of interest. Selection of a different input location permitted greater force to be imparted while maintaining high response at the frequencies of interest. The resulting frequency response functions permitted a determination of the calibration value which was very close to the calibration obtained through conventional means.

7.6 Conclusion

Spectral domain calibration was performed with an uncalibrated impact hammer and a different, calibrated impact hammer. The resulting calibration value was acceptable when compared with the value obtained from conventional calibration via impact against a pendulous mass. Reciprocal measurements were also obtained using a single impact hammer for both measurements: the reciprocal measurements provided a calibration value very close to the accepted calibration value. The results of the spectral domain calibration with conventional instrumentation strongly suggest that, when applied to a focused ultrasonic transducer, a reasonable calibration value may be obtained.

Acknowledgements Some of the work presented herein was partially funded by NSF Civil, Mechanical and Manufacturing Innovation (CMMI) Grant No. 1266019 entitled “Collaborative Research: Enabling Non-contact Structural Dynamic Identification with Focused Ultrasound Radiation Force.” Any opinions, findings, and conclusions or recommendations expressed in this material are those of the authors and do not necessarily reflect the views of the particular funding agency. The authors are grateful for the support obtained.

References

1. Avitabile, P.: Can you describe reciprocity? It just doesn’t make sense to me. SEM Exp. Tech. (2008).
2. Model 086E80 ICP® impact hammer installation and operating manual. PCB Piezotronics. (2007).
3. Polytec scanning laser Doppler vibrometer. Polytec. Opt. Meas. Syst.
4. LMS Test. Lab—Leuven Measurement Systems, Leuven, Belgium.

Chapter 8
Calibration Techniques for Non-contacting Force Excitation Part 2: Time Domain Methods

Tina Dardeno and Peter Avitabile

Abstract Experimental characterization of the higher frequency modes of a structure presents challenges due to the frequency limitations of traditional excitation techniques. Non-contact excitation via low power ultrasonic transducer presents the possibility of exciting higher frequencies not currently possible with shakers or impact hammers. However, quantification of the actual force applied by the ultrasonic transducer requires that a relationship between the ultrasonic pressure field and the voltage driving the transducer be established.

Part 1 of this paper described calibration methods using frequency domain techniques. Part 2 of this paper, described herein, explores time domain calibration methods using conventional instrumentation before extending the techniques to the ultrasonic transducer. Time domain methods of calibration in the context of this paper involve: (1) prediction of a response for a given excitation using analytical and experimental models; and (2) determination of the sensitivity of an uncalibrated force transducer. Specifically, an analytical model based on the principles of mode superposition is shown to accurately predict the response of a structure to a digitized excitation. Furthermore, if the response of a structure due to an uncalibrated force is plotted against that due to a calibrated force, the slope of the line can be used to determine the sensitivity of the uncalibrated force transducer.

Keywords Non-contact excitation • High frequency excitation • Non-intrusive excitation • Ultrasonic transducer • Calibration methods

8.1 Introduction

Use of ultrasonic waves is being explored as a means by which higher frequency modes of a test article may be characterized without the need for direct contact. Traditional excitation via impact hammers and shakers permits measurement of the force applied to a test article by measuring the voltage output from a force gage, but no analogous mechanism exists for the ultrasonic transducer, which produces an ultrasonic pressure field that is dependent upon the voltage driving the transducer. While some ultrasonic transducers produce an ultrasonic field which acts over a wide area, certain transducers focus the ultrasonic pressure field over an area small enough to be approximated as a discrete point. The question then arises as to how the effective force acting at the focal point can be related to the voltage driving the ultrasonic transducer.

The time domain method of ultrasonic transducer calibration is being developed to complement frequency domain techniques [1]. This method, which utilizes the principle of mode superposition to compute the response of a structure to a digitized excitation, has the benefit of being customizable to even very high frequencies. Furthermore, this method can compute the response of a structure to single or multiple-frequency excitations. To validate the time domain method of transducer calibration, testing was performed using a hammer of known calibration.

8.2 Physical System and Models Developed

A previously designed and fabricated aluminum cantilever structure was used throughout the analyses. The structure is comprised of a cantilever beam with a mass at the base to approximate a built-in condition (Fig. 8.1).

T. Dardeno (✉) • P. Avitabile
Structural Dynamics and Acoustic Systems Laboratory, University of Massachusetts Lowell, One University Avenue, Lowell, MA 01854, USA
e-mail: tina_dardeno@student.uml.edu

E. Wee Sit (ed.), *Sensors and Instrumentation, Volume 5*, Conference Proceedings of the Society for Experimental Mechanics Series, DOI 10.1007/978-3-319-29859-7_8

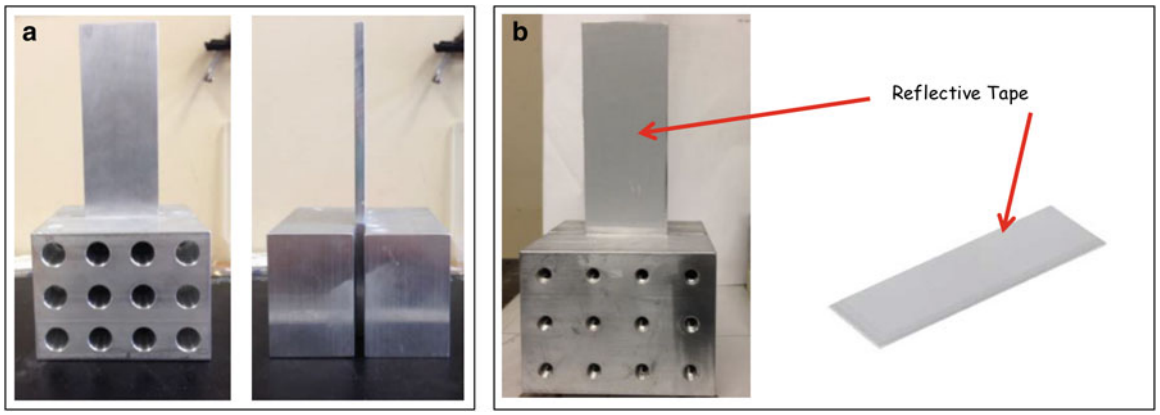

Fig. 8.1 (**a**) Cantilever calibration structure; (**b**) Structure with reflective tape applied

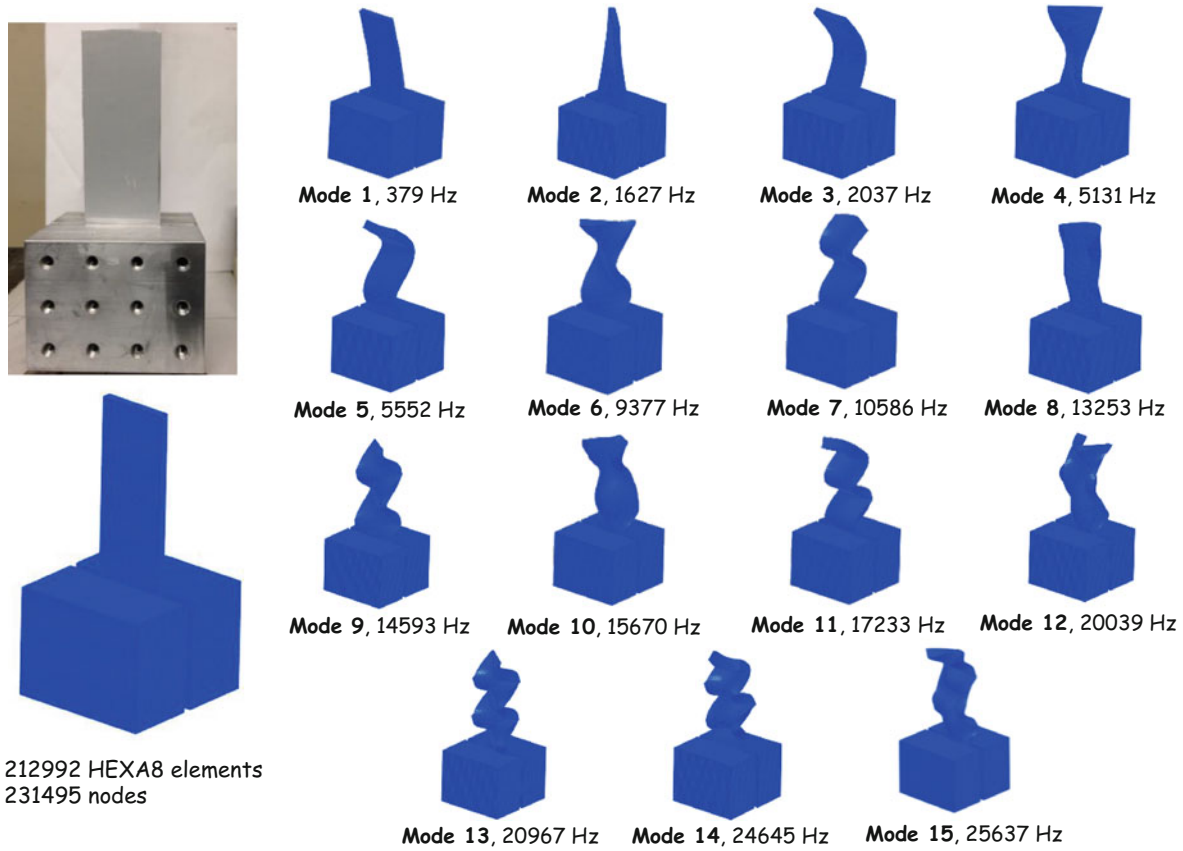

Fig. 8.2 Cantilever model and out-of-plane mode shapes

This structure was designed to mimic turbine blade qualification tests and with dimensions and material properties to generate high frequency mode shapes for calibration of the ultrasonic transducer. To improve laser signal for testing, reflective tape was applied to the face of the structure. The structure was modeled in FEMAP as a plate mounted to a large mass with a refined mesh of eight-noded bricks as shown in Fig. 8.2 [2]. The eigensolution was performed in FEMtools version 3.8 [3]. Only out-of-plane cantilever shapes were considered as no in-plane or base measurements were obtained.

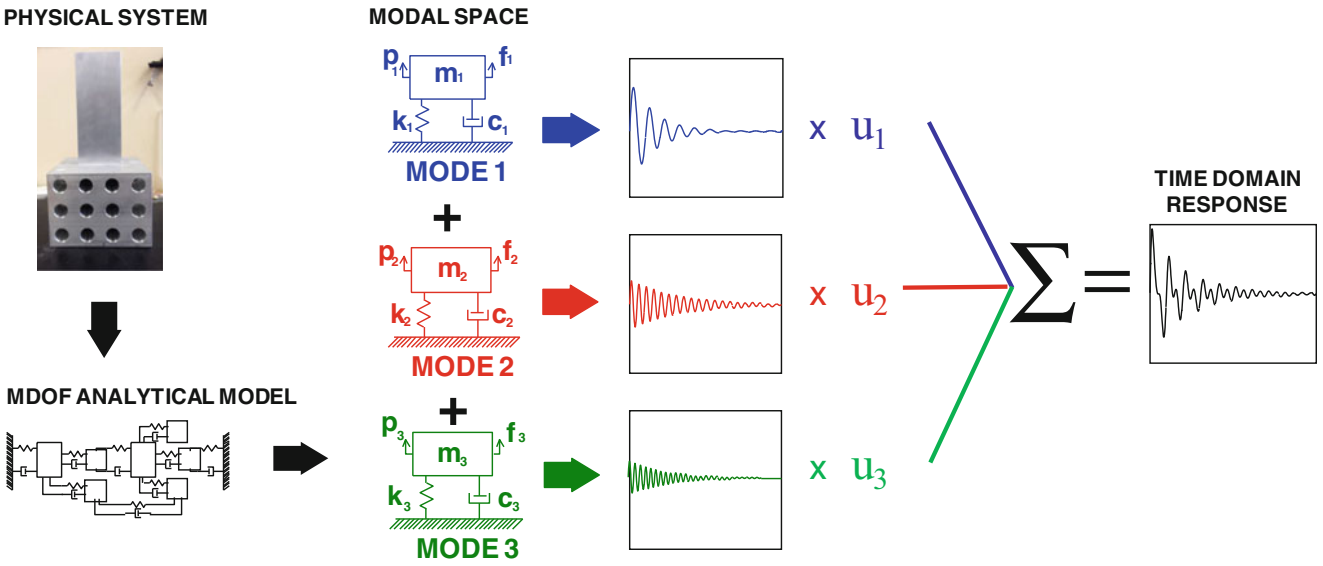

Fig. 8.3 Schematic of mode superposition approach

8.3 Theoretical Background

The analytical models described herein utilize the method of mode superposition to compute an analytical response to a digitized excitation [4]. The basic approach is schematically shown in Fig. 8.3, where the structural system is decomposed into single degree of freedom modal oscillators and the response of each mode is identified. The response is then expanded from the modal response to the physically distributed response on the structure for each mode which is then summed to identify the total response of the system.

The principle of mode superposition described in Fig. 8.3 can be used to estimate the response of a physical system to an actual force excitation. First, frequencies and damping are obtained via experimental frequency response spectra, which are then used to generate mass, stiffness, and damping matrices in modal space. Next, mode shapes corresponding to the test point(s) can be obtained through test or a reliable finite element model. Digitized, instantaneous time data is obtained via test, and the digitized force excitation is transformed to modal space to identify the force contribution of each modal oscillator. The Newmark direct integration method is then used to solve the differential equations of motion for each modal oscillator. The response contribution of each modal oscillator in modal space is then scaled using the corresponding mode shape and summed to compute the total system physical response at a given point. This computed response can be compared to the measured response using overlay and response correlation metrics such as TRAC, as shown in Fig. 8.4. These computations are performed using scripts and functions generated in MATLAB [5].

This response estimation method can be expanded to include transducer calibration. A digitized excitation is obtained; however, an unscaled sensitivity is entered into the channel setup. The response is then computed using a numerical integration scheme. A calibration curve can then be generated by plotting the measured response versus the calculated response and determining the best linear fit of the data. The slope of the line can then be used to compute the sensitivity of the force transducer.

8.4 Characterization of Cantilever Structure

This mode superposition approach requires frequencies, mode shapes, and damping from FEA, test, or both to compute the response. Prior to data collection, measurement point geometry was generated in FEMtools using the sensor placement method of nodal kinetic energy (NKE) and the sensor elimination method of effective independence (EIM) [3]. For computational efficiency, the cantilever calibration structure was modeled as a fixed plate for the pre-test analysis. The test geometry was then exported as a universal file for import into Polytec [6] and LMS [7]. Prior to importing the test geometry into the Polytec data acquisition module [6], 2D and 3D alignments of the laser were performed to align the laser with the measurement points and identify the coordinate system, respectively.

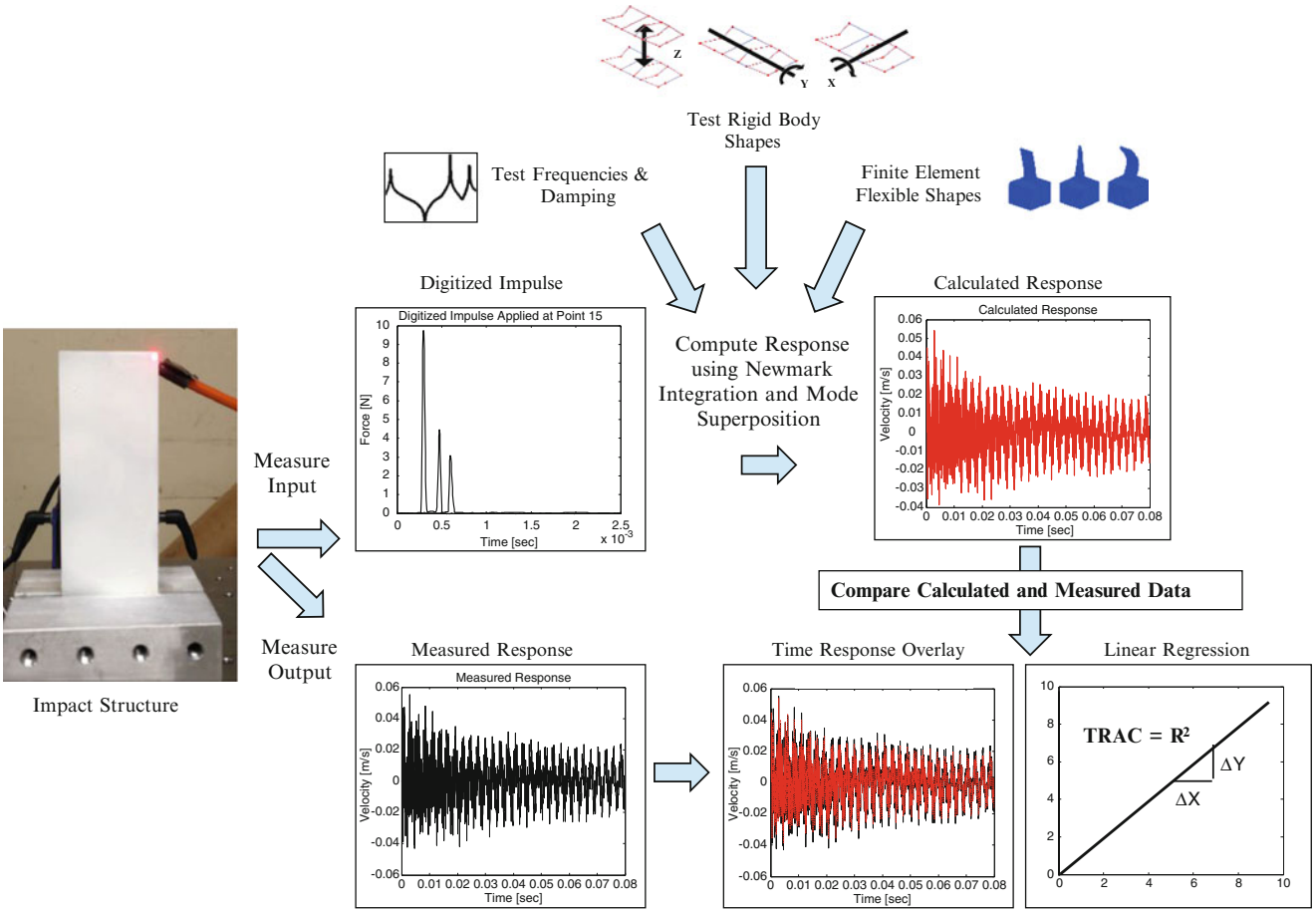

Fig. 8.4 Time response estimation procedure

An impact test was performed to determine the out-of-plane rigid body and flexible modes up to approximately 20 kHz. Figure 8.5 displays the equipment and test geometry used as well as the coherence, input spectrum, and frequency response spectrum at the drive-point. A small metal-tipped hammer was used to excite the structure while velocity measurements were obtained via a single Polytec laser head [6]. Note that the hammer was mounted to a tripod to ensure repeatability of impacts. The hammer remained stationary at point 2645, which is located at the left corner of the free end of the cantilever, while the laser was moved to each measurement point. Point 2645 was selected as the impact location because 2645 was one of the few measurement points that significantly excited all of the target modes. However, point 2645 corresponded to a point of high local flexibility, resulting in many multiple impacts. Five linear averages were taken to minimize error. Data collection was performed in LMS with vibrometer data directly output to the LMS impact testing module [7]. Three rigid body modes and 15 out-of-plane flexible modes were obtained. These shapes were typical for a cantilever plate, as shown in Fig. 8.6. The test results were correlated to the finite element model in FEMtools [3], as shown in Table 8.1. Table 8.1 shows good correlation between model and test, as diagonal MAC values were consistently high for the 15 correlated mode pairs. Furthermore a maximum frequency error of only 4.6 Hz was noted.

8.5 Concept Verification Study Using Hammer of Known Calibration

After determining the frequencies and mode shapes of the structure, time data was collected at point 2671 for response estimation using the LMS spectral testing module [7], as shown in Fig. 8.7. A hammer with a plastic tip (nominal sensitivity 1.99 mV/N) was used to excite the structure at point 2671 to a frequency range less than that excited by the metal tipped hammer. An uncalibrated sensitivity of 1000 mV/N was entered for the hammer into the channel setup. To satisfy requirements of the numerical integration scheme, the smallest possible time step was used for data collection (4.88E-06s).

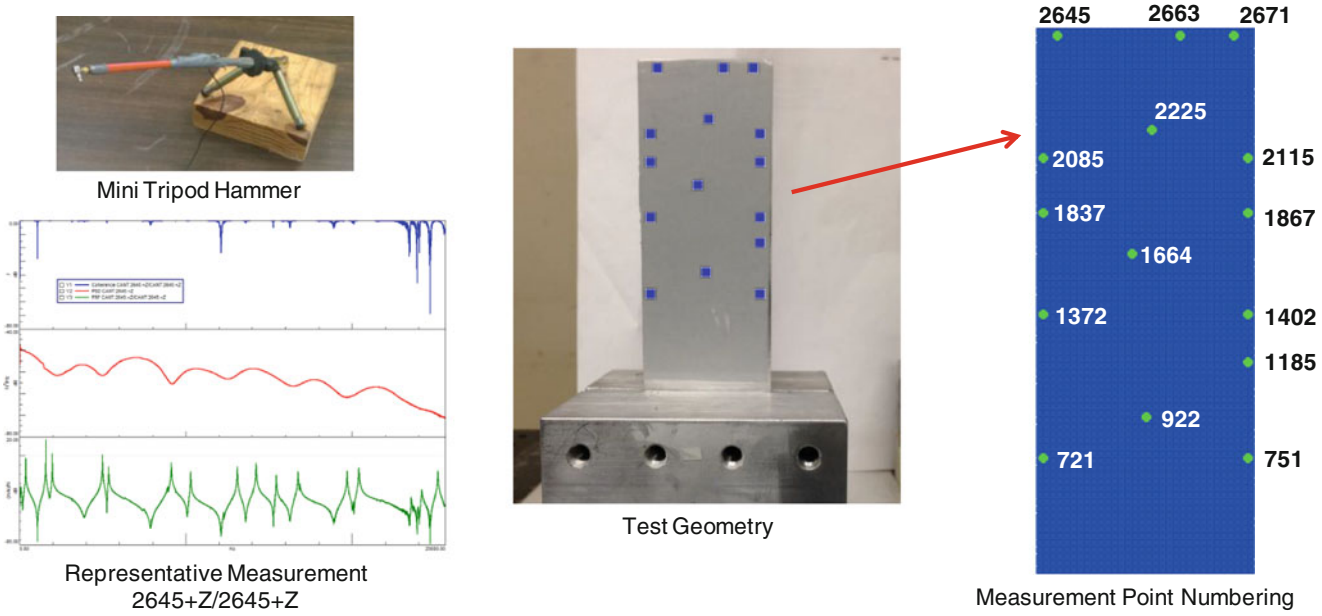

Fig. 8.5 Instrumentation, representative measurement, and measurement point setup for determination of flexible and rigid body mode shapes of cantilever structure

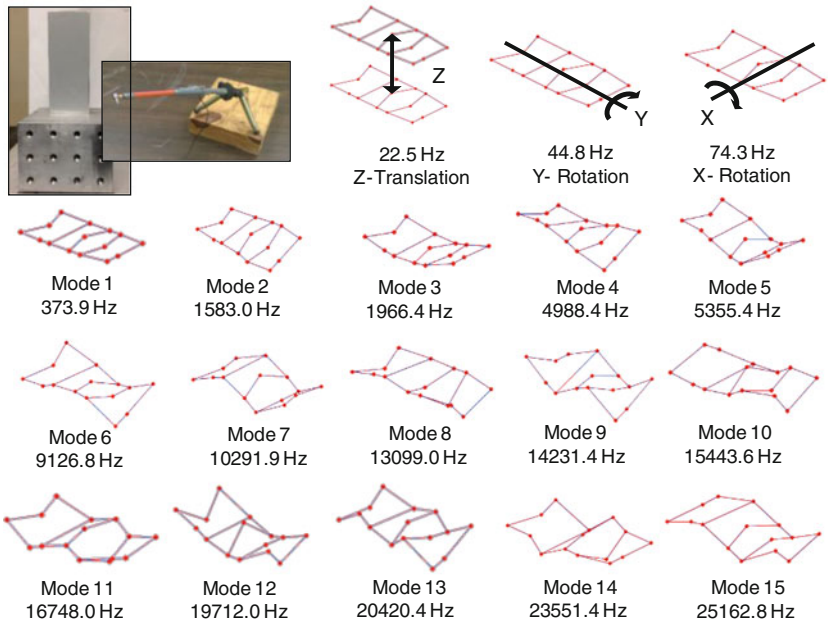

Mode	Freq. [Hz]	Damping [%]
RBM 1	22.5	24.41%
RBM 2	44.8	14.56%
RBM 3	74.3	27.84%
1	373.9	0.71%
2	1583.0	0.02%
3	1966.4	0.08%
4	4988.4	0.07%
5	5355.3	0.13%
6	9126.9	0.08%
7	10293.1	0.05%
8	13098.5	0.05%
9	14231.1	0.05%
10	15443.3	0.05%
11	16748.5	0.07%
12	19713.0	0.04%
13	20417.4	0.05%
14	23552.2	0.11%
15	25163.1	0.04%

Fig. 8.6 Experimental modal analysis frequencies, damping, and mode shapes

To determine how many flexible modes to include in the calculations, the input auto-spectrum was computed. The spectrum indicated significant excitation up to approximately 10 kHz. Therefore, a total of three rigid body and six flexible modes were included in the analysis (Fig. 8.8).

The digitized impulse, test frequencies, test damping, test rigid body shapes, and finite element flexible shapes from the cantilever and block model were used to compute the unscaled response via mode superposition with Newmark integration. In order to identify the calibration, a plot of the calculated time response versus measured time response will provide an approximate straight line. The sensitivity was then computed via linear regression of the calculated and measured responses, as shown in Fig. 8.9. Then, for better visualization, the calculated response was rescaled using the computed sensitivity, as shown in Fig. 8.10.

Table 8.1 Correlation between finite element and test data

Mode	FEA [Hz]	MAC	EMA [Hz]	% Diff.
1	378.8	99.9	373.9	1.3
2	1626.8	98.6	1583.0	2.8
3	2036.9	98.9	1966.4	3.6
4	5130.8	98.4	4988.4	2.9
5	5552.4	98.2	5355.3	3.7
6	9377.3	99.2	9126.9	2.7
7	10586.0	99.2	10293.1	2.9
8	13253.0	97.0	13098.5	1.2
9	14593.0	99.3	14231.1	2.5
10	15670.0	98.3	15443.3	1.5
11	17233.0	97.6	16748.5	2.9
12	20039.0	97.1	19713.0	1.7
13	20967.0	98.9	20417.4	2.7
14	24645.0	89.4	23552.2	4.6
15	25637.0	95.0	25163.1	1.9

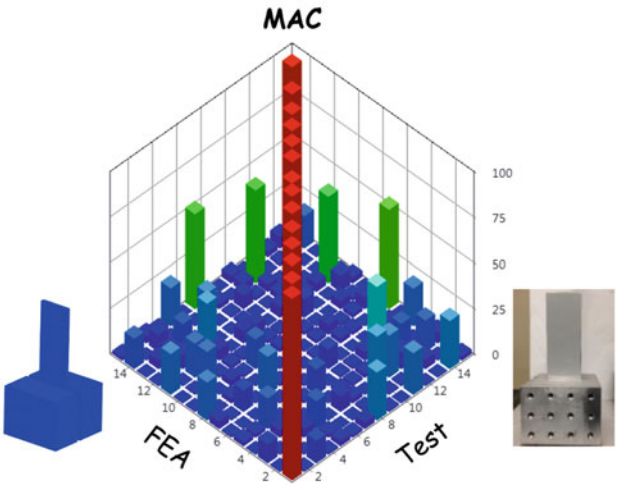

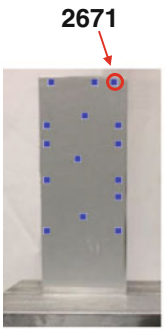

Impact at Point 2671

Modally Tuned Hammer with White Plastic Tip, Manufacturer's Nominal Sensitivity 1.99 mV/N

Polytec PSV-400 Laser Head

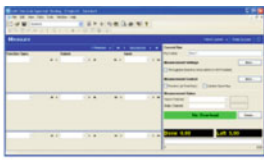

LMS Spectral Testing Module

Sample Parameters

BW [Hz]	204800
Lines	16384
df [Hz]	6.2536
Period [s]	0.16
dt [s]	4.88E-06
Averages	None

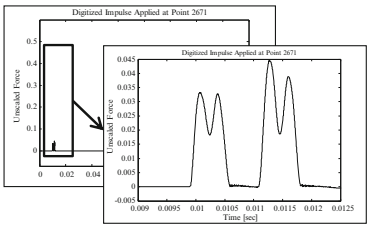

Uncalibrated Sensitivity of 1000 mV/N Entered for Hammer

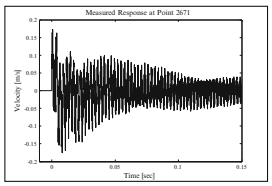

Manufacturer's Nominal Calibration Entered for Vibrometer

Fig. 8.7 Collection of digitized impulse and time response for hammer calibration

The calculated sensitivity of 2.0066 mV/N is 0.83 % higher than the manufacturer's nominal sensitivity of 1.99 mV/N. The R^2 value of 0.9570 shows a high correlation between the measured and calculated responses. The results shown are very promising; this time domain approach to force calibration presents a viable way to further validate the calibration values obtained from frequency domain methods.

8.6 Observations

The time domain/mode superposition approach to transducer calibration presented herein appears promising. Several observations related to accuracy of this method were made while performing the analyses. First, because the response is calculated using finite element shapes, model accuracy is crucial. The analysis performed in the previous section utilized a simple fixed cantilever model to develop the pre-test geometry, but extracted shapes from a more detailed model to compute

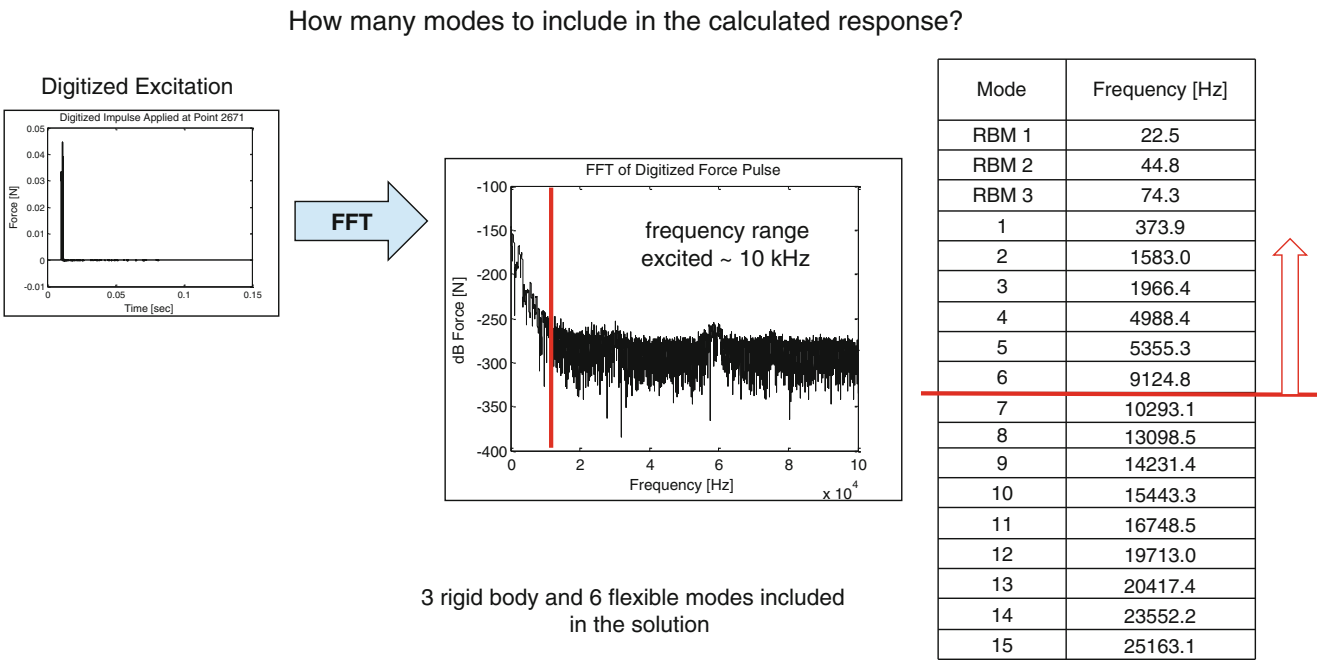

Mode	Frequency [Hz]
RBM 1	22.5
RBM 2	44.8
RBM 3	74.3
1	373.9
2	1583.0
3	1966.4
4	4988.4
5	5355.3
6	9124.8
7	10293.1
8	13098.5
9	14231.4
10	15443.3
11	16748.5
12	19713.0
13	20417.4
14	23552.2
15	25163.1

Fig. 8.8 Mode participation in computed response

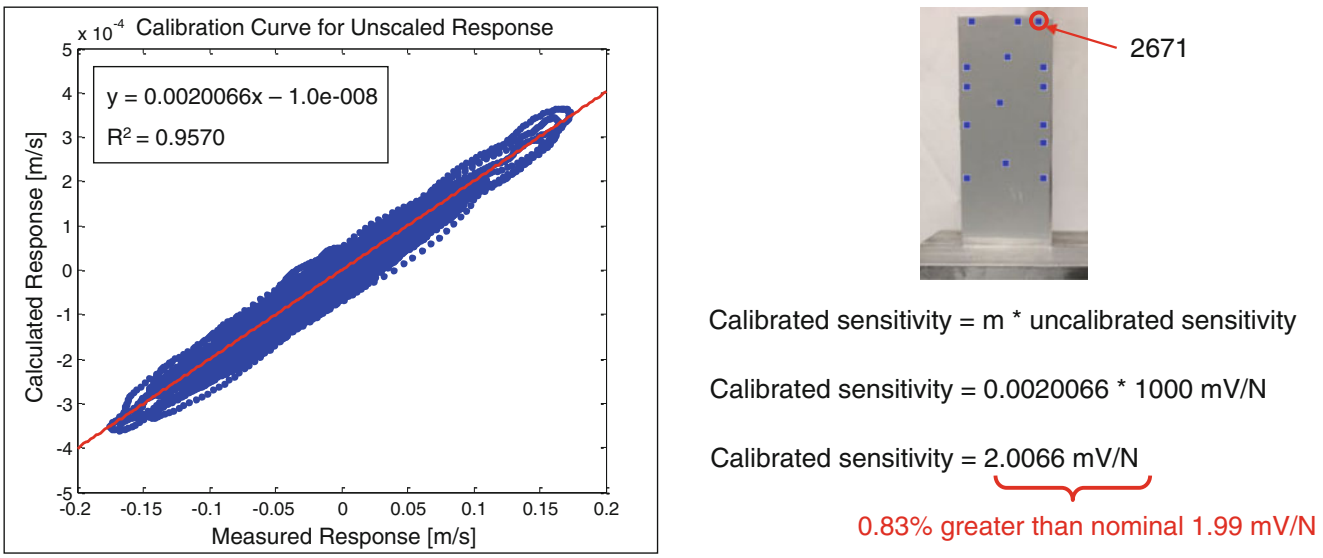

Fig. 8.9 Plot of calculated time response vs. measured time response at point 2671 and calculations to determine hammer calibration value

the response. To demonstrate the importance of the calibration finite element model, the fixed cantilever model is revisited. Figure 8.11 shows the model, shape pairs between the model and test, and correlation results between the model and test.

Figure 8.11 shows that while finite element and test frequencies exhibited some variation, the first six flexible modes demonstrated high diagonal MAC correlation. Test frequencies and finite element mode shapes are used to compute the time response for calibration; therefore, having accurate finite element mode shapes is far more important than having accurate finite element frequencies. Using the finite element shape values from the fixed cantilever model, the transducer sensitivity was recomputed. The original calibration results using shapes from the cantilever and block model are compared to the calibration results using shapes from the fixed cantilever model in Fig. 8.12.

Figure 8.12 shows that both the correlation coefficient and sensitivity value were affected by the model used. The correlation coefficient reduced from 0.9570 to 0.9482 when the response was computed using fixed cantilever shapes. Likewise, the error in the computed sensitivity increased from 0.83 to 12.22 %. Even though the fixed cantilever model

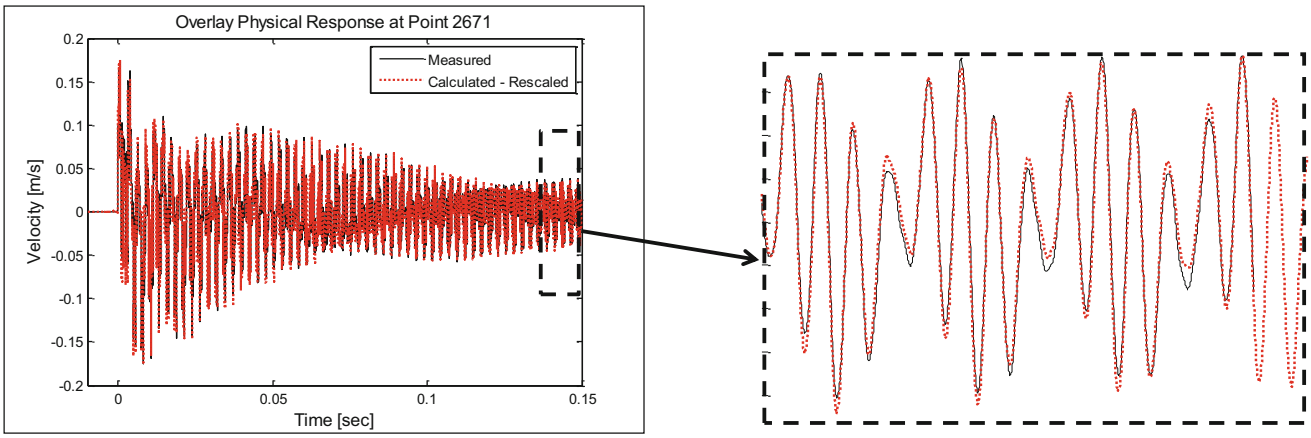

Fig. 8.10 Comparison of measured and rescaled calculated responses at point 2671, cantilever and block model shapes

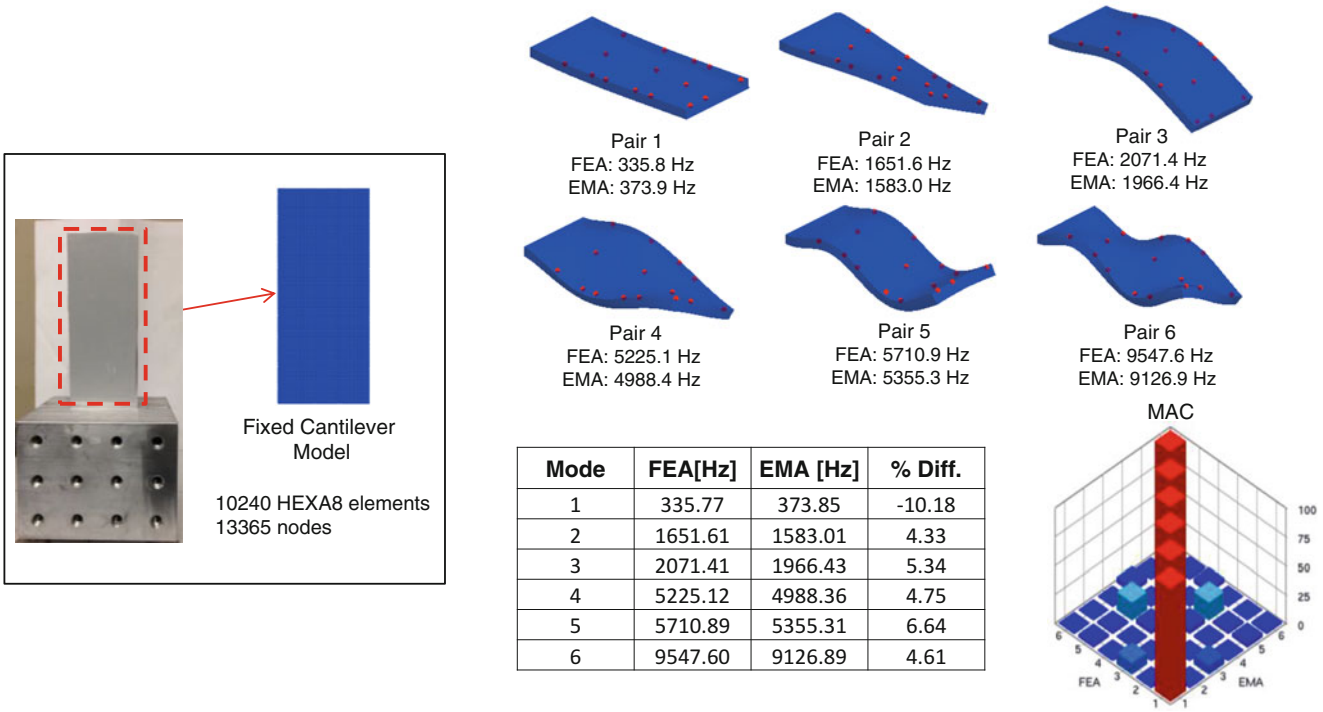

Mode	FEA[Hz]	EMA [Hz]	% Diff.
1	335.77	373.85	-10.18
2	1651.61	1583.01	4.33
3	2071.41	1966.43	5.34
4	5225.12	4988.36	4.75
5	5710.89	5355.31	6.64
6	9547.60	9126.89	4.61

Fig. 8.11 Correlation between test and fixed cantilever model

was shown to correlate highly to the test results via MAC, the local shape values at the measurement location were clearly different for the fixed model compared to the cantilever and block model. These results stress the importance of model accuracy when performing this calibration method.

The second observation is that improper node-point pairing can occur due to discrepancies between test and model coordinates. If the test geometry does not align perfectly with the model, the test points may be paired with finite element nodes that do not share the same dynamic characteristics, as shown in Fig. 8.13.

The cantilever and block model has a distance of 0.0625 in. between each node. Recall that the measurement obtained for input into the mode superposition code was taken at point 2671, which corresponds to the model node shown in Fig. 8.13. This node returns a shape value of 5.32 (normalized to unit modal mass, metric) for the first mode. However, if the model were aligned such that point 2671 was paired with the node directly below (error of 0.0625 in.), the shape value returned would be 5.22. Likewise, if the model were aligned such that point 2671 was paired with two nodes directly below (error of 0.125 in.), the shape value returned would be 5.11. The hammer calibration was recomputed using these nearby nodes, as shown in Fig. 8.14.

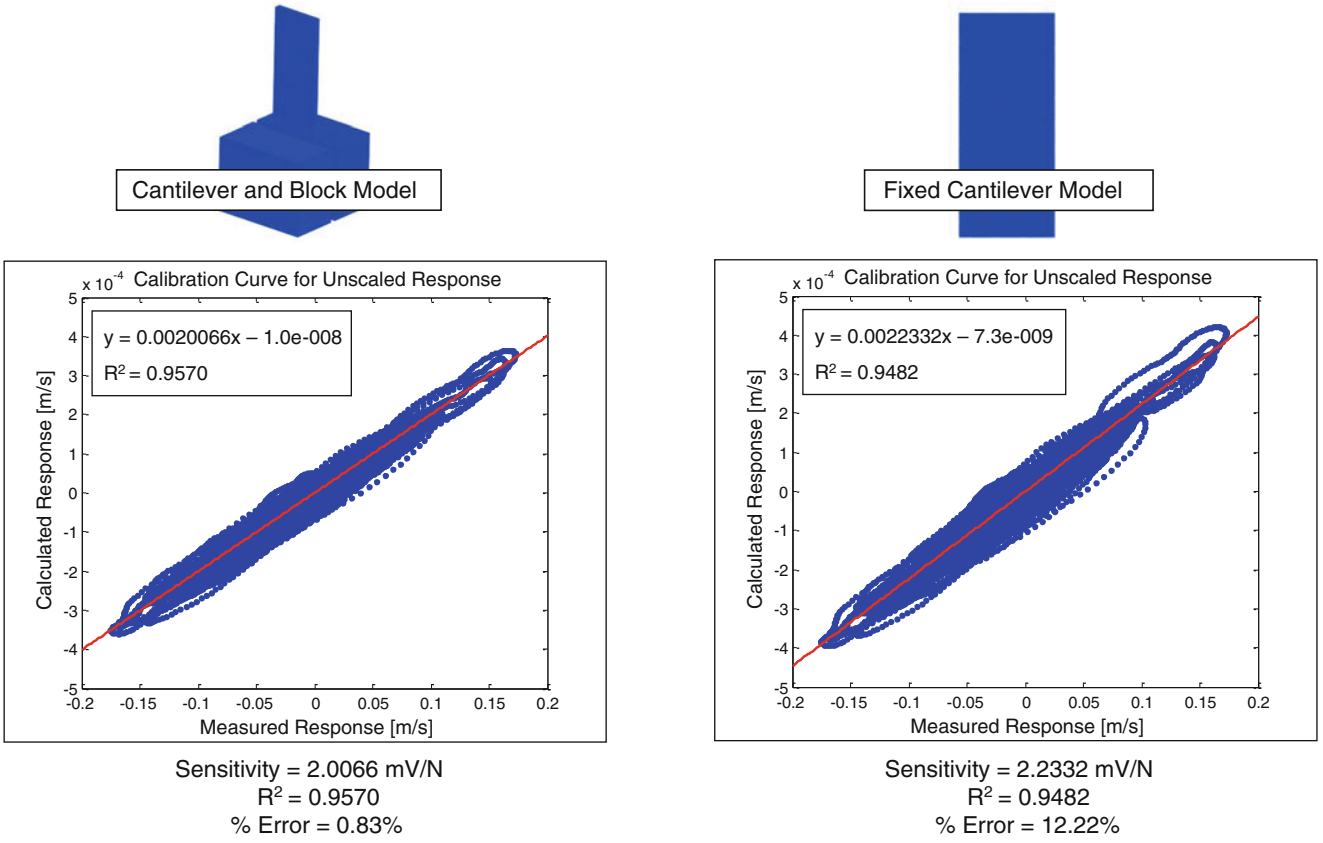

Fig. 8.12 Original hammer calibration results using shapes from cantilever and block model compared to hammer calibration results recomputed using shapes from fixed cantilever model

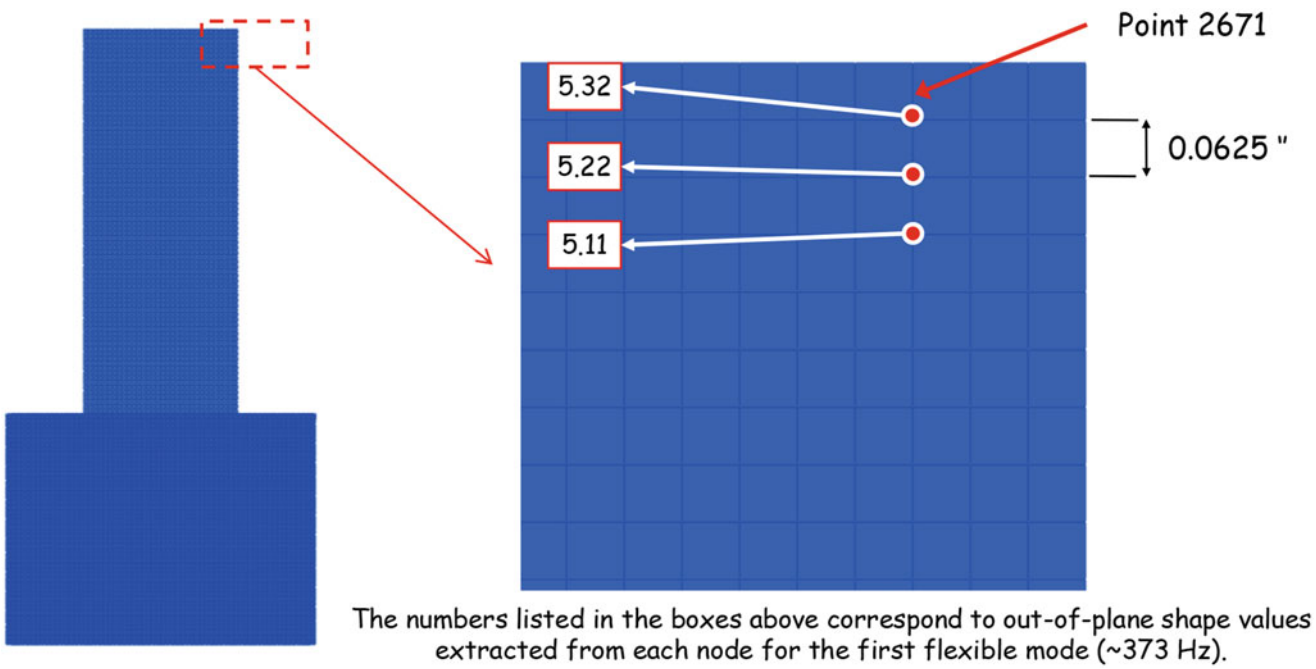

Fig. 8.13 Differences in mode shape values among adjacent nodes

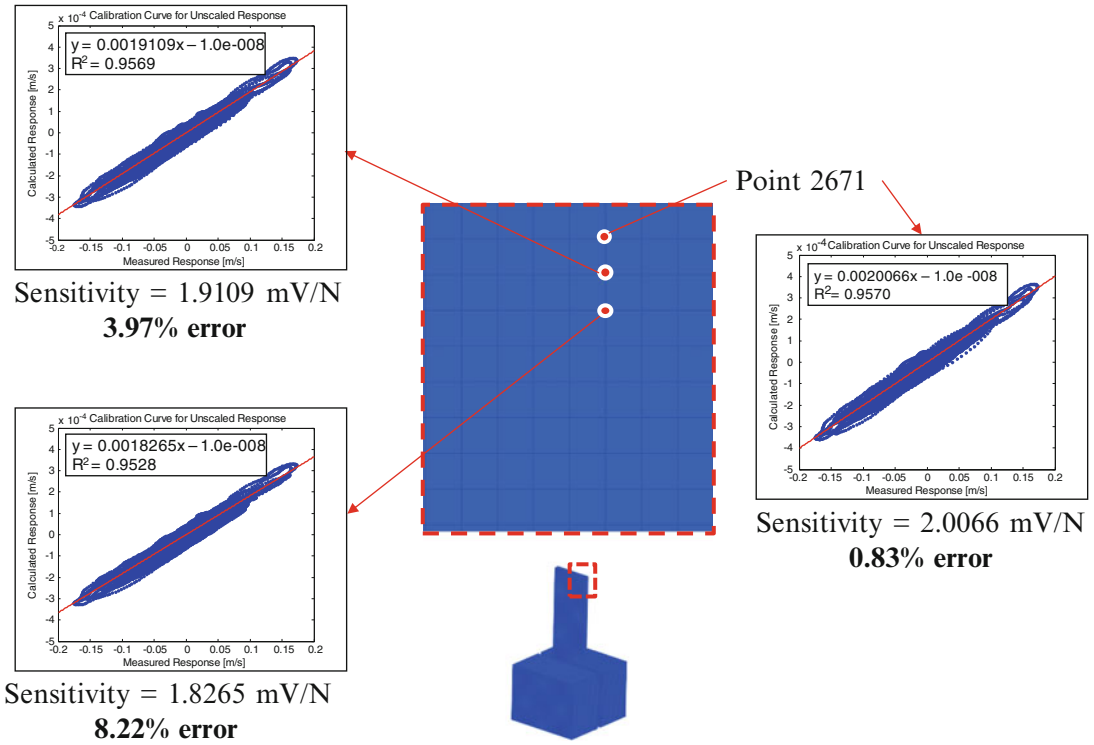

Fig. 8.14 Effect of node-point pairing selection on transducer calibration results

Figure 8.14 shows that an error in node-point pairing can markedly affect the accuracy of the time domain approach to calibration. An error of 0.0625 in. in node placement resulted in an increase from 0.83 % error to 3.97 % error. Likewise, an error of 0.125 in. in node placement increased the error to 8.22 %.

Secondly, Newmark integration has been shown to result in frequency distortion of higher order modes which appears to be related to refinement of the integration time step. As such, other acquisition parameters such as sample rate and window length need to be adjusted to obtain a sufficiently fine time step. When collecting the digitized impulse for this analysis, the parameters were adjusted until the finest possible time step was achieved (dt = 4.88E-06s). This required that the maximum sample rate of the system be used. Recall that the response solution included modes up to approximately 10 kHz. Ultrasonic transducers are designed to operate at much higher frequencies, and as such issues may arise when using Newmark integration to compute the response of the structure to an acoustic force. MATLAB's resample function is a powerful tool that can be used to prevent the frequency distortion that may result from numerical integration with an insufficient time step. This function resamples uniform or non-uniform data to a new fixed rate and applies a low-pass filter to prevent aliasing [8]. This function also provides compensation for the phase delay caused by the low-pass filter [8]. To demonstrate the effectiveness of this function, the response of the structure to the same, unrefined digitized impulse (dt = 4.88E-06s) was recomputed using all 15 flexible modes. The digitized impulse was then refined by a factor of four (dt = 1.22E-06s) and the response recomputed. The FFT was then computed for both responses, as shown in Fig. 8.15.

Figure 8.15 shows that higher order modes exhibited a frequency shift due to the integration process, and that resampling the digitized impulse to a finer time step corrected the distortion. Note that resampling the data to compute the response as described in the previous section was not necessary as the higher order modes contributed very little to the overall response.

However, resampling the data can result in some accumulation of error. Although MATLAB's resample function does provide compensation for the phase delay caused by the low-pass filter [8], phase distortion still has an effect on the calibration curve, as shown in Fig. 8.16.

Figure 8.16 shows that some differences in the calibration results exist between the raw and resampled data. Notice that when the full response was included in the calibration curve, the sensitivity did not change but the correlation coefficient diminished slightly from 0.957 to 0.934. When only the trailing end of the response was included in the calibration curve, the raw data actually showed an improvement in correlation from 0.957 to 0.984; however, the resampled data showed a decreased correlation from 0.934 to 0.890 as well as a reduction in the accuracy of the computed sensitivity from less than 1 % error to more than 4 % error. The calibration curves computed using only the trailing portion of the response demonstrate

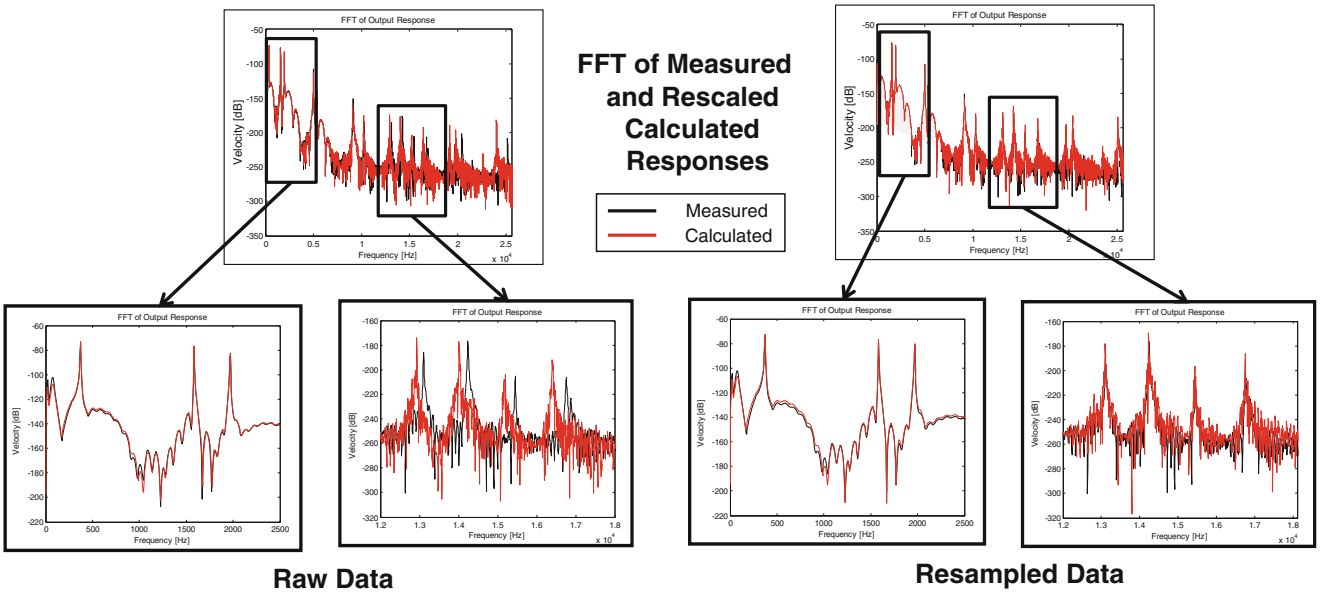

Fig. 8.15 Correction of frequency distortion due to Newmark integration using MATLAB's resample function

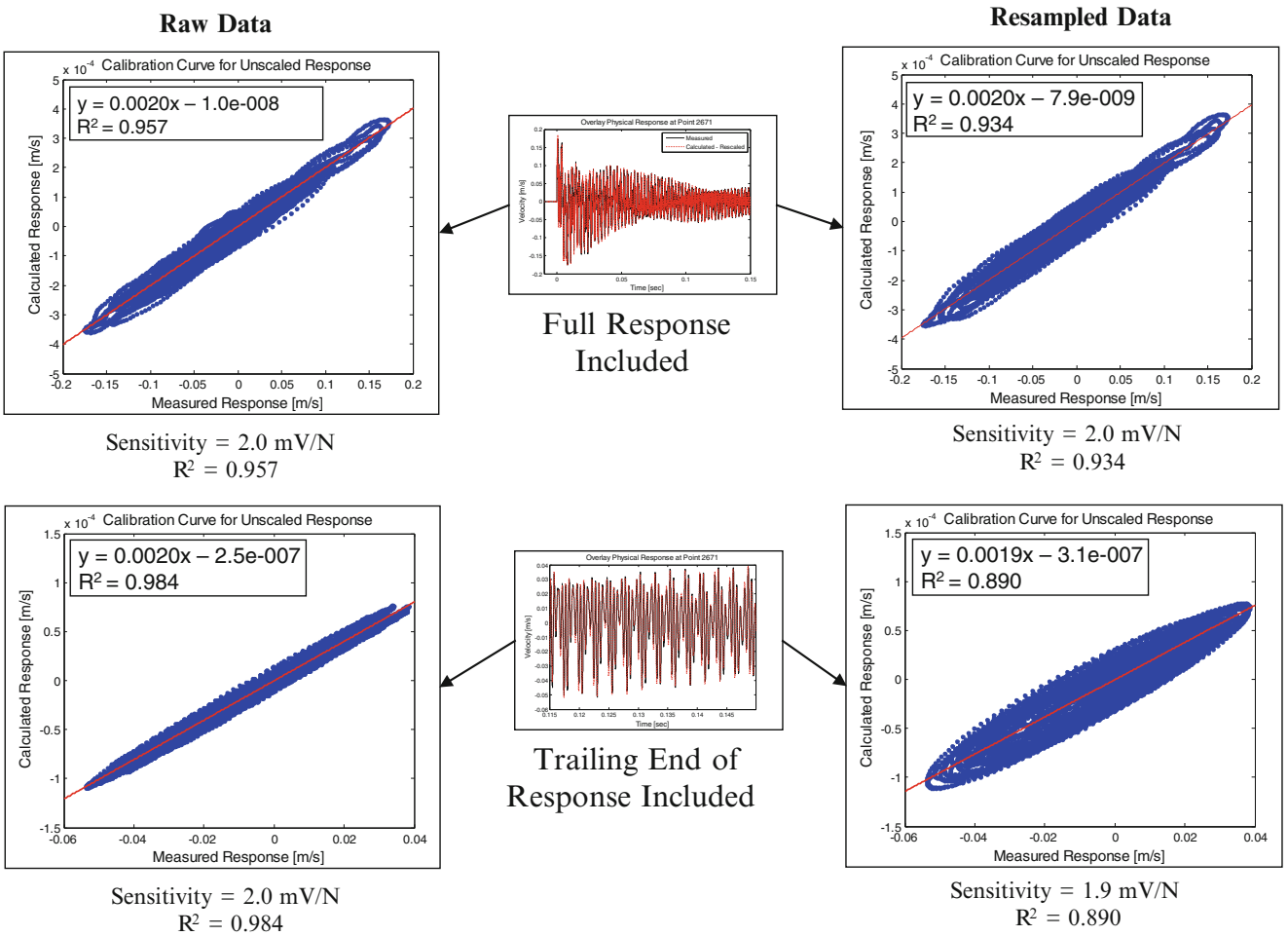

Fig. 8.16 Effect of phase distortion caused by MATLAB's resample function on the calibration curve

that phase distortion was present following MATLAB's resample function. However, most of the higher frequency energy had dissipated by the end of the response indicating that the phase distortion may have been limited to the lower order modes. Investigation into whether this phase distortion will present a problem when extending this calibration method to the ultrasonic transducer is ongoing.

Lastly, the acoustic pressure and subsequently the acoustic force must be characterized for this calibration method to be successful, as the unscaled modal force and input location must be known. Current efforts to characterize this force using both experimental data and simulation are in progress [9].

8.7 Conclusion

The results presented have shown that an analytical model based on the principles of mode superposition can produce an effective representation of a structural response when provided with a digitized input of the excitation. Furthermore, this analytical model has been shown to provide an accurate method of transducer calibration. The measured response from an uncalibrated excitation can be scaled and calibrated using a comparison to the calculated response in order to determine the force applied. The slope of the calculated response verses the measured response provides the unknown calibration. While further investigation is required before extending this calibration approach to an ultrasonic transducer, the preliminary results indicate good accuracy using this method.

Acknowledgements Some of the work presented herein was partially funded by NSF Civil, Mechanical and Manufacturing Innovation (CMMI) Grant No. 1266019 entitled "Collaborative Research: Enabling Non-contact Structural Dynamic Identification with Focused Ultrasound Radiation Force." Any opinions, findings, and conclusions or recommendations expressed in this material are those of the authors and do not necessarily reflect the views of the particular funding agency. The authors are grateful for the support obtained.

References

1. Logan, P., Avitabile, P.: Calibration techniques for non-contacting force excitation part 1. Frequency domain methods. Proceedings of the 34th IMAC. Orlando, FL (2016).
2. Femap—Finite Element Modeling and Postprocessing, Version 10.0.2. UGS Corp.
3. FEMtools 3.8—Dynamic Design Solutions. Leuven, Belgium.
4. Itoh, T.: Damped vibration mode superposition method for dynamic response analysis. Earthquake Eng. Struct. Dynam. **2**(1), 47–57 (1973)
5. MATLAB—Matrix Analysis Software. The MathWorks, Inc., Natick MA.
6. Polytec Scanning Laser Doppler Vibrometer. Polytec. Opt. Meas. Syst.
7. LMS Test. Lab—Leuven Measurement Systems, Leuven, Belgium
8. The Mathworks, Inc.: Signal processing toolbox: user's guide (r2015b). http://www.mathworks.com/help/pdf_doc/signal/signal_tb.pdf (2015). Accessed 16 Sept 2015.
9. Chen, S., Niezrecki, C., Avitabile, P.: Experimental mapping of the acoustic field generated by ultrasonic transducers. Proceedings of the 34th IMAC. Orlando, FL (2016).

Chapter 9
Responses of Structures to SDoF vs. MDoF Vibration Testing

Laura D. Jacobs, Garrett D. Nelson, and John H. Hofer

Abstract The vibration excitation mechanisms for structures in service are typically multi-directional. However, during product testing conducted in a lab setting the standard practice is to replicate these environments with three orthogonal single axis vibration tests. Recent advances in technology have made it possible to perform multi-axis simulations in the laboratory. Simultaneous multi-axis excitation can result in different stress states, rates of damage accumulation, and peak accelerations and strains than those resulting from sequential single axis testing. Accordingly, a series of experiments were run on a plate structure to investigate and quantify these differences. The experiments included single and multiple axis tests with different excitation amplitudes. The single axis tests were performed on both uniaxial and multiaxial shaker systems. The control levels, response energy, modal behavior, and peak accelerations were compared for each test condition. The data illustrates the differences between the structural response for single and multi-axis tests and enables an objective comparison between testing conducted on single and multiple axis shaker systems.

Keywords Multi-axis • Vibration • Experimental • Structural response • Dynamics

9.1 Introduction

Traditional product life-cycle and environmental vibration testing are conducted on uniaxial vibration test platforms. These tests have been established as a method to detect part failures and predict the effects of service loads without the need of costly and time consuming field testing. The most widely referenced standard for these tests, MIL-STD-810G, specifies the use of sequential single axis tests in each of three orthogonal axes to characterize the performance of both components and assemblies [1]. Comparable methods are provided by the U.S. Navy in NAVMAT P-9492 and the electronics industry's JESD22-B103B [2, 3]. Per these standards, the device is first tested along a single axis and then rotated 90° about the appropriate axis, with a test conducted after each rotation.

In many environments, the effects of cross-axis excitation can have large impacts on the resulting dynamics of a structure [4]. Accordingly, the combined loading effects caused by these multi-axis excitations can result in different stress states [5, 6], failure modes [7], rates of damage accumulation [8–10], and peak accelerations and strains. Accordingly, a potential limitation of single axis testing is the presence of uncontrolled off-axis vibrations. In both electrodynamic and hydraulic shaker systems, the excitation along the primary test axis is accompanied by varying levels of off-axis excitation due to internal coupling within the equipment and test item. MIL-STD-810G recommends that these off-axis vibrations are monitored and maintained at levels below 0.45 times the primary axis. In the event that this exceeds the recommended value, it may be necessary to reduce the primary axis excitation to satisfy this condition. With multi-axis shaker equipment, not only can these levels be monitored, but they can also be controlled to actively ensure that these conditions are met. This enables true uniaxial testing capabilities. This can aid in both system identification and model validation methods.

A plate structure was tested using a six degree of freedom electrodynamic shaker system. Both uniaxial and multi-axis tests were conducted on the test articles to compare its response under the different loading conditions. This included testing with uniaxial, biaxial, and triaxial random vibration excitation. In order to compare these results to existing test methods,

Sandia is a multi-program laboratory operated by Sandia Corporation, a Lockheed Martin Company, for the United States Department of Energy under contract DE-AC04-94AL85000.

L.D. Jacobs (✉) • G.D. Nelson • J.H. Hofer
Vibration/Acoustics Simulation, Sandia National Laboratories, P.O. Box 5800, MS 0557, Albuquerque, NM 87185, USA
e-mail: ldjacob@sandia.gov

E. Wee Sit (ed.), *Sensors and Instrumentation, Volume 5*, Conference Proceedings of the Society for Experimental Mechanics Series, DOI 10.1007/978-3-319-29859-7_9

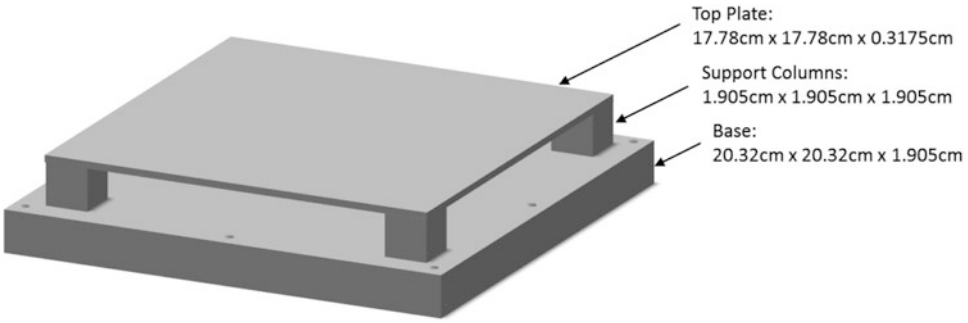

Fig. 9.1 Square aluminum plate test article

each uniaxial test was repeated on a single degree of freedom electrodynamic shaker system. A description of the test article's designs, construction, and anticipated dynamics is given in the following section. Subsequently, details about the equipment and specific test methods employed are provided. The energy level of the plate's response have been calculated for each test to enable objective comparisons between each loading scenario. This data and accompanying discussions are provided in Sect. 9.2.

9.1.1 Test Article

The test article selected for this research was a column supported square aluminum 6061 plate (see Fig. 9.1). In order to eliminate the added dynamics due to support boundaries, the test article's base, columns, and top plate are made of a continuous piece of material. The material can be regarded as both homogenous and isotropic.

The test article was designed such that only the top plate surface was dynamically active. The plate thickness (0.3175 cm) was selected to ensure that the first five primary modes were within the control bandwidth of the test equipment. The support columns (1.905 cm) and base (1.905 cm) are six times the thickness of the plate to ensure that they contribute little or no dynamics to the plate's response. For small amplitudes and predominantly low frequencies, this assumption is valid.

The plate was fastened to the shaker system with bolts evenly spaced along its perimeter. Eight holes/bolts are located circumferentially. One bolt positioned at a central hole constrains bending of the test article's base. A uniform torque of 3.62 N-m was applied to each bolt.

A plate was selected as the preliminary test article, because its dynamics have been well documented. In contrast to component assemblies and parts with complex geometries, the dynamics governing its motion can be generally regarded as simple. The expected mode shapes and resonant frequencies for a thin plate with four corner supports are given by Blevins [11]. Future work by other authors has extended this result to include non-symmetric supports [12], corner column supports [13], and symmetric column supports [14]. From these results, it was possible to predict the plate's dynamic response to various stimuli. However, in order to obtain a more accurate estimate of the plate's dynamics, a finite element model was employed. This allowed the analysis to fully incorporate the effects of all test article geometry. The finite element simulations were specifically used to determine the natural frequencies and mode shapes of the plate. Eigen analyses were performed using Sierra/SD, the structural dynamics package in the Sierra Mechanics code suite developed by Sandia National Laboratories. The relevant material properties used for this and all future analysis are as follows: $E = 68.9$ GPa, $\rho = 2.7$ g/cm^3, $\nu = 0.33$, and $Sut = 310$ MPa [15]. The resulting modal response estimates can be seen in Fig. 9.2.

In order to experimentally validate the model, digital image correlation was used to extract and verify the mode shapes when subjected to out of plane excitation. Digital image correlation is a method which uses optical data and correlation analysis to monitor the deformation of a structure [16]. Specifically, by using cameras and tracking the motion of an array of random dots on the plate's surface, the VIC-2D software can be used to extract strain data. From the resulting analysis, the following experimental mode shapes were obtained (see Fig. 9.3).

The experimental mode shapes and their frequencies agree closely to those originally predicted by the model. Accordingly, it can be anticipated that each of the experimental responses discussed in the section which follows will be dominated by one of the four illustrated mode shapes or a combination thereof.

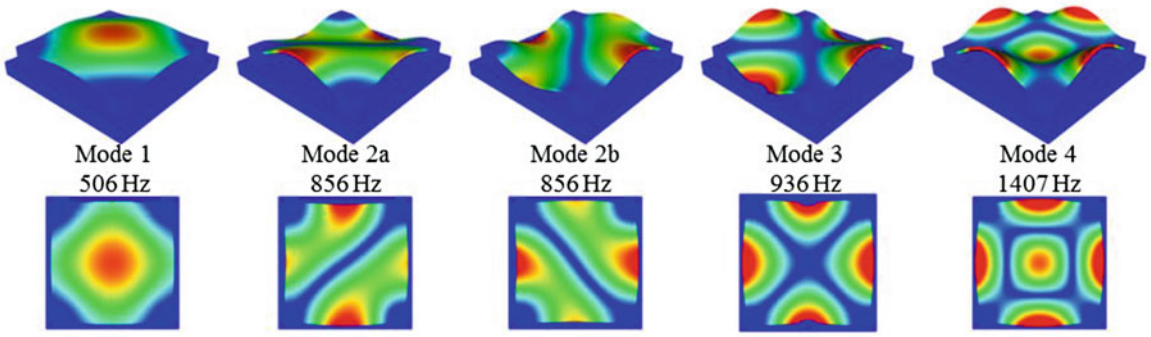

Fig. 9.2 Test article mode shapes

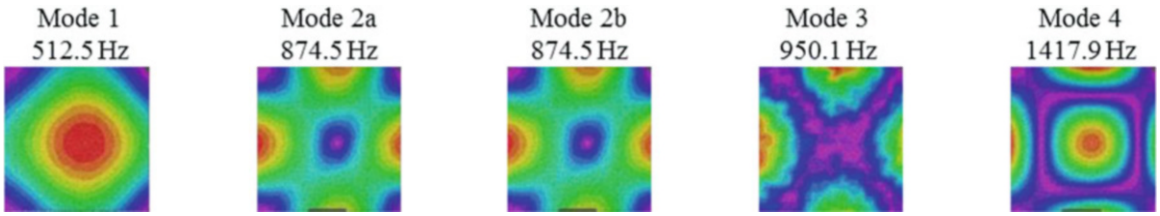

Fig. 9.3 Experimental test article mode shapes

Fig. 9.4 Tensor 900 multi-axis vibration test system [17]

9.1.2 Test Equipment

There were two different shaker and control systems employed to conduct the experiments in this report. What follows is a brief description of each set of equipment highlighting their differences.

For physical testing conducted on the plate using a multi-axis shaker system, Team Corporation's Tensor 900 (TE6-900) multi-axis high frequency vibration test system was employed (see Fig. 9.4). Due to the unit's configuration of 12 independent electrodynamic shakers, it is capable of full six degree of freedom vibration testing. Four shakers are aligned along each of three orthogonal axes with opposing pairs of shakers positioned on either horizontal side of the base fixture and four vertical shakers positioned on the bottom of the fixture. By controlling the relative amplitude and phase of each shaker, it is possible to achieve the desired translational and rotational accelerations of the base fixture. At its maximum payload, the shaker system is capable of achieving 10g acceleration along each primary axis from 10 Hz to 5 kHz [17]. A preliminary characterization of the performance of this shaker system is provided by Smallwood [18].

Fig. 9.5 Unholtz-Dickie T1000/T2000 series shaker

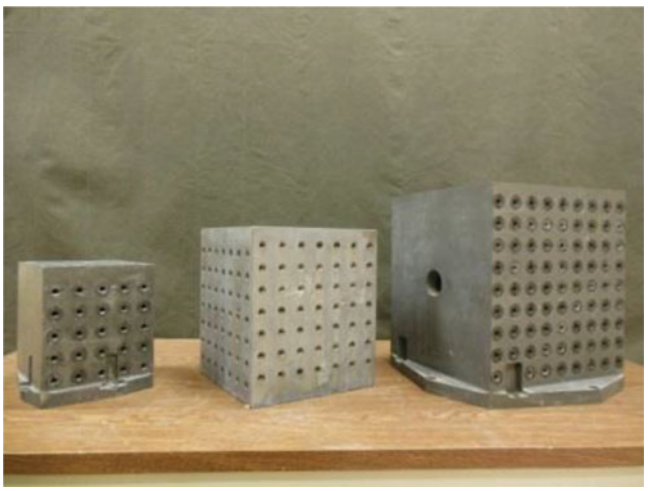

Fig. 9.6 Adapter cubes for uniaxial testing

For the physical testing conducted on the plate using a uniaxial shaker, Unholtz-Dickie's T1000/2000 systems are employed (see Fig. 9.5). The T1000/2000 shakers are capable of supporting a payload of up to 680 kg. The T1000 shaker is capable of 78 kN-peak for sine tests and 71 kN-rms for random. The T2000 shaker is capable of 111 kN-peak for sine tests and 107 kN-rms for random. The shakers are rated for a frequency range of 10 Hz to 3 kHz, although it is frequently run to 4 kHz on random tests with minimal difficulty. In order to excite the different axes of a test article, an adaptor cube is added to the top of the shaker (see Fig. 9.6).

The test article was equipped with an array of triaxial accelerometers for control and response monitoring. Four control accelerometers were positioned symmetrically about both lateral axes at the mid-plane of the test article's base for testing on the multi-axis system. The response accelerometers were placed in a symmetric pattern on the top surface of the plate. During tests conducted on the uniaxial system, the four response accelerometers located at the corners on the top plate surface were used for control. Shown in Figs. 9.7 and 9.8 is the test article equipped with accelerometer arrays for testing on both the multi-axis and uniaxial shaker systems.

A schematic of the exact positions of both control and response accelerometers for multiaxial and uniaxial systems can be seen in Figs. 9.9 and 9.10 respectively.

During analysis, the response accelerometers will be grouped according to their general location and referred to as follows: corner (response accelerometers #'s 1–4), center (#5), side (#'s 6–9), and diagonal (#'s 10–13).

Testing was conducted for all combinations of translational excitation. First the test article was tested in each translational axis individually, then two axes simultaneously, and finally triaxial testing. The control input for each test was 2 min of white Gaussian noise band-limited from 20 Hz to 2 kHz. For each sequence of multi-axis tests, the coherence between the

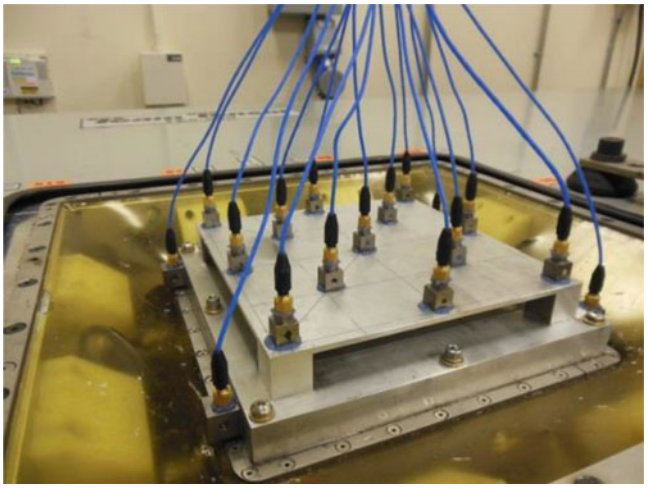

Fig. 9.7 Control and response accelerometer placement on test article for multi-axis system

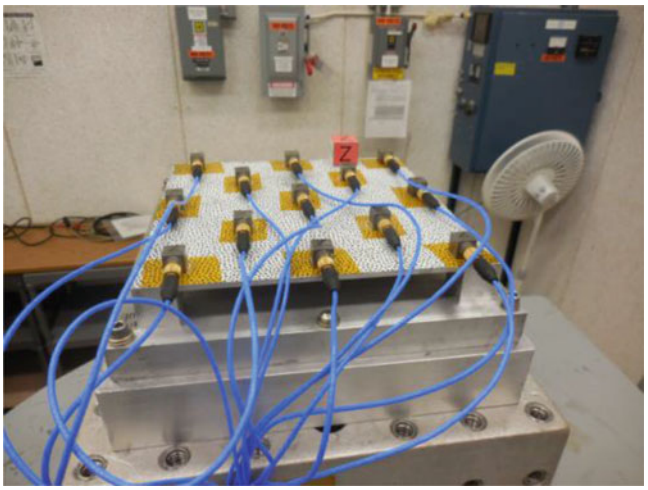

Fig. 9.8 Control and response accelerometer placement on test article for uniaxial system

active axes was varied between low ($C \approx 0.0$), medium ($C \approx 0.5$), and high ($C \approx 1.0$) levels. The phase was kept constant at zero degrees for all tests irrespective of the coherence level. In addition to varying the active axes and coherence levels, the multi-axis tests were conducted at both 1g and 2g root mean squared (RMS) acceleration levels and the uniaxial tests at 1–3g to verify that any observed effects were scale independent.

9.2 Results

For all tests, each active axis was kept to within 2% of the desired level. If we look at the level of off axis translations relative to the level of the primary axis under test, we can see that the amount of off axis energy varies significantly during the different testing scenarios (see Table 9.1).

The most difficult off axis vibration to control was the vertical direction. In this axis, on the multi-axis shaker system the maximum level observed was as much as 13.24 % the active lateral axis control level. Although it appears that a greater level of off axis control was achieved during 2g than 1g testing on the multi-axis system, this is only a relativistic effect. For both sets of tests, the off-axis RMS levels were comparable. However, relative to the active axis the noise floor level is smaller during the 2g testing.

More importantly, on the uniaxial shaker system the vertical axis observed up to 36.54 % the active lateral axis control level. On many real world structures, this significant off-axis energy contribution is more than enough to alter the dynamics

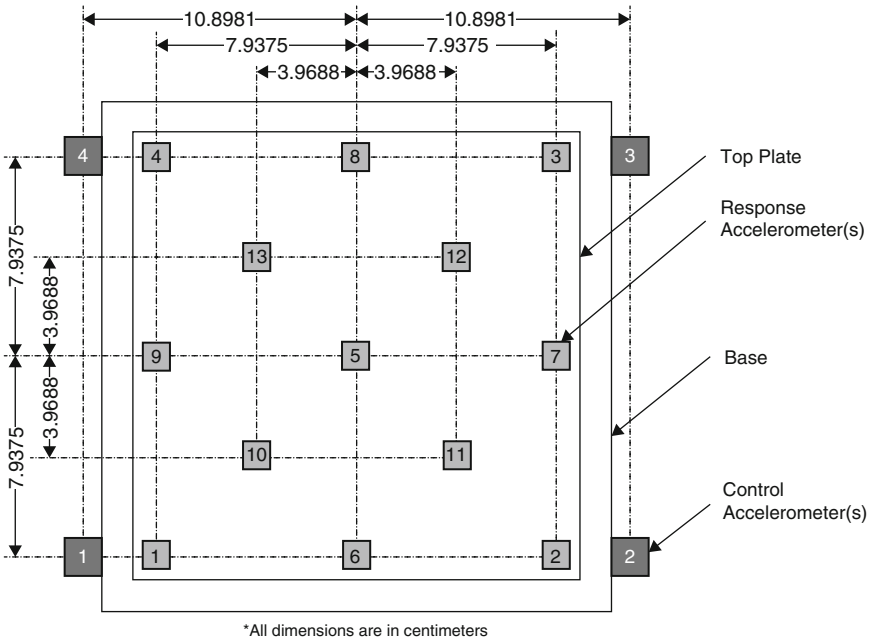

Fig. 9.9 Schematic of control and response accelerometer placement on test article for multi-axis system

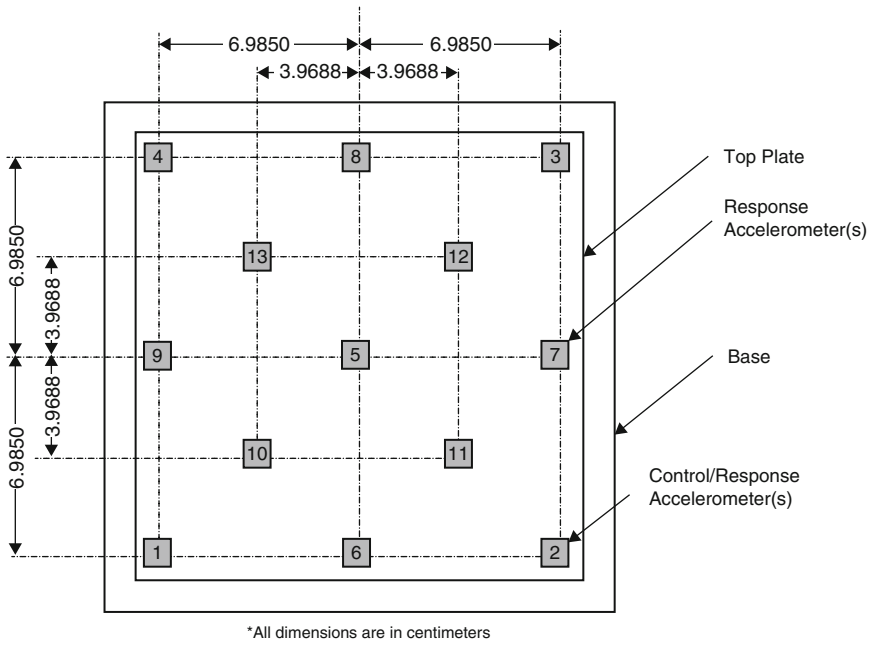

Fig. 9.10 Schematic of control and response accelerometer placement on test article for uniaxial system

from those which would be predicted in the presence of true single degree of freedom testing. Although this level falls below the upper bound recommended by MIL-STD-810G, it is critical that the presence of this additional energy is noted. This is particularly relevant when using this equipment for model validation purposes.

During testing of the plate's dominant axis (vertical, Z-axis) at the 1g level, the maximum RMS rotational acceleration level experienced was below 8 rad/s^2. Similarly, during testing of the same axis at the 2g level, the maximum RMS rotational acceleration level experienced was below 11 rad/s^2. Very little difference was observed in the level of rotation about any axis, whether the test was conducted on the multi-axis or uniaxial shaker system. As the vertical (Z-axis) input acceleration level was increased by 1g, the rotational level for the multi-axis test increased by approximately 5g and 2g on the uniaxial and multi-axis shaker systems respectively.

Table 9.1 Off axis acceleration levels as a percentage of the control axis level during uniaxial vibration testing 20 Hz to 2 kHz

System	Test	Level	Acceleration		
			Transverse X (g)	Longitudinal Y (g)	Vertical Z (g)
1D	X	1g	–	[a]	[a]
		2g	–	7.01 %	36.54 %
	Z	1g	6.95 %	9.10 %	–
		2g	6.35 %	8.44 %	–
6D	X	1g	–	6.17 %	11.64 %
		2g	–	3.24 %	13.24 %
	Y	1g	6.03 %	–	8.18 %
		2g	3.13 %	–	5.78 %
	Z	1g	6.08 %	6.46 %	–
		2g	3.29 %	3.38 %	–

[a]Data not available

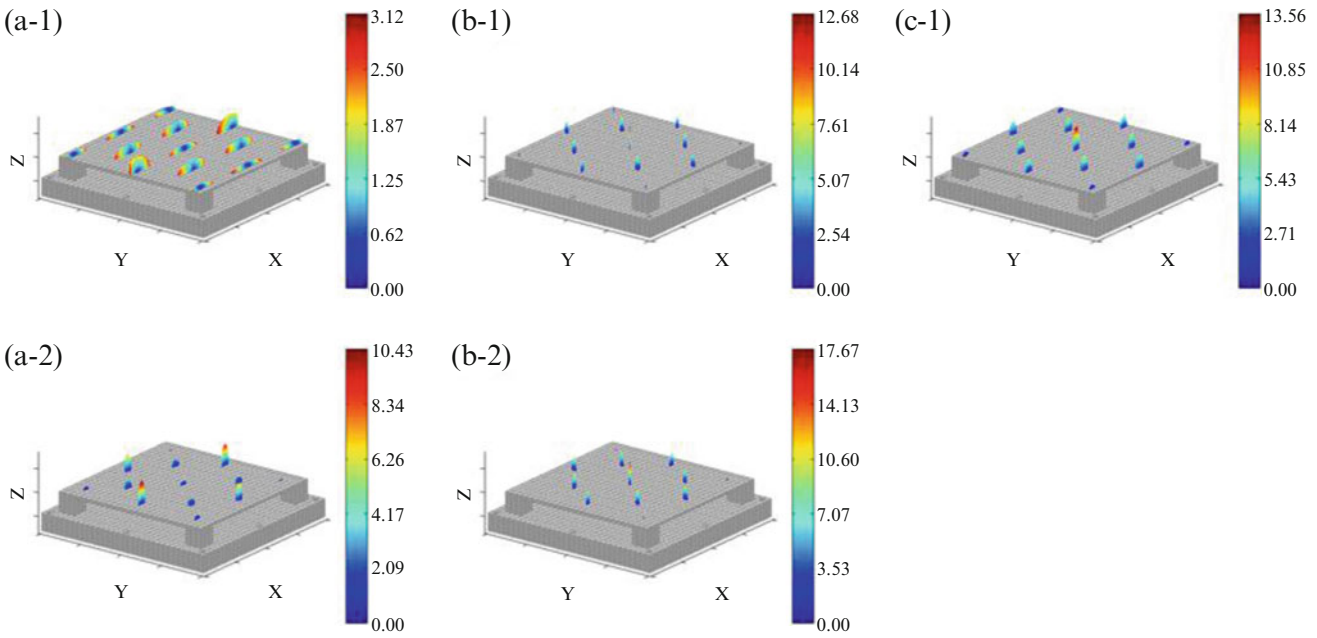

Fig. 9.11 RMS accelerometer responses (in g's) to incoherent 2g input in the X- (**a**), Z- (**b**), and XZ axes (**c**) on the multi-axis (1) and uniaxial (2) shaker systems

During translational testing (X-axis), higher rotational levels were observed on both test systems. At the 2g level, both the roll and yaw rotations were comparable, but the device on the uniaxial shaker system experienced a little over twice as much pitch rotation (110 rad/s^2 versus 45 rad/s^2).

As an early examination of the plate's response to varying the axis or method of excitation, the root mean square (RMS) acceleration level of each accelerometer was obtained. First, it is informative to observe the response of the plate to a uniaxial or biaxial 2g input (see Fig. 9.11). The RMS level in the x, y, and z axes at each sensor location is represented by the width of the ellipsoid's semi-principle axis in line with the plate's global X, Y, and Z axes.

For the testing conducted on the multi-axis shaker (a-1, b-1, c-1), the nature of the response agrees well with the anticipated behavior for the plate structure. In the presence of only lateral (X-axis) excitation, the RMS levels are most significant along the lateral response axis. Conversely, during vertical (Z-axis) excitation the RMS levels are largest in the vertical axis for each response accelerometer. The multi-axis loading scenario is anticipated to be a combination of the two responses. This is confirmed by looking at the simultaneous x- and Z-axis excitation response in c-1. As can be seen in the figure, in the presence of equal lateral and vertical input levels, the response of the plate is heavily dominated by the Z-axis, with the peak level always occurring at the center response accelerometer. Additionally, the plate response appears to be approximately symmetric with respect to both the x and y axes. Repeating the single axis tests on the uniaxial shaker system, a different

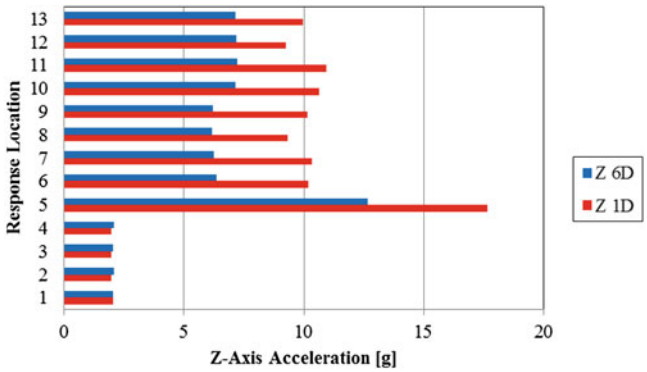

Fig. 9.12 Response accelerometers' RMS level due to uniaxial Z-axis 2g input on both uniaxial (1D) and multi-axis (6D) shaker systems

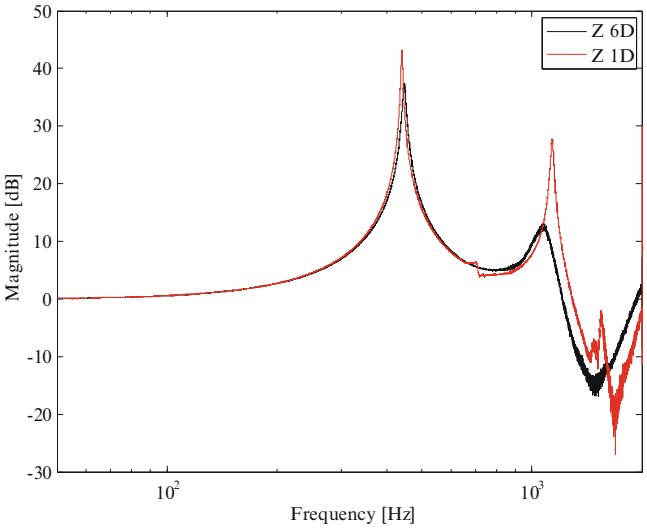

Fig. 9.13 Central response accelerometers' transfer function due to uniaxial Z-axis 2g input on both uniaxial (1D) and multi-axis (6D) shaker systems

characteristic response is obtained. When conducting the X-axis tests, the presence of uncontrolled off axis energy (along the plate's most sensitive axis) has resulted in a response dominated mostly by this axis. Thus, for analysis conducted on this data set, it will be difficult to isolate whether response behavior was due to the lateral or vertical input components. On a more complicated structure, the lack of this traceability can make model validation difficult.

Despite controlling the vertical acceleration to the same level on both the uniaxial and multi-axis shaker systems, the RMS level of the plate response on each system differed substantially. This can be seen most clearly by looking at the Z-axis acceleration at each response location during Z-axis testing (see Fig. 9.12).

As pictured, at the control locations on the corners (responses #1–4), the same excitation level has been experienced. However, at all other locations on the plate surface, a larger response was observed during testing on the uniaxial shaker system. Looking just at the accelerometer located at the center of the plate (#5), it is helpful to look at the transfer function between the Z-axis control input and the Z-axis response. This demonstrates how the response specifically differed at this location (see Fig. 9.13).

The response is heavily influenced by two critical modes. During testing on the multi-axis shaker system, these modes are located at 446 Hz and 1073 Hz. During testing on the uniaxial shaker, these modes are seen to have shifted slightly to 440 Hz and 1137 Hz. More importantly, the level of the response at each mode has changed. A larger resonance occurred for both modes on the uniaxial shaker system. Looking at the transfer function at all other locations on the plate surface, a similar trend can be noted.

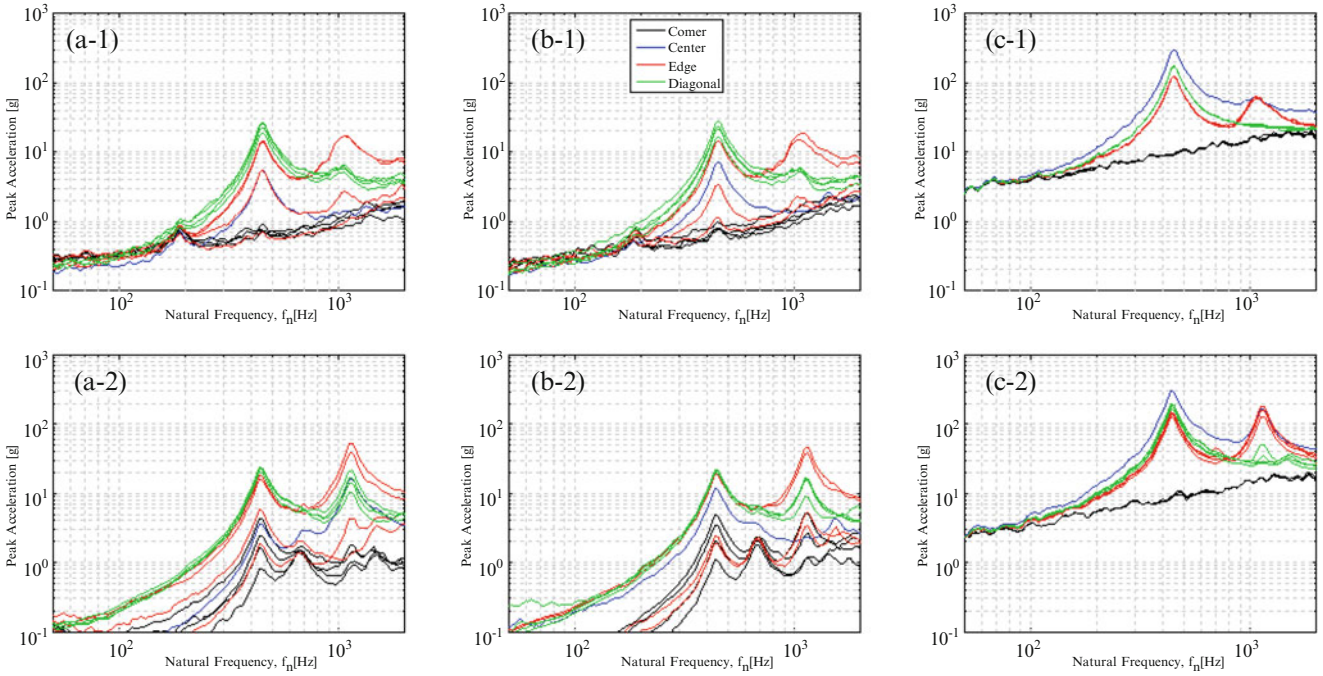

Fig. 9.14 Response accelerometers' X- (**a**), Y- (**b**) and Z-axis (**c**) SRS with Q = 10 due to uniaxial 2g Z-axis excitation on the multiaxial (1) and uniaxial (2) shaker systems

9.2.1 Shock Response Spectrum (SRS)

In order to assess the test severity on the plate with consideration to the applied frequency content, the Shock Response Spectrum (SRS) of the acceleration time histories were evaluated for each test scenario. The SRS graphically portrays the peak acceleration that would be experienced by a series of single degree of freedom systems with natural frequency, f_n, due to the base input acceleration provided [19].

Before processing, the raw accelerometer data was detrended with a third order polynomial to remove the spurious effects of low frequency components. In order to obtain the damped single degree of freedom system responses, the ramp invariant absolute acceleration method was employed [20]. The natural frequency, f_n, was varied in the preferred 1/12th octave increments from 50 Hz to 2 kHz. As is common for comparison analysis, for initial investigations a constant amplification factor of Q = 10 (5% structural damping) was employed for all natural frequencies [21]. After having verified that the negative and positive extremal value curves did not differ significantly, only the maximum absolute value will be presented here. The SRS obtained for the plate's response to uniaxial 2g Z-axis excitation can be seen in Fig. 9.14 below.

From the figure, it is evident that the response along all three axes is dominated by two modes (first mode at 437 Hz and the fourth mode at 1150 Hz). As expected, the highest shock levels are observed out of plane with the plate—along the Z-axis. Qualitatively, the modal distribution for the respective groups of accelerometers is generally comparable for tests run on both the uniaxial and multi-axis shaker systems. However, the shock levels at each resonant frequency appear to be amplified on the uniaxial system. For analysis of part failure, the Z-axis SRS is most critical, but it is informative to note differences in the response along each axis. These differences could have greater significance in parts with more complex geometries. Particularly, the resonance of the central accelerometer at 1150 Hz in the X-axis SRS on the uniaxial system can be seen to differ substantially from that for the same test on the multi-axis shaker system where it was not observed altogether.

The SRS in each axis due to uniaxial 2g X-axis excitation has also been obtained and can be seen in Fig. 9.15.

In these responses, more substantial differences between the spectra from tests on each set of equipment can be observed. The central accelerometer for tests on the uniaxial shaker system once again exhibits large shock responses at frequencies not observed on the multi-axis tests despite being controlled to the same input acceleration levels. This is clearly shown in the Z-axis SRS. These differences can be more carefully examined by computing the SRS with a larger quality factor. Effectively, this reduces the assumed damping of each single degree of freedom oscillator and produces a spectrum with less "smoothing". The Z-axis SRS with Q = 50 obtained for the plate's response to uniaxial 2g X-axis excitation can be seen in Fig. 9.16 below.

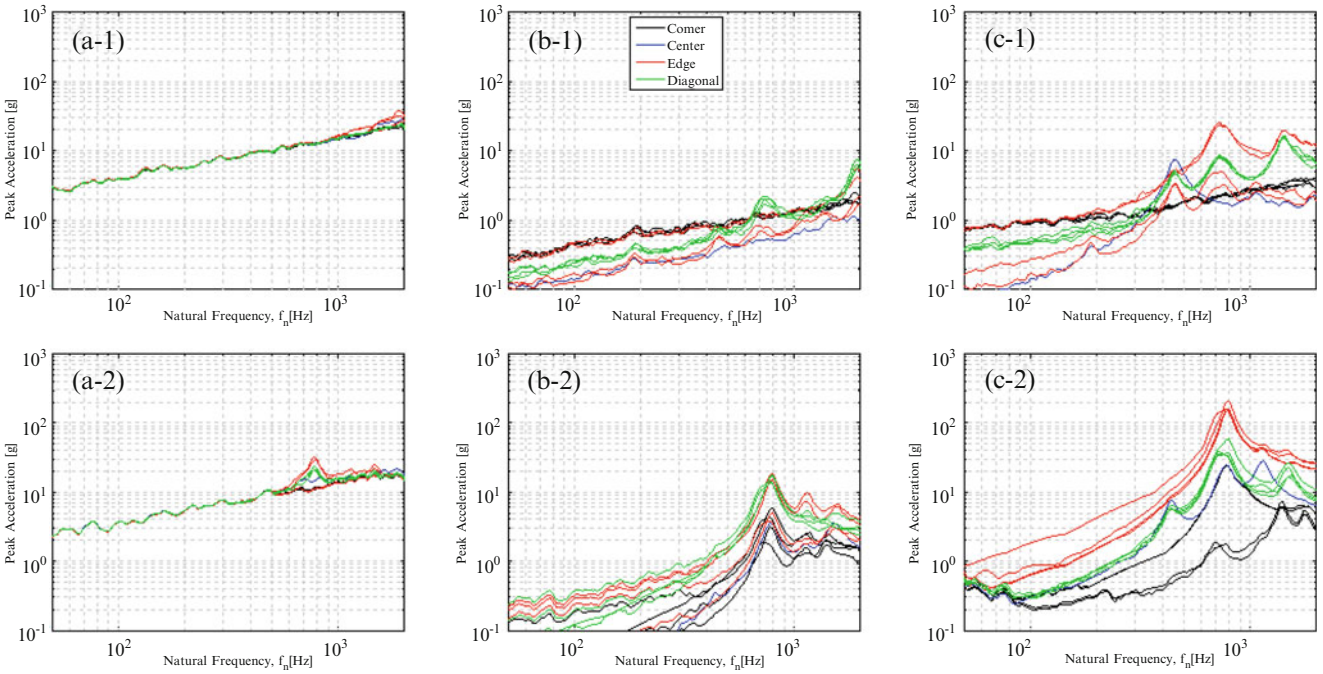

Fig. 9.15 Response accelerometers' X- (**a**), Y- (**b**) and Z-axis (**c**) SRS with Q = 10 due to uniaxial 2g X-axis excitation on the multiaxial (1) and uniaxial (2) shaker systems

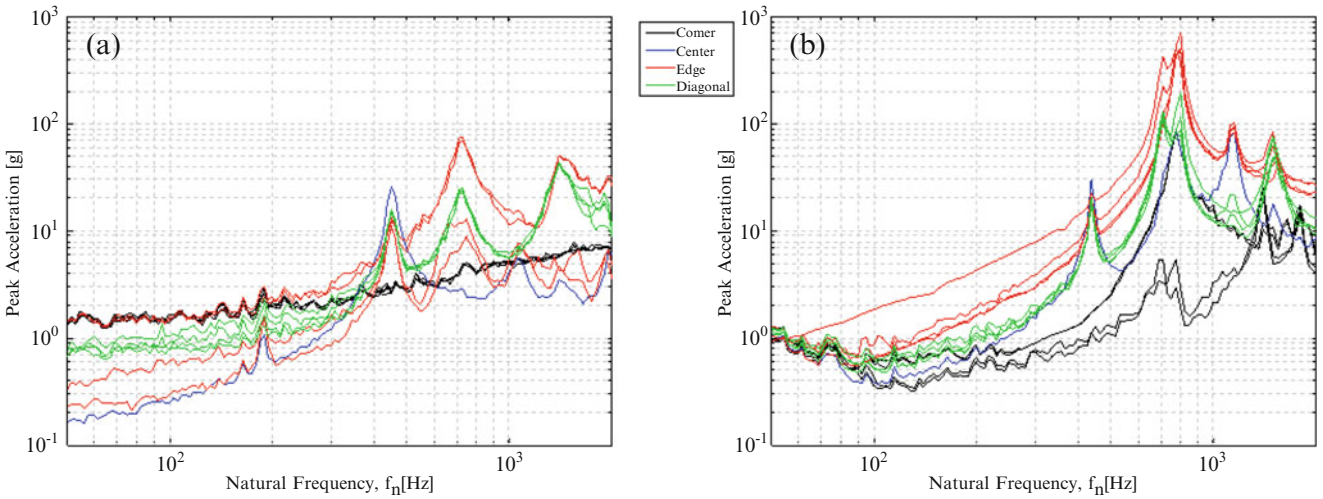

Fig. 9.16 Response accelerometers' Z-axis SRS with Q = 50 due to uniaxial 2g X-axis excitation on the multiaxial (**a**) and uniaxial (**b**) shaker systems

The SRS from the uniaxial shaker system shows high levels of response at five distinct frequencies (437 Hz, 710 Hz, 800 Hz, 1150 Hz, and 1500 Hz). This can be sharply contrasted with the response on the multi-axis system where only three dominant frequencies were observed (450 Hz, 730 Hz, and 1400 Hz). The largest discrepancy is the presence of the two modes at 800 Hz and 1150 Hz. These modes were not observed in any uniaxial, biaxial, or triaxial test conducted on the multiaxis shaker system irrespective of the coherence level between excitation axes. Thus, their presence is due to the specific testing conditions present on the uniaxial shaker system. As previously mentioned, an adapter cube was required to conduct tests on each axis of the plate with the uniaxial shaker system. During X-axis tests, the adapter cube is rotated such that the X-axis of the test article is in line with the active axis of the shaker (see Fig. 9.17).

It is suspected that these modal contributions are due to the support boundary condition created by the cube fixture. Without the ability to control more than one degree of freedom, it is possible that out-of-axis deformation of the cube could

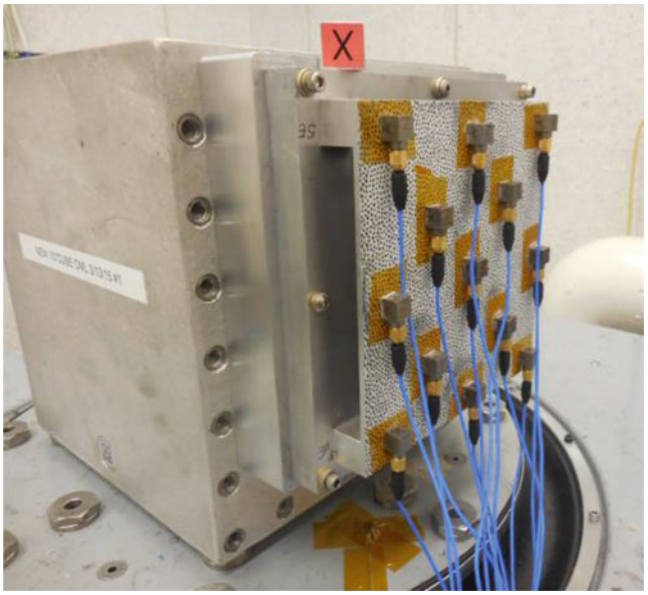

Fig. 9.17 Test article on adapter cube for X-axis tests on the uniaxial shaker system

contribute to the observed dynamics in the plate. The dynamics of a similar adapter cube fixture have been previously investigated by DeLima [22]. It is reported that the cube has a 800 Hz off axis resonance. This aligns closely with the unexpected modal contribution observed during X-axis testing. Additionally, this explains the large levels of pitch rotation (about the y-axis) which were noted during these tests. Looking at the individual Z-axis responses of the corner accelerometers, this mode dominates the response of the top two corners and has little contribution at the bottom two corners. Thus, it is reasonable to conclude that these dynamics are due to a "rocking" mode of the cube fixture.

9.3 Conclusions

By utilizing an electrodynamic shaker system capable of full six degree of freedom vibration control, the response of a plate structure to uniaxial and multi-axis random vibration loading was investigated. For each uniaxial loading scenario, the experiments were repeated on both a conventional single axis shaker and a new multi-axis shaker system. It was anticipated that uncontrolled off-axis excitation present during testing on the single axis shaker system could result in different loading conditions when compared to true single axis testing conducted on a system where these off-axis levels are controlled.

Using the root mean square level as an indicator of the overall response energy of the plate, it was found that the single axis testing conducted on the uniaxial shaker resulted in larger peak response energy levels. At the observed resonant modes, reduced damping was observed. Comparing this result to multi-axis loading scenarios conducted on a six degree of freedom shaker system, it can be determined that this effect is not due to a simple contribution of off-axis translational excitation. A comparable modal response was not observed for all biaxial or triaxial tests on the multi-axis system irrespective of the level of coherence between axes. However, tests were not conducted with added rotational levels which may have contributed to this effect.

The peak acceleration of the plate was found to correspond to the first and primary 'oil-can' mode. Hence, the largest dynamic response was observed at the center of the plate for most loading conditions. For any test in which Z-axis stimuli was present, this mode dominated the response. For X-axis testing on the uniaxial system, large levels of off axis excitation in line with the Z-axis of the plate resulted in a large response which made it difficult to isolate the response energy due to the primary X-axis excitation. The peak acceleration levels found by the Shock Response Spectrum illustrated that the primary modes of the plate were predominantly invariant to the addition of lateral axis excitation. However, the cube fixture required to complete X-axis testing on the uniaxial system resulted in the presence of additional modes in the measured responses. For some loading conditions, the contribution due to this mode dominated the response and distorted the expected modal response.

For model identification or validation, the uncontrolled effects due to the testing system employed must be well documented. For components or assemblies with more complex geometries, the effects of undesired additional dynamics may be amplified and require more careful analysis. The ability to conduct testing on equipment which is capable of reproducing true single or multi-axis loads can improve analysis and minimize these effects. The development of multi-axis shaker systems has made this possible, but further research is required to continue to investigate these differences in both a theoretical and experimental framework.

References

1. U.S. Department of Defense Environmental Engineering Considerations and Laboratory Tests, MIL-STD-810G. October 2008
2. U.S. Navy Manufacturing Screening Test Standards, NAVMAT P-9492. May 1979
3. JEDEC Standard: Vibration Variable Frequency, JESD22-B103B. June 2006
4. Chang, K.Y., Frydman, A.M.: Three-dimensional random vibration testing definition and simulation. Proc. 36th Annual Mtg., pp. 129–139. Institute of Environmental Sciences, Mount Prospect, IL (1990)
5. Gregory, D.L., Bitsie, F., Smallwood, D.O.: Comparison of the response of a simple structure to single axis and multiple axis random vibration inputs. Proc. 80th Shock and Vibration Symp., San Diego, CA, October 2009
6. Habtour, E., et al.: Novel approach to improve electronics reliability in the next generation of US Army small unmanned ground vehicles under complex vibration conditions. J. Fail. Anal. Preven. **12**(1), 86–95 (2012)
7. French, R.M., Handy, R., Cooper, H.L.: A comparison of simultaneous and sequential single-axis durability testing. Exp. Tech. **30**(5), 32–37 (2006)
8. Himelblau, H., et al.: Effects of triaxial and uniaxial random excitation on the vibration response and fatigue damage of typical spacecraft hardware. Proc. 66th Shock and Vibration Symp., Arlington, VA, October 1995
9. Peterson, C.: Time-to-failure testing using single- and multi-axis vibration. Sound Vib. **47**(3), 13–17 (2013)
10. Whiteman, W.E., Berman, M.S.: Fatigue failure results for multi-axial versus uniaxial stress screen vibration testing. Shock Vib. **9**(6), 319–328 (2002)
11. Blevins, R.D.: Plates. In: Formulas for Natural Frequency and Mode Shape, pp. 264–269. Krieger, Malabar, FL (2001)
12. Johns, D.J., Nataraja, R.: Vibration of a square plate symmetrically supported at four points. J. Sound Vib. **25**(1), 75–82 (1972)
13. Felemban, M.B.: Vibration analysis of point and column supported mindlin plates. M.S. thesis, Mech. Eng., King Fahd Univ. of Petroleum & Minerals, Dharan, Saudi Arabia (1989)
14. Petyt, M., Mirza, W.H.: Vibration of column-supported floor slabs. J. Sound Vib. **21**(3), 355–364 (1972)
15. Aluminum 6061-T6 (Online). http://www.matweb.com/search/datasheet_print.aspx?matguid=1b8c06d0ca7c456694c7777d9e10be5b
16. Correlated Solutions, Inc. Digital image correlation. http://www.correlatedsolutions.com/index.php?option=com_content&task=view&id=23&Itemid=36. Accessed 16 June 2008
17. Team Corporation. Tensor 900 multi-axis high frequency vibration test system (Online). http://www.teamcorporation.com/images/brochures_A4/Tensor900_A4.pdf
18. Smallwood, D.O., Gregory, D.L.: Evaluation of a 6-DOF electrodynamic shaker system. Proc. 79th Shock and Vibration Symp., Orlando, FL, October 2008
19. Piersol, A.G., Paez, T.L.: Shock data analysis. In: Piersol, A.G., Paez, T.L. (eds.) Harris' Shock and Vibration Handbook, 6th edn. McGraw-Hill, New York (2010). Ch. 20
20. Smallwood, D.O.: An improved recursive formula for calculating shock response spectra. 51st Shock Vib. Bull. **51**(2), 211–217 (1981)
21. Halfpenny, A., Walton, T.C.: New techniques for vibration qualification of vibrating equipment on aircraft. Proc. Aircraft Airworthiness & Sustainment 2010, Austin, TX, May 2010
22. DeLima, W.J., Ambrose, M.N.: Experimental characterization and simulation of vibration environmental test. In: Mains, M. (ed.) Topics in Modal Analysis, vol. 10. Springer, New York (2015). Ch. 6

Chapter 10
High Gap Maglev Model and Experimental Validation

Francesco Braghin, Francesco Castelli-Dezza, and Stefano Ghiringhelli

Abstract Magnetic Levitation is a powerful physical phenomena which, if correctly controlled, allows frictionless relative motion between two bodies. One of the main features of this system is that it could also provide active damping. However, in order to damp vibrations, a high gap is requested. The analytical model is insufficient to correctly describe the behaviour of such a system, as a lot of secondary effects rise. In order to study this problem in detail, the study of a simple single degree of freedom Maglev is proposed. The paper shows how the analytical model, which is used to build the active control, can influence the behaviour of the real system, and then a way to improve this model is discussed. Relying on FEM analysis, analytical and numerical models are compared, and the analytical one is improved, in order to guarantee a higher performance control. Both analytical and numerical model-based control are tested on an experimental test-bench. Results prove how the numerical model-based control can guarantee much better performance with the same computational costs.

Keywords Active magnetic bearings • Maglev • Analytical model • Numerical model • Experimental test • Active control

10.1 Introduction

Active Magnetic Bearings (AMB from now on) allow relative rotation between rotor and stator, without contact between parts. As a consequence the relative motion take place without friction. This important feature of the device makes it really interesting in industry applications, where high performance and high energy savings are required [3, 18, 20]. In fact, electromagnetic dissipations in AMB are orders of magnitude lower than dissipations due to friction in normal contact bearings. However this technology has not widespread yet, because of its design and production costs, which are much higher than ball bearings. Figure 10.1 shows a common AMB's structure. It's possible to notice the small clearance between the rotor and the shaft, of order of μm [4, 14]. This leads to a high active stiffness so, in order to damp vibrations, an external passive system is required. Aim of this research will be enlarging this clearance, in order to reach a 1 cm gap. This allows higher shaft movements, so that they can be actively damped in the bearings itself. This new AMB equipped with active vibration damping is shown by Fig. 10.2. It's possible to notice that the passive damping system has disappeared, included in the active control.

Before studying a 6 dof hovering shaft, an easier 1 dof model was built. In fact the system modelling is really hard, because of field's non-linearities, material hysteresis, leakage, fringing effects. In order to concentrate on all this effects, neglecting at first the complexity of an hovering rotor [8, 10, 13, 15], it was preferred to study a single dof system [1, 5, 7, 12, 16, 19, 21]. At first an analytical model was built (Sect. 10.2), relying on electromagnetic constitutive equations. Then a FEM analysis was launched (Sect. 10.3), and its results compared with the analytical model. By this comparison a new dynamic model was derived (Sect. 10.4), taking into account all the secondary effects previously mentioned. On the basis of this new model Active Control Logics were designed (Sect. 10.5). In order to validate this procedure, an experimental test-bench was built, and 1 dof test performance executed (Sect. 10.6). Results (Sect. 10.7) will show how this new way of building the model can guarantee much better performances, without higher computational costs.

F. Braghin • F. Castelli-Dezza • S. Ghiringhelli (✉)
Politecnico di Milano, Dipartimento di Meccanica, via La Masa 1, Milano, Italy
e-mail: stefano.ghiringhelli@polimi.it

E. Wee Sit (ed.), *Sensors and Instrumentation, Volume 5*, Conference Proceedings of the Society for Experimental Mechanics Series, DOI 10.1007/978-3-319-29859-7_10

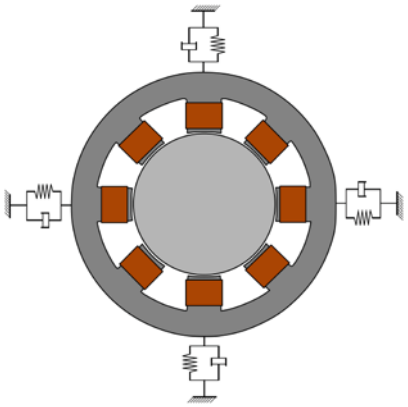

Fig. 10.1 Common structure of an AMB with an external passive damping vibration system

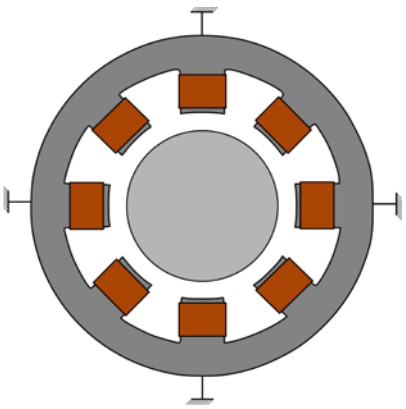

Fig. 10.2 New concept of AMB. The larger clearance allows the active vibration damping in the bearing itself

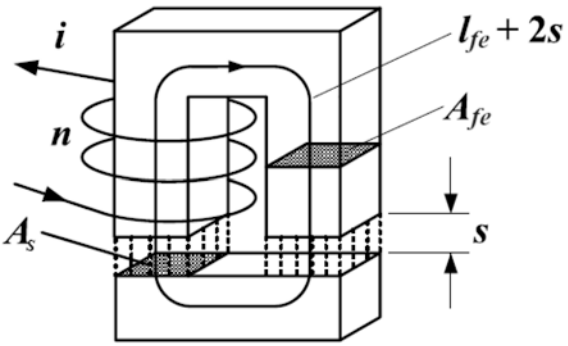

Fig. 10.3 Maglev, nomenclature

10.2 Analytical Model

We want to build the model of the system in Fig. 10.3. The two most important parameters that describe this system are the force and the auto-inductance. They can be computed starting from the magnetic energy stored in the field between the U core and the hovering mass [2, 25]:

$$W = \frac{1}{2} B H_s Vol_s = \frac{1}{2} B H_s A_s \times (2s) \tag{10.1}$$

The force is computed as the derivative of the magnetic field with respect to the displacement:

$$F = -\frac{\partial W}{\partial s} = -\frac{B^2 A_s}{\mu_0} \tag{10.2}$$

The force is always negative, which means attractive. From now on the *"minus"* in front of the force equation will be neglected. B is computed from the circulation law by Biot-Savart:

$$\oint_L \vec{H}\, d\vec{r} = \sum_k I = L_{fe}H_{fe} + 2L_sH_s = NI \tag{10.3}$$

where

$$B = \mu_0\mu_r H \tag{10.4}$$

and

$$B = \mu_0 \times \frac{NI}{\frac{l_{fe}}{\mu_r} + 2s} \tag{10.5}$$

This process leads to:

$$F(I,s) = \mu_0 A_s N^2 \frac{I^2}{\left(\frac{L_{fe}}{\mu_r} + 2s\right)^2} \tag{10.6}$$

In the same way:

$$L(I,s) = N\frac{\Phi}{I} = \frac{\mu_0 N^2 A_s}{\frac{L_{fe}}{\mu_r} + 2s} \tag{10.7}$$

These two parameters govern both the statics and the dynamics of the system. They are functions of s (clearance) and I (current). In order to get this results some hypothesis were assumed:

- linear relationship between B and H, neglecting the material hysteresis;
- flux fully enclosed in the ferromagnetic core, neglecting leakage, fringing effects.

In a more realistic contest, the behaviour of the system would appear like in Fig. 10.4. From Eq. (10.6) it's possible to notice the instability of the system [11]. In fact the force goes with inverse of the displacement. This means that if the hovering mass approaches to the U-core, the force increases, in contrast with the behaviour of a stable spring. Moreover the sign of the current has no influence at all, as it disappear with the square power. It's evident how the system is delicate, and in order to get good control performances it's required a reliable model. To proceed with this task a FEM analysis was done with the software Ansys Maxwell®.

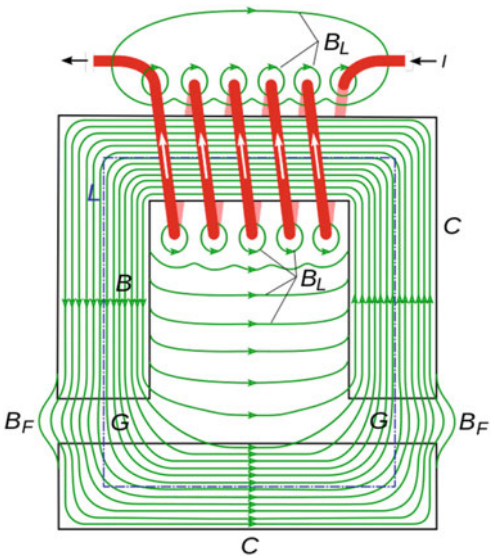

Fig. 10.4 Maglev, field distribution and secondary effects. B_L is the flux responsible for leakage, B_F causes fringing effects, C is the useful flux. L is the ideal line where in the analytical model the flux is supposed to be concentrated

10.3 Numerical vs Analytical Model

In Ansys Maxwell environment was built a single dof model, geometrically identical to the one used to derive the analytical one (ferromagnetic core section, electrical coil, etc.). Figure 10.5 shows it. Ansys Maxwell support a library of materials, and for this task an already present ferrite was used. This kind of material presents a magnetic permeability almost constant, so we can focus on the flux line of the field. A sensitivity analysis with respect to the current (I) and the clearance (s) was carried out. Figure 10.6 shows a first comparison between the behaviour of the analytical model versus the FEM one. It is obtained for a constant current, varying the clearance. It's possible to notice that the gap is much higher than the target of this research. This was done only to have a better understanding of the physics of the system. From an experimental point of view the gap was limited to 1 cm.

From this graphs three regions can be distinguished:

- **Small Gap Region** ($s << 1$ **mm):** the term $\frac{L_{fe}}{\mu_r}$ in Eq. (10.6) takes over, and as s decrease, the force reachs a flat region, as well for the inductance.
- **Nominal Gap Region** 1 **mm** $< s <$ 10 **mm:** between the different secondary effects, the fringing one takes over. This effect brings to an increase of the area where the flux insists. Both force and inductance are proportional to the flux area, so they are both higher than what was expected from the analytical model.
- **High Gap Region** $s >$ 10 **mm:** as s grows, the force suddenly goes to zero, and the inductance settles on a constant value. This behaviour is due to the fact that the hovering mass is too far from the ferromagnetic core, and the flux lines closes between the legs of the U-core, without touching the mass. This leads to a constant auto-inductance and a null force.

In order to follow the purpose of the research Fig. 10.7 shows the behaviour of the system in the gap of interest.

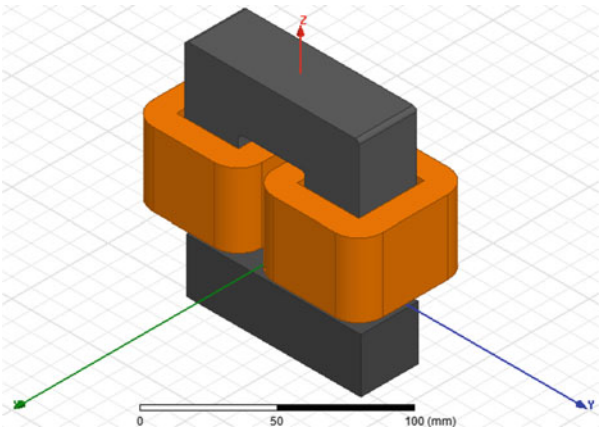

Fig. 10.5 Single dof maglev in Maxwell

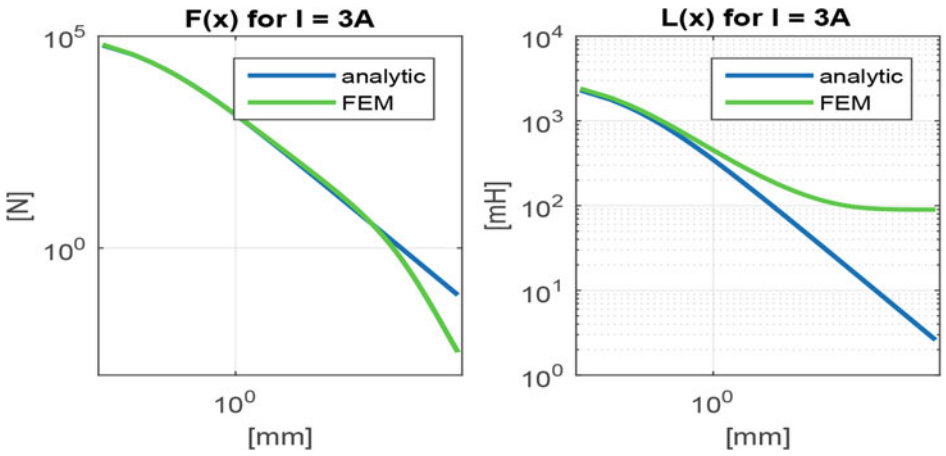

Fig. 10.6 Comparison between analytical and FEM model in a high range

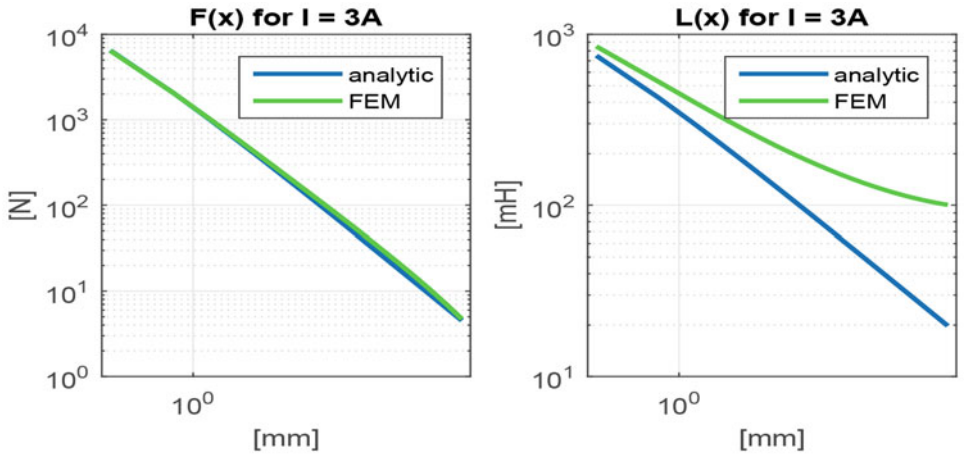

Fig. 10.7 Comparison between analytical and FEM model in the range of interest

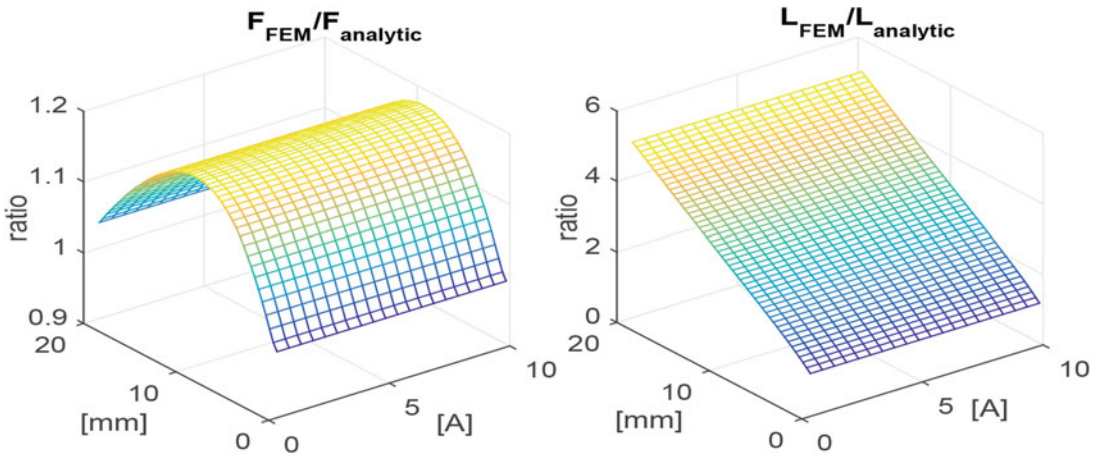

Fig. 10.8 Comparison between analytical and FEM model. Sensitivity analysis with respect to the gap and the current

It's clear that, although the force seems to be well-described by the analytical model, the FEM inductance is much higher than the analytical one. This causes the real system to be slower than how the analytical model describes it, causing serious problems to the active control. In order to complete the sensitivity analysis as function of both the gap and the current, Fig. 10.8 shows the evolution of the ratios $F_{FEM}/F_{analytic}$ and $L_{FEM}/L_{analytic}$.

It is possible to notice that both the ratios do not vary with the current I. This is due to the fact that both the analytical and FEM models consider a magnetic permeability μ constant. The behaviour of the two models grows different with the gap. Especially the ratio between the auto-inductance grows higher and higher as the gap increase.

To prevent bad performances, or even failure, of the active control, it was decided to introduce some coefficient to correct the behaviour of the analytical model. The idea is to describe the two ratios in Fig. 10.8 with a polynomial, function of the gap (as previously mentioned the current does not influence this analysis):

$$\begin{aligned} f_F(s) &= a_{F3}s^3 + a_{F2}s^2 + a_{F1}s + a_{F0} \\ f_L(s) &= a_{L3}s^3 + a_{L2}s^2 + a_{L1}s + a_{L0} \end{aligned} \tag{10.8}$$

It was decided to use third grade polynomial functions, because they offer a good trade off between computational costs and accuracy. a_{fi} and a_{li} are the coefficient found through interpolation. The following expression for the force and the auto-inductance are obtained:

$$\begin{aligned} F_{correct}(s, I) &= F_{analytic}(s, I) \times f_F(s) \\ L_{correct}(s, I) &= L_{analytic}(s, I) \times f_L(s) \end{aligned} \tag{10.9}$$

With these new functions that correctly describes the behaviour of the system in the whole range of interest it's possible to build a reliable dynamic model.

10.4 Complete Dynamic Model

The dynamics of the whole system is influenced both by the mechanical and electrical part. They can be written this way:

$$\begin{cases} m\ddot{x} + mg = F_c(x, i) \\ V = RI + \dfrac{d}{dt}\left[L_c(x)I\right] \end{cases} \tag{10.10}$$

where x is the displacement from the equilibrium position s_0 which is set equal to 10 mm. By substituting $F(x, I)$ and $L(x)$ it's possible to get the state-form expression of the system:

$$\begin{cases} \ddot{x} = -g + \dfrac{1}{m}F_c(x, i) \\ \dot{x} = \dot{x} \\ \dot{I} = \dfrac{1}{L_c(x)}\left\{V - \left[\dfrac{dL_c(x)}{dx}\dot{x} + R\right]I\right\} \end{cases} \tag{10.11}$$

The subscript *"c"* below F and L stands for *"correct"*, and refers to the Eq. (10.9). In order to have a complete control of the system, it must be possible to generate a two directions force. With this single Maglev it's impossible, because the force can be only attractive. It's necessary to introduce another ferromagnetic U-core in the opposite direction. This system leads to another set of equations, where also the *"inferior"* component of the Maglev appears. The equilibrium position will be in $x = 0$, where the distance ($\delta_0 = 10$ mm) of the hovering mass is the same from the upper ferromagnetic core and the lower. Inputs of the control will be the voltages V_{sup} and V_{inf}, aim of the control will be to keep $x = 0$. The state-form equations of the systems can be written this way:

$$\dot{\bar{x}} = [\mathcal{F}(\bar{x})] + [\mathcal{B}(\bar{x})] \times \bar{u} \tag{10.12}$$

10.5 Active Control

This paper present the differences between analytical and numerical model. So at the moment only linear controls where considered. Further readings will provide for a comparison between linear and non-linear controls [6, 17, 22–24]. First of all the system (10.12) is linearized, than both current and tension control were tested.

Current control is based on a PID logic, which treats the system like a SISO. However Fig. 10.9 shows a system with two inputs and one output. It's possible to bring this system back to a SISO with a mathematical transformations of coordinates:

$$\begin{aligned} I_{bias} &= \frac{I_{sup} + I_{inf}}{2} \\ I_{delta} &= \frac{I_{sup} - I_{inf}}{2} \end{aligned} \tag{10.13}$$

At the equilibrium position:

$$\begin{aligned} I_{sup0} &= I_{bias} + I_{delta0} \\ I_{inf0} &= I_{bias} - I_{delta0} \end{aligned} \tag{10.14}$$

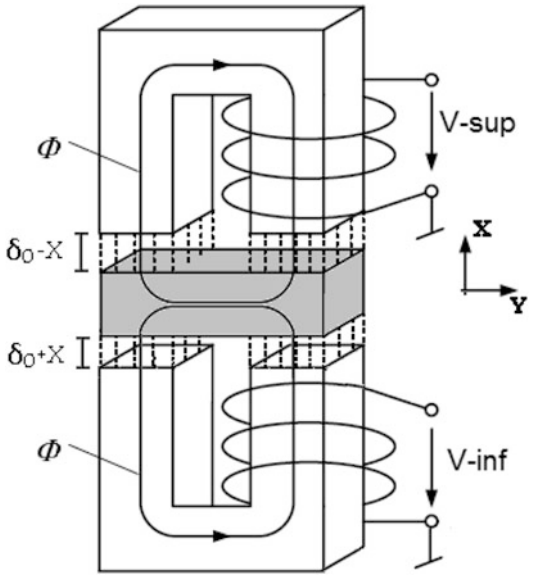

Fig. 10.9 Complete Maglev model

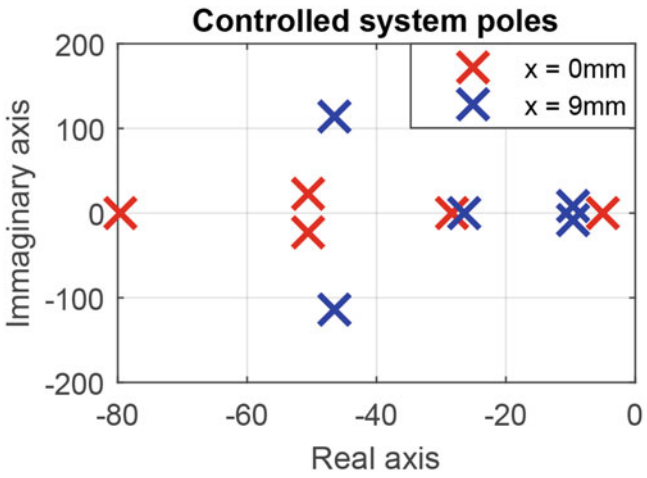

Fig. 10.10 Poles of the controlled system at the equilibrium and in $x = 9\,\text{mm}$

otherwise:

$$\begin{aligned} I_{sup,rif} &= I_{bias} + (I_{delta0} + \mathbf{I_{delta}}) \\ I_{inf,rif} &= I_{bias} - (I_{delta0} + \mathbf{I_{delta}}) \end{aligned} \tag{10.15}$$

where $\mathbf{I_{delta}}$ is the new single input we need to control. The PID itself is not able to stabilize the system and control its performances, so two loops are required. The first one, based on a Pole Placement algorithm, enable the pole stabilization, while a second external loop, based on a PI logic controls the performances. Also the two references for the coil's currents [Eq. (10.15)] needs to be controlled in feedback. So another inner current loop, which must be at least five times faster than the external position loops, controls the current of the coils. This design is really easy to use, and also robust against control failure and short-cut circuit. However, because of the high non-linearity and instability of the system, as soon as the hovering mass slightly moves from the equilibrium position, it's performances fall down, until the system is no more stable. An LQR logic is able to improve the behaviour of the system. First of all it consider it as a MIMO, so the currents become independent each other. Figure 10.10 shows the poles of the LQR controlled system, both at the equilibrium position ($x = 0\,\text{mm}$) and away from the equilibrium position ($x = 9\,\text{mm}$), but with the control always designed linearizing the system in $x = 0$. It's possible to notice that the systems, although the performances get worst, remains stable. This feature make this control appealing to be tested on an experimental test-bench. A brief discussion is necessary for what concerns saturations. In fact each U-core generate an attractive force, independent of the sign of the current. However the linear control, based on a linearization can't

discern this physical problem. There may be operation condition which would require negative currents, if the system was linear. But the system is not linear, so the current should be saturated to a positive region. In the PID current control this is straightforward. It's just required the saturation of the current references. While for what concerns the tension control, if we want to exploit both positive and negative voltage, preventing the current from becoming negative, some further conditions are necessaries:

- Se $V > 0$ & $I > I_{minimum} \rightarrow V_{sat} = V$;
- Se $V > 0$ & $I < I_{minimum} \rightarrow V_{sat} = V$;
- Se $V < 0$ & $I > I_{minimum} \rightarrow V_{sat} = V$;
- Se $V < 0$ & $I < I_{minimum} \rightarrow V_{sat} = 0$;

The choice of $I_{minimum}$ is arbitrary, it depends on the velocity of the loop. Of course it would be easier to saturate the voltage from 0 to V_{max}. This conditions wouldn't allow to use the negative voltage, and would slow down the control.

10.6 Experimental Tests

Experimental tests were made to proof the reliability of the mixed analytical and numerical model, with respect to the analytical one. Two kind of controllers were designed. One based on the simple analytical model, while the second based on the model corrected through FEM coefficients. Both the controllers were designed with the LQR method, which is based on two matrices, R and Q, which weight the contribution or the importance of the state variables and input variables. In both designs R and Q were kept constant, so that the only difference in the controller is due to the model. The test-bench was built such that it's geometry and characteristics were identical to the model. This had been a really hard task, and actually the model was reviewed in order to make it equal to the test-bench itself. The material used during the experiments was the following:

- Ferrite: the ferromagnetic core is composed of N87 ferrite, with $\mu_r = 1900$;
- Current coils: two 430 turns coil per each core (so that each core has 860 turns) obtained with enamelled copper wire with external diameter equal to $\Phi_{ext} = 1.12$ mm, internal diameter $\Phi_{int} = 1.06$ mm;
- Control board: dsPICDEM MCLV-2 development board (Microchip);
- Power unit: embedded on the board limited to 48 V and 15 A;
- Inductive position sensors with range from 0 to 15 mm;
- PicKit3 programmer for data exchange between pc and board;
- Continuous power supply unit (60 V–20 A) for the power unit;
- Plug-In power supply 24 V–0.75 A for the control circuit.

Figure 10.11 shows how the ferromagnetic core with the coils appears. The two coils are connected in series, such that the generated field has the same direction.

The final test-bench appear to be like in Fig. 10.12. The paper scotch-tape does not affect the magnetic field. There are two ferrite I-core, first of all to be sure that the magnetic field of the upper and lower cores are decoupled, than for ease of mounting. The aluminium transverse beam (length greater than 1 m), would allow a small rotation around its inch, which, in a field of small displacement ($x_{max} = 20$ mm) let the hovering mass move only vertically.

Unfortunately the spanning range of the sensor was not large enough to reach our target (20 mm of maximum displacement), so we restricted it to 14 mm, with a nominal gap of $\delta_0 = 7$ mm. A sort of paper-touchdown bearing was

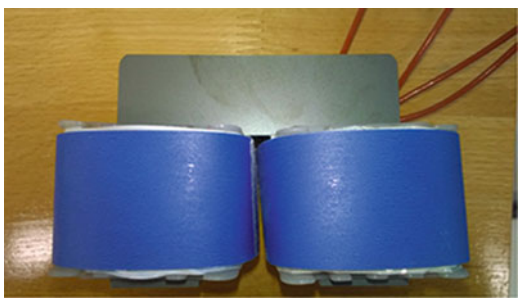

Fig. 10.11 Ferromagnetic core, dimensions

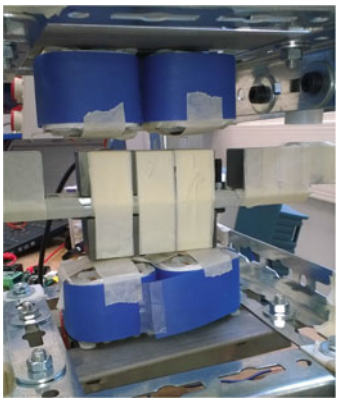

Fig. 10.12 Maglev, test-bench

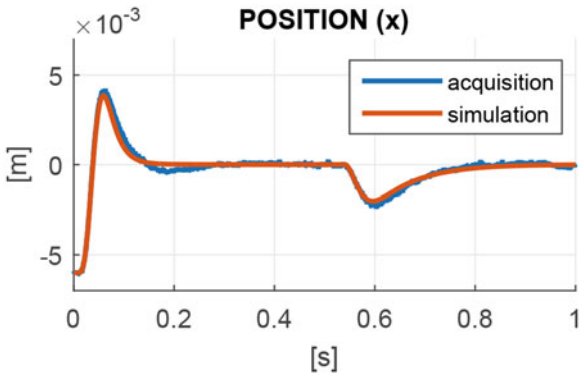

Fig. 10.13 Comparison between Maglev test-bench behaviour and a numerical simulation. The model and control of the system is based on the corrected analytical model

introduced, in order to avoid dangerous contact between U and I-cores. The thickness of this paper is almost 1 mm, so the free-motion range of the hovering mass is reduced to 12 mm ($x_{max} = \pm 6$).

10.7 Results and Conclusions

Results will show the behaviour of the test-bench in Fig. 10.12 with two kind of controls applied [9]. Both are based on an LQR logic, both have the same weight matrices, but the first is designed on the simple analytical model, while the second is based on the analytical model corrected through the FEM coefficients.

Figure 10.13 shows the behaviour of the system controlled with the correct-analytical model controller design. The motion of the real system is compared to the evolution of a numerical simulation, carried out in Simulink, Matlab. It's possible to notice the almost perfect correlation between the behaviour of the two systems.

The acquisition is noisier than the simulation because of electrical noise coming from sensor, power supply, etc. The system is asked to swing up (from $t = 0$ to $t = 0.15$ s) and face an external disturb, which in this case was a sudden increment in its mass (at $t = 0.55$ s). It's possible to see that the system is always stabilized around the equilibrium position ($x = 0$).

Figure 10.14 shows the comparison between the behaviour of the simple analytical model, and the test-bench controlled via the analytical-model based control.

It's possible to notice that the controller isn't even able to stabilize the real system.

We have seen how an improvement in the model used to design the control can lead to a strong improvement in the behaviour of the physical system. The model was improved through a FEM analysis and an addition of polynomial functions to correct the trend of force and auto-inductance. It's clear how this procedure could improve the behaviour of a 6 dof system, or would be even necessary to guarantee stability in case of large gap, of order 10 mm.

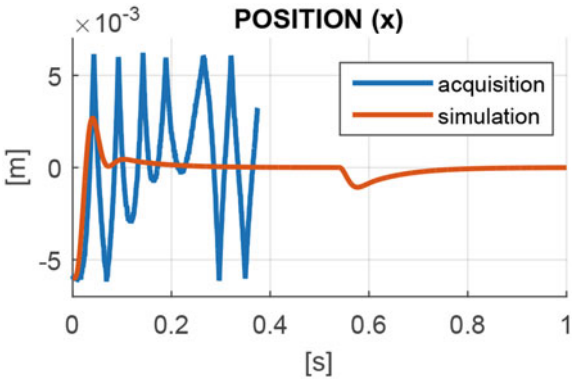

Fig. 10.14 Comparison between Maglev test-bench behaviour and a numerical simulation. The model and control of the system is based on the simple analytical model

References

1. Al-Muthairi, N.F., Zribi, M.: Sliding mode control of a magnetic levitation system, Math. Probl. Eng. 93–107 (2004)
2. Bleuler, H.: A survey of magnetic levitation and magnetic bearing types. JSME Int. J. Ser. 3 Vib. Control Eng. Eng. Ind. **35**, 335–342 (1992)
3. Bleuler, H.: Overview on various types of AMBs and their respective potential for applications. In: 14th International Symposium on Magnetic Bearings (2014)
4. Bleuler, H., et al.: In: Swhweitzer, G., Maslen, E. (eds.). Magnetic Bearings: Theory, Design and Applications to Rotating Machinery. Springer, Berlin (2009)
5. Bohagen, B.: Magnetic Levitation, Norwegian University of Science and Technology (2003)
6. Bolzern, P., Scattolini, R., Schiavoni, N.: Fondamenti di controlli automatici. McGraw-Hill, New York, NY (2008)
7. Braghin, F.: Appunti del corso: Sistemi meccatronici e laboratorio A, Politecnico di Milano (2014)
8. Chiba, A., Fukao, T., Ichikawa, O., Oshima, M., Takemoto, M., Dorrell, D.: Magnetic Bearings and Bearingless Drives. Elsevier, Amsterdam (2005)
9. di Milano, P.: Modello e Controllo di Cuscinetti Magnetici Attivi ad Elevato Traferro, Politecnico, University of di Milano. Mechanical Engineering thesis, Mattia Fornoni (2014)
10. Diana, G., Cheli, F.: Dinamica dei sistemi meccanici, vol. 2. Polipress, Assago (2010)
11. Earnshaw: On the nature of molecular forces which regulate the constitution of lumiferous ether. Trans. Cambridge Philos. Soc. **7**, 97–112 (1842)
12. Fornoni, M., Castelli-Dezza, F.: Cuscinetti a Levitazione Magnetica (2013)
13. Gerami, A., Allaire, P., Fittro, R.: Modeling and control of magnetic bearings with nonlinear magnetization. In: 14th International Symposium on Magnetic Bearings (2014)
14. Gerhard, S.: Active magnetic bearings-chances and limitations. International Centre for Magnetic Bearings, ETH Zurich (2006)
15. Giorgio, D., Cheli, F.: Dinamica dei sistemi meccanici, Politecnico di Milano, vol. 1 (2010)
16. Hossain, S.: Design of a Robust Controller for a Magnetic Levitation System, Graduate Student (ECE), Wichita State University
17. Isidori, A.: Nonlinear Control System. Springer, New York (2000)
18. Knospe, C.R.: Active magnetic bearings for machining applications. Control Eng. Pract. 307–313 (2007)
19. Liu, G., Chen, Y.: Levitation force analysis of medium and low speed maglev vehicles. J. Mod. Transp. 93–97 (2012)
20. Repcic, N., Saric, I., Muminovic, A.: Opportunities to improve production using active magnetic bearing systems. In: 15th International Research/Expert Conference, "Trends in the Development of Machinery and Associated Technology" (2011)
21. Shameli, E., Behrad Khamesee, M., Paul Huissoon, J.: Real-time control of a magnetic levitation device based on instantaneous modeling of magnetic field. Mechatron. J. 536–544 (2008)
22. Smirnov, A., Jastrzebski, R., Hynynen, K., Pyrhonen, O.: Comparison of suboptimal control method in magnetic levitation system, pp. 1–10, 2-6 Sept. 2013
23. Yang, Z.-J., Tateishi, M.: Adaptive robust nonlinear control of a magnetic levitation system. Autom. J. 1125–1131 (2001)
24. Yin, L., Zhao, L.: Nonlinear control for a large air gap magnetic bearing system. In: Transactions, SMiRT 19, Toronto, August 2007 (2007)
25. Yoon, S.Y., et al.: Control of Surge in Centrifugal Compressor. Springer, Berlin (2013)

Chapter 11
Blind Identification of Operational Deflection Shapes from Continuous Scanning Laser Doppler Vibrometry Data

L. Mignanelli, P. Chiariotti, P. Castellini, and M. Martarelli

Abstract Continuous Scanning Laser Doppler Vibrometry (CSLDV) is a well known technique that makes it possible to extract the Operational Deflection Shapes (ODSs) of a vibrating structure in a very fast and efficient way. The spatial evolution of the ODS with respect to the scanned path determines an amplitude modulation effect on CSLDV vibration data: this effect causes the presence of sidebands with respect to the ODS resonance frequency (central frequency) spaced by integer multiple of the scanning frequency used to sweep the laser spot over the target. However, depending on the structure under analysis and on the testing condition, the spectrum measured might present unclear patterns of sidebands, therefore an extraction of ODSs using a standard peak peaking approach can provide erroneous results. This paper aims at presenting a blind approach for recovery ODSs in these challenging situations. The algorithm is based on the solution, in least square sense, of a set of linear equation defining the relations between the contributions of each cluster of frequencies (central frequency + sidebands) potentially defining the spectral pattern of a certain ODS to the complex spectrum measured. Results on a virtual experiment involving a cantilever beam having its first three modes within a very narrow bandwidth (3 Hz) are presented and discussed.

Keywords Laser Doppler vibrometry • Continuous scanning laser Doppler vibrometry • Close modes • Vibration testing • Operational deflection shapes recovery

11.1 Introduction

In recent years, Continuous Scanning Laser Doppler Vibrometry (CSLDV) has demonstrated to be a very versatile and powerful technique for recovering Operational Deflection Shapes (ODSs) of vibrating objects. It found application not only in the mechanical sector, i.e. vibro-acoustics [1], damage detection [2], rotor dynamics [3, 4] but also in the biomedical field [5] or in landmine detection [6].

The concept of CSLDV was originally presented by Sriram et al. [7], but the main development of this measurement technique is due to Stanbridge et al. [8, 9], who proposed a method to extract ODSs from LDV output time history by exploiting the amplitude modulation effect induced by the ODSs themselves.

In CSLDV the laser spot is continuously moved over the target surface while acquiring vibration data: this makes it possible to collect time and spatial data simultaneously using a spatial resolution that depends on the sampling frequency used to collect data. Originally, CSLDV was applied to structures vibrating at a single frequency and therefore the output time history was modulated by a unique ODS. The related spectrum has the characteristic profile with peaks at the excitation frequency and at the sidebands spaced by the laser beam scanning frequency. The number of sidebands is equal to the order of the polynomial representing the ODS. The spectrum amplitude and phase at the excitation frequency and its sidebands can be exploited to recover the amplitude and phase of the ODS, thus requiring that sidebands peaks are easily distinguished, and this limits the application in more complex vibration scenarios.

L. Mignanelli
TU Clausthal, Leibnizstraße 28, 38678 Clausthal-Zellerfeld, Germany

P. Chiariotti • P. Castellini (✉)
Università Politecnica delle Marche, via Brecce Bianche, 60131 Ancona, Italy
e-mail: p.castellini@univpm.it

M. Martarelli
Università degli Studi e-Campus, via Isimbardi, Novedrate (CO), Italy

E. Wee Sit (ed.), *Sensors and Instrumentation, Volume 5*, Conference Proceedings of the Society for Experimental Mechanics Series, DOI 10.1007/978-3-319-29859-7_11

Several authors extended the applicability of the method to non-purely sinusoidal excitations. Impact hammer, [10], and random tests, [11], have been performed but only to low damped structures with low modal density. Nevertheless, laser's scanning frequency has to be carefully selected in order to avoid sideband's superposition.

Alternative CSLDV processing methods have been developed, as the "lifting" approach proposed by Allen [12–14] that exploits high scanning rates to rearrange data collected at each point along the scan path as they were measured in Discrete Scanning mode.

In this paper, a blind approach for the extraction of the CSLDV characteristic spectrum, called in the following sideband spectrum, is proposed. The processing bases on the hypothesis that an ODS can be modelled by a polynomial whose coefficients are directly related to the sidebands that characterise the vibration spectrum of the CSLDV signal, as proposed by Stanbridge, Martarelli and Ewins is proposed. Conventionally, the recognition of resonance frequencies and the recovery of ODSs in the processing of CSLDV data are performed starting from the observation of the CSLDV output spectrum. Some alternative extraction methods have been proposed in the past [15, 16].

The proposed method exploits the mathematical representation of sidebands and their superposition to extract amplitude and phase at each frequency of the sideband spectrum. The technique has been demonstrated for a line scan, but the extension to area scan is straightforward.

11.2 Material and Method

11.2.1 Description of the Algorithm

During a CSLDV measurement, the laser beam scans the surface at a frequency $\omega_{scan}/2\pi$. The velocity signal thus recorded results in an amplitude modulated signal whose modulating frequency is the scan frequency adopted. A CSLDV characteristic spectrum will therefore show sidebands, apart from the excitation frequency, at

$$\omega_{excited} + l \cdot \omega_{scan}, \qquad l = -m, \ldots, m, \qquad m \in \mathbb{N} \tag{11.1}$$

If only one frequency is excited, the identification of the amplitudes of the central frequency and of its sidebands are easily detectable. However, when more than one characteristic frequency of the structure is excited, there will be a cluster of sidebands for each one of such frequencies. It might happen that some sidebands will superimpose each other: this could be the case, for instance, when two structural resonances are close to each other (Fig. 11.1). Whenever this happens, the resulting spectrum will show as the summation of the complex contributions of each spectrum (real and imaginary parts) and the sideband pattern, which typically define the Operational Deflection Shape (ODS) that is taking place at a certain resonance frequency, messes up and cannot make it possible to recover the ODS properly. Figure 11.1 reports the problem formulation in terms of amplitude contributions, but the extension to the complex case is straightforward. The aim of the algorithm proposed in this paper is to separate the contribution of each cluster of frequencies (central frequency and related sidebands) and therefore to allow a correct recovery of ODSs. This results in a complete blind processing of CSLDV data, that also overcomes the method presented in [17, 18].

The problem, for a single scan frequency combination, can be formulated as a linear system (11.2)

$$A_s X = B_s \tag{11.2}$$

where B_s is a vector representing the complex spectrum (estimated over n spectral lines) of the CSLDV vibration velocity signal (each row element b_k corresponds to a spectral line), X is the matrix of unknowns and A_s is a coefficient matrix. Matrices X and A_s are block matrices defined as in (11.3) and (11.4), where m represents the number of sidebands taken into account for the complete set of ODSs considered and therefore the polynomial order of the ODSs themselves.

$$\begin{cases} X = (X_h) & h = 1, \ldots, n \\ x_{h+l} \in X_h & l = -m, \ldots, m \end{cases} \tag{11.3}$$

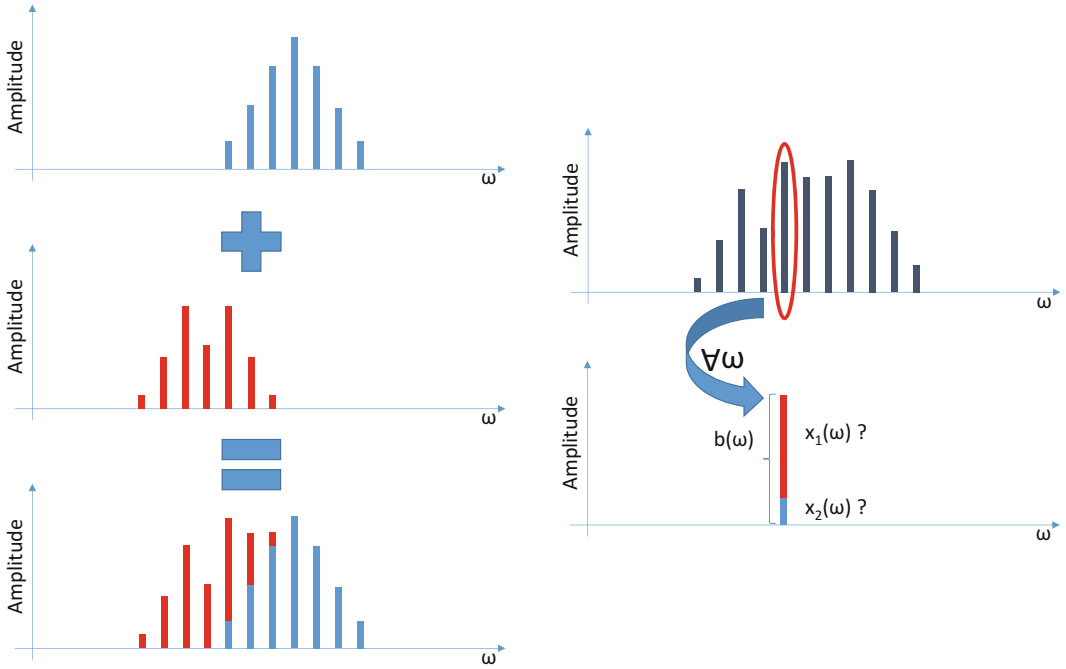

Spectrum synthesis during the experiment Equations preparation from the experiment

Fig. 11.1 Spectrum obtained during the experiment and equation system preparation

$$\begin{cases} A_s = \left(A_{s,\alpha\beta}\right) & \alpha = 1,\ldots,n, \quad \beta = 1,\ldots,2m+1 \\ & \left(\alpha_{ij}\right)_{s,\alpha\beta} \in A_{s,\alpha\beta} \\ & \left(\alpha_{ij}\right)_{s,\alpha\beta} = \begin{cases} 1 \; if \; \omega_k = \omega_{h+l} \\ 0 \quad otherwise \end{cases} \end{cases} \tag{11.4}$$

In order to solve for $x_{s,h+l}$ it is important to consider multiple scan frequencies (n_s). This implies to reformulate the problem in (11.2) as a block matrices system (11.5).

$$\begin{cases} AX = B \\ A = (A_s) \quad s = 1,\ldots,n_s \\ B = (B_s) \end{cases} \tag{11.5}$$

Such system can then be solved in a least square sense, thus obtaining the coefficients of each cluster of frequencies (central frequency and related sidebands) that are needed to identify the related ODS. Indeed, once such coefficients are estimated in least square sense, the ODS can be recovered exploiting the classical polynomial approach proposed by Stanbridge et al. in [8, 9].

11.2.2 Virtual Experiment

A numerical model was developed to generate synthetic CSLDV data reproducing a virtual test on a cantilever beam (Fig. 11.2). The choice to perform such virtual experiment was related to the higher degrees of freedom in changing the test conditions, as for instance in modifying modes parameters (amplitudes, frequencies, damping), in simulating different experimental parameters (scanning frequency) and in verifying the influence of different Signal-to-Noise Ratios (SNRs). In such a way, a sensitivity analysis (which is not reported in this paper) can be performed under more controlled conditions.

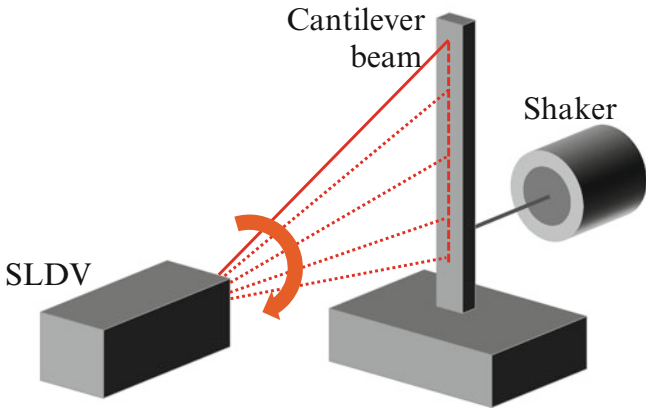

Fig. 11.2 Scheme of the virtual experiment simulated

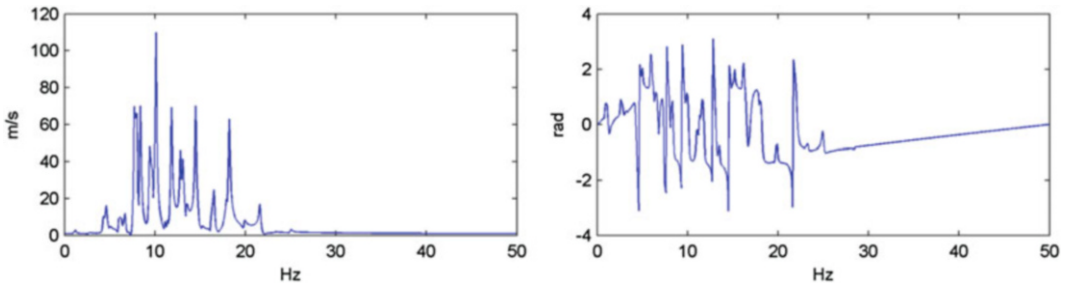

Fig. 11.3 Simulated CSLDV output spectrum: amplitude (*left*) and phase (*right*) data

For a cantilever beam, mode shapes can be calculated analytically [19], as a function of the distance to the constraint, using (11.6)

$$X_i(x) = \left[cosh\left(\lambda_i \frac{x}{L}\right) - cos\left(\lambda_i \frac{x}{L}\right)\right] - \sigma_i \left[sinh\left(\lambda_i \frac{x}{L}\right) - sin\left(\lambda_i \frac{x}{L}\right)\right] \tag{11.6}$$

where:

x is the coordinate position along the beam length L

λ_i, σ_i are the non-dimensional frequency amplitude parameters.

Mode shapes thus obtained can be exploited to simulate both step scan and continuous scan vibration data.

11.3 Results

A multi-sine excitation test has been simulated. The excitation frequencies considered, 10 Hz, 11 Hz and 13 Hz, corresponds to the virtual resonance frequencies of the first three modes of the beam. The related mode shapes have been calculated using (11.6). The CSLDV output spectrum obtained when the laser beam virtually scans over a straight line along the beam at the frequency of 1 Hz is shown in Fig. 11.3. The overlapping of the sidebands belonging to the three different clusters (one for each mode involved) is evident and the characteristic sideband spectral patterns at the different central frequencies are unrecognizable. A classical peak peaking approach would not make it possible a correct estimation of the ODSs excited.

However, the approach presented in Sect. 11.2.1 managed to recover properly the three ODSs. This is clear when looking at Fig. 11.4, where the ODSs obtained from the virtual continuous scan test are compared with the ODSs extracted from a simulated step scan test, the latter constituting the reference test.

The mismatch between the ODSs recovered from the CSLDV approach and those extracted from the reference method (step scan) is due to numerical errors taking place in the least square solution. These errors result in an erroneous estimation

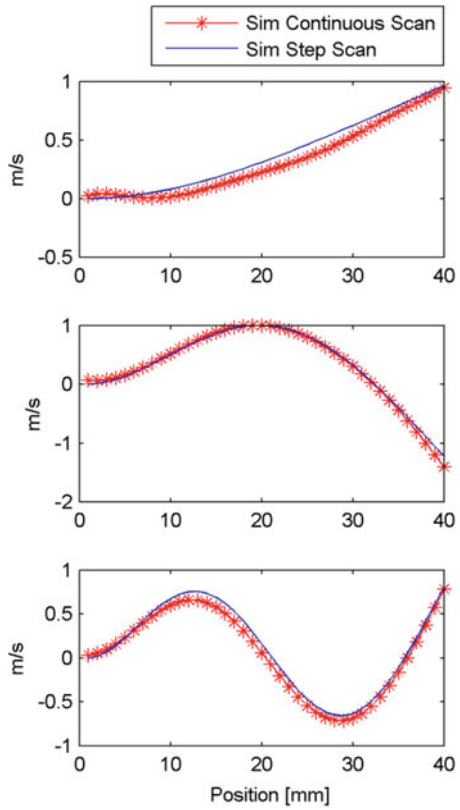

Fig. 11.4 ODSs extracted from the virtual multi-sine excitation test: comparison between simulated CSLDV and step scan (reference) results

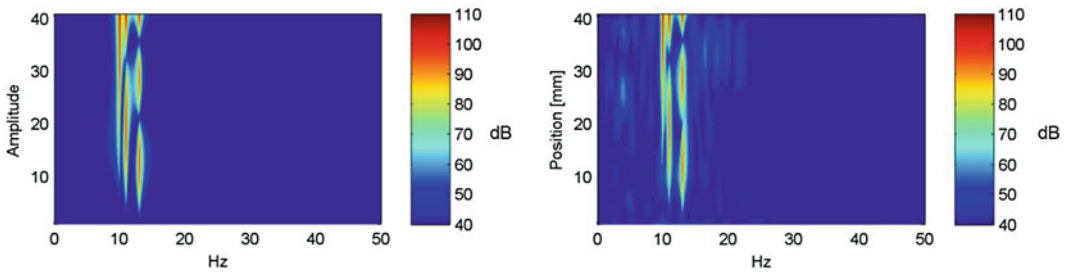

Fig. 11.5 ODSs amplitude matrix plotted in terms of frequency and spatial position: virtual step scan (*left*) and continuous scan (*right*) recovered data

of some contributions at certain frequencies, as it clearly noticeable in Fig. 11.5 where the plot of the complete matrix of spectral amplitudes at each frequency and at each spatial position is illustrated for both the virtual step scan (Fig. 11.5-left) and continuous scan (Fig. 11.5-right) experiments. The same effect is even more visible in Fig. 11.6, where the spectra averaged over the measurement positions are reported.

11.4 Conclusions

The paper has presented an approach to blindly process CSLDV vibration data. The method aims at overcoming the limits that characterize CSLDV, in the polynomial approach formulation, when the spectrum of the structure under test does not present clear patterns of sideband. Such condition can take place, for instance, when the target structure presents close modes or very noisy data. In such conditions, the sideband patterns can overlap or can be masked by noise, therefore reducing the possibility of reconstructing ODSs correctly. The methods is based on the hypothesis that the pattern of the cluster of frequencies (central frequencies + sidebands) identifying a certain ODS does not change with the scan frequencies. This means that the contribution of each sideband to the cluster, and of course the central frequency, are invariant to the scan frequency and only depend on the spatial evolution of the ODS causing the amplitude modulation on the CSLDV signal. The

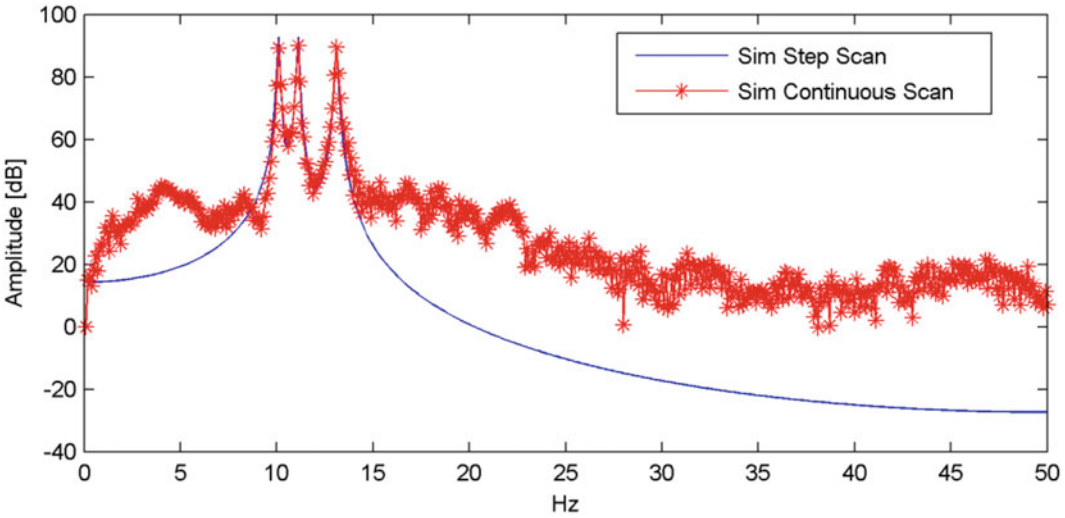

Fig. 11.6 Spatial average spectra obtained from the virtual step scan (*left*) and continuous scan (*right*) recovered data

method has been tested on a virtual test reproducing a cantilever beam presenting three modes in the range 10–13 Hz. The approach shows promising capabilities in reconstructing correctly the ODSs of the structure in such a challenging virtual set-up. Further tests on real test cases and a sensitivity analysis will be presented in future works.

References

1. Chiariotti, M., Martarelli, M., Revel, G.M.: Exploiting continuous scanning laser Doppler vibrometry (CSLDV) in time domain correlation methods for noise source identification. Meas. Sci. Technol. **25**(7), 075204 (2014)
2. Chiariotti, P., Revel, G.M., Martarelli, M.: Exploiting Continuous Scanning Laser Doppler Vibrometry and Wavelet Processing for Damage Detection, Experimental Techniques, Rotating Machinery and Acoustics, vol. 8, pp. 189–196. Springer International Publishing, Cham, Switzerland (2015)
3. Martarelli, M., Castellini, P., Santolini, C., Tomasini, E.P.: Laser Doppler vibrometry on rotating structures in coast-down: resonance frequencies and operational deflection shape characterization. Meas. Sci. Technol. **22**, 115106 (2011)
4. Martarelli, M., Castellini, P.: Performance analysis of continuous tracking laser Doppler vibrometry applied to rotating structures in coast-down. Meas. Sci. Technol. **23**, 065202 (2012)
5. Salman, M., Sabra, K.G.: Synchronized vibrations measurements at multiple locations using a single continuously scanning laser Doppler vibrometer. Applications to non-contact sensing of human body vibrations. J. Acoust. Soc. Am. **130**(4), 2394–2394 (2011)
6. Aranchuk, V., Lal, A.K., Zhang, H.C., Hess, F., Sabatier, J.M.: Acoustic sensor for landmine detection using a continuously scanning multi-beam LDV. Proceedings of the SPIE, vol. 5415, p. 61. Orlando (2004)
7. Sriram, P., Craig, J.I., Hanagud, S.: Scanning Laser Doppler vibrometer for modal testing. Int. J. Anal. Exp. Modal Anal. **5**, 155–167 (1990)
8. Stanbridge, A.B., Martarelli, M., Ewins, D.J.: Measuring area mode shapes with a scanning laser Doppler vibrometer. Proceedings of the International Modal Analysis Conference - IMAC XVII, pp. 980–985 (1999)
9. Stanbridge, A.B., Martarelli, M., Ewins, D.J.: Measuring area vibration mode shapes with a continuous-scan LDV. Meas. J. Int. Meas. Confederation **35**, 181–189 (2004). 2
10. Stanbridge, A.B., Martarelli, M., Ewins, D.J.: The scanning laser Doppler vibrometer applied to impact modal testing. Proceedings of 17th International Modal Analysis Conference (IMAC XVII), Orlando (1999)
11. Vanlanduit, S., Guillaume, P., Schoukens, J.: Broadband vibration measurements using a continuously scanning laser vibrometer. Meas. Sci. Technol. **13**(10), 1574–1582 (2002)
12. Allen, M.S., Sracic, M.W.: Mass normalized mode shapes using impact excitation and continuous-scan laser Doppler Vibrometry. In: Italian Association of Laser Velocimetry and non-Invasive Diagnostics, Ancona, Italy (2008)
13. Allen, M.S., Sracic, M.W.: A method for generating Pseudo Single-Point FRFs from Continuous Scan Laser Vibrometer Measurements. 26th International Modal Analysis Conference (IMAC XXVI), Orlando, Florida (2008)
14. Allen, M.S.: Continuous-scan vibrometry technique for broadband vibration measurements with high spatial detail. J. Acoust. Soc. Am. **126**(4), 2255–2255 (2009)
15. Chiariotti, P., Castellini, P., Martarelli, M.: Frequency domain mode matching of continuous scanning Laser Doppler vibrometer. XXXII IMAC conference, Orlando (2014)
16. Castellini, P., Chiariotti, P., Martarelli, M.: Mode filtering of continuous scanning Laser Doppler vibration data, special topics in structural dynamics, vol. 6: Proceedings of the 31st IMAC, A Conference on Structural Dynamics (2013) Conference Proceedings of the Society for Experimental Mechanics Series 43

17. Castellini, P., Chiariotti, P., Martarelli, M.: Mode filtering of continuous scanning Laser Doppler vibration data. Proceedings of the IMAC XXXI -International Modal Analysis Conference, Hyatt Regency Orange County, Garden Grove, California, USA, 11–14 February 2013
18. PChiariotti, P., Castellini, P., Martarelli, M.: Recovery of mode shapes from continuous scanning Laser Doppler vibration data: a mode matching frequency domain approach. Proceedings of the IMAC XXXII – International Modal Analysis Conference, Orlando, Florida, USA, 3–6 February 2014
19. Blevins, R.D.: Formulas for natural frequency and mode shape. Van Nostrand Reinhold Co., New York (1979)

Chapter 12
Digital Image Correlation for Timing Belts Dynamic Characterization: Potentials and Critical Aspects

P. Castellini, P. Chiariotti, M. Martarelli, and E. P. Tomasini

Abstract Characterizing the dynamic behaviour of timing belt represents a challenge among the engineering community. Even though there exists several numerical methods to predict the dynamics of these systems, the tuning of such models by experimental approaches still represents an issue. Indeed, an accurate characterization does require a measurement in operative condition since the belt mounting condition might severely affect its dynamic behaviour. Moreover, since the belt is moving, non-contact measurement methods are needed. In such context, Laser Doppler Vibrometry (LDV) and imaging techniques do represent valid candidates for such purpose.

This paper aims at describing the use of Digital Image Correlation (DIC) for the extraction of timing belts out-of-plane vibration and the recovery of Operational Deflection Shapes (ODSs). Results are compared with vibration data obtained by measuring on a moving belt with a standard LDV scanning, in step-scanning mode, over a grid points on the belt surface.

Keywords Digital image correlation • Laser Doppler vibrometry • Timing belts • Vibration analysis • Folded optics

12.1 Introduction

Timing belts belong to the synchronous drive category and therefore they can transmit large torques, withstand large acceleration and give the designer great layout flexibility, since the transmission components can be placed at large distance without paying a price penalty. This is true also in Internal Combustion (IC) engines, where the main use of timing belts is in synchronising the camshaft (governing the opening and closing of valves) to the crankshaft. When compared to chains and gears, timing belts present indeed better properties: they do not require lubrication, they are lighter and quieter (the composite rubber material they are made of does imply higher damping levels than in chains/gears). However, durability represents one of the main drawback of such systems. Indeed, the dynamic behaviour of the belt affects its durability: unwanted resonances of the belt that might occur during engine run-up or coast-down operations decrease the belt life and introduce vibration and noise phenomena.

Identifying a measurement technique that makes it possible an accurate and efficient measurement of the dynamic behaviour of the belt in operating conditions thus represents a useful tool for analysing the performances of the timing belt itself and of the whole transmission line.

Scanning Laser Doppler Vibrometry (SLDV) represents for sure a valid technique for tackling the belt dynamic characterization issue. This has been proved, over the years, by several researchers. Di Sante et al. [1, 2] were among the first addressing SLDV as a useful tool for assessing the dynamics of timing belt, even though they were more interested in showing the noise phenomena related to the belt vibration (at the timing belt meshing frequency) rather than on extracting Operational Deflection Shapes (ODSs) under the influence of whole body translation at constant speed. The latter subject was deeply analysed by Martin and Rothberg [3], who also further analysed the concept of pseudo-vibrations introduced by Rothberg et al. in [4] to address vibrations due to speckle pattern changes.

The progress in image-based measurement techniques has increased the interest of the scientific community in trying to use such methods in more and more challenging task. Among other approaches, Digital Image Correlation (DIC) [5, 6], does represent an appealing technique for estimating 2D and 3D displacements (and from that, for instance, velocity, deformation and strain) by analysing the changes of certain features on the images recorded. During the last decade, with the increased

P. Castellini (✉) • P. Chiariotti • E.P. Tomasini
Università Politecnica delle Marche, via Brecce Bianche, 60131 Ancona, Italy
e-mail: p.castellini@univpm.it

M. Martarelli
Università degli Studi e-Campus, via Isimbardi, Novedrate (CO), Italy

E. Wee Sit (ed.), *Sensors and Instrumentation, Volume 5*, Conference Proceedings of the Society for Experimental Mechanics Series, DOI 10.1007/978-3-319-29859-7_12

performances of recording cameras (frame rate and resolution), DIC has raised interest in the vibration field, especially for the reconstruction of Operational Deflection Shapes (ODSs) and Frequency Response Functions (FRFs). An example of such is reported in [7] and [8] where authors exploited 3D DIC on fan and turbine blades for the estimation of ODSs and FRFs and compared results thus obtained with data gathered from standard acceleration and LDV-based measurements. A 3D DIC system was also exploited in [9] to determine shape-descriptor frequency response functions of the field response of a complex-shaped object as a car bonnet. Dynamic point tracking using DIC has also been successfully demonstrated in [10], where operational modal analysis of helicopter rotors was conducted. In [11] a further step forward has been made by applying three dimensional point tracking (3DPT) and stereophotogrammetry to the rotor of a Robinson R44 helicopter.

This paper represents a feasibility study to understand the potentials and the critical aspects of using DIC for measuring span vibration, i.e. out-of-plane ODSs, of timing belts in running condition. The paper is organised as follows: the test bench and its experimental characterisation in controlled conditions (impact hammer test) are presented in Sect. 12.2; Sect. 12.3 will describe the DIC experimental set-up used and the processing approach adopted; Sect. 12.4 will discuss the main results obtained. The main conclusions of the work are reported in Sect. 12.5.

12.2 Test Bench

12.2.1 Experimental Test Bench

The object under test is a timing belt for distribution driveline of IC engines. The timing belt investigated synchronizes the rotation of the crankshaft and the camshaft of a 4-cylinder engine head, fully equipped with four valves per cylinder and springs. An electrical motor drives the crankshaft and is controlled by an inverter in order to select the desired speed or speed profile for run-ups or coast-down tests. In this work, the vibration of the belt was measured in operating conditions at three camshaft constant speed, as reported in Fig. 12.1 together with the corresponding belt axial speed.

The excitation transmitted to the timing belt during rotation in operating condition is forced by the dynamics of the elements connected to the crankshaft and camshaft: such elements present bigger moving masses with respect to the belt mass and therefore they act as excitation sources on the belt. Moreover, the action of different cams on the camshaft induces strong torque fluctuation, concentrated at several harmonics of the camshaft rotation [12, 13]. The excitation will then result

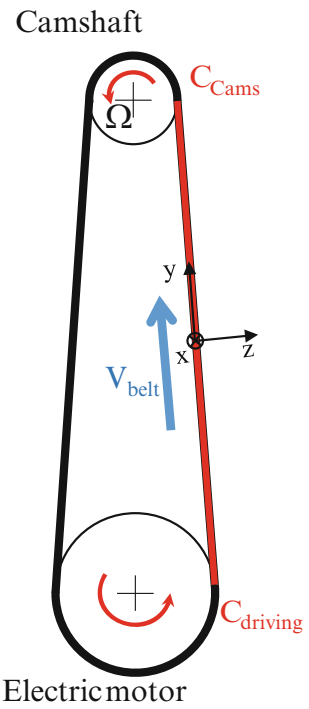

Camshaft Speed [Hz]	Belt Axial Speed [m/s]
14.6	3.4
19.4	4.5
28.4	6.6

Fig. 12.1 Axially moving belt scheme and operating conditions tested

in a multi-harmonic excitation at the engine orders with the predominance of the fourth order and its harmonics. Such excitation implies that ODSs of the belt are not excited at the mode shapes natural frequencies, but they will show up at frequencies directly related to the engine/camshaft orders.

12.2.2 Test Bench Characterization

A modal test was performed to estimate natural frequencies and relative mode shapes of the timing belt under analysis. This test was intended to provide a baseline for validating and comparing results of discrete SLDV and 3D DIC. The Laser Doppler Vibrometer was placed 1.5 m far from the target belt, aligned in such a way to have the laser beam orthogonal to the target surface when the scanning mirrors are in their rest position. The laser spanned a total length of 0.500 m (±0.250 m) in the belt moving direction, *y*-direction in Fig. 12.1, and 0.028 m (±0.014 m) in the cross direction, *x*-direction in Fig. 12.1. This configuration made it possible to have good balance between mirror angle aperture and amount of light backscattered to the sensor.

The belt was excited via an impact hammer while a Laser Doppler Vibrometer, scanning sequentially over a 3×25 points grid, recorded out-of-plane vibration. The natural frequencies and corresponding mode shapes, estimated using PolyMAX curvefitting algorithm, are reported in Table 12.1. Mode shapes are given in terms of Nodal Lines (NL) in Table 12.1. Bending mode shapes amplitude and phase maps are provided in Fig. 12.2. The choice of reporting only the bending modes, skipping the torsional modes, is related to the optical set-up chosen for the DIC test, see Sect. 12.3, that does limit the resolution in the belt transversal direction and therefore does not make it possible a correct assessment of torsional ODSs.

Table 12.1 Timing belt natural frequencies

Mode N.	Natural frequency (Hz)	NL
I	64.76	00
II	130.16	10
III	195.77	20
IV	261.65	30

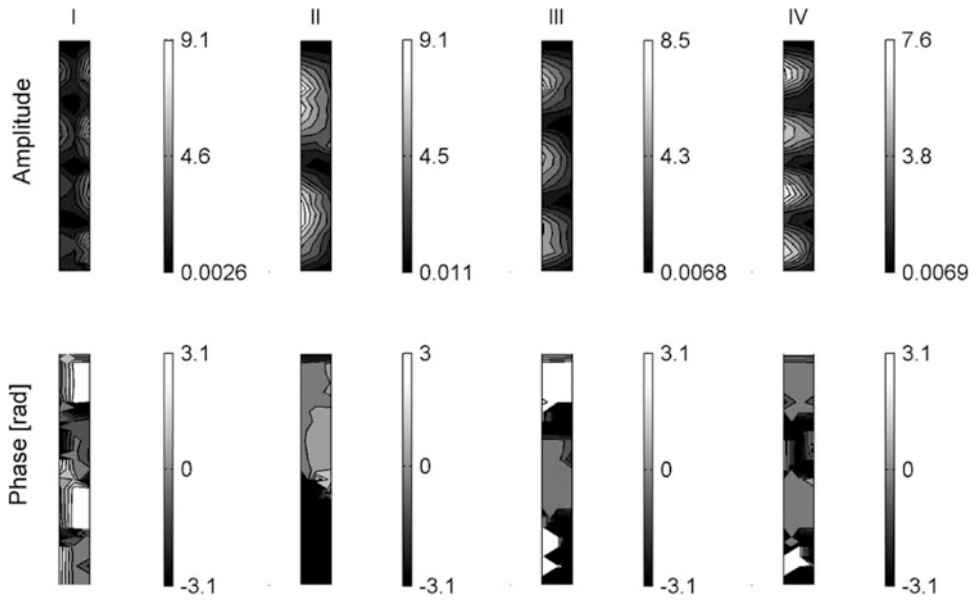

Fig. 12.2 Timing belt mode shapes

12.3 Digital Image Correlation Measurement

DIC is based on the observation of a random pattern characterising the surface of a structure as the latter vibrates. Typically, the pattern is a black and white speckle randomly distributed all over the target surface in order to ensure high contrast in the grayscale image formed in the digital camera (higher grey level intensity variations). Speckle pattern can be critical whenever a quantitative analysis is wanted in a DIC measurement. Pan demonstrated in [14] that indeed measurement error is strictly related to the speckle pattern morphology. Therefore, particular attention should be put in preparing the target surface, in order to ease the following pattern recognition step.

A black and white speckle pattern was created on the belt surface as reported in Fig. 12.3a, wherein the coordinate reference system adopted is also shown. Being the belt moving in the *y*-direction, the belt surface motion consists of the superimposition of the vibration pattern (with the most relevant component along the *z*-direction) and the "transport speed" (along the *y*-direction).

A stereo-DIC approach was exploited in order to estimate the out-of-plane (*z*-direction) vibration component. However, a folded optic solution, Fig. 12.3b, that makes it possible to use just one recording camera, was adopted. Indeed, a stereo set-up based on fast cameras is very expensive, due to the cost of high performance cameras. Moreover, cameras need to be synchronized, therefore the complexity of the whole measurement system increases. The folded optics solution is a good alternative that can be used for stereo photogrammetry whenever just one camera is available. This solution is realised by splitting the CMOS sensor line of sight into two projections by means of a set of mirrors, as shown in Fig. 12.3b. In such a way, two images of the object under observation form on the CMOS sensor. An example of folded image acquired on the timing belt is given in Fig. 12.3c where the Regions-Of-Interest (ROIs) selected are also shown. Despite the folded optics approach presents some drawbacks (the camera resolution is halved, the Scheimpflug condition is not respected and the amplitude of the angle between the two line-of-sight is limited) the advantages named above (i.e. low cost and no need of synchronization) make it a very interesting technique for 3D stereo image correlation. Anyway, it is to be clear that the halving of the number of pixels in the captured image and the halving of the spatial resolution in the *x*-direction limits the precision of the measurements, as described in [15].

The measuring system (camera—focal length f60 mm—and folded optic device) was placed 1 m far from the target surface. A proper lightning system was also set-up in order to increase the image contrast at an 840 fps frame rate.

A proper calibration of the whole DIC measurement system was done prior to perform any measurement on the belt. Calibration, as usual in vision based techniques, makes it possible to extract the intrinsic and the extrinsic parameters of the camera/cameras (camera resectioning). Such operation is fundamental for properly combining two images acquired from different lines of sight. Lens distortions were evaluated as well. The distortion effect induced on straight lines, which appears as curved lines on the sensor, is a quite common effect that takes place when wide-angle lenses are used. Compensating for such distortion becomes of primary importance in the folded optic configuration adopted, since the peripheral parts of the sensor are mainly involved in the image registration process. Despite different calibration procedures do exist, the common

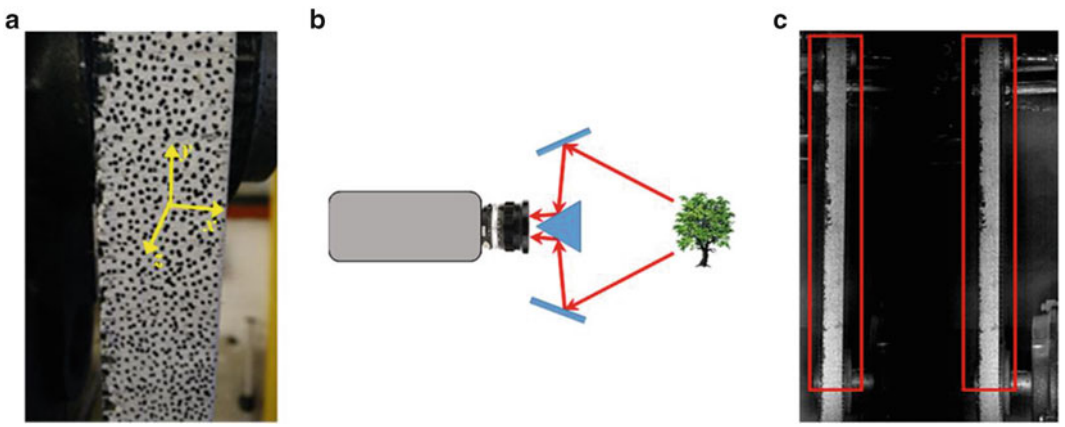

Fig. 12.3 DIC experimental set-up: speckle pattern applied on the belt surface and coordinate reference system adopted (**a**); folded optics scheme adopted for 3D motion measurement (**b**); belt folded image with the selection of *left* and *right* ROI (**c**)

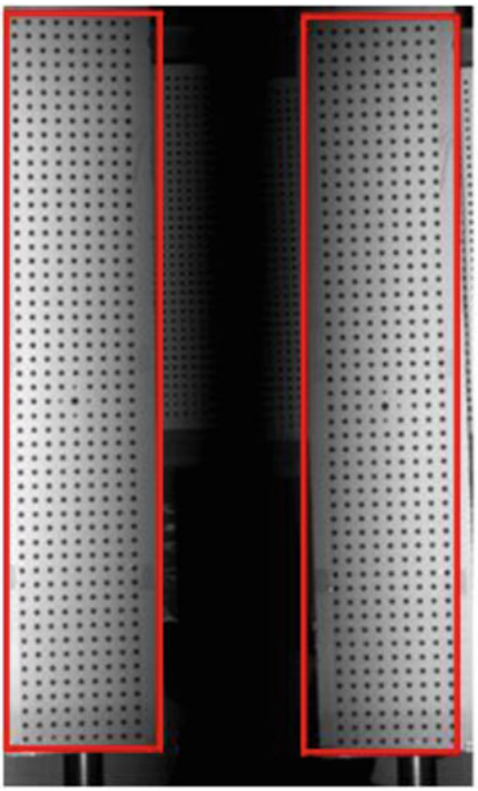

Fig. 12.4 Calibration panels with ROIs

approach consists in using a target with known dimensions that is framed by the camera/cameras from different lines of sight, under the condition of covering the whole volume wherein the structure of interest it is supposed to move. Different calibration target, having different calibration patterns, can be adopted. We used two panels characterized by equally spaced black markers (Fig. 12.4), the centre marker on each panel being bigger in size in order to ease its recognition by the calibration algorithm (third order XYZ Polynomial).

In order to cope with the belt translational movements an incremental approach was adopted. Such approach makes it possible to refer the ith frame to the $(i-1)$th frame and therefore to estimate the actual displacement of the target (or velocity, once the time increment is considered). An adaptive approach belonging to the Adaptive Correlation methods (see, for instance, [16]) was also exploited.

12.4 Results and Discussion

A DIC test was performed by exciting the belt with an impact hammer. Such test was intended to be the starting test in order to understand the DIC potentials and performances in extracting ODSs on a challenging target as the timing belt is. Figure 12.5 reports the ODSs extracted using the DIC processing described in the previous section. ODSs are well reconstructed in terms of amplitude and phase. This is not true for the third bending ODS, that does not recall the characteristic shape of the third bending mode neither in terms of amplitude nor in phase.

The challenging test was the one with the belt in running condition. The out-of-plane vibration of the timing belt was also measured exploiting Scanning LDV in discrete scanning mode. Such a measurement aimed at representing the reference measurement in terms of spectra and ODSs comparison. The scan grid consisted in 5×54 points evenly distributed over the belt surface. Since in discrete scanning mode a phase reference needs to be considered if looking at ODSs of a target, we used an accelerometer placed on the cylinder head to keep phase relations among the scanned points and to have possibility of performing complex averaging. The valve train dynamics produces a multi-harmonic excitation on the timing belt that is directly related to the engine orders (in the experimental set-up considered here, it is better to refer to the camshaft orders).

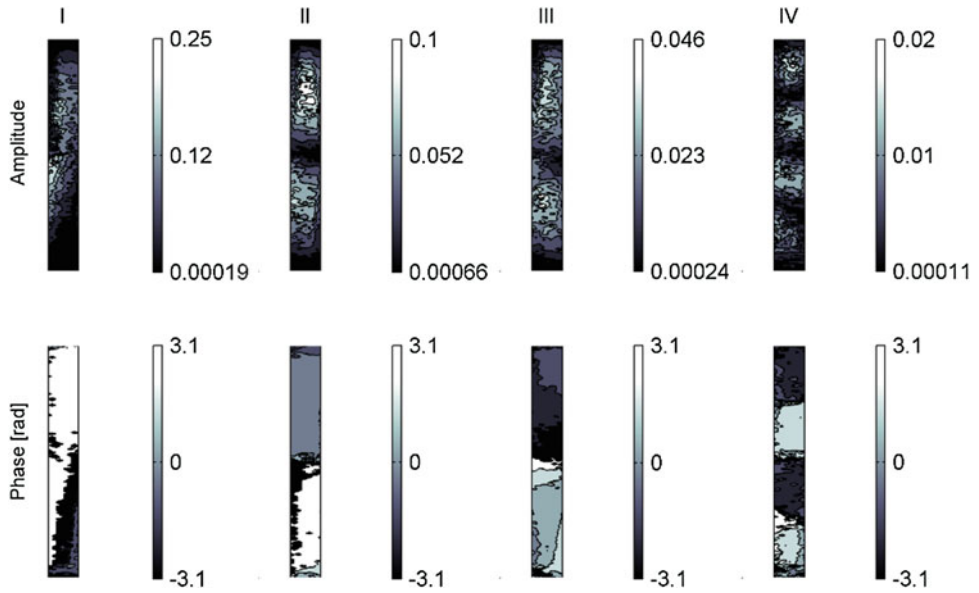

Fig. 12.5 Timing Belt ODSs obtained from Impact Hammer test processing

Table 12.2 Timing belt operating vibration frequencies

	Camshaft rotation frequency (Hz)						
	14.6		19.4		28.4		
ODS N	Vibration freq. (Hz)	Order	Vibration freq. (Hz)	Order	Vibration freq. (Hz)	Order	NL
I	58.4	4	58.2	3	56.8	2	00
II	131.4	9	135.8	7	142	5	10
III	189.8	13	194	10	198.8	7	20
IV	233.6	16	232.8	12	227.2	8	21

The ODSs reproducing shapes closest to the mode shapes will therefore show up at those orders that are the closest to the belt natural frequencies. This means that a particular ODS will show up only if a certain order gets close to the corresponding belt natural frequency. The resulting operating vibration frequencies do change with the camshaft rotation frequency, as reported in Table 12.2.

For sake of brevity, only ODSs obtained at the highest camshaft rotation frequency are presented hereafter. This represents the most challenging configuration in terms of DIC processing because of the high translational speed of the belt. These data, reported in Fig. 12.6, are to be compared with ODSs extracted using DIC processing (Fig. 12.7).

It is clear, comparing Figs. 12.6 and 12.7, that DIC can indeed correctly recover the timing belt ODSs even though some issues still remains. The ODS related to the 3rd bending mode cannot be resolved by DIC, it resembling a fourth bending mode (both in amplitude and phase). The authors have not understood this phenomenon yet. Moreover it is still unclear why the ODS related to the third bending mode cannot be well resolved in a hammer test either, where there is no translational movement of the belt. It is not a matter of aliasing (the ODS related to the fourth bending mode is well recovered) nor an issue related to superposition of velocity vectors belonging to different directions. The authors are currently trying to solve such issue, but these results will reported in future works.

The averaged frequency spectra gathered from DIC and SLDV results are reported in Fig. 12.8. They have been obtained by averaging the spectra at the different DIC sensing pixels and SLDV grid's acquisition points. The DIC spectra have been scaled progressively with an attenuation factor increasing with the increase of the camshaft rotation frequency. The fact that the DIC procedure experiences a higher vibration level and therefore needs to be scaled is attributed to the sensitivity of the

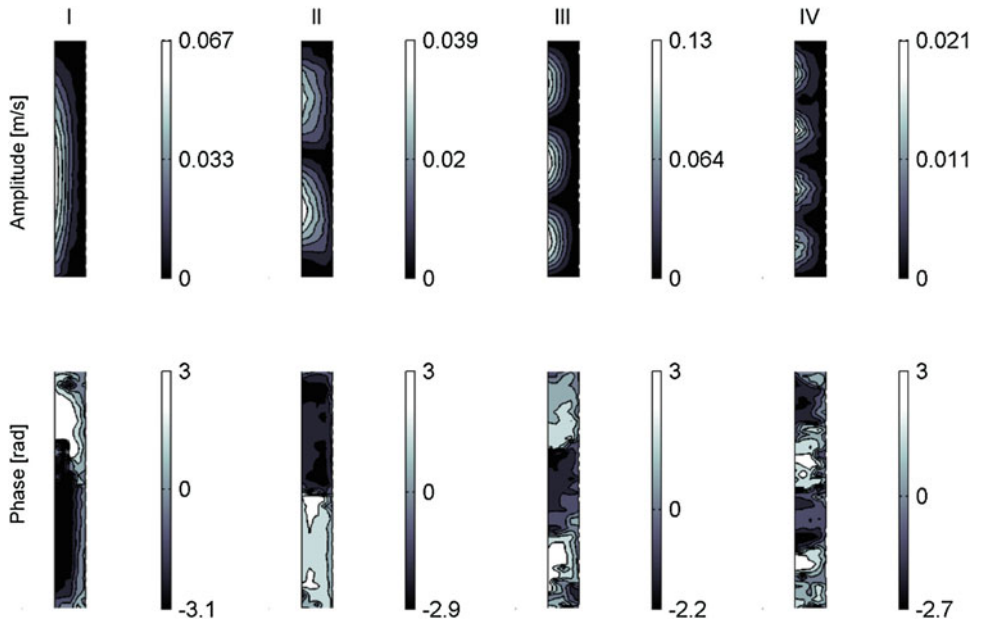

Fig. 12.6 ODSs for the camshaft rotation frequency of 28.4 Hz—Discrete Scanning

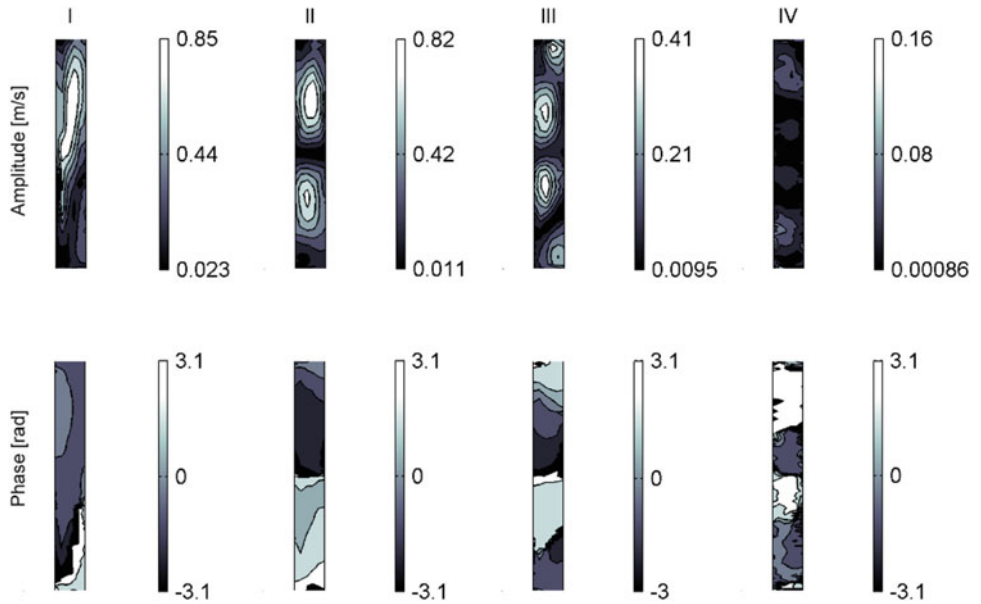

Fig. 12.7 ODSs for the camshaft rotation frequency of 28.4 Hz—DIC

image correlation to the transport speed of the belt that increases with increasing frequency. That means that the stereo-DIC is not able to completely decouple the vibration component in z-direction to the one in y-direction, strictly related to the transport speed. Nevertheless, it is clear that DIC and SLDV results are in good agreement when vibration amplitudes are high and therefore at the highest camshaft rotation frequency of 28.4 Hz. In this case, indeed, the large belt's displacements allow the image correlation algorithm to perform better.

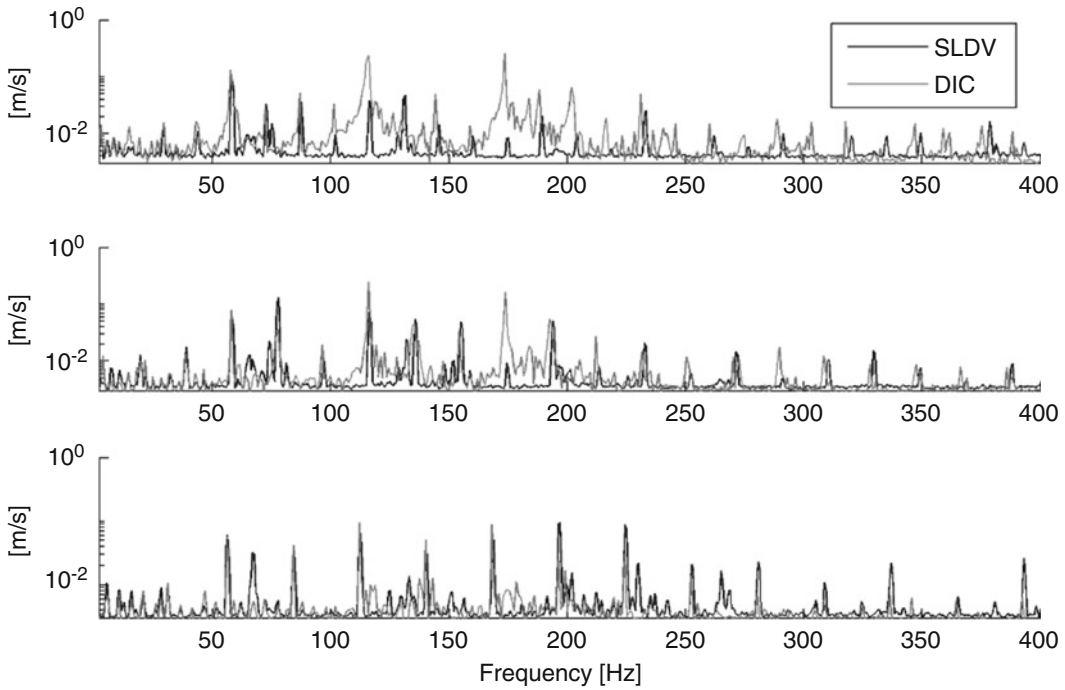

Fig. 12.8 Averaged spectra obtained from DIC and SLDV for the camshaft rotation frequency analyzed: 14.6 Hz (*top* plot), 19.4 Hz (*central* plot), and 28.4 Hz (*bottom* plot)

12.5 Conclusions

This paper aimed at showing the applicability of a full field technique as Digital Image Correlation for measuring out-of-plane vibration of timing belts. Timing belts represent a challenge for vibration analysis, mainly because of the superposition of out-of-plane and translational movements when the measurement is performed in operating conditions. The other critical point is excitation that is order-driven in timing belts. Different belt speeds and different orders have to be considered in the experiment for a complete identification of the ODSs of the belt. The stereo-DIC approach presented in this paper has shown interesting results in terms of potentials and critical issues. Operational Deflection Shapes can be generally well reconstructed even though some open questions remain regarding the inability of the method to recover the third bending mode both in steady and in running conditions. It has been also enhanced that, despite the incremental approach and the adaptive correlation method adopted, an overestimation of the out-of-plane vibration amplitude still exists. Such overestimation seems to be proportional to the belt translational speed. This phenomenon suggest that actual correlation algorithms are still not able to correctly decouple the out-of-plane vibration displacement (velocity if the time vector is taken into account) from the in-plane one. Nevertheless, potentials of the technique on such a challenging test case are evident and this represents a stimulus for keeping investigating in order to overcome current limitations.

Acknowledgement The authors wants to acknowledge Prof. Emanuele Zappa from Politecnico di Milano for the interesting and fruitful discussions regarding DIC processing on targets undergoing translational movements.

References

1. Di Sante, R., Rossi, G.L.: A new approach to the measurement of transverse vibration and acoustic radiation of automotive belts using laser Doppler vibrometry and acoustic intensity techniques. Meas. Sci. Technol. **12**(4), 525–533 (2001)
2. Di Sante, R., Revel, G.M., Rossi, G.L.: Measurement techniques for the acoustic analysis of synchronous belts. Meas. Sci. Technol. **11**(10), 1463 (2000)
3. Martin, P., Rothberg, S.: Methods for the quantification of pseudo-vibration sensitivities in laser vibrometry. Meas. Sci. Technol. **22**(3), 035302 (2011). doi:10.1088/0957-0233/22/3/035302
4. Rothberg, S.J., Baker, J.R., Halliwell, N.A.: Laser vibrometry: pseudo-vibrations. J. Sound Vib. **135**(3), 516–522 (1989)

5. Keating, T.J., Wolf, P.R., Scarpace, F.L.: An improved method of digital image correlation. Photogramm. Eng. Remote Sensing **41**(8), 993–1002 (1975)
6. Sutton, M.A., Orteu, J.-J., Schreier, H.W.: Book - Image Correlation for Shape, Motion and Deformation Measurements, Hardcover. ISBN 978-0-387-78746-6
7. Helfrick, M.N., Pingle, P., Niezrecki, C., Avitabile, P: Optical non-contacting vibration measurement of rotating turbine blades. Proceedings of the IMAC-XXVII, pp. 1–5 (2009)
8. Warren, C., Niezrecki, C., Avitabile, P., Pingle, P.: Comparison of FRF measurements and mode shapes determined using optically image based, laser, and accelerometer measurements. Mech. Syst. Signal Process. **25**, 2191–2202 (2011)
9. Wang, W., Mottershead, J.E., Siebert, T., Pipino, A.: Frequency response functions of shape features from full-field vibration measurements using digital image correlation. Mech. Syst. Signal Process. **28**, 333–347 (2012)
10. Javad, J.B., Lundstrom, T., Niezrecki, C., Avitabile, P.: Measuring the dynamics of operating helicopter rotors and wind turbines using 3D digital stereophotogrammetry. Ann. Forum Proc. AHS Int. **3**, 2250–2256 (2013)
11. Lundstrom, T., Baqersad, J., Niezrecki, C.: Using high-speed stereo-photogrammetry to collect operating data on a Robinson R44 Helicopter. Conference Proceedings of the Society for Experimental Mechanics Series, vol. 6 (2013)
12. Tounsi, M., Chaari, F., Walha, L., Fakhfakh, T., Haddar, M.: Dynamic behavior of a valve train system in presence of camshaft errors. WSEAS Trans. Appl. Theor. Mech. **1**(6) (2011)
13. Saka, Z., Yilmaz, Y.: Torsional vibrations of camshafts. Mech. Mach. Theor. **27**(3), 225–233 (1992)
14. Pan, B.: Recent progress in digital image correlation. Exp. Mech. **51**(7), 1223–1235 (2010)
15. Crammond, G., Boyd, S.W., Dulieu-Barton, J.M.: Speckle pattern characterisation for high-resolution digital image correlation. Appl. Mech. Mater. **70**, 261–266 (2011)
16. Wittevrongel, L., Lava, P., Lomov, S.V., Debruyne, D.: A self adaptive global digital image correlation algorithm. Exp. Mech. **55**(2), 361–378 (2015)

Chapter 13
Stiffness Characterization of an Inflated Airbag Based Three Axis Motion Platform

Eddy Trinklein, Jason Blough, Gordon Parker, Jacob Thill, and Michael Plackett

Abstract An actively controlled airbag system used as a three axis motion platform is characterized by a unique application of the multiple input H_1 Frequency Response Function (FRF) estimator. The goal of the testing is to understand the lateral (in-plane) stiffness properties of the inflated airbag at different inflation pressures and heights. The characterization is required to explore the controllability of the platform. The dynamic lateral magnitude increased 11.3 %, from 0.62 to 0.69 G/N, on average while damping decreased by 11.5 %, from 0.164 to 0.147, as height increased. Furthermore, the natural frequency shifted from 8.6 to 4.2 Hz as pressure and height varied. The static lateral stiffness increased on average 3.4 fold, from 6.5 to 22.2 N/cm from the lowest to highest pressure.

Keywords Airbag • Motion • Platform • Stiffness • Estimation

13.1 Introduction

A Stewart-Gough (S-G) platform [1] provides the means of simulating six degrees of freedom via selective control of an array of six actuators attached to the underside of a platform structure. S-G platforms are employed in a broad range of commercial applications including crane technology, flight simulation and machine tool control to name but a few. Precisely controlled hydraulic actuators are typically used where the payload being manipulated by the S-G platform are medium weight (e.g. less than 4 tons such as flight simulators). However, when the manipulation of payloads weighing hundreds of tons over amplitude ranges of several feet are required, the size and powering required for the S-G type hydraulic systems becomes extremely large, heavy and expensive to manufacture and operate. An alternate means of supporting very heavy payloads on a controllable platform structure is to employ low-pressure air cushion technology similar to the basic principals of the Hovercraft or Air Cushion Vehicle (ACV). Combining air cushion technology with plenum air pressure/flow control, similar to that demonstrated by the ride control systems employed on many Surface Effect Ships [2–4], provides the means of controlling the attitude of a platform with lightweight, simple actuation methods. Supporting a heavy payload on an air cushion system with a large surface area enables the platform to be controlled in roll, pitch and heave with relatively lightweight and low powered actuators. Control systems can include cables and/or hydraulic actuator combinations to control motions similar to the capabilities of the S-G platform. The geometry of the special airbag plenum system that encloses the air cushion, combined with the integrated air supply and method of pressure/flow control, are key to managing the remaining degrees of control (i.e. yaw, sway and surge).

The air supported motion platform concept offers several advantages to standard rigid actuator designs. Since the platform is suspended by air pressure, it doesn't require full actuation of the six degrees of motion (DOF) due to its natural tendency to return to a nominal position set by the lightweight actuator control system. This also allows for reduced cost and complexity by reducing the number of servo actuated controls required to position the platform. For example, the platform under investigation uses four control lines attached to the underside of the air supported platform to actuate three degrees of motion, z position (heave), x rotation (roll), and y rotation (pitch). While only three control lines are required for these three states, a forth, redundant actuator was selected to manage loads more evenly on a square platform design. This leaves three un-actuated rigid body platform motions that are in plane lateral x and y motion and z rotation (yaw). These free DOFs are damped by the airbag geometry, shear forces in the airbag material and vary with air pressure. To ensure the motion platform

E. Trinklein (✉) • J. Blough • G. Parker • J. Thill
Michigan Technological University, 1400 Townsend Dr., 815 RL Smith BLDG, Houghton, MI 49931, USA
e-mail: ehtrinkl@mtu.edu

M. Plackett
Quantum Engineering Design, Inc., 30487 Peterson Road, Corvallis, OR 97333, USA

E. Wee Sit (ed.), *Sensors and Instrumentation, Volume 5*, Conference Proceedings of the Society for Experimental Mechanics Series, DOI 10.1007/978-3-319-29859-7_13

does not experience unstable states from either external loading or actuator control inputs, the un-actuated lateral DOFs was investigated in this paper. For the expected loading cases of the platform, it is assumed that the yaw motion will not get excited and was therefore not explored.

A practical advantage of the air supported platform over a large conventional hydraulically actuated S-G system is the even distribution of loads and minimal structure required to assemble the system on ground surfaces or floating platforms such as flat-deck barges. The system lends itself to being developed as a modular kit that can be easily assembled, disassembled and transported.

A potential drawback of the large air cushion supported 6-DOF platform is the limitations of frequency response over large heave amplitudes (e.g. greater than 3 m). This is largely a function of the ability of the air supply system to fill the airbag plenum at a sufficient rate to raise the platform at the desired speed. Increasing the airflow rate at a given pressure provides the solution at additional expense and total system weight.

13.2 Theory

Characterization of the lateral rigid body stiffness for the airbag motion platform presents a unique signal processing problem caused by vibration from its centrifugal fan. The solution was implementing the H_1 multiple FRF estimator where the fan was instrumented with an accelerometer in the radial direction and considered a measured noise input. A second input was a modal hammer used to excite the lateral modes. A triaxial DC accelerometer was used to measure the response from the two inputs and mounted to the top surface of airbag deck. Due to the broadband nature of the centrifugal fan, its input is considered uncorrelated to the modal hammer input. This allowed for only five averages to obtain quality coherence and FRF measurements. The mathematical relationship between outputs, the transfer paths, and force inputs are given in Eq. (13.1) [5, 6].

The system response, $x(\omega)$, is a result of an external forcing function, $F(\omega)$ and a measured noise function, $N(\omega)$, where the two transfer paths are unknowns; $H_{XF}(\omega)$ and $H_{XN}(\omega)$ respectively.

$$x(\omega) = H_{XF}(\omega)F(\omega) + H_{XN}(\omega)N(\omega) \tag{13.1}$$

The unknown H_{XF} FRF can be written in terms of auto-spectra and cross-spectra with respect to the output, X, the forcing function F, and noise input N, as shown in Eq. (13.2).

$$H_{XF}(\omega) = \frac{det\begin{bmatrix} G_{XF}(\omega)G_{NF}(\omega) \\ G_{XN}(\omega)G_{NN}(\omega) \end{bmatrix}}{det\begin{bmatrix} G_{FF}(\omega)G_{NF}(\omega) \\ G_{FN}(\omega)G_{NN}(\omega) \end{bmatrix}} \tag{13.2}$$

A further simplification of Eq. (13.2) is given in Eq. (13.3), where the determinants are expanded.

$$H_{XF}(\omega) = \frac{G_{XF}(\omega)G_{NN}(\omega) - G_{XN}(\omega)G_{NF}(\omega)}{G_{FF}(\omega)G_{NN}(\omega) - G_{FN}(\omega)G_{NF}(\omega)} \tag{13.3}$$

The resulting expression in Eq. (13.3) removes the effects of noise from the fan, leaving the desired FRF between the point of external excitation and the sensing location. This method allowed for efficiently identifying the lateral rigid body mode of the airbag motion platform which is described in detail below.

13.3 Experimental Setup

The main components of the airbag platform are shown in Fig. 13.1 with dimensional information given in Table 13.1. Starting at the top of Fig. 13.1 a brief description of each component and function will be described below.

The airbag deck is the working surface of the motion platform, which is oriented with respect to the base in either dynamic or static positioning. Depending on the motion objectives, the deck can mitigate base motion or track an external position reference.

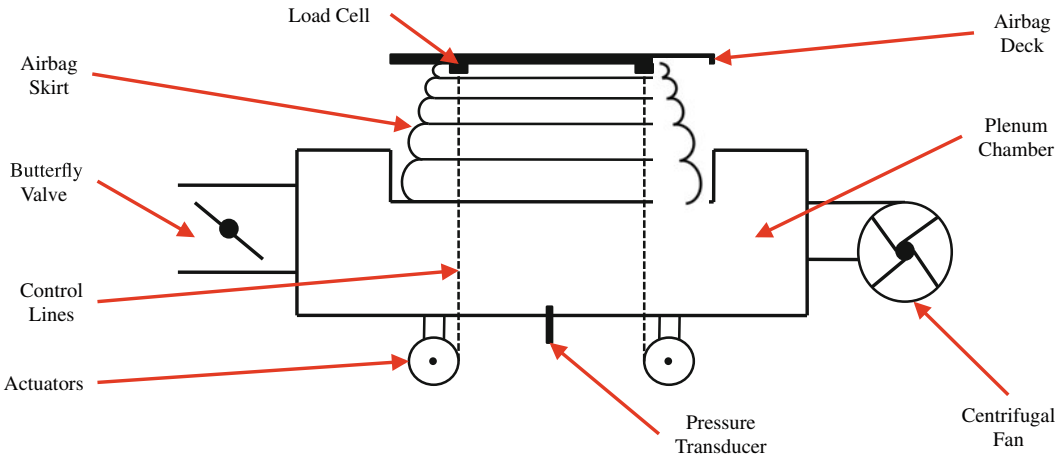

Fig. 13.1 Airbag motion platform components

Table 13.1 Airbag motion platform model parameters and dimensions

Deck dimensions	87.0 cm (square)
Deck mass	6.34 kg
Inflatable surface area under deck	5428.3 cm^2
Max working height	17.0 cm
Pressure range	156.8–551.4 Pa

Below the deck resides the airbag skirt which provides a flexible, airtight seal between the plenum chamber and deck. The skirt is designed as a multi-lobe bellows with internal webbing that maintains the nodal circumference between the lodes. The lobes are linearly scaled to be larger at the bottom and smaller near the deck. These features allow for the skirt to collapse in a controlled manner, where the upper lobe collapses first due to its smaller surface area compared to other lobes. Furthermore, the skirt has a smaller circumference at the top than at the bottom, analogous to a stepped pyramid, which increases the natural stiffness of the platform, a feature to be explored later.

The plenum chamber serves several functions. First, it's the main structural component which the actuators, valve assembly, fan and skirt attach. Second, the chamber allows for the incoming air from the fan to uniformly stabilize in pressure. Third, the section where the skirt attaches is recessed, so the deck and skirt can collapses flush with the upper surface of the plenum chamber. The working height of the platform is considered the distance between the top surface of the plenum chamber and the underside of the deck.

A butterfly value assembly and centrifugal fan provide the means to inflate and control the internal platform pressure. There are two methods for changing the pressure; varying the fan RPM or changing the butterfly plate angle with respect to the airflow. In general, for a given RPM, the fan mass flow rate and pressure vary quadratically and are negatively correlated. In this research, the fan speeds were set to specific constant RPM levels.

Four spool type cable actuators were used to maintain the deck orientation with respect to the plenum chamber. As mentioned above, four spools were utilized to minimize actuator loading due to the square deck geometry. In general the cables could form compound angles with respect to the vertical direction (z axis) when the deck and plenum chamber are parallel. This would have the benefit of increased lateral stiffness at the cost of increase actuator forces. In the model, the cables are nominally vertical, and therefore provide little lateral support. Also incorporated into each cable are load cells which provide tension feedback and are incorporated into the control design.

For determining the airbag platform lateral modal and static stiffness, the platform was setup on concrete blocks on top of an iron bed plate. By blocking up the platform, the modal testing was isolated from external vibrations and increase testing robustness. The modal testing, as partly described above, was conducted using a fixed DC accelerometer to measure both fan noise and external excitation. It was located near the center of the deck, offset by the width of the accelerometer with the x and y axes pointing perpendicular with the deck edge, and z axes pointing vertical, normal to the deck surface. A second AC accelerometer was placed onto the fan, with the sensitive axis aligning with the radial axis of the centrifugal fan. This accelerometer allowed for direct measurement of the vibratory noise component contributing to the DC accelerometer output. Both accelerometers were calibrated with a 1 G sinusoidal shaker. A modal hammer was used to strike the edge of

the deck to excite the lateral modes. The hammer was weighted and outfitted with a soft plastic tip to ensure adequate energy transfer to the deck. A Quattro Signal Ace from Data Physics was used to acquire and process the FRF response traces. During preliminary testing, the lateral mode was identified in the 4–6 Hz range, therefore a frequency range up to 50 Hz was selected.

13.4 Results

The quantities of interest from a controls perspective are the lateral rigid body natural frequencies and their dependance on air pressure and working height. These rigid body natural frequencies must be above both the external excitation and actuator control frequencies. A second quantity of interest is the static lateral stiffness. For the modal testing, a total of 25 FRFs were collected at five pressures and heights. An example FRF of the lateral rigid body mode is given in Fig. 13.2. Due to the symmetry of the platform, its assumed the x and y modes are equal, so data was collected arbitrarily in the y direction. As mentioned earlier, the multiple H_1 FRF estimator provided a high quality response and coherence measurements near one for frequencies above the accelerometer rolloff at 2 Hz. To understand how both the magnitude of the lateral mode and its frequency varies with height and pressure, these quantities were tabulated and plotted in Figs. 13.3 and 13.4.

A general trend observed in Fig. 13.3 is increased pressure results in higher resonance frequencies, with the exception of 14 cm at 425 Pa. Between the 5 and 11 cm heights, most resonances increase with both height and pressure. At 14 cm height, the resonances are grouped more closely together than in other heights and likely caused by airbag lobe interactions. Furthermore, transitioning from 14 to 17 cm for the three lower pressures, the resonance magnitudes drop with increased height while the highest pressure shows an increase in resonance. These relationships show distinct non-linearities caused by the lobed airbag structure in both height and pressure. Also of interest, the modal damping was estimated for the lateral motion using Eq. (13.4), where ζ is the damping ratio, ω_n is the natural frequency, ω_1 and ω_2 are the lower and upper frequencies at which the FRF magnitude is equal to $x_{max}/\sqrt{2}$ or the half power point for the resonance peak under investigation. The damping ratio also have markedly non-linear characteristics at the 156.8 and 232.5 Pa pressures. The

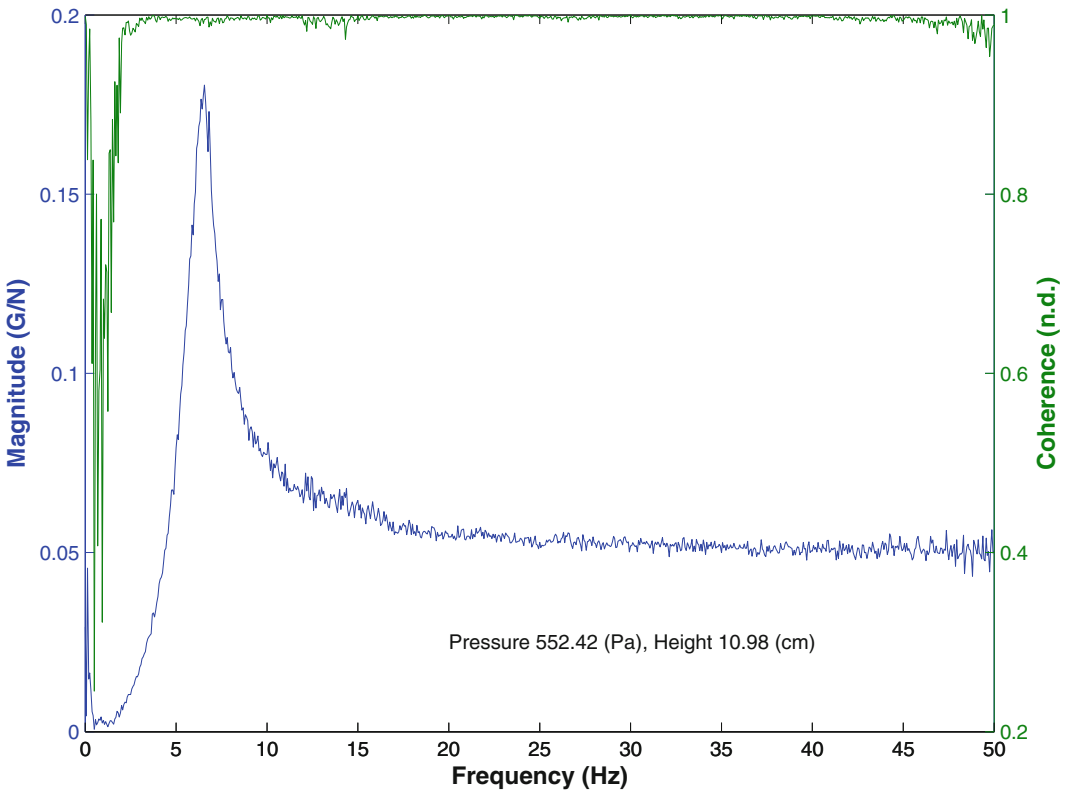

Fig. 13.2 Sample FRF magnitude and coherence plot

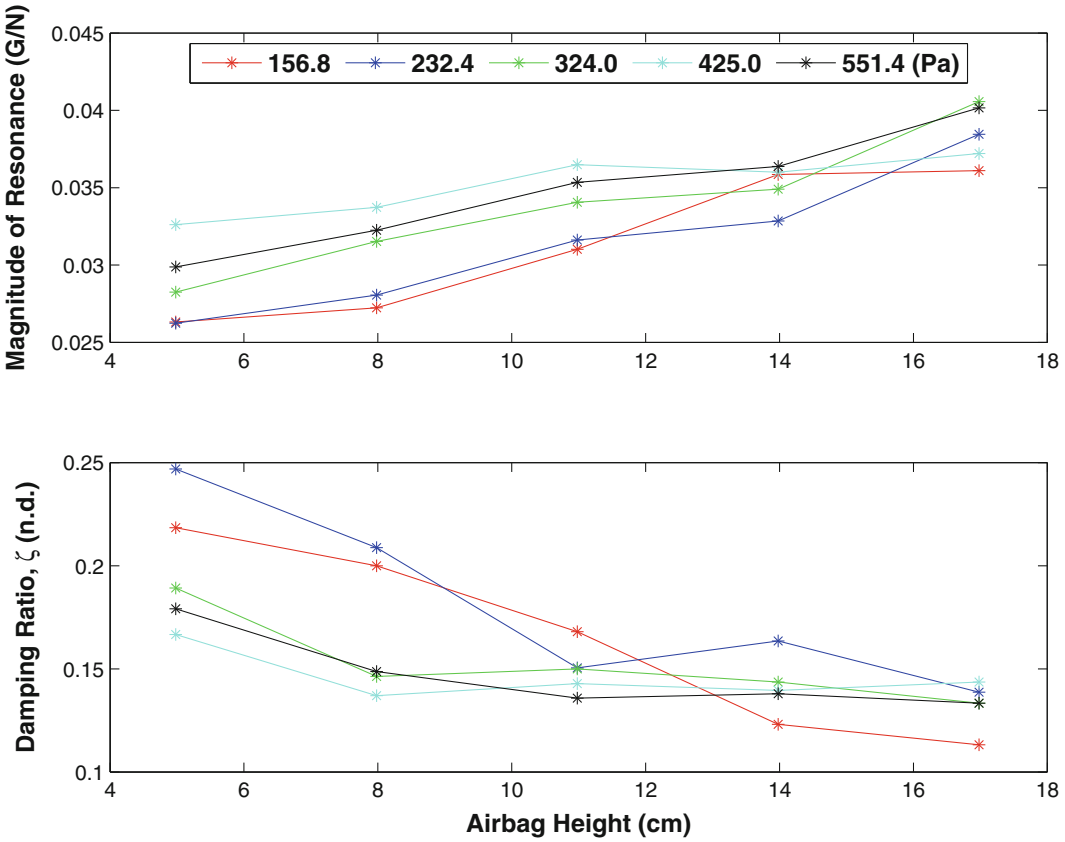

Fig. 13.3 Magnitude of lateral Y resonance vs. height at five pressures

three highest pressures approach linear damping ratio curves beyond 8 cm heights in the 0.13–0.14 range. At the 156.8 Pa pressure, the damping ratio is around double that of the 551.4 Pa pressure. One explanation is the energy transfer path through the airbag material is less efficient at lower pressures because the material is less taut.

$$2\zeta = \frac{\omega_2 - \omega_1}{\omega_n} \tag{13.4}$$

In Fig. 13.4, a significant shift in the lateral modal frequency is observed. The trends are non-linear with a near quadratic nature. Furthermore, the effect of pressure is clearly evident with higher pressures driving the frequencies up. The frequency span observed ranges from 4.2 to 8.6 Hz.

A second concern of the motion platform was the static lateral stiffness. Since the lateral restoring force is mainly due to control line tensions and shear forces in the skirt material, its limits must be understood to prevent the platform from collapsing from side loading. Therefore, a series of static forces were applied to the deck and its lateral displacement recorded. The same heights are pressures were used as in the modal tests. For each pressure and height, five displacements and forces were recorded and averaged, yielding Fig. 13.5. At low pressures, the lateral stiffness is the lowest with a nearly linear relationship with height. As pressure increases, so does the lateral stiffness. Furthermore, stiffness tends to decrease with height. At a height of 11 cm, the skirt lobe geometry changes resulting in the dog-leg relationship observed in the three highest pressure traces. At 14 cm, the skirt lobes are each fully inflated and the decreasing stiffness with height trend continues till the tallest test height.

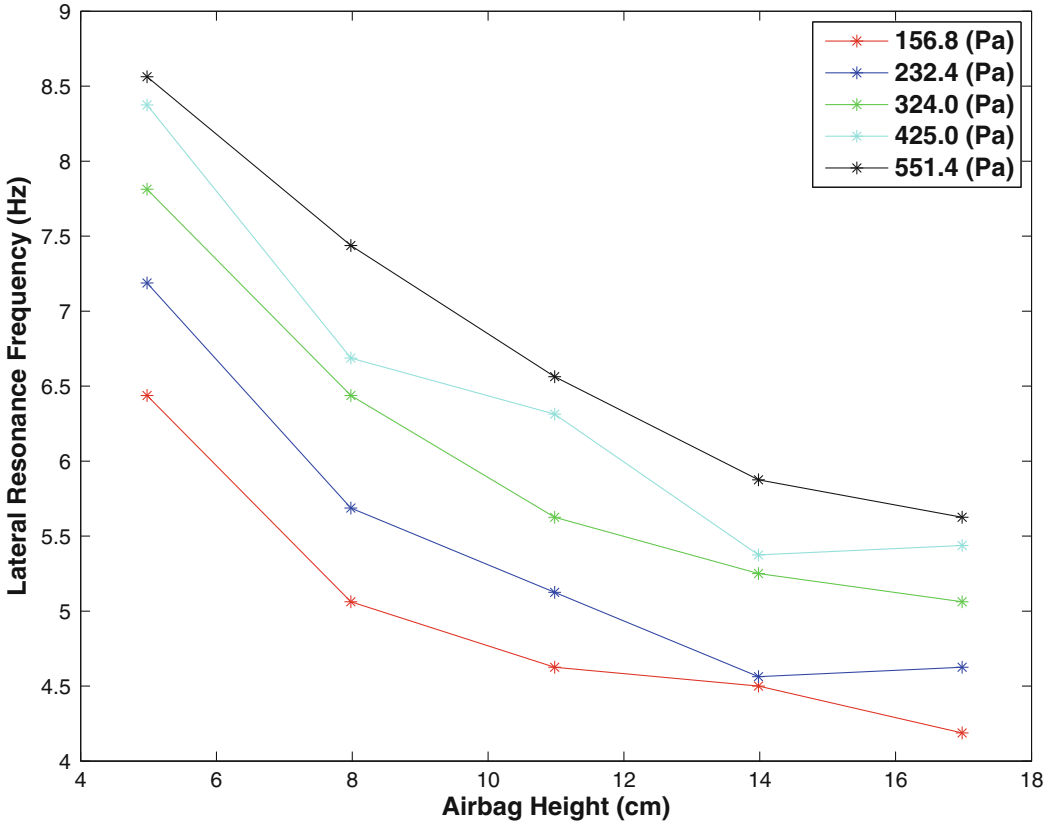

Fig. 13.4 Lateral Y resonance frequency vs. height at five pressures

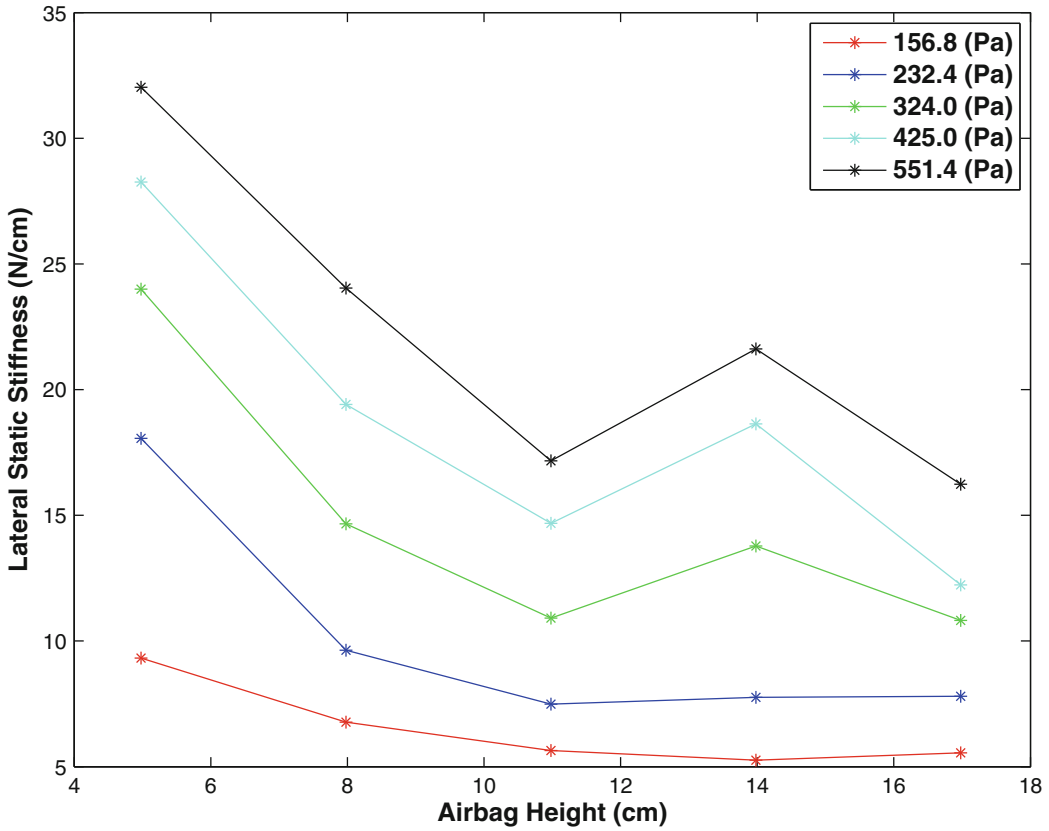

Fig. 13.5 Average static lateral stiffness vs. height at five pressures

13.5 Conclusions

In this paper, an alternative motion platform design is presented based on Air Cushion Vehicle technology. A method for characterizing the un-controlled lateral stiffness was presented and implemented using H_1 multiple FRF estimator. This estimator removed the noise and vibration caused by the centrifugal fan, and provided high quality FRF measurements. These measurements will provide the basis for developing and calibrating a dynamic model of the airbag motion platform and extrapolated for the design of large scale platforms.

The airbag motion platform lateral stiffness was determined to be both a function of working height and pressure. Dynamically, the magnitude of the lateral mode increased on average by 11.3 % from 0.62 to 0.69 G/N with height increase. This magnitude increase was attributed to reduced damping ratio, which dropped by an average 11.5 %, from 0.164 to 0.147, at increased heights. A possible cause was reduced friction between the lobes of the skirt at taller working heights. The lateral natural frequency also varied significantly. As the heights increased, the frequency decreased. Conversely, as pressure increased so did the natural frequency. Over the range of test points the natural frequency varied from 4.2 Hz at low pressure and maximum height to 8.6 Hz and the lowest height and highest pressure. Since the mass of the platform remained constant, with increased air mass considered negligible, the airbag modal spring constant decreased with natural frequency. This result is correlated with the static lateral testing which yields the highest spring constant of 33 N/cm at lowest height and highest pressure. Furthermore, pressure had a significant effect on the static lateral stiffness, where stiffness increased on average, from 6.5 to 22.2 N/cm, or 3.4 times from the lowest to highest pressure.

There is ample area for further research and future work related to the airbag motion platform concept. The lateral stiffness study requires additional test cases where additional mass is place onto the deck and determine how the stiffness changes. The effect of line tension needs further investigation and how changing the angle effects the lateral stiffness. The yaw stiffness is also an area for expansion. Ultimately, a relation of material properties, geometry, and a unifying dynamics model is sought.

References

1. Stewart, D.: A platform with six degrees of freedom. Proc. Inst. Mech. Eng. **180**(5), 371–386 (1965/1966)
2. Crewe, P., Eggington, W.: The hovercraft - a new concept in maritime transport. Trans. R. Inst. Nav. Archit. **102**, 315–356 (1960)
3. Sørensen, A., Egeland, O.: Design of ride control system for surface effect ships using dissipative control. Automatica **31**(2), 183–199 (1995)
4. Hinchey, M., Sullivan, P., Dupuis, A.: On the heave dynamics of large air cushion platforms. J. Sound Vib. **96**(4), 469–484 (1984)
5. Blough, J.R., DeClerck, J.P.: Application and development of some signal processing procedures to estimate frequency response functions of a system during operation. In: Proceedings of the 15th International Seminar of Modal Analysis Conference (1996)
6. Bendat, J.S., Piersol, A.G.: Random Data. Analysis and Measurement Procedures. Wiley, New York (2000)

Chapter 14
Experimental Evaluation of the Force Transmissibility of Phononic-Inspired Vibration Isolators

H. Policarpo, M.M. Neves, and N. M. M Maia

Abstract This article is devoted to the experimental evaluation of force transmissibility observed at Phononic-inspired Vibration Isolators (PIVIs) built of two-materials (alternately steel and cork agglomerate) and their combination in series with helical coil springs (HS). The fact that traditional vibration isolators may present a satisfactory performance in a narrow frequency range motivates the development of the PIVI as an alternative solution. Indeed, the PIVI can be designed to present significant wider frequency gaps, designated as Attenuation Regions (ARs), between two consecutive axial natural frequencies. Hence, in this study, three different devices are experimentally evaluated in terms of force transmissibility: the HS, the PIVI and the combined structure (CS) composed of a PIVI in series with a HS. The results clearly demonstrate the capability of the CS in attenuating the force transmissibility, where the PIVI contributes with its AR, thus operating as a "filter" in a specific frequency range, while the HSs add flexibility to the CSs, which may be advantageous for impact loads and/or transient-case scenarios. The authors believe that the capability, relevance and impact of the PIVIs have high potential for noise and vibration reduction applications, in a wide-range of engineering applications.

Keywords Transmissibility • Vibration isolation • Phononics • Cork agglomerate • Experimental • Passive devices

14.1 Introduction

A diversity of devices dedicated to passive vibration reduction (some of which are tuned and/or optimized) are commercially available [1]. One of the simplest and most used devices is the HS. Being inexpensive and critical to the reliability of many systems (especially under shock and/or transient conditions), HSs do not always provide a satisfactory performance in a wider frequency range [2], as they present a regular spaced distribution of the natural frequencies along the spectrum, originating unwanted/undesirable natural frequencies in the frequency range of interest. In contrast, finite periodic structures composed of alternating layers of two materials, called PIVIs [3] (See Fig. 14.1), may be designed to present wider gaps between adjacent natural frequencies, known as attenuation regions (ARs), when compared to the HSs, as well as their best positioning in the frequency range [4]. For more details refer to [5–13].

Hence, as verified through numerical simulation results [14, 15], a CS composed by a HS in series with a PIVI is advantageous in the sense that it combines the shock/transient load absorption capability of the HS with the "filtering" capability within the ARs of the PIVIs. This is a real need in most applications and as far as the authors are aware it has not been described in the technical scientific literature.

In general terms, transmissibility T_r is defined as being the ratio between the magnitudes of output and input entities (between forces, displacements, velocities or accelerations). If the ratio is greater than 1, the entity is amplified, and if the ratio is less than 1, the entity is reduced, isolated or attenuated; in the case of forces, one has:

$$T_r = \frac{F_{\text{output}}}{F_{\text{input}}}. \tag{14.1}$$

Note that these ratios are equivalent for 1D linear systems [16]. For MDOF systems see Lage et al. [17] and the respective references.

H. Policarpo
IDEMC, Instituto Superior Técnico, Universidade de Lisboa, Av. Rovisco Pais, 1049-001 Lisboa, Portugal

LAETA, IDEMC, Instituto Superior Técnico, Universidade de Lisboa, Av. Rovisco Pais, 1049-001 Lisboa, Portugal

M.M. Neves • N.M.M Maia (✉)
LAETA, IDMEC, Instituto Superior Técnico, Universidade de Lisboa, Av. Rovisco Pais, 1049-001 Lisboa, Portugal
e-mail: nmaia@dem.ist.utl.pt

E. Wee Sit (ed.), *Sensors and Instrumentation, Volume 5*, Conference Proceedings of the Society for Experimental Mechanics Series, DOI 10.1007/978-3-319-29859-7_14

Fig. 14.1 Two-material PIVI device for longitudinal vibration attenuation

This work, being a natural continuation of previous ones [3, 4] and [15], consists of an experimental evaluation of force transmissibility for three different devices: a PIVI, a HS and a CS composed of a PIVI in series with a HS.

14.2 Specimens and Methodology

14.2.1 Specimens

Three devices are used to support a vibrating mass of 3.2 kg:

i. HS, illustrated in Fig. 14.2a, with a height of 20.4 mm, a diameter of the steel wire of 1.5 mm, an inner diameter of 12 mm, four active coils and two close plain coils at each end;
ii. PIVI, illustrated in Fig. 14.2b, composed of steel-cork agglomerate (ref. VC5200) layers, described e.g. at [15], with a total length of approximately 80 mm.
iii. CS, illustrated in Fig. 14.2c, which is a combination of the HS from (i) in series with the PIVI specimen from (ii).

The PIVI specimen, illustrated in Fig. 14.2b, has a square cross-section with 20 mm of length and is composed of steel and cork composite (ref. VC 5200) material layers with thicknesses of 20.5 mm and 10.1 mm, respectively.

A description on the selection of the pair of materials and the respective proportions, which are essential for the location and width of the ARs in the frequency range, has been presented by Policarpo et al. in [4] and further developed by Policarpo in [15]; hence, it will not be discussed here.

14.2.2 Experimental Methodology

The experimental setup used to obtain the force transmissibility curves of the three specimens that are used to support a vibrating mass is illustrated in Fig. 14.3. Note that the support configurations change between HSs, PIVIs and a combination of both (CSs).

The vibrating mass is a portion of a cylindrical aluminum rod with a diameter of 150 mm, a length of 65 mm and a mass of 3.2 kg approximately.

The experimental setup may be described as: a signal is generated and transmitted to the vibration exciter (Brüel & Kjær 4809) which is suspended from a fix support by metallic chains. The force effectively applied to the mass (input signal) is measured through a force transducer (PCB 208C01). The dynamical deformation propagates throughout the prototype and, at the opposite extremity, force transducers measure the force effectively transmitted to the foundation (output signal).

The input and output signals are acquired using a data acquisition unit (Brüel & Kjær 3560D) and analyzed by a proper software (Bruel & Kjær PULSE® LabShop Version 6.1.5.65).

14.3 Results and Discussion

In the following the main experimental results are presented, using the experimental setup previously described in Fig. 14.3, to study the dynamic behavior, in terms of force transmissibility of the three different devices, i.e., HSs, PIVIs and the CSs (PIVIs and HSs) that are used to support a mass of approximately 3.2 kg.

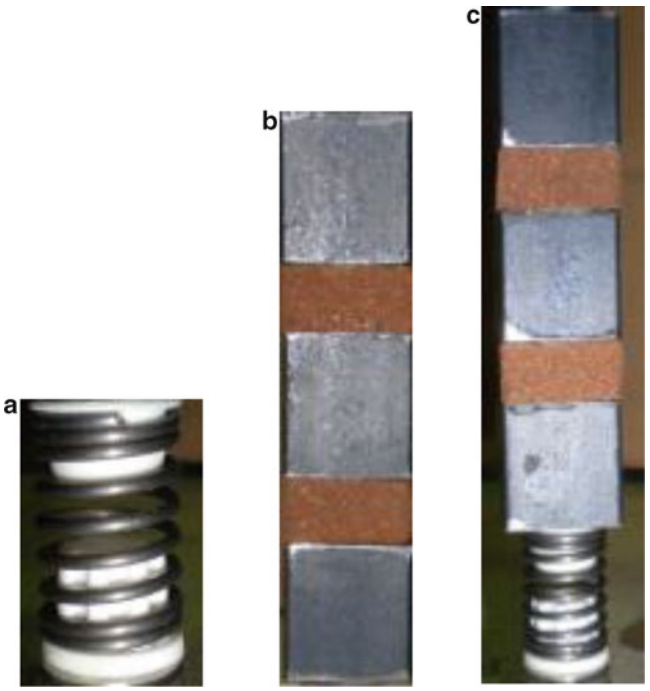

Fig. 14.2 Support devices: (**a**) Helical coil spring (the white terminations are plastic connection devices); (**b**) Phononic-inspired vibration isolator; (**c**) Combined structure (HS + PIVI)

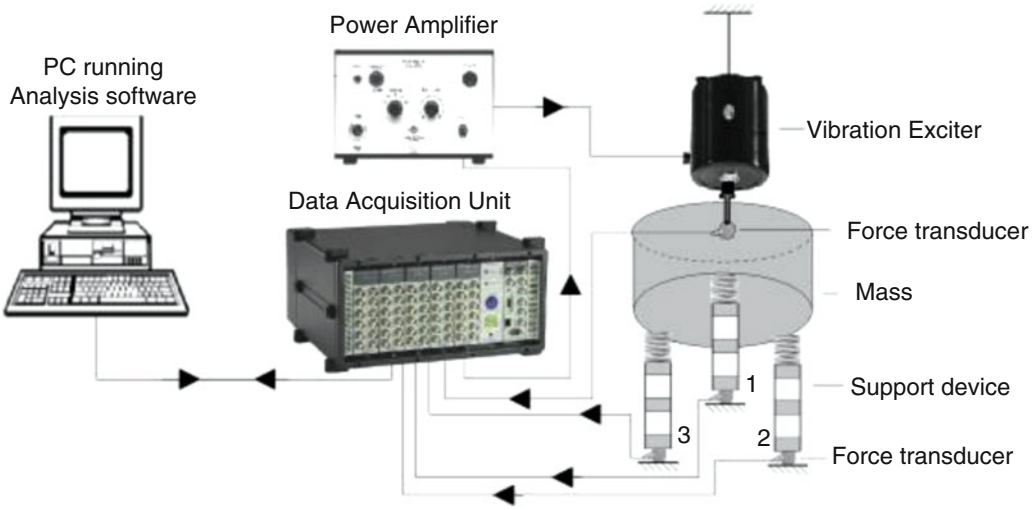

Fig. 14.3 Basic layout of the experimental setup to obtain the force transmissibility curves using three devices to support the load mass

Let us consider that: (i) the mass is supported by three HSs, as illustrated in the photograph of Fig. 14.4a; (ii) the mass is supported by three PIVIs, as illustrated in Fig. 14.5a; and (iii) the load mass is supported by three CSs (PIVIs and HSs), as illustrated in Fig. 14.6a.

For case (i), it was verified that the dynamical behavior (with emphasis on the natural frequencies), of the three HSs are not equal, as expected (see Fig. 14.4b), due to geometric deviations in the manufacturing of the HSs. However, it may be considered similar and located within a small enough bound that allows for the identification of the natural frequencies. One may identify the first longitudinal natural frequencies at approximately 700 Hz and 1380 Hz.

In case (ii), it is verified that the PIVIs present a similar dynamic behavior presenting an AR of interest after approximately 800 Hz (see Fig. 14.5b). Note that even though two flexural modes are present nearby 1 kHz and 1.23 kHz, with more significance for prototypes 1 and 2, the authors consider that it does not significantly influence the longitudinal vibration AR of interest.

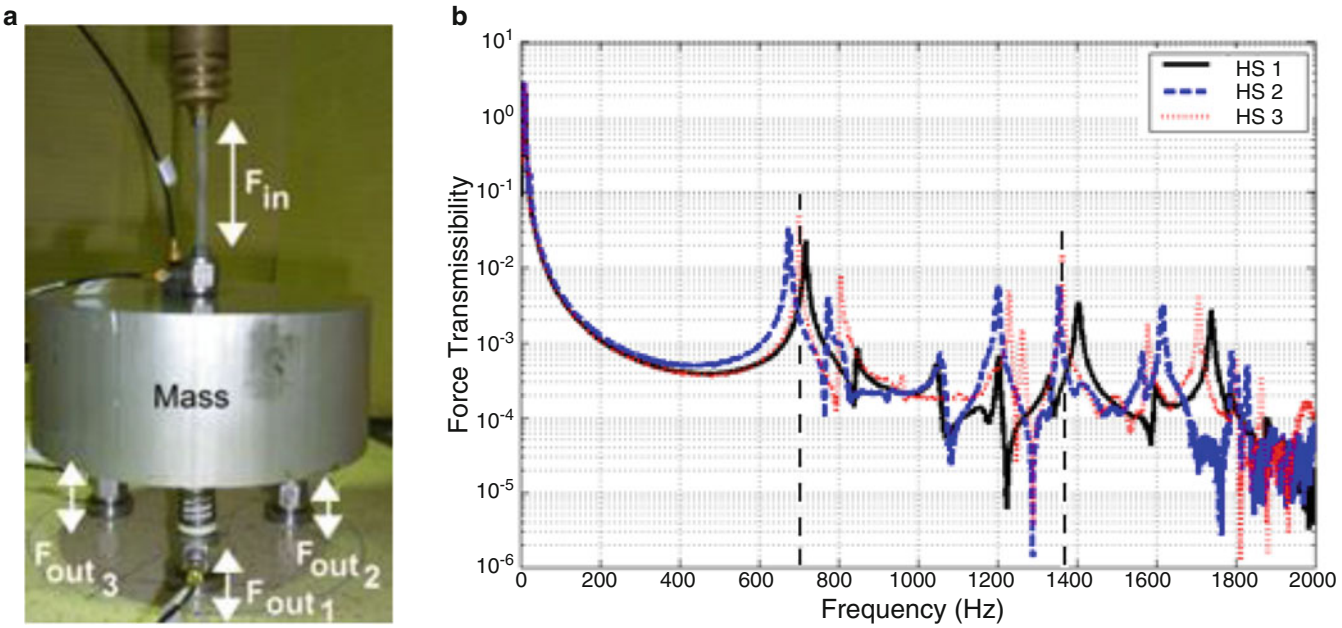

Fig. 14.4 Case (i): Mass supported by HSs: (**a**) part of the experimental setup; (**b**) force transmissibility curves

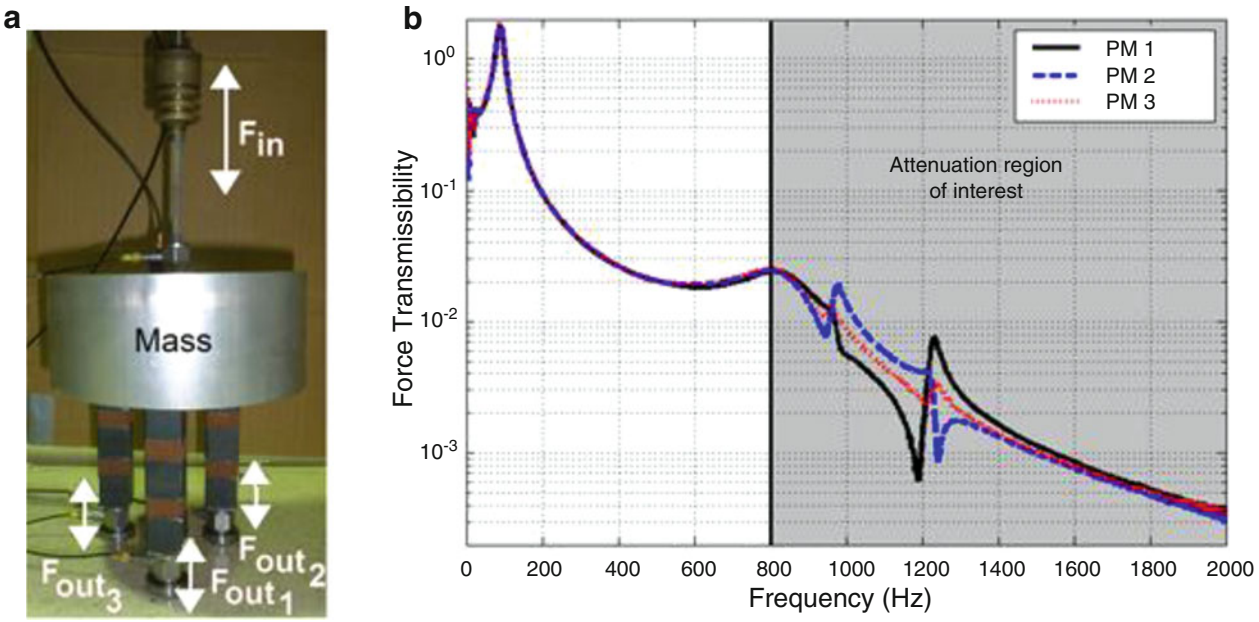

Fig. 14.5 Case (ii): mass supported by PIVIs: (**a**) part of the experimental setup; (**b**) force transmissibility curves

In case (iii), the CSs (PIVIs + HSs) present a similar dynamic behavior even though, the combined structure 1 (solid curve) presents a slightly lower natural frequency relative to the other two combined structures (see Fig. 14.6). Similarly to case (i), it is considered to be located within a small enough bound that allows identification.

To compare the relative performance, in terms of force transmissibility, of each type of supporting device, i.e., HSs, PIVIs and the CSs (PIVIs + HSs) the force transmissibility curves of each of device (in this case position 3 was chosen) are illustrated in Fig. 14.7.

From Fig. 14.7, it is verified that the CS (solid line) is capable of effectively reduce the amplitude of the spring responses (dashed line) with emphasis at the natural frequency within the prototypes AR (shaded area), i.e., mainly after approximately 800–1700 Hz.

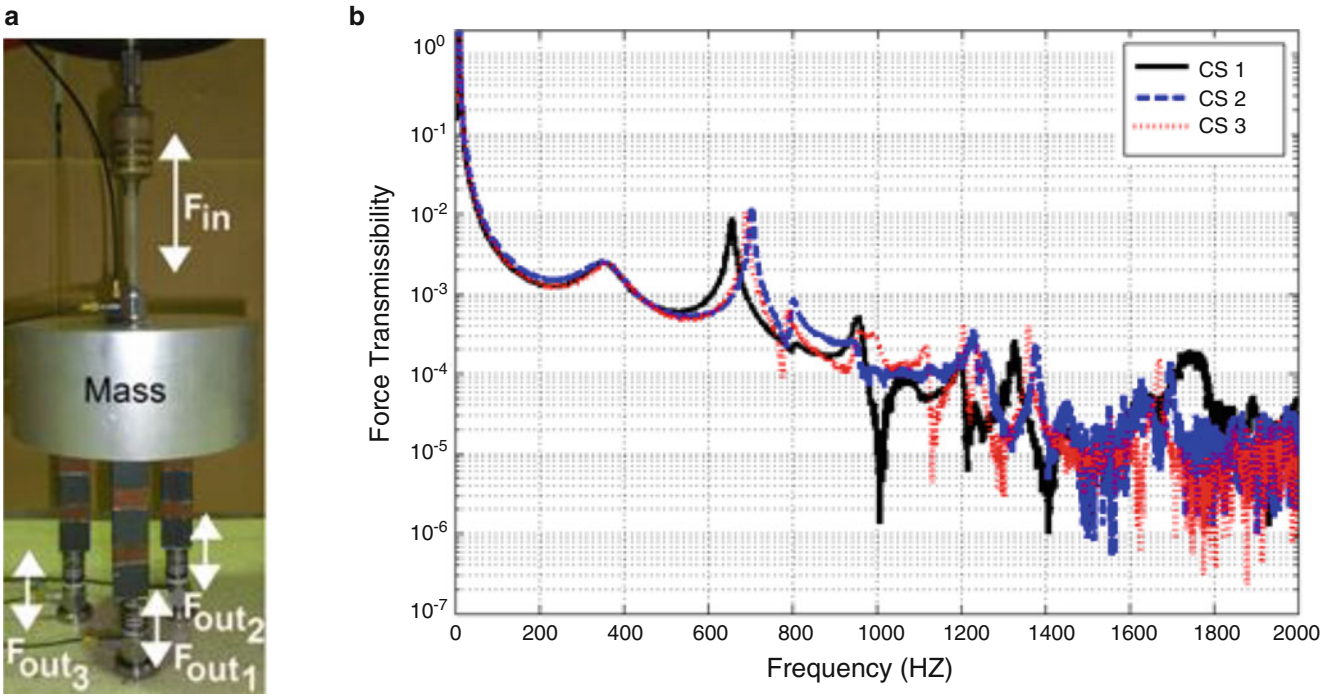

Fig. 14.6 Case (iii): mass supported by the CSs (PIVI + HS): (**a**) part of the experimental setup; (**b**) force transmissibility curves

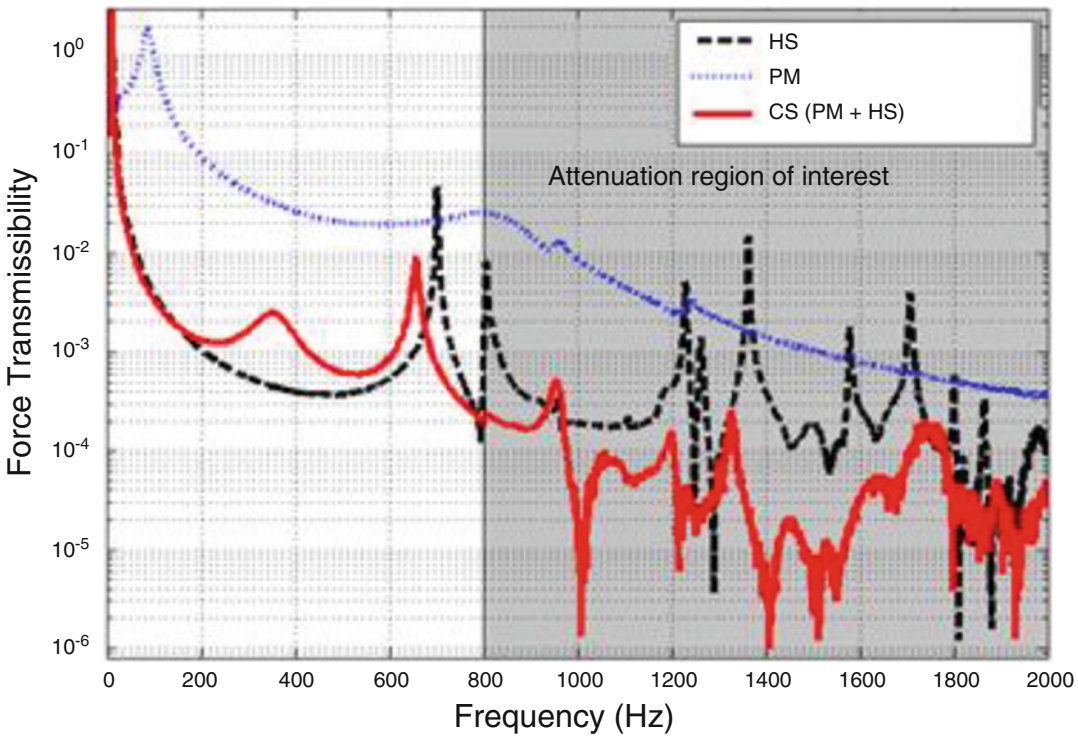

Fig. 14.7 Force transmissibility curves of the HS, the PIVI; and the CS (PIVI + HS)

Thus, with the CS it is possible to improve isolation of a source of vibration, in terms of force, with a PIVI device that has an AR in a specific frequency range, which acts as a "filter", and still maintains the flexibility of the support due to the combined HS. Although that flexibility is important for shock absorption, its details are out of the scope of this study.

14.4 Conclusions

The authors present an experimental study to evaluate, in terms of force transmissibility, three types of supporting devices (namely, HSs, PIVIs and CSs) that are tested while supporting a load mass of approximately 3.2 kg. The results demonstrate a reduction on the force transmitted from the mass to the foundation when supported by the CSs in alternative to the HSs.

Hence, from this point of view, the concept, design and application of PIVIs are sought to have a significant impact in the development of new vibration isolation devices, as they represent a real isolation improved alternative and/or solution for several mechanical applications.

Acknowledgments The authors would like to acknowledge: the Fundação para a Ciência e a Tecnologia (FCT) for the financial support of a working member of this work through the Instituto de Plasmas and Fusão Nuclear (IPFN), a research institute of Instituto Superior Técnico (IST) and through the PhD grant SFRH/BD/61186/2009; and Instituto de Engenharia Mecânica (IDMEC), a research unit of IST, for additional financial support.

References

1. Mead, D.J.: Passive Vibration Control. John Wiley & Sons, New York (1999)
2. Timoshenko, S., Young, D.H., Weaver Jr., W.: Vibration Problems in Engineering, 4th edn, p. 521. John Wiley & Sons, New York (1974). ISBN 0471873152
3. Policarpo, H.: A steel-composition cork phononic device for low frequency vibration attenuation. II LAETA Young Researchers Meeting 2012, FEUP, Porto, Portugal, 10–11 April 2012
4. Policarpo, H., Neves, M.M., Ribeiro, A.M.R.: Dynamical response of a multi-laminated periodic bar: analytical, numerical and experimental study. Shock Vib. **17**(4-5), 521–535 (2010)
5. Hussein, M.I., Leamy, M.J., Ruzzene, M.: Dynamics of phononic materials and structures: historical origins, recent progress, and future outlook. Appl. Mech. Rev. **66**(4), 040802 (2014)
6. Yuan, C., Jing, L., Jingdong, Z., Tao, H., Minggang, Z., Yuan, D.Y.: Phononic first band gap of quaternary layered periodic structure with the lumped-mass method. Shock Vib. **2014**, 9 (2014)
7. Guo, Y.Q., Fang, D.N.: Analysis and interpretation of longitudinal waves in periodic multiphase rods using the method of reverberation-ray matrix combined with the Floquet-Bloch theorem. J. Vib. Acoust. **136**(1), 13 (2013)
8. Xiao, Y., Wen, J., Wang, G., Wen, X.: Theoretical and experimental study of locally resonant and Bragg band gaps in flexural beams carrying periodic arrays of beam-like resonators. J. Vib. Acoust. **135**(4), 17 (2013)
9. Junyi, L., Balint, D.S.: An inverse method to determine the dispersion curves of periodic structures based on wave superposition. J. Sound Vib. **350**, 41–72 (2015)
10. Swinteck, N., Lucas, P., Deymier, P.A.: Optically tunable acoustic wave band-pass filter. AIP Adv. **4**, 124603 (2014)
11. Yan, Y., Laskar, A., Cheng, Z., Menq, F., Tang, Y., Mo, Y.L., Shi, Z.: Seismic isolation of two dimensional periodic foundations. J. Appl. Phys. **116**, 044908 (2014)
12. Aravantinos-Zafiris, N., Sigalas, M.M.: Band gaps in phononic strip waveguides. J. Appl. Phys. **111**, 123516 (2012)
13. Davis, B.L., Tomchek, A.S., Flores, E.A.: Analysis of periodicity terminations in phononic crystals. International Mechanical Engineering Congress and Exposition, Colorado, USA, 11–17 November 2011
14. Policarpo, H.: Analytical, numerical and experimental study of the dynamical response of helicoidal springs and periodic bars. M.Sc. thesis, Instituto Superior Técnico, Universidade Técnica de Lisboa, Portugal (2008)
15. Policarpo, H.: Numerical and experimental models for vibration attenuation using cork composite materials. Ph.D. thesis, Instituto Superior Técnico, Universidade de Lisboa, Portugal (2013)
16. Ungar, E.E.: Equality of force and motion transmissibilities. J. Acoust. Soc. Am. **90**(1), 596–597 (1991)
17. Lage, Y.E., Neves, M.M., Maia, N.M.M., Tcherniak, D.: Force transmissibility versus displacement transmissibility. J. Sound Vib. **333**(22), 5708–5722 (2014)

Chapter 15
Vibro-Impact NES: A Correlation Between Experimental Investigation and Analytical Description

Giuseppe Pennisi, Cyrille Stéphan, and Guilhem Michon

Abstract In this work the dynamics of a Vibro-Impact Nonlinear Energy Sink (VI-NES) is experimentally investigated via a harmonically forced single-degree-of- freedom linear oscillator (LO) to which a VI-NES is attached. Depending on external force amplitude and frequency, either a Strongly Modulated Response (SMR) or a constant amplitude response (CAR) is observed. In both cases an irreversible transfer of energy occurs from the LO towards the VI-NES: process known as passive Targeted Energy Transfer(TET). Furthermore, the problem is analytically studied by using the multiple scales method. For the fast and the slow time scales the Slow Invariant Manifold (SIM) is obtained. The 0-order SIM shows the existence of a stable and an unstable branch of solution, and of an energy threshold (a saddle-node bifurcation) for the solutions to appear. Subsequently the 1-order SIM is calculated to find the fixed points of the problem. When a stable fixed point exists, the system is naturally drawn to it and a CAR is reached. Otherwise a SMR state is established and no stable point is attained. Finally a good agreement between experimental and analytical results is shown.

Keywords Nonlinear dynamics • Vibro-Impact • Vibrations absorber • Experimental • Analytical

15.1 Introduction

A Nonlinear Energy Sink (NES) is defined as a vibration absorber with a relatively light mass, nonlinearly attached to a primary system whose vibrations are to be mitigated. The use of an NES as a vibration absorber has been object of interest in the field of Nonlinear Dynamics in the last decade as studies have shown that, if compared to the classical linear Tuned Mass Damper (TMD), it could be efficient in a broader frequency range and for a smaller addition of mass to the primary system. It has been shown that the nonlinear attachments can lead to an irreversible energy transfer from the primary system towards the NES, this process is known as Targeted Energy Transfer (TET) or pumping [1–5]. TET under external forcing has been investigated theoretically [6] and experimentally [7] showing that in addition to the steady state constant amplitude response regime, another type of response can arise referred to as Strongly Modulated Response (SMR). Many of the first works on Vibro-Impacts were based on numerical simulations. Recently, similarly to what was used for smooth nonlinearities, an analytical approach adopting the Multiple Scales method has been proposed in [8] for impulsive forces and extended to the case of a harmonic forcing in [9]. In [10] an experimental observation of the different regimes of response has been achieved for a VI-NES applied to a harmonically forced Linear Oscillator.

In this work the experimental and analytic study of the response regimes of a Vibro-Impact NES coupled to a Linear Oscillator is carried out. Firstly the experimental investigation is illustrated and the results presented. Subsequently the mathematical model is analytically treated and the Slow Invariant Manifold at the fast and slow scale obtained. Finally the analytical results are used to explain the behavior experimentally observed.

G. Pennisi (✉)
ONERA, The French Aerospace Lab, Université de Toulouse, ICA, ISAE, F-92320 Châtillon, France
e-mail: giuseppe.pennisi@onera.fr

C. Stéphan
ONERA, The French Aerospace Lab, F-92320 Châtillon, France
e-mail: cyrille.stephan@onera.fr

G. Michon
Université de Toulouse, ICA, ISAE, F-31055 Toulouse, France
e-mail: guilhem.michon@isae.fr

E. Wee Sit (ed.), *Sensors and Instrumentation, Volume 5*, Conference Proceedings of the Society for Experimental Mechanics Series, DOI 10.1007/978-3-319-29859-7_15

15.2 Experimental Tests

The experimental study has been conducted aiming to observe the behavior of the system and to explore the different existing types of response which can arise and how they are related to the external forcing in terms of magnitude and frequency.

The experimental setup is shown in Fig. 15.1 and is constituted by a primary single-degree-of-freedom linear oscillator (LO) to which the VI-NES is attached. The LO is harmonically forced by an electrodynamic shaker coupled to a vibrating table the LO is mounted on.

The system is forced by a swept-sine external force with constant amplitude and the displacement of the primary mass is measured by means of a Laser Doppler Vibrometer (LVD).

The modal parameters of the LO and the masses values are shown in Table 15.1. It is important to highlight the very small mass ratio between the VI-NES and the primary system, that is less than 1 %.

Figure 15.2 (left) shows the displacement spectra for the system with and without VI-NES. Figure 15.2 (right) shows the measured displacement time signals for a strongly modulated response. We can observe that two types of qualitatively different responses exist when the VI-NES is active, and depending on magnitude and frequency of external forcing either one or another can appear.

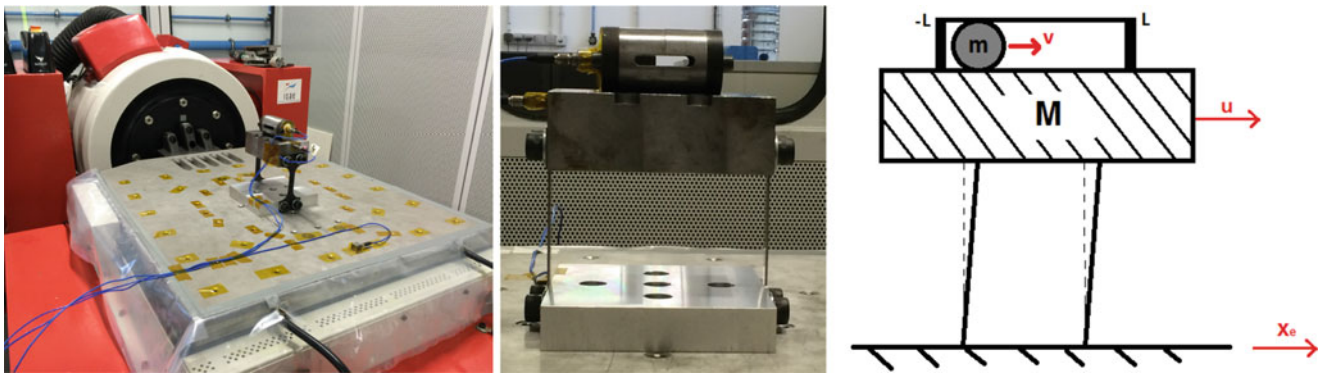

Fig. 15.1 LO coupled to VI-NES: the system mounted on the vibrating table (*left*), the LO and VI-NES (*center*) and its schematic (*right*)

Table 15.1 Modal parameters of primary system and mass value of the primary system M, of the VI-NES m and their ratio ϵ

f_0 (Hz)	K (N/m)	C (N/ms)	ξ	M (kg)	m (kg)	$\epsilon = m/M$
21.18	67,421	8.566	0.008	3.807	0.032	0.84 %

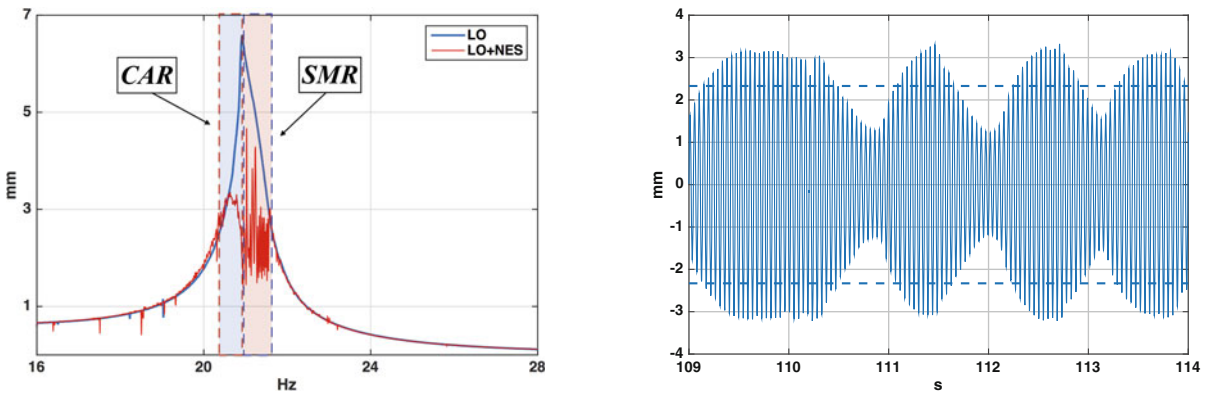

Fig. 15.2 *Left*: experimental spectra of the primary mass displacement with (*red*) and without (*blue*) the VI-NES. *Right*: recorded time signal of a strongly modulated response, the *dashed lines* indicate the amplitude of the LO without the VINES at the same forcing conditions

We can classify the quality responses as:

- Strongly Modulated Response (SMR): the primary system goes through alternatively increasing and decreasing amplitude cycles and therefore the fast oscillations appear to be modulated. This behavior is caused by a cycling activation and deactivation of the VI-NES.
- Constant Amplitude Response (CAR): the VI-NES is stably active and the amplitude of primary mass displacement remains constant.

The VI-NES seems to well accomplish its task as a vibration absorber since the response is actually reduced nearby the resonance of the primary system. This is the proof that a Targeted Energy Transfer occurs from the LO towards the VI-NES and that the energy is then dissipated by the impacts. It is important to highlight that this goal has been achieved although a proper sizing process has not been carried out and with a significantly small mass ratio $\epsilon = 0.84\,\%$. This result proves that the VI-NES is able to automatically tune itself to the primary system. This is a relevant general feature of nonlinear absorbers due to the absence of a natural frequency for these devices.

Looking at the spectrum of Fig. 15.2 one can draw the conclusion that there exists a criterion on primary mass displacement in order to activate the VI-NES. Indeed a threshold in amplitude/energy is observed beyond which the VI-NES goes through a 1:1 resonance with respect to the LO.

15.3 Analytic Treatment

The schematic of the model is presented in Fig. 15.1 (right). We define the variables u, v, and x_e as the displacements of the primary mass M, of the NES mass m and of the base respectively. We model the shocks as instantaneous impacts by using the basic concepts of Newton mechanics:

$$\dot{u}(t_j^+) - \dot{v}(t_j^+) = -r(\dot{u}(t_j^-) - \dot{v}(t_j^-)) \tag{15.1}$$

$$M\dot{u}(t_j^+) + m\dot{v}(t_j^+) = M\dot{u}(t_j^-) + m\dot{v}(t_j^-) \tag{15.2}$$

where t_j^+ and t_j^- are the time instants after and before the jth impact respectively. Equation (15.1) provides a relation for the relative velocity of the two colliding masses after and before the impact by use of the restitution coefficient $0 < r < 1$. That allows to characterize the impact from completely elastic $r = 1$ to completely plastic $r = 0$. Equation (15.2) expresses the momentum conservation throughout the impact. Then, the motion equations are:

$$\begin{aligned} \ddot{u} + 2\omega_0\xi\dot{u} + \omega_0^2 u + \frac{m(1+r)}{M+m}\sum_j \dot{w}^-\delta_j^- &= \omega_0^2 x_e + 2\omega\xi\dot{x}_e \\ \epsilon\ddot{v} - \frac{m(1+r)}{M+m}\sum_j \dot{w}^-\delta_j^- &= 0 \end{aligned} \tag{15.3}$$

where $\omega_0^2, = \mathrm{K/M}$, $2\omega_0\xi = \lambda/\mathrm{M}$ and $\epsilon = \mathrm{m/M}$. Defining the barycentric coordinates:

$$\begin{aligned} X &:= u + \epsilon v \\ w &:= u - v \end{aligned} \tag{15.4}$$

We end up with a system of two equations for X and w. Assuming that the mass of the VI-NES m is small with respect to the primary mass M, $\epsilon = m/M << 1$ can be use as a small parameter in multiple scale analysis.

By keeping only the ϵ^0-order terms, that yields:

$$\begin{aligned} \frac{\partial^2 X_0}{\partial t_0^2} + X_0 &= X_{e_0} \\ \frac{\partial^2 w_0}{\partial t_0^2} + X_0 + (1+r)\sum_j \frac{\partial w_0^-}{\partial t_0}\delta_j^- &= X_{e_0} \end{aligned} \tag{15.5}$$

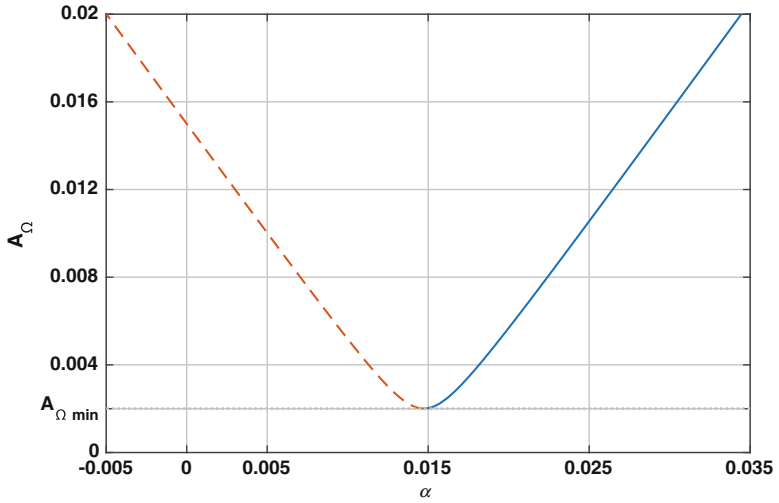

Fig. 15.3 Slow invariant manifold $-r = 0 : 65, L = 15\,\text{mm}$

where the subscript 0 means ϵ^0-order.

After a few steps we reach to the analytical definition of the Slow Invariant Manifold of the problem at ϵ^0 order. A_Ω and α are two variables related to displacements X and w.

$$\alpha = \frac{L \pm \sqrt{1+\sigma^2}\sqrt{A_\Omega^2 - A_{\Omega_{min}}^2}}{1+\sigma^2} \tag{15.6}$$

With $\sigma = \frac{2(1-r)}{\pi(1+r)}$, and where $A_{\Omega_{min}} = \frac{\sigma L}{\sqrt{1+\sigma^2}}$ is a minimum value of amplitude A_Ω for solutions to exist.

Equation (15.6) defines the Slow Invariant Manifold at the order ϵ^0. An important information we can draw from Eq. (15.6) is that a minimum for A_Ω exists for solutions to appear. This point mathematically represents a saddle-node bifurcation.

Once the ϵ^0-order SIM obtained, we push further our analysis and study system (15.3) at ϵ-order. Similarly, we reach an expression relating A and α (which will not be reported here for the sake of conciseness) which represents the ϵ order SIM. We should notice that the ϵ-order SIM is strongly dependent on magnitude and frequency of the external force. Its intersections with the ϵ^0-order SIM will represent the fixed points of the system (Fig. 15.3).

15.4 Experimental and Analytical Results Comparison

Figure 15.4a shows the experimental spectra of the primary mass displacement with and without the VI-NES attached. The two different kinds of regime, constant amplitude and strongly modulated responses, have been highlighted. We can see that for $F = 0.2\,\text{g}$, then for a low level of external force, the only type of response observed is the strongly modulated. Whereas, when the external force level increases the constant amplitude response appears and the transition from a type of regime to another is a function of the external force frequency.

Figure 15.4b shows the SIMs for two different case of external force level and frequency. For the lower level (Fig. 15.4b left) the only fixed points attainable are unstable points. And this for any frequency Ω. The only type of possible response is then the strongly modulated. This results is in perfect agreement with the experimental observations. For the higher level of eternal force (Fig. 15.4b right) the behavior of the SIMs is different. As Ω grows the system goes from a state of no-solution (VI-NES idle) to a state where two fixed points exist: one stable and one unstable. The stable one is reached and the system present a constant amplitude response. When Ω increases further, just before the disappearing of solutions, the two intersection of the SIMs are both unstable points. Then the system shows a strongly modulated response. Also this behavior is in perfect agreement with the experimental observations of Fig. 15.4a.

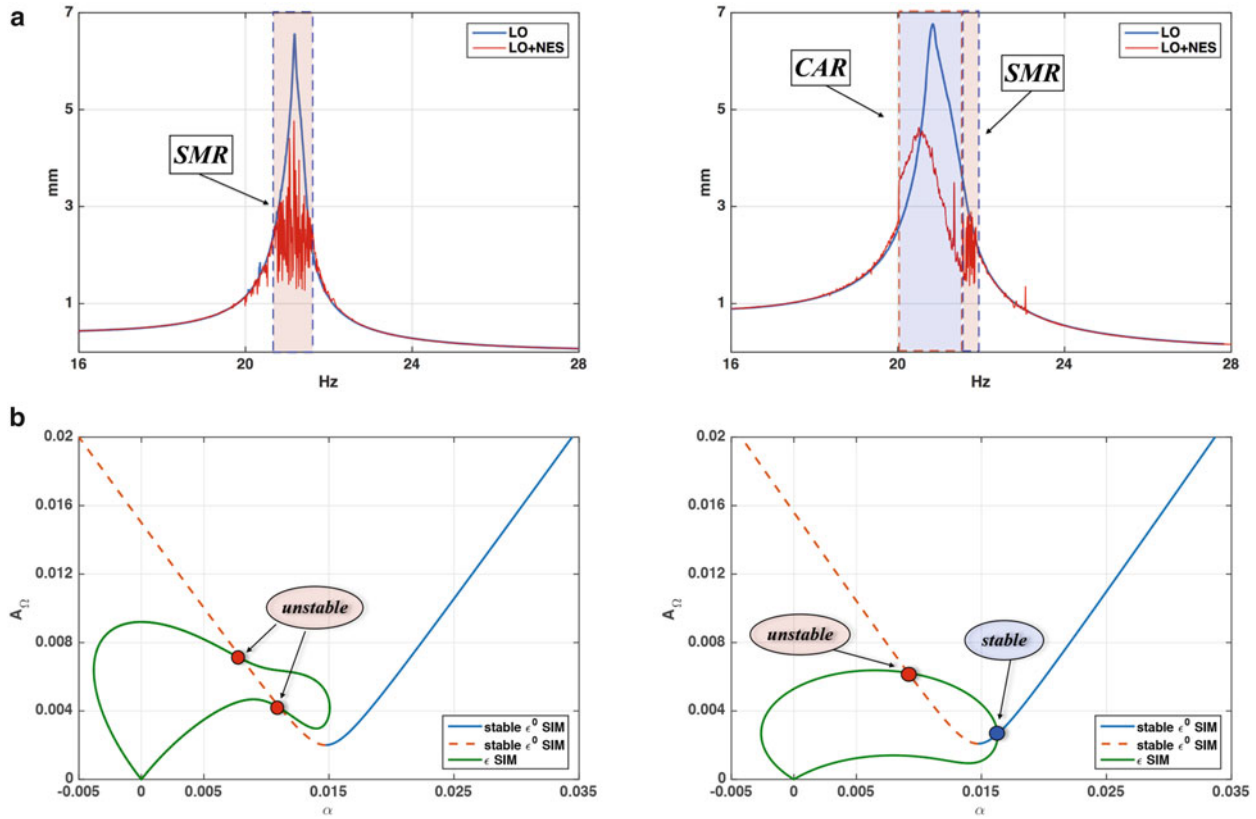

Fig. 15.4 Experimental and analytical evidence of the different regimes of response. (**a**) Spectra of primary mass displacement with and without VI-NES for $F = 0:2\,\mathrm{g}$ (*left*) and $F = 0:4\,\mathrm{g}$ (*right*). (**b**) ϵ^0- and ϵ-order SIMs for an external force level of $F = 0:2\,\mathrm{g}$ and $\Omega = \omega/\omega_0 = 1$ (*left*) and $F = 0.4\,\mathrm{g}$ and $\Omega = \omega/\omega_0 = 1.02$ (*right*)

15.5 Conclusion

In this work the dynamical behavior of a harmonically forced 1-dof LO coupled to a VI-NES has been explored. An experimental study has been carried out which showed the different regimes of response that may arise (constant amplitude and strongly modulated) and their dependence on the external forcing in terms of magnitude and frequency. The spectra of the primary mass displacement have shown that a Targeted Energy Transfer occurs and that the VI-NES may actually works as dynamic vibration absorber even with a very small mass ratio ($\epsilon = 0.84\,\%$). Then the system has been analytically studied by using the multiple scales method and the Slow Invariant Manifolds for the fast and the slow time scale have been obtained. Finally an analytical explanation to the experimental observations has been provided. These results will constitute the basis for further investigation and design of VI-NES as vibration absorber.

References

1. Gendelman, O.V.: Transition of energy to a nonlinear localized mode in a highly asymmetric system of two oscillators. Nonlinear Dyn. **25**, 237–253 (2001)
2. Vakakis, A.F., Gendelman, O.V.: Energy pumping in nonlinear mechanical oscillators: part II resonance capture. J. Appl. Mech. Trans. ASME **68**, 42–48 (2001)
3. Gendelman, O.V., Vakakis, A.F., Manevitch, L.I., McCloskey, R.: Energy pumping in nonlinear mechanical oscillators I: dynamics of the underlying Hamiltonian system. J. Appl. Mech. Trans. ASME **68**, 34–41 (2001)
4. Manevitch, L.I., Gourdon, E., Lamarque, C.H.: Towards the design of an optimal energetic sink in a strongly inhomogeneous two-degree-of-freedom system. ASME J. Appl. Mech. **74**, 1078–1086 (2007)
5. Kerschen, G., Lee, Y.S., Vakakis, A.F., McFarland, D.M., Bergman, L.A.: Irreversible passive energy transfer in coupled oscillators with essential nonlinearity. SIAM J. Appl. Math. **66**(2), 648–679 (2005)

6. Starosvetsky, Y., Gendelman, O.: Strongly modulated response in forced 2D of oscillatory system with essential mass and potential asymmetry. Physica D **237**(13), 1719–1733 (2008)
7. Gourc, E., Michon, G., Seguy, S., Berlioz, A.: Experimental investigation and design optimization of targeted energy transfer under periodic forcing. ASME J. Vib. Acoust. **136**(2), 021021 (2013)
8. Gendelman, O.: Analytic treatment of a system with a vibro-impact nonlinear energy sink. J. Sound Vib. **331**, 4599–4608 (2012)
9. Gendelman, O.V., Alloni, A.: Dynamics of forced system with vibro-impact energy sink. J. Sound Vib. (2015). http://dx.doi.org/10.1016/j.jsv.2015.08.020i
10. Gourc, E., Michon, G., Seguy, S., Berlioz, A.: Theoretical and experimental study of an harmonically forced vibro-impact nonlinear energy sink. J. Vib. Acoust. (2014). VIB-14-1008. doi:10.1115/1.4029285

Chapter 16
Fixed Base Modal Testing Using the NASA GRC Mechanical Vibration Facility

Lucas D. Staab, James P. Winkel, Vicente J. Suárez, Trevor M. Jones, and Kevin L. Napolitano

Abstract The Space Power Facility at NASA's Plum Brook Station houses the world's largest and most powerful space environment simulation facilities, including the Mechanical Vibration Facility (MVF), which offers the world's highest-capacity multi-axis spacecraft shaker system. The MVF was designed to perform sine vibration testing of a Crew Exploration Vehicle (CEV)-class spacecraft with a total mass of 75,000 lb, center of gravity (cg) height above the table of 284 in., diameter of 18 ft, and capability of 1.25 g pk in the vertical and 1.0 g pk in the lateral directions. The MVF is a six-degree-of-freedom, servohydraulic, sinusoidal base-shake vibration system that has the advantage of being able to perform single-axis sine vibration testing of large structures in the vertical and two lateral axes without the need to reconfigure the test article for each axis. This paper discusses efforts to extend the MVF's capabilities so that it can also be used to determine fixed base modes of its test article without the need for an expensive test-correlated facility simulation.

Keywords Modal testing • Vibrations • Base-shake • Environmental testing • Fixed base

16.1 Introduction

The Space Power Facility (SPF) is the home of the world's largest and most powerful space environment simulation facilities. The Space Simulation Vacuum Chamber is the world's largest, measuring 329 m (100 ft) in diameter by 400 m (122 ft) high. The Reverberant Acoustic Test Facility (RATF) is the world's most powerful spacecraft acoustic test chamber, and the Mechanical Vibration Facility (MVF) is the world's highest-capacity and most powerful spacecraft shaker system. The SPF is located at the NASA Glenn Research Center, Plum Brook Station, in Sandusky, Ohio. An aerial photograph of the SPF is shown in Fig. 16.1.

A plan view of the SPF is shown in Fig. 16.2. The highbay on the east side of the SPF, the Assembly Highbay, is primarily used for receiving, assembling, and preparing test hardware. The Vibroacoustic Highbay on the west side of the facility (formerly the Disassembly Highbay) houses the Mechanical Vibration Facility (MVF) and the Reverberant Acoustic Test Facility (RATF). North and south of the vacuum chamber and highbays are various supporting areas. North of the vacuum chamber are the facility control rooms, signal conditioning and instrumentation areas, machine shop, and a two-story office building. South of the vacuum chamber are the electric substations, cryogenics room, vacuum room, and mechanical rooms. The south outdoor courtyard areas behind the SPF support the liquid and gaseous nitrogen storage bottles, vaporizers, and cooling tower.

The test hardware was received and primarily assembled in the SPF assembly area. The room is temperature and humidity controlled. The SPF assembly area has a data acquisition area, a loading/handling area of about 46 m (150 ft) × 23 m (75 ft), an overhead crane with capability of 25 tons and crane hook maximum free height of 22 m (72 ft). The main door to the SPF is located on the east side of the lab and has dimensions of 15.2 m (50 ft) tall × 15.2 m (50 ft) wide.

L.D. Staab • J.P. Winkel • V.J. Suárez • T.M. Jones
NASA Glenn Research Center, 21000 Brookpark Road, Cleveland, OH 44135, USA

K.L. Napolitano (✉)
ATA Engineering, Inc., 13290 Evening Creek Drive South, Suite 250, San Diego, CA 92128, USA
e-mail: kevin.napolitano@ata-e.com

E. Wee Sit (ed.), *Sensors and Instrumentation, Volume 5*, Conference Proceedings of the Society for Experimental Mechanics Series, DOI 10.1007/978-3-319-29859-7_16

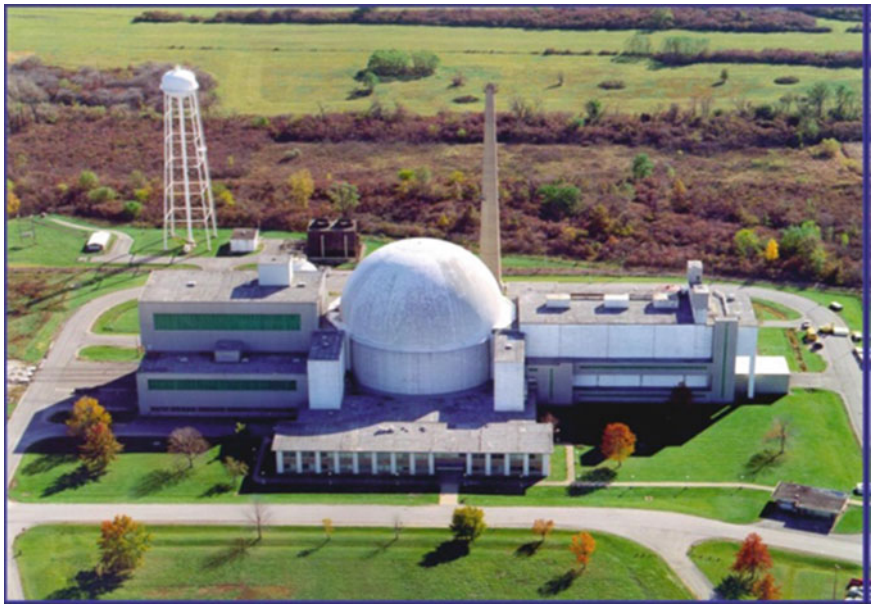

Fig. 16.1 Aerial view of space power facility

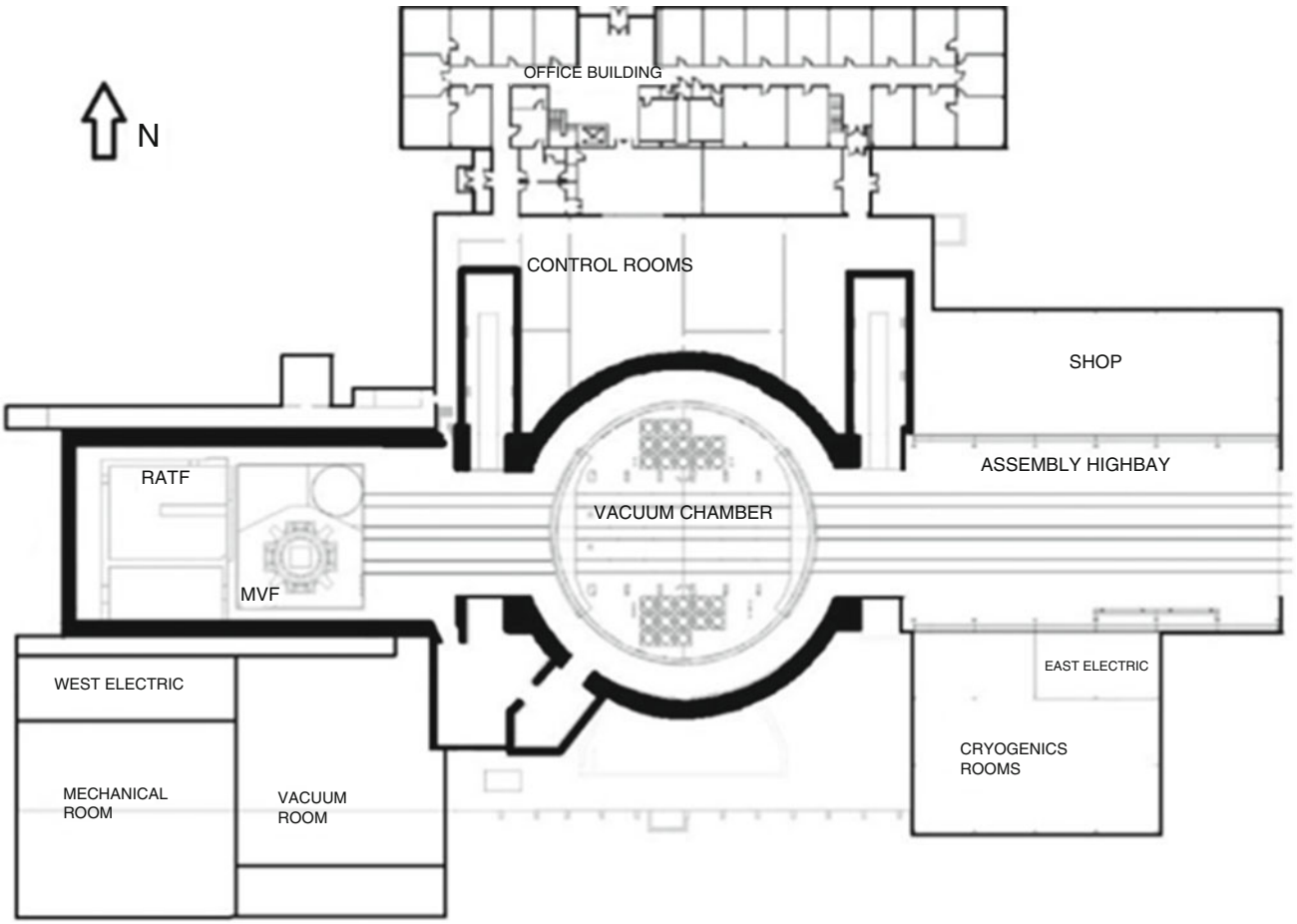

Fig. 16.2 Plan view of Plum Brook Station

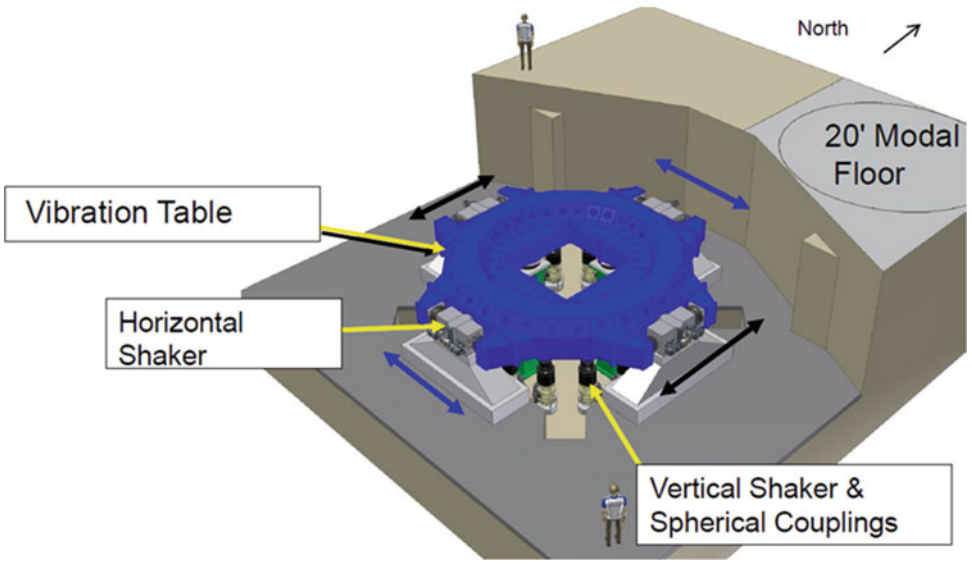

Fig. 16.3 Plan view of MVF three-axis base shake table

16.1.1 Mechanical Vibration Facility (MVF)

The MVF is a three-axis vibration system that consists of reaction mass, 4 airbags, 4 horizontal servohydraulic actuators, 16 vertical servohydraulic actuators mounted on double spherical couplings, aluminum table, hydraulic supply system, Table Control System (TCON), Vibration Control System (VCON), and the same Facility Control System (FCS) used by the RATF. The MVF was designed to perform sine vibration testing of a CEV-class spacecraft with a total mass of 75,000 lb, center of gravity (cg) height above the table of 284 in., diameter of 18 ft, and capability of 1.25 g pk in the vertical and 1.0 g pk in the lateral directions.

The MVF will apply vibration in each of the three orthogonal axes (not simultaneously) with one direction in parallel to the Earth-launch thrust axis at 5–150 Hz, 0–1.25 g-pk vertical, and 5–150 Hz, 0–1.0 g-pk for the horizontal axes. Vertical, or the thrust axis, shaking is accomplished by using 16 vertical actuators manufactured by TEAM Corporation, each capable of a dynamic force of 133 K-Newton (30,000 lbf). The 16 vertical actuators allow for testing of up to a 34,019 kg (75,000 lb) article at the previously stated frequency and amplitude limits. The 16 vertical actuators are locked out during horizontal shaking. Horizontal shaking is accomplished through use of four TEAM Corporation horizontal actuators; two in each direction, each capable of a dynamic force of 380 K-Newton (85,400 lbf). The horizontal actuators are used during vertical testing to counteract cross-axis forces and overturning moments. Additionally, the MVF provides excitation, control, and data acquisition and processing capabilities. Figure 16.3 shows the MVF plan view. This vibration system is anchored to a reaction mass of 2041 tons (4.5 million pounds), which itself is secured to the underlying ground via rock bolts. MVF can support up to 8 drive signals (i.e., independent references), up to 12 control accelerometers (i.e., control inputs), up to a total of 32 response limiting channels, and another 32 monitoring channels.

This paper discusses efforts to use the MVF to conduct modal tests which yield fixed base results, including characterization of the MVF table dynamics, and methods to extend the usable frequency range of the table for modal tests.

16.2 Review of Fixed Base Correction Techniques

The desire to extract fixed base modes from structures mounted on shake tables has received a great deal of attention in recent years [1–6]. Difficulties arise when the shake table moves in more than one direction, such as when the inertia forces imparted by the test article cause the table to rock at the combined system natural frequency rather than the test article fixed base natural frequency.

Currently, there are two promising methods that account for shake table motion. The first, developed by Sandia National Laboratories [7], is a transformation of measured modes to fixed base modes, and the second, developed by ATA Engineering [8], uses shake table accelerations as references when calculating FRFs. The key element in both methods is using a small number of shapes that adequately describe shaker table motion.

16.2.1 Mode Shape Correction Method

The first method, hereafter called the mode shape correction method, assumes that fixed base modes are a linear combination of the test-measured mode shapes. Conceptually, a coordinate transformation matrix between the measured modes and the resultant fixed base modes is calculated by enforcing a constraint that the base does not move. In practice, the constraint is relaxed to a small number of shapes associated with the largest motion of the shake table.

Once the shapes are defined, the coordinate transformation matrix is calculated and used to turn the equation of motion in modal coordinates to the fixed base equation of motion. Natural frequency, damping, and fixed base shapes in modal coordinates are then solved for from the fixed base equation of motion.

16.2.2 FRF Correction Method

The second method, hereafter called the FRF correction method, uses a small number of shapes associated with the largest motion of the shake table as virtual degrees of freedom. A coordinate transformation matrix defining the linear relationship between the physical degrees of freedom on the shaker table and the virtual degrees of freedom associated with the shape is created by taking the pseudo-inverse of these shapes. Virtual channels are created by applying the coordinate transformation to the measured time-history functions, and then these channels, along with load cells associated with shakers mounted on the test article, are used as references when calculating frequency response functions. Fixed base modes are then estimated using modal analysis techniques. In practice, there must be at least as many linearly independent excitations applied to the table as there are deformed shapes used as references.

Some advantages and disadvantages to using both methods are presented in Table 16.1. The mode shape correction method requires that the modal mass must be calculated as one of the modal parameters, which means the peaks in the FRF must be clearly defined in the drive point FRF. It also requires that the fixed base modes must be a linear combination of the measured mode shapes; the accuracy of the method degrades as this requirement is violated. The clear advantage of using this method, however, is that the number of shapes used to define the table deformations is not limited to the number of excitations applied to the table. On the other hand, the major drawback of the FRF correction method is that the number of table shapes is limited by the number of linearly independent excitations applied to the table. The advantage is that fixed base modes are calculated directly from the calculated fixed base FRF.

16.2.3 Determination of Table Shapes

The key to both methods is using a reduced set of shapes to describe table motion. A single optimal method for determining these shapes has not yet been defined, and there are several ways to calculate the shapes. All methods involve parsing test or analysis data down to the degrees of freedom that measure table motion. A list of shape estimation options is as follows:

Table 16.1 Comparison of mode shape correction and FRF correction methods

Method	Mode shape correction	FRF correction
Advantages	Number of constraint shapes not limited to number of shakers.	Direct measurement of fixed base modes.
Disadvantages	Modal mass must be calculated.	Number of constraint shapes must be less than or equal to the number of exciters mounted to the shaker table.
	Fixed base modes must be linear combination of measured modes.	

1. Singular value decomposition (SVD) of time-history functions
2. SVD of FRFs
3. SVD of analysis mode shapes
4. A set of analysis mode shapes
5. SVD of test measured mode shapes
6. A set of test measured mode shapes
7. Calculation of rigid body shapes based on geometry
8. Measured rigid body shapes from test

One can use any combination of these methods to define the table shapes. The accuracy of the final results is commensurate with how well these estimates reflect the actual table motion.

16.3 Modal Test of Free-Free Bare MVF Table

Figure 16.4 shows the MVF and actuators. In the back of the photograph is the MVF table, which is currently installed on the actuators.

Figure 16.5 is the assembled MVF table. This is the test article for this modal survey. The torus-shaped center of the table is a one-piece 5083 aluminum weldment. Eight "ears" (also 5083 aluminum) are fastened to the center weldment. Additionally, there are a total of eight ballast plates that can be added to the table. The assembled table with no ballast plates weighs 23.51 metric tons (51,826 lb). The assembled table is approximately 0.1 m × 0.6 m × 0.6 m (4′ × 26′ × 26′).

Fig. 16.4 MVF table (*above*) separated from MVF pit (*below*) containing actuators and support structure

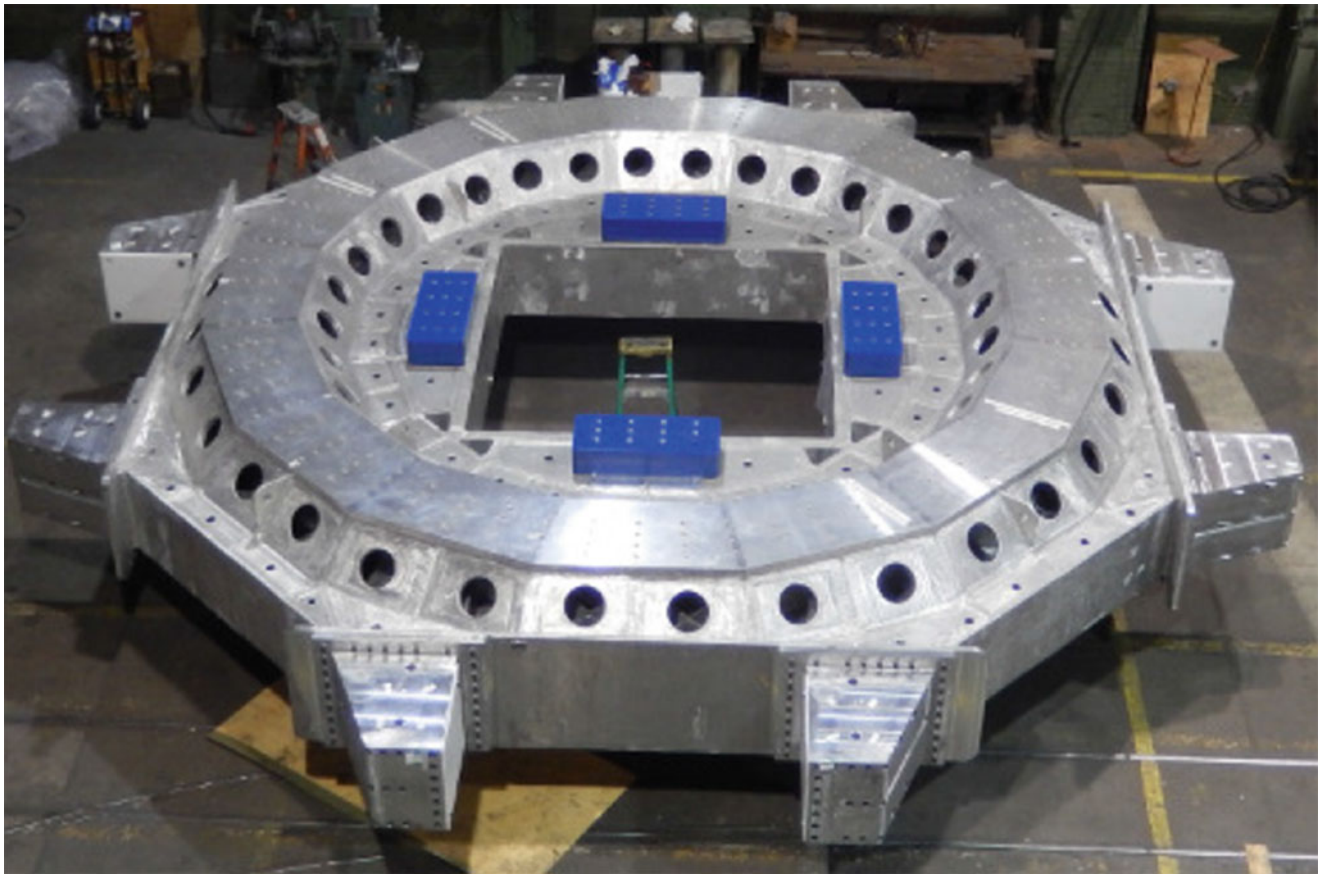

Fig. 16.5 MVF resting on airbags

16.3.1 Test Setup

The test setup is intended to simulate close to a free-free boundary condition. The table is mounted on airbags. There are four large airbags under the table supporting it in the vertical direction (Fig. 16.6), and there are four additional airbags providing lateral support (Fig. 16.7). The lateral airbags are mounted to every other table ear. A stability analysis was completed to ensure that the table would remain suspended and not tip over.

16.3.2 Instrumentation

Modal hammer: A large-sized modal hammer (PCB 086C50) with a brown rubber medium-soft tip was used to tap on the MVF table.

Response accelerometers: Up to 66 response accelerometers were mounted to the MVF table to capture the dynamic responses. A drive point response accelerometer located close to the tapping point of the modal hammer was also used. If the drive point did not correspond to an existing response accelerometer location, an additional accelerometer was mounted at the drive location of impact for each point of impact, or an existing nearby response accelerometer was used. All instrumentation was in calibration.

Fig. 16.6 Vertical airbags

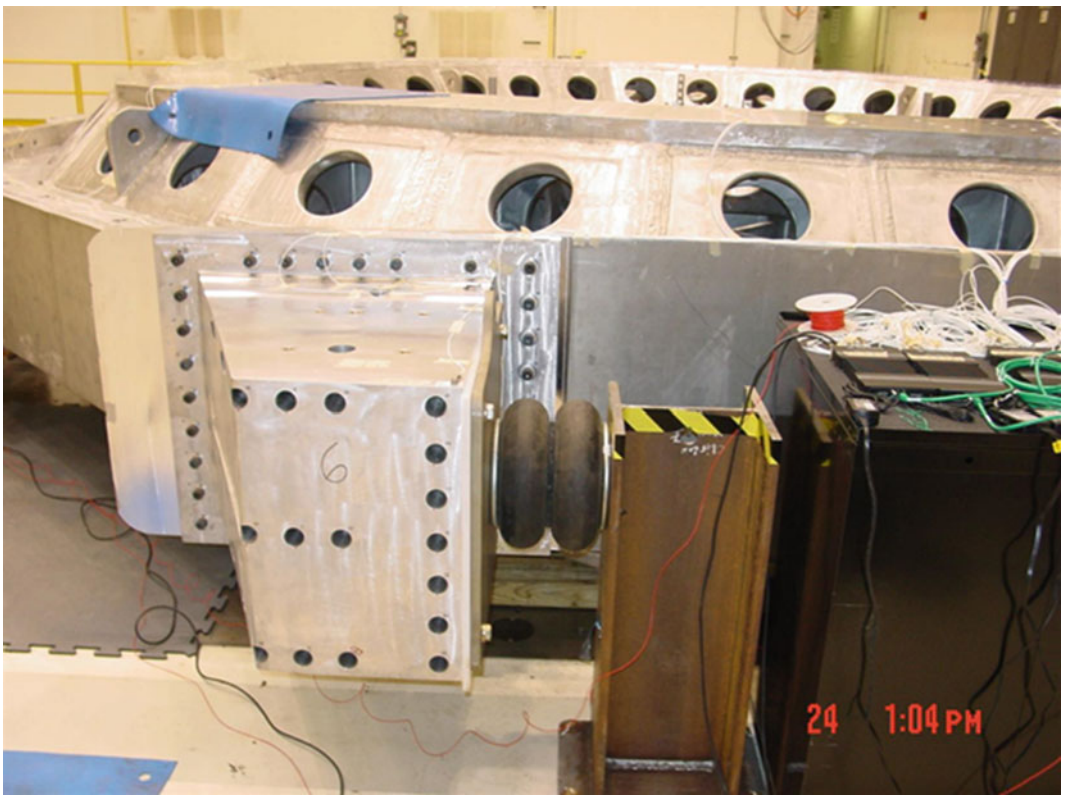

Fig. 16.7 Horizontal airbags

16.4 Test Results

A modal pretest analysis was performed on the MVF table using the test configuration finite element model (FEM), and a test analysis model (TAM) for test configuration 1 was produced. The TAM consists of the selection and location of test degrees of freedom, the associated test display model (TDM) that is used to visually display mode shapes, the reduced FEM produced by reducing the full FEM to the test DOF using a Guyan reduction, the mass and stiffness matrices of the reduced FEM used to compute the cross-orthogonalities (x-orthos) between the full FEM and reduced FEM mode shapes, and the x-orthos themselves. The TDM for all test configurations is shown in Fig. 16.8.

Figure 16.9 shows the full FEM from which the TDM was derived.

The pretest cross-orthogonality table is shown in Table 16.2. This x-ortho table shows that the test DOF are sufficient to capture the desired FEM mode shapes and support a model correlation effort.

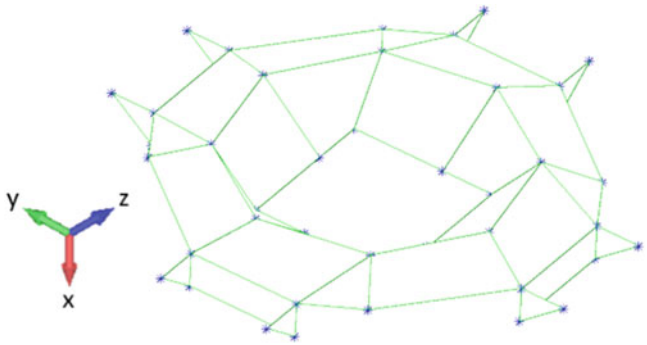

Fig. 16.8 MVF table test display model

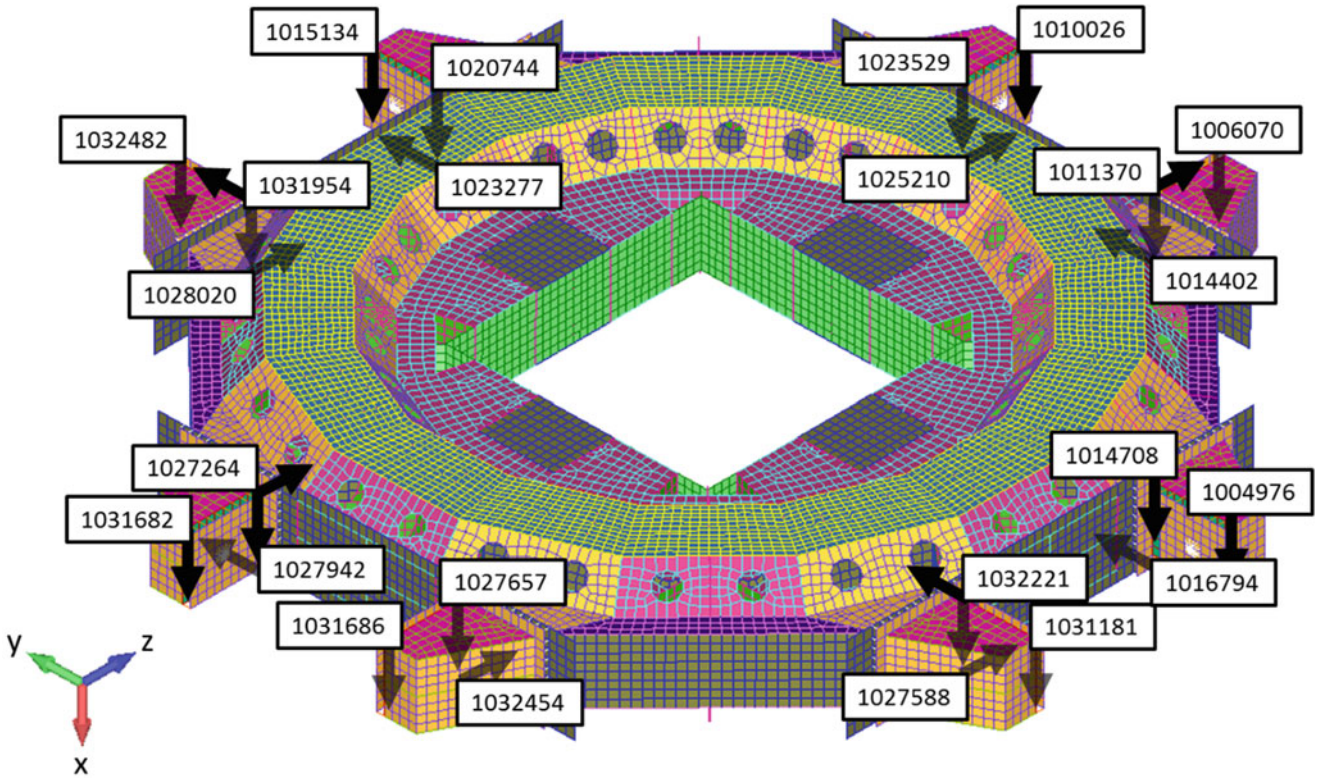

Fig. 16.9 MVF table full finite element model

Table 16.2 Pretest analysis x-ortho table

Mode	Hz	Hz %diff	PORTHO	XORTHO	Mode Shape Description
7	50.24	1.3	95.25	99.90	Potato Chip +/- Z ears in-phase oposite of +/- Y ears
8	53.12	1.8	92.74	99.83	Potato Chip +YZ / -YZ corners in-phase oposite of +Y-Z / -Y+Z
9	90.60	5.2	70.11	99.98	Squeeze Mode (motion in YZ plane only) +YZ / -YZ corners in-phase oposite of +Y-Z / -Y+Z
10	97.69	4.0	85.86	99.91	Oil can mode
11	107.92	4.8	82.30	99.82	"+Y-Z / -Y+Z ear torsion about +Y-Z axis
12	107.92	4.7	82.60	99.83	"+YZ / -YZ ear torsion about +YZ axis
13	116.52	5.4	69.66	99.90	Squeeze Mode (motion in YZ plane only) +/- Z ears in-phase oposite of +/- Y ears
14	133.58	5.9	79.45	99.66	Every Ear out bending out-of-phase with adjacent ear
15	138.34	5.8	68.29	73.95	Second oil can mode (two lobes in Y-Direction)
16	138.34	5.4	68.39	73.80	Second oil can mode (two lobes in Z-Direction)

Key:
Mode Pair

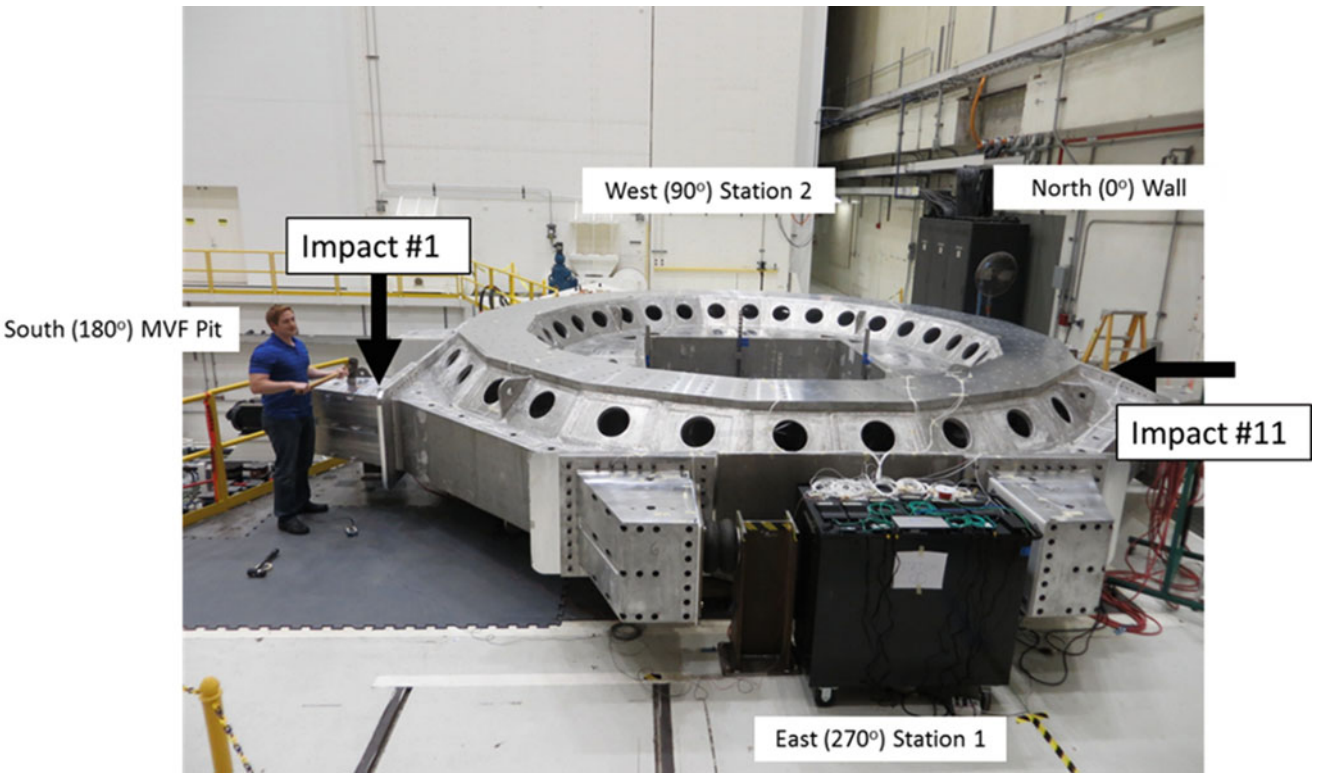

Fig. 16.10 Impact locations

Modal survey testing was conducted using several different impact points in order to excite the modes of interest. The impact locations were selected using engineering judgment based on the FEM mode shapes seen. The tapping locations are shown in Fig. 16.10. Impact location 1 was at the top face of the southeast ear in the +X axis. Impact location 11 was at the north outward face between the ears in the −Z axis. Upon postprocessing the data, it was shown that impact location 1 captured all the modes of interest.

Modal extraction was relatively straightforward for this test and did not require any manual "tweaking" of the extracted modal parameters. Table 16.3 lists all of the extracted modes, and parameters used for all of the modes extracted.

Table 16.3 Bare table test modal parameters

Modal parameters			
ID1:	Poly reference	REF:	1X+
PARM	Shape	Frequency (Hz)	Damping (%)
LABEL	REC		
1	1	52.727	0.048
2	2	54.978	0.112
1	11	96.187	0.034
4	4	102.851	0.065
5	5	111.015	0.314
6	6	114.839	0.057
1	1	123.766	0.31
1	8	140.753	0.047
2	9	142.018	0.054
3	10	144.334	0.042

Table 16.4 Initial x-ortho matrix

			Analysis Modes										
	Mode #		7	8	9	10	12	11	13	14	16	15	Frequency
		Freq (Hz)	50.29	53.25	91.05	97.91	108.00	108.00	116.93	133.70	139.02	139.02	% Error
Test Modes	1	52.73	1.00										-4.62%
	2	54.98		1.00									-3.15%
	3	96.19			1.00								-5.34%
	4	102.85				0.99							-4.81%
	5	111.01					0.99	0.14					-2.72%
	6	114.84					0.17	0.97			0.13		-5.96%
	7	123.77							1.00				-5.52%
	8	140.75								0.99	0.11		-5.01%
	9	142.02								0.15	0.97		-2.11%
	10	144.33										0.98	-3.68%

16.5 Finite Element Model Updating

An initial cross-orthogonality (x-ortho) between experimental and analytical modal vectors was calculated to check the adequacy of the FEM. Table 16.4 shows a small frequency error on mode 5 and small cross-talk in a few modes. Ideally, the goals for acceptable correlation are absolute values of diagonal terms greater than 0.9 with absolute values for all off-diagonal terms being less than 0.1 for significant modes. For the fundamental frequency, the goal in each axis is ± 5 %, while the correlation goal for higher-order frequencies is agreement within ± 10 %.

Part of the correlation effort was to update the FEM and rerun the x-ortho until the correlation goals were achieved. The lateral stiffness of the airbags was changed to match the actual test configuration, the density of the table was changed to represent the actual mass of the hardware, the horizontal actuator attachment plates were removed in the FEM, and four horizontal airbag ear plate attachments were added in the FEM to represent test configuration 1. After making those changes x-ortho was again calculated, and it is shown in Table 16.5. This table shows that the goals were achieved.

Figure 16.11 shows the mode shapes of the correlated FEM without the ballast plates.

16.6 Data Analysis of Bare MVF Table on Actuators

To assess the feasibility of using the MVF table for fixed base modal testing, sine-sweep and random data from bare table testing were analyzed. A total of four tests were analyzed: X (vertical) sine sweep, Y (lateral) sine sweep, Z (lateral) sine sweep, and multi-DOF random with all actuators activated (X vertical configuration). A list of test runs is presented in Table 16.6. Over 40 accelerometer channels were mounted on the MVF table, and forces were measured at a total of 11 out of a possible 20 actuators. Actuator forces were not measured directly. Instead, oil pressure in the double spherical couplings was used to estimate force in the vertical actuators, and actuator pressure differential was used to estimate force

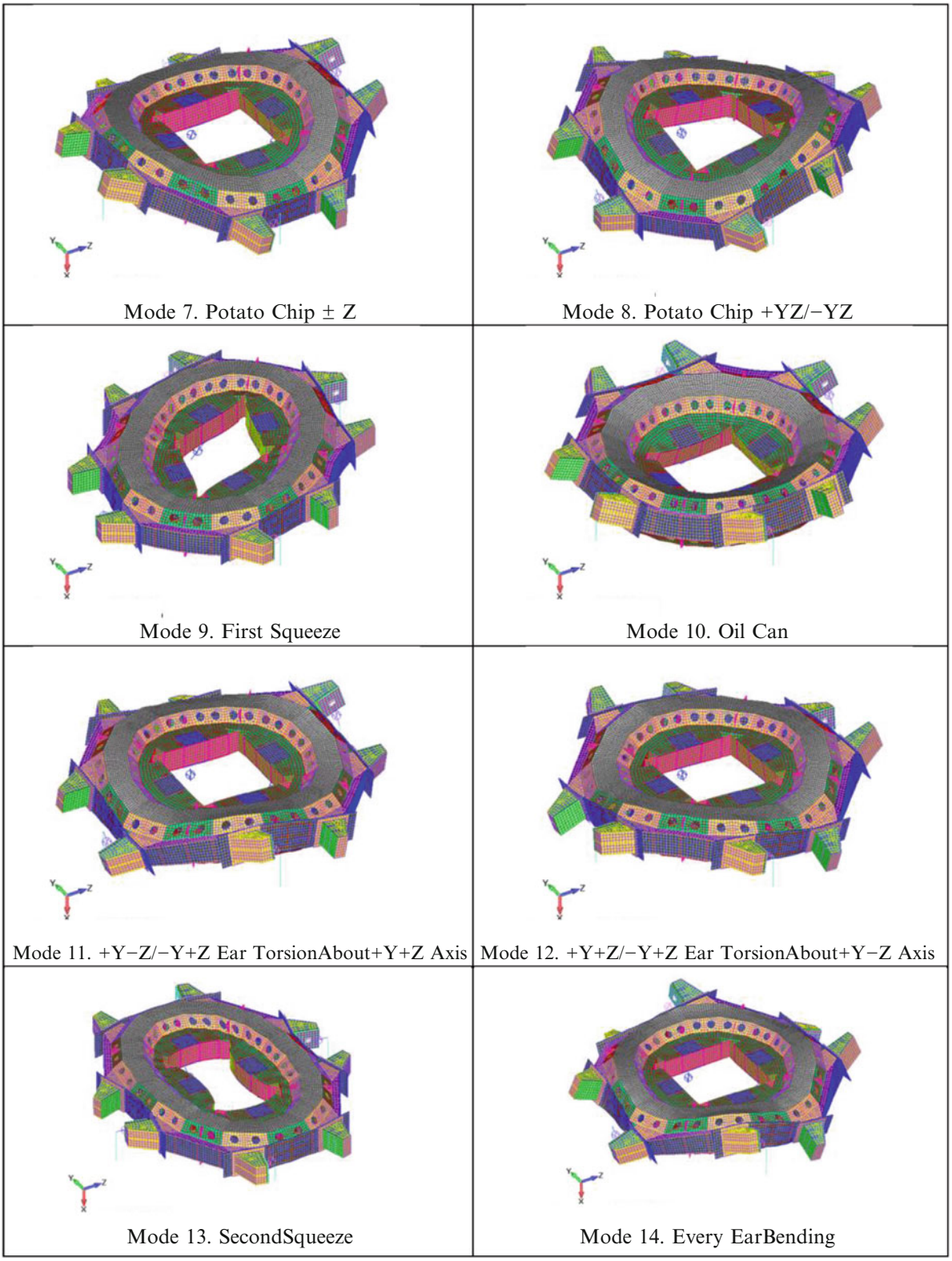

Fig. 16.11 MVF free-free mode shapes

Table 16.5 Final x-ortho matrix for MVF table

			Analysis Modes										
	Mode #		7	8	9	10	11	12	13	14	15	16	Frequency
		Freq (Hz)	52.78	55.60	94.77	102.39	111.84	114.98	122.11	140.80	144.22	146.27	Error %
Impact Test Modes	1	52.73	1.00										0.10%
	2	54.98		1.00									1.13%
	3	96.19			1.00								-1.47%
	4	102.85				0.99							-0.45%
	5	111.01					1.00						0.74%
	6	114.84						0.99			0.14		0.12%
	7	123.77							1.00				-1.33%
	8	140.75								0.99	0.11		0.03%
	9	142.02								0.15	0.97		1.55%
	10	144.33										0.98	1.34%

for the in-plane actuators. Pressure readings in 9 of the 16 vertical actuators were not measured, but at least one pressure in each four-actuator quadrant was measured. Future testing will record all pressures, but measurement of a reduced number of forces was sufficient for this preliminary test because at least one force associated with each of the eight individual sources was measured.

A test display model identifying the accelerometer locations and the actuator attachment point locations is presented in Fig. 16.12. Accelerometers were selected to be able to observe and differentiate the first six rigid body modes and several flexible body modes of the bare MVF table.

16.6.1 MVF Bare Table Sine-Sweep Test Data

Acceleration and force time histories were collected with the MVF performing 5–150 Hz sine-sweep tests in the X-axis (vertical), Y-axis (lateral), and Z-axis (lateral) with a bare MVF Table. These tests were performed prior to installing the verification test article (VTA) in order to ring out basic system performance characteristics. For the X-axis shakes, all 20 actuators are active and driven by eight source signals, with the vertical actuators providing X-axis translation and minimizing pitching about the lateral Y and Z axes and the horizontal actuators minimizing the lateral Y and Z axes translations. For the Y- and Z-axis shakes, the MVF table is locked down so that the vertical actuators are not active and only the horizontal actuators are active, producing translation in the shake axis and minimizing translation in the off-axis and rotation about the X-axis.

The number of independent references that can be used to calculate FRFs is equal to the lesser of the number of independent source signals and the number of actuators. Since all of the source signals for the sine-sweep tests are correlated, only single reference FRFs can be calculated. Note that this reference can be a single data channel or a linear combination of channels. The acceleration/acceleration (A/A) FRFs computed here use the average acceleration in the drive direction of the MVF table as the reference.

One can view the resulting FRFs to determine the frequency at which the table moves in a non-drive direction, such as the table rocking. The FRF will be constant as a function of frequency if there are no dynamics. A summary plot of the FRFs for each of the three sweeps using the power spectrum mode indicator function (PSMIF) is presented in Fig. 16.13, which can be used to observe the significant behavior of the table and shows the response of the table in the drive direction. The vertical configuration response is amplified above 30 Hz, while the lateral configuration accelerometers start their amplification above 60 Hz. It is expected that the maximum frequency for the lateral configuration will decrease as the size of the structure mounted to the table increases.

Lower-frequency dynamics are better viewed by observing accelerometer response in the off direction. The PSMIFs for each sine-sweep test, broken out by accelerometer direction, are presented in Fig. 16.14. The X-direction response shows low-responding, low-frequency modes below 20 Hz, which are likely rigid body modes the controller is attempting to remove with the in-plane shakers. There is also a very highly damped dynamic amplification that peaks near 70 Hz. There is very little dynamics associated with the X-axis motion for the Y- and Z-direction sine sweeps below 80 Hz. This is likely due to the fact that the vertical actuators are locked and not activated. The control system is doing a good job of minimizing the off-axis in-plane motion in the Y- and Z-direction sine sweeps, but there is evidence of some dynamic amplification.

Table 16.6 Test runs analyzed

Run title	Configuration	Excitation
SV0063_UFF.ATI	X (vertical)	5–150 Hz sine sweep
SV0098_UFF.ATI	Z (lateral)	5–150 Hz sine sweep
SV0110_UFF.ATI	Y (lateral)	5–150 Hz sine sweep
SV0115_UFF.ATI	X (vertical)	10 min random

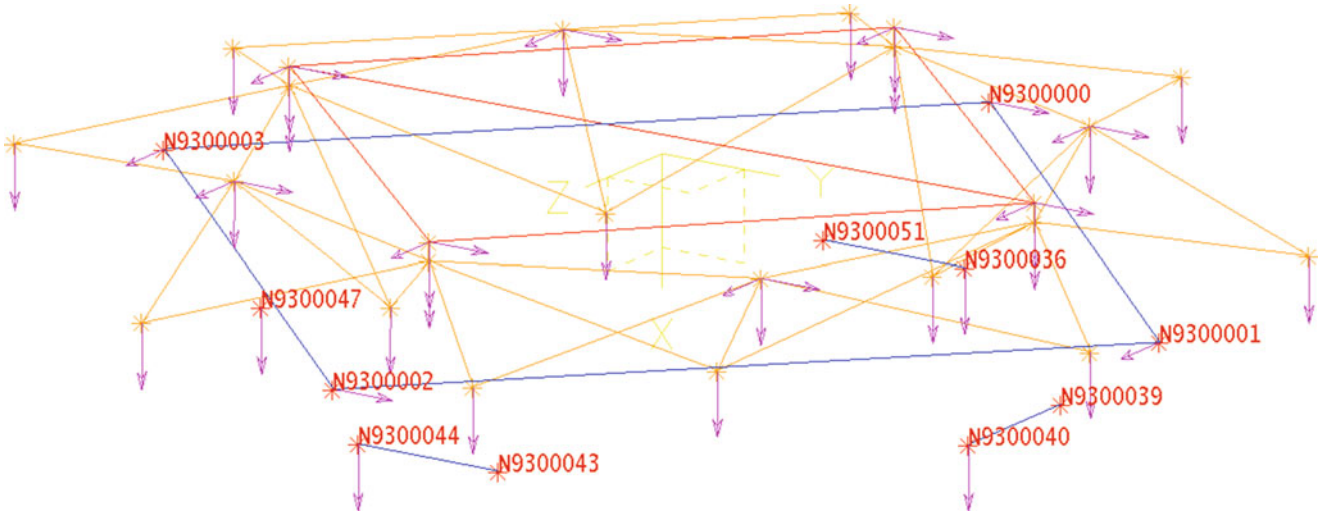

Fig. 16.12 Test display model showing accelerometer and load cell locations; each *arrow* corresponds to an accelerometer or load produced by the actuators and load application locations are identified with node labels

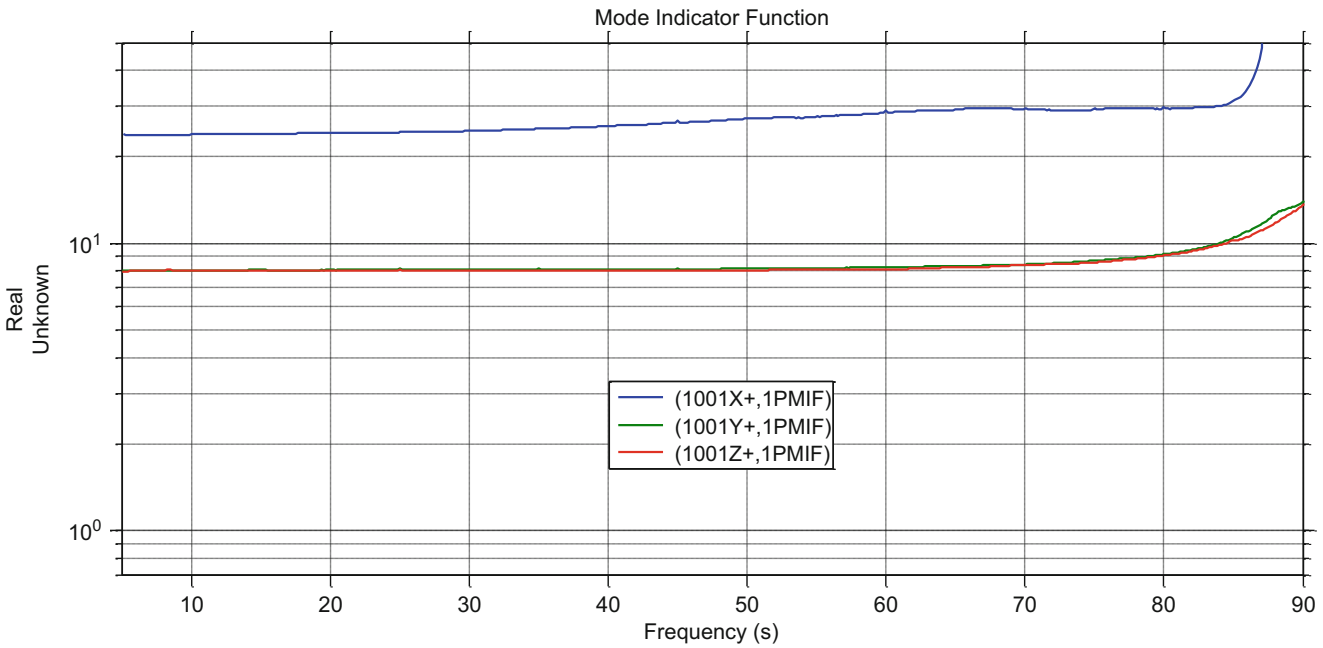

Fig. 16.13 Sine-sweep test PSMIF comparisons: 1001X+ X-axis shake reference (*blue*), 1001Y+ Y-axis shake reference (*green*), 1001Z+ Z-axis shake reference (*red*)

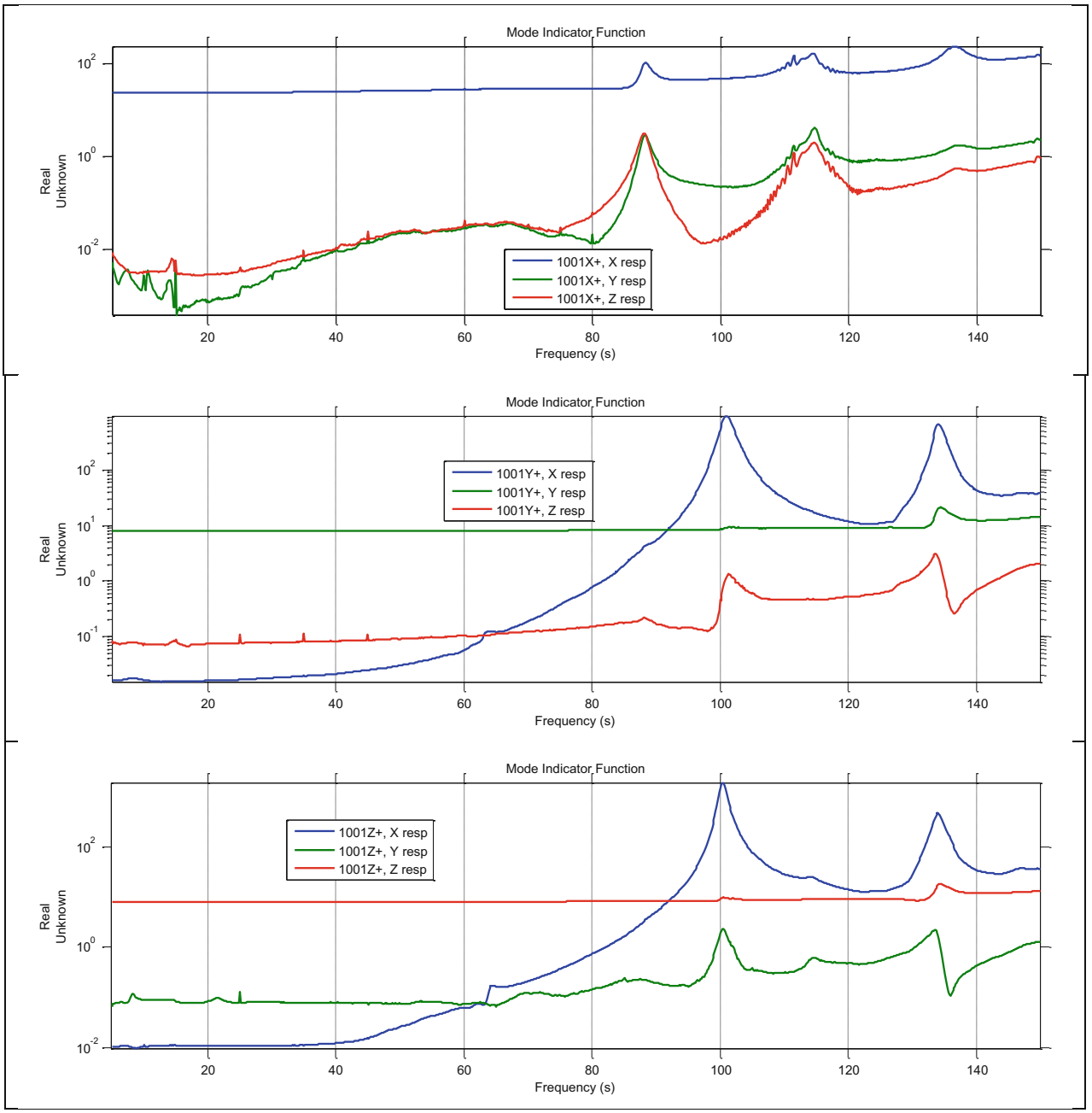

Fig. 16.14 Power spectrum mode indicator functions for sine-sweep tests by accelerometer group

16.6.2 MVF Bare Table Random Data

Ten minutes of low-level random base input using the eight independent actuator groups (four vertical, four lateral) from 5 to 150 Hz was collected when the MVF was configured for testing in the vertical direction. This random characterization run is necessary to provide the control system the transfer functions needed to provide a pure vertical (X) direction sine-sweep excitation. A representative force measurement from each of the eight independent actuator groups was used to calculate acceleration/force (A/F) FRFs. Viewing the complex mode indicator function (CMIF) of the A/F FRF identifies the rigid body and flexible modes of the table (Fig. 16.15). The reason the CMIF is used instead of the PSMIF is that the CMIF can identify closely spaced or lightly excited modes. Three rigid body modes are near 10 Hz, and three more rigid body modes are below 5 Hz. Flexible modes are observable beginning near 50 Hz.

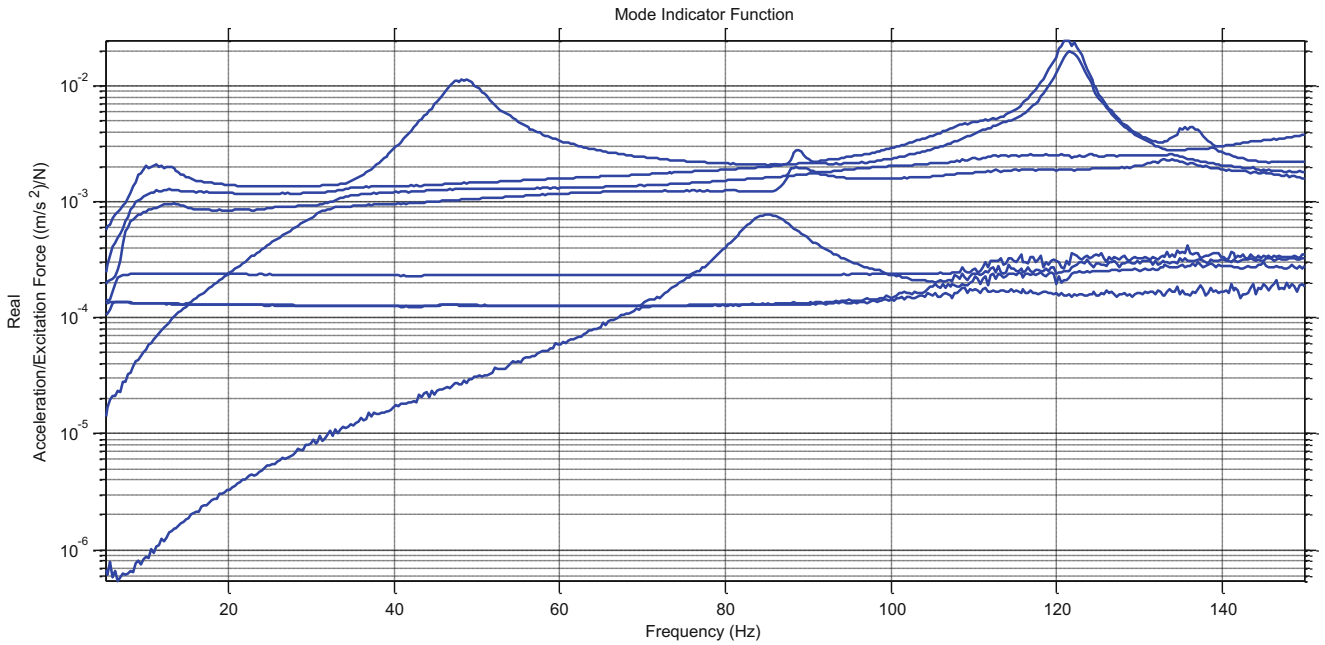

Fig. 16.15 Complex mode indicator function A/F FRF, with six flexible table modes above 40 Hz

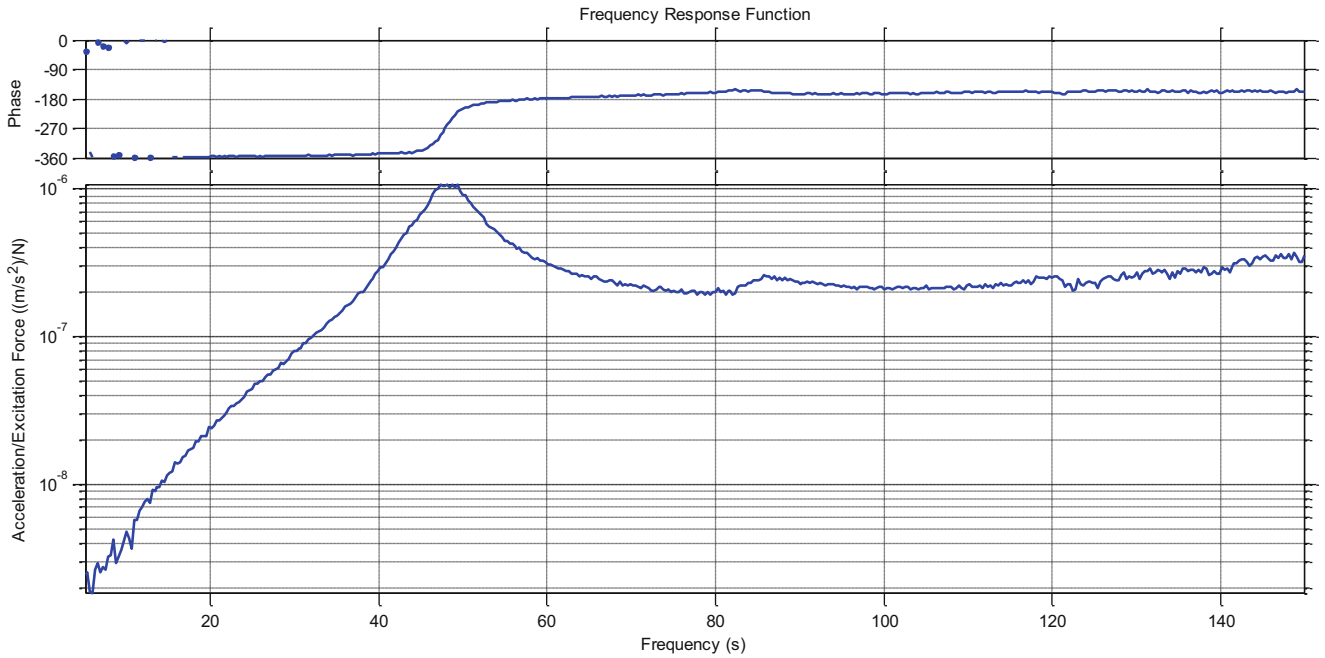

Fig. 16.16 Representative A/F FRF: increasing phase at resonance indicates negative damping, which is not realizable in a passive structure

While the complex mode indicator function clearly shows the resonant frequencies, there is a phase discrepancy for the primary mode at 48 Hz. An example FRF plot is presented below. The phase should decrease through resonance, not increase; an increase in phase would correspond to negative damping. Increasing phase suggests that the indirect measure of force is not completely accurate. This is likely due to the fact that the vertical actuator oil column resonance is near 50 Hz (Fig. 16.16).

The flexible body modes of the table are presented in Table 16.7. Plots of the modes are shown in Fig. 16.17.

A comparison between extracted mode shapes with the MVF table in the test stand and the results from the MVF modal test is presented in Table 16.8. One “potato chip” mode and the second squeeze modes were not extracted from this data due

Table 16.7 Free-free table modes

Mode no.	Freq (Hz)	Damp (% crit)	Description
1	47.9	−3.3	Potato-chip
2	86.4	4.6	Oil can
3	87.9	2.3	Squeeze
4	122.0	0.9	2nd bending (1)
5	122.0	0.9	2nd bending (2)
6	136.6	1.7	Ear twist

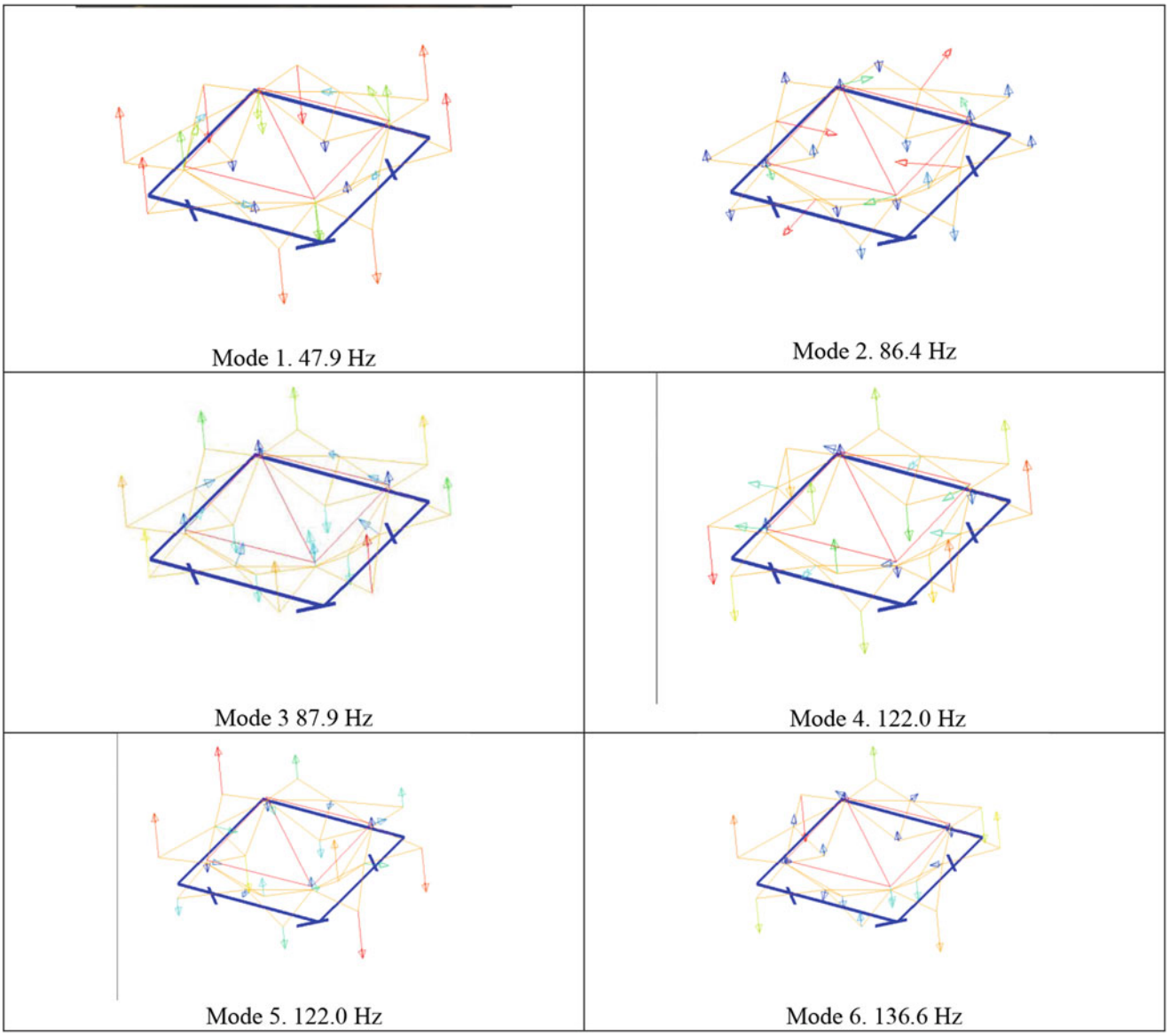

Fig. 16.17 Bare table mode shapes using actuator forces as references

to the actuator configuration not being able to excite them; the vertical actuators were installed in groups of four, and a node line for the second potato chip mode was between the second and third actuator. To excite this mode, the first two actuators in each set would need to apply a positive force while the second two actuators were applying a negative force. However, each set was linked so that all four actuators in each set input forces that all had the same sign; therefore, the mode was not excited. The second squeeze mode would likely require significant effort to extract since it is a low-responding in-plane mode that is excited by only two of the four in-plane actuators. The two highest-frequency modes appear to have moved

Table 16.8 Comparison between modal tests

	Base Shake		Modal Test		
Mode No.	Freq Hz	Damp % crit	Freq Hz	Damp % crit	Description
1	47.9	-3.30	52.7	0.05	Potato Chip +/-Z
2			55.0	0.11	Potato Chip +Y-Z/-Y+Z
3	87.9	2.34	96.2	0.03	1st Squeeze
4	86.4	4.59	102.8	0.07	Oil Can
5	122.0	0.87	111.0	0.31	+Y-Z/-Y+Z Ear Torsion about +Y+Z axis
6	122.0	0.87	114.8	0.06	+Y+Z/-Y+Z Ear Torsion about +Y-Z axis
7			123.8	0.31	2nd Squeeze
8	136.6	1.69	140.7	0.05	Ear Bending o-o-p with adjacent ear

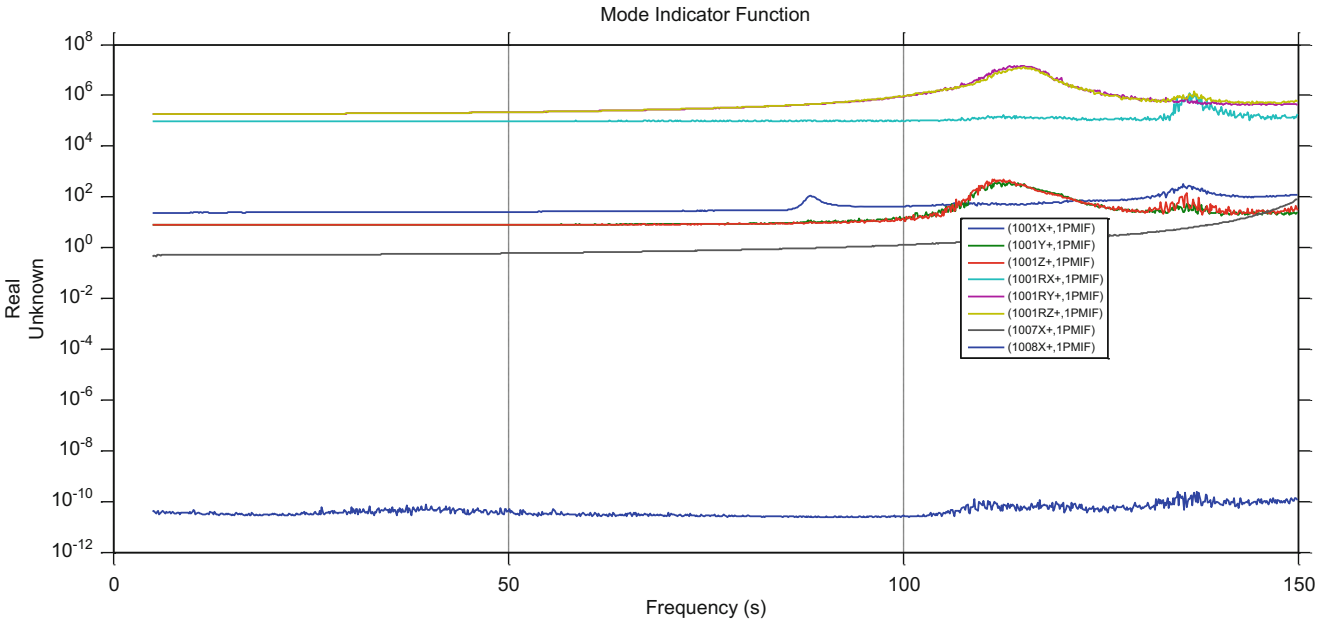

Fig. 16.18 PSMIF for A/A FRFs of MVF table

outside the frequency range of the test. Modes 5 and 6 are highlighted since the shapes from the base shake test are a linear combination of the shapes extracted from the free-free modal survey; essentially these shapes are repeated roots, and having rotated modes is not unexpected.

Another item to note is that the frequencies are different between the two tests, and with the exception of the first mode, the damping from the base shake test is higher. The difference in frequencies is due to the difference in mass of the MVF table between the two configurations.

The potential capability and limitation of using the FRF correction method to extract fixed base modes from MVF X-axis shake random tests can be assessed by using the FRF correction method on the MVF bare table X-axis shake random test data. Since there are currently eight independent references available, eight shapes can be removed from the table response. For this study, we chose the six rigid body modes based on the FEM geometry and the first two flexible body mode shapes, the 47.9 Hz potato-chip mode and the 86.4 Hz oil can mode, which are shown in Fig. 16.17. The four independent vertical actuator sets should be able to control rigid body vertical, tip, and tilt modes as well as the first out-of-plane flexible mode. The four independent in-plane actuator sets should be able to control rigid body lateral Y, lateral Z, and yaw, and the first in-plane flexible body mode.

PSMIFs using the six rigid body modes (1001X+ through 1001RZ+), the first bending mode (1007X+), and the first in-plane mode (1008X+) are presented in Figs. 16.18 and 16.19. The PSMIF was used here to visualize the dynamics of the

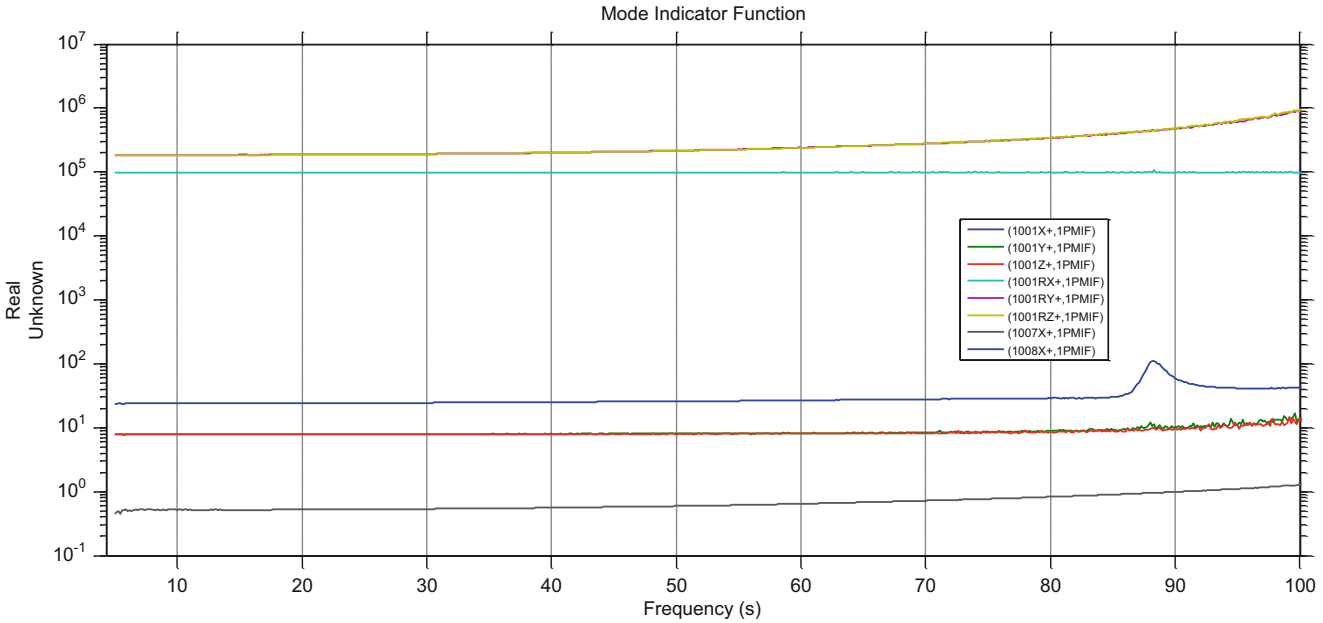

Fig. 16.19 PSMIF for A/A FRFs of MVF table—close up

system associated with each reference. There are no peaks in the FRFs until the frequency of the plunge mode near 88 Hz. The FRF correction method was able to remove all six rigid body modes and the first two flexible body modes that are excited during X-axis random shaking.

The PSMIF associated with the eighth mode shape that was removed, the first in-plane flexible body mode of the MVF bare table, has a much lower overall response than the other reference shapes. This is most likely because that excitation does not excite the vertical response of the MVF table. The PSMIF associated with the first out-of-plane mode has no dynamics below 150 Hz, but the PSMIF begins to increase near 150 Hz. Otherwise, the only rigid body shape that excites the oil can mode is the vertical rigid body shape (1001X+), while the rigid body yaw shape (1001RX+) excites the ear-twist mode. The other rigid body shapes excite the two second bending modes.

There is a possibility that the other flexible modes could be controlled if the number of independent references were increased. An example would be to add four references to the control system and then group the vertical actuators into sets of two instead of four. However, the current system is not configured for 12 references. Even so, there are questions as to whether one could control the plunge mode since the vertical actuators are aligned such that they would use the same force pattern as the vertical rigid body mode. In other words, the mode shapes measured only from drive point accelerometers at each of the actuators would be the same for the vertical rigid body mode and the plunge mode. This suggests that one would need to add vertical actuators near the edges of the MVF table to be able to control the plunge mode.

Another potential way to remove more than two flexible body modes is to use the mode shape correction method. The mode shape correction method is not limited by the number of actuators and offers a possible method for preventing the higher-frequency modes from influencing the test results. However, it has a limitation that the mode shapes used in the method must be mass-normalized. Therefore it was not studied in this effort for two reasons:

1. Test-measured mass-normalized mode shapes could not be calculated because the shakers did not all have drive point accelerometers.
2. Negative damping in the primary flexible mode indicated that there was a test setup issue with the method for measuring actuator force.

While drive-point accelerometers can be installed for future tests, there may not be a feasible method of accurately measuring vertical actuator force above 50 Hz.

16.7 Summary

This paper discussed preliminary analysis indicating the viability and frequency limitations of using the FRF correction method on MVF to be able to extract fixed base modal parameters from MVF X-axis vertical random shake tests. Being able to extract fixed base modal parameters using MVF would result in a significant reduction in testing schedule and risk to the test articles due to reduced handling.

The current MVF X-axis vertical random shake configuration uses eight independent references, which have been shown to be able to remove the effect of the six rigid body modes and two flexible modes. Additionally, the effect of higher frequency MVF table modes could potentially be removed if the vertical actuators were reconfigured into eight groups of two actuators each or the mode shape correction method was able to be implemented. Due to the current vertical actuator configuration and independent references, it may not be possible to remove the oil can mode without adding supplemental vertical actuators.

The next step in this effort is to perform two modal surveys on a representative test article called the verification test article (VTA). The first modal survey will be a traditional fixed base modal survey having the VTA mounted to the MVF modal floor. The second modal survey will be performed with the VTA mounted on the MVF table, MVF performing an X-axis vertical random shake test, and using the FRF correction method to extract fixed base modal parameters. The validity of the implementation of the FRF correction method on MVF will be accomplished by comparing the fixed base modal parameters extracted from these two modal surveys.

References

1. Carne, T.G., Martinez, D.R., Nord, A.R.: A comparison of fixed-base and driven base modal testing of an electronics package. Proceedings of the Seventh International Modal Analysis Conference, Las Vegas, NV, pp. 672–679 (1989)
2. Beliveau, J.G., Vigneron, F.R., Soucy, Y., Draisey, S.: Modal parameter estimation from base excitation. J. Sound Vib. **107**, 435–449 (1986)
3. Fullekrug, U.: Determination of effective masses and modal masses from base-driven tests. Proceedings of the 14th International Modal Analysis Conference, Dearborn, MI, pp. 671–681 (1996)
4. Sinapius, J.M.: Identification of fixed and free interface normal modes by base excitation. Proceedings of the 14th International Modal Analysis Conference, Dearborn, MI, pp. 23–31 (1996)
5. Mayes, R.L., Bridgers, L.D.: Extracting fixed base modal models from vibration tests on flexible tables. Proceedings of the 27th International Modal Analysis Conference, Orlando, FL (2009)
6. Napolitano, K., Yoder, N.: Fixed base FRF using boundary measurements as references – analytical derivation. Proceedings of the 30th International Modal Analysis Conference, Jacksonville, FL (2012)
7. Napolitano, K., Yoder, N.: Fixed base FRF using boundary measurements as references – experimental investigation. Proceedings of the 30th International Modal Analysis Conference, Jacksonville, FL (2012)
8. Napolitano, K., Yoder, N.: Extraction of fixed-base modes of a structure mounted on a shake table. Proceedings of the 31st International Modal Analysis Conference, Jacksonville, FL (2013)

Chapter 17
Observer-Based Distributed Controllers Design for a Cantilever Beam

Xueji Zhang, Zhongzhe Dong, Cassio Faria, Kristian Hengster-Movric, and Wim Desmet

Abstract Advancement of piezoelectric transducer technology enables distributed actuation and sensing along flexible structures for vibration suppression. This study addresses the controller design under the paradigm of cooperative control and optimisation. A finite element model of a cantilever beam, coupled with piezoelectric actuators and accelerometers is constructed and then validated with a physical setup. Based on the finite element model, distributed controllers are designed. Considering the existence of feed-through terms in the system, each controller applies its control action based not only on its local measurement and state estimations from a few neighboring agents, but also on the exact control actions of all the other controllers as well, to realize global vibration suppression. The control design problem is reformulated as optimising a scalar subject to a set of linear matrix inequalities (LMIs). The vibration suppression performance of the cooperative control scheme is examined in both time domain and frequency domain via simulations.

Keywords Vibration damping • FEM • Observer • Cooperative control • LMIs

Nomenclature

$[S]$	Matrix
$[\ddots]$	Diagonal matrix
(S_{11})	Single element of $[S]$
$\otimes$	Kronecker product
$\mathbf{1}_n$	Column vector of dimension n with all entries equal to 1
I_n	Identity matrix of dimension n
I	Identity matrix of appropriate dimension
$\begin{bmatrix} a & b \\ * & d \end{bmatrix}$	Symmetric matrix, equals to $\begin{bmatrix} a & b \\ b^T & d \end{bmatrix}$

X. Zhang (✉) • Z. Dong
Faculty of Electrical Engineering, ČVUT v Praze, Karlovo náměstí 13, 121 35 Prague 2, Czech Republic

Engineering Service Division, Siemens Industry Software NV, Interleuvenlaan 68, 3001 Leuven, Belgium

Department of Mechanical Engineering, KU Leuven, Celestijnenlaan 300, 3001 Heverlee, Belgium
e-mail: xueji.zhang@siemens.com

C. Faria
Engineering Service Division, Siemens Industry Software NV, Interleuvenlaan 68, 3001 Leuven, Belgium

K. Hengster-Movric
Faculty of Electrical Engineering, ČVUT v Praze, Karlovo náměstí 13, 121 35 Prague 2, Czech Republic

W. Desmet
Department of Mechanical Engineering, KU Leuven, Celestijnenlaan 300, 3001 Heverlee, Belgium

E. Wee Sit (ed.), *Sensors and Instrumentation, Volume 5*, Conference Proceedings of the Society for Experimental Mechanics Series, DOI 10.1007/978-3-319-29859-7_17

17.1 Introduction

Active vibration damping of flexible structures with smart materials has attracted attentions of researchers in the automatic control community for the past few decades [1–5]. The advancement of materials technology makes it easier to integrate piezoelectric elements on the flexible structures, enabling distributed actuation and sensing capabilities [6, 7]. Generally speaking, this puts a challenging task for the controller design since many sensing and control decisions are supposed to be carried out simultaneously. To develop the control algorithm, three different control schemes can be considered [8]: (1) centralized control scheme, under which the central controller will process the information from all sensing units simultaneously and send the control efforts to all the actuation units; (2) decentralized control scheme, under which each actuation and sensing unit forms a local closed loop with a decentralized controller; (3) distributed control scheme, under which each controller at a given position needs the information from a number of neighboring sensing units to determine the actuation at that very position. Due to the large number of actuation and sensing units, the centralized control scheme has the drawback of scalability issue, while decentralized control scheme is exploited in parallel to address this issue [9, 10].

The smart sensing technology provides another opportunity to address vibration damping problems [11]. The high connectivity and cooperation capabilities of networked controllers and sensors—coined as 'agent' in this work—provide the potential to accomplish better performance while preserving the scalability of decentralized scheme. Frampton [12] and Frampton et al. [13] extend the decentralized control to distributed control to solve the structural accoustic problem for flexible structures. However, in those works, each agent aims to minimise its local cost function, hence the overall system-wide performance is not globally optimal. To introduce cooperation behavior of each agent, cooperative control framework is adopted in this paper [14]. The aim of this work is to apply cooperative control strategy on the flexible beam problem. An observer-based distributed control scheme is implemented following the work of [15]. A main contribution is to extend the observer-based distributed control scheme to dynamical vibrating systems with feed-through terms. This has been achieved by introducing the exact control signal of all agents to each observer.

This paper is structured as follows: Sect. 17.2 builds up the numerical finite element (FE) model of a cantilever beam, validated via an experimental setup. A brief preliminary about communication network description and structure of observer-based distributed controller is given in Sect. 17.3. Section 17.4 formulates the controller design problem. Simulation results are presented in Sect. 17.5, followed by conclusions and future work in Sect. 17.6.

17.2 Plant Modeling and Validation

A cantilever beam is modeled with finite element method based on Euler-Bernoulli beam theory. Given the small dimension, accelerometers are integrated as point masses in the beam model. The electro-mechanical dynamics of piezoelectric elements are integrated in the beam model using the generalized Hamilton's principle [16, 17]. The equation of motion of the coupled beam is:

$$[M]\ddot{q} + [C]\dot{q} + [K_{aug}]q = K_{u\phi}\underline{v}, \tag{17.1}$$

where $\underline{v}$ is the vector of voltages applied on the piezoelectric elements and $K_{u\phi}$ is the electro-mechanical coupling matrix [16], q is the generalized displacement vector, $[K_{aug}]$ is the stiffness matrix of the coupled system, $[C]$ is the proportional damping matrix, and $[M]$ is the structural mass matrix. The physical parameter of the beam and piezoelectric elements are listed in Table. 17.1. For the ease of controller design, only the first five modes are extracted in the FE model. The sketch of the physical setup is shown in Fig. 17.1a. It is measured with three accelerometers and actuated with three piezoelectric patches

Table 17.1 Parameter table

Parameter	Value
Length	0.5 m
Width	0.03 m
Poisson ratio	0.33
Beam thickness	0.001 m
Density	2700 kg/m^3
Young's Modulus	69 $\times$ 10^9 Pa
Piezo type	PZT 5 A
Actuator thickness	0.0005 m

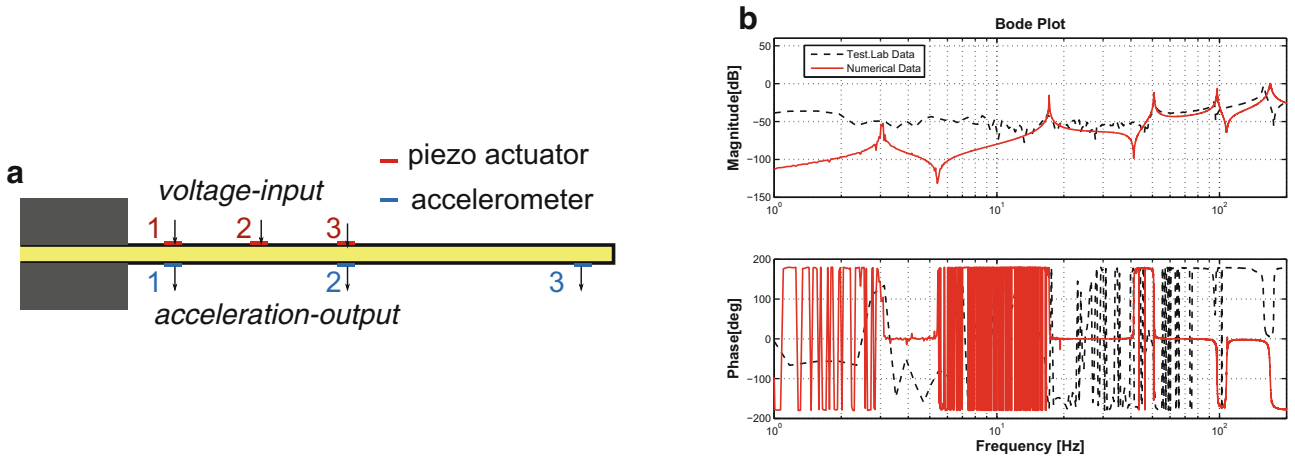

Fig. 17.1 Model validation. (**a**) Experimental setup sketch: a cantilever beam. (**b**) FRF: FE model versus experimental measurements

(not in a completely collocated fashion). One of the frequency response functions (FRFs) measured with LMS SCADAS and Test.Lab is shown in Fig. 17.1b, compared with the numerical finite element model. Due to the small signal-to-noise ratio (SNR), the measured FRFs at low frequencies are not authentic.

17.3 Preliminaries

17.3.1 MIMO State-Space Model

Equation (17.1) can be simply recast as a state-space model [18]. Given the fact that all the digital controllers are implemented in a discrete-time manner, the continuous-time FE model of beam are discretized with the first-order hold (FOH) method. The discrete-time state space model of the coupled beam is in the form of

$$\begin{cases} x(k+1) = Ax(k) + \sum_{i=1}^{p} B_i u_i(k) \\ y_i(k) = C_i x(k) + \sum_{j=1}^{p} D_{ij} u_j(k), i = 1, 2 \ldots, p. \end{cases}$$

where $x = \begin{bmatrix} q \\ \dot{q} \end{bmatrix} \in R^n$ is the state and $u_i \in R$ is the control signal of agent i, $y_i \in R$ is the measured signal of agent i, p is the total number of agents.
Define the augmented control matrix as

$$B := \begin{bmatrix} B_1 & B_2 & \ldots & B_p \end{bmatrix}$$

and the augmented control signal vector as

$$\mathcal{U}(k) := \begin{bmatrix} u_1(k) & u_2(k) & \ldots & u_p(k) \end{bmatrix}^T.$$

Therefore the dynamics of states in a compact form is:

$$x(k+1) = Ax(k) + B\mathcal{U}(k).$$

Define the augmented measurement matrix as

$$C := \begin{bmatrix} C_1^T & C_2^T & \ldots & C_p^T \end{bmatrix}^T.$$

Without loss of generality, it is presumed that (A, B) is stabilizable and (C, A) is detectable [19].

17.3.2 State Estimation Communication Graph Topology

The communication topology of state estimation information can be expressed by a directed graph [20]. A directed graph $\mathcal{G} = (\mathcal{V}, \mathcal{E}, \mathcal{N})$ consists of a set of nodes $\mathcal{V} = \{1, 2, \ldots, p\}$, a set of edges $\mathcal{E} \subset \mathcal{V} \times \mathcal{V}$ and an associated weighed adjacency matrix $\mathcal{N} = [N_{ij}]$. An edge (i, j) is graphically elaborated by an arrow with head node i and tail node j, indicating the information flow is from node j to node i. Each entry (N_{ij}) of the adjacency matrix $\mathcal{N}$ is the weight gain with a pair (i, j) and $N_{ij} \neq 0$ if $(i, j) \in \mathcal{E}$. Since the adjacency matrix $\mathcal{N}$ indicates communication of different agents, it is assumed that $N_{ii} = 0, \forall i \in \mathcal{V}$. The set of neighbors of node i is denoted as $\mathcal{N}_i = \{j | (i, j) \in \mathcal{E}\}$. Define the in-degree of node i as $d_i^{in} = \sum_{j=1}^{p} N_{ij}$ and in-degree matrix as $\mathcal{D}_{in} = [\ d_i^{in}\ ]$, and then the so-called graph Laplacian matrix is

$$L = \mathcal{D}_{in} - \mathcal{N}.$$

17.3.3 Distributed Controller and Observer

An observer-based scheme is adopted here for each agent to estimate the states of the FE model and construct the control signal. For agent i the control signal u_i is constructed based on its own state estimation:

$$u_i(k) = K_i \hat{x}_i(k) \tag{17.2}$$

K_i is the local state feedback gain matrix of agent i. Define the augmented feedback matrix

$$K := \left[K_1^T \ K_2^T \ \ldots \ K_p^T \right]^T.$$

The dynamics of observer of agent i is in the form of :

$$\begin{cases} \hat{x}_i(k+1) = A\hat{x}_i(k) + B\mathcal{U}_i(k) + L_i(y_i(k) - \hat{y}_i(k)) + \sum_{j \in \mathcal{N}_i} N_{ij}(\hat{x}_j(k) - \hat{x}_i(k)) \\ \hat{y}_i(k) = C_i \hat{x}_i(k) + \sum_{j=1}^{p} D_{ij} u_j(k) \\ \mathcal{U}_i(k) = K\hat{x}_i(k) \end{cases} \tag{17.3}$$

Herein $\mathcal{U}_i(k) = K\hat{x}_i(k)$ is the estimation of the whole control actions applied on the beam. Each observer corrects its state estimation based on its local measurement, state estimation of neighboring agents and the exact control signals of all agents applied on the beam.

17.4 Distributed Control Design

17.4.1 Control Problem Statement

Defining the state estimation error $e_i(k) = x(k) - \hat{x}_i(x), i \in \mathcal{V}$, the cost function is given as

$$J := \sum_{k=0}^{\infty} x^T(k) Q_x x(k) + \sum_{k=0}^{\infty} \sum_{i \in \mathcal{V}} [e_i^T(k) Q_i e_i(k) + u_i^T(k) R_i u_i(k)] \tag{17.4}$$

Q_x, Q_i, R_i are positive definite matrices. Define the sets:

$$\mathcal{L} := \{L_i, i \in \mathcal{V}\}$$
$$\mathcal{K} := \{K_i, i \in \mathcal{V}\}$$
$$\mathcal{N}_\Delta := \{N_{ij}, (i, j) \in \mathcal{E}\}$$

The distributed control optimisation problem can be formulated as:

$$\begin{aligned}
&\underset{\mathcal{L},\mathcal{K},\mathcal{N}_\Delta}{\text{minimise}} \quad J \\
&\text{subjectto} \quad \begin{cases} x(k+1) = Ax(k) + \sum_{i=1}^{p} B_i u_i(k) \\ y_i(k) = C_i x(k) + \sum_{j=1}^{p} D_{ij} u_j(k) \\ u_i(k) = K_i \hat{x}_i(k) \end{cases}, i = 1, 2, \ldots p. \\
&\qquad\qquad \begin{cases} \hat{x}_i(k+1) = A\hat{x}_i(k) + B\mathcal{U}_i(k) + L_i(y_i(k) - \hat{y}_i(k)) + \sum_{j \in \mathcal{N}_i} N_{ij}(\hat{x}_j(k) - \hat{x}_i(k)) \\ \hat{y}_i(k) = C_i \hat{x}_i(k) + \sum_{j=1}^{p} D_{ij} u_j(k) \\ \mathcal{U}_i(k) = K\hat{x}_i(k) \end{cases}, i = 1, 2, \ldots p.
\end{aligned} \tag{17.5}$$

Define the estimation error vector as $e(k) = [e_1^T(k), e_2^T(k), \ldots e_p^T(k)]^T$ and the augmented state vector as $\xi(k) = [x^T(k), e^T(k)]^T$. Via simple mathematical manipulation, the dynamics of closed-loop system can be derived as

$$\xi(k+1) = \Omega(\mathcal{L}, \mathcal{K}, \mathcal{N}_\Delta)\xi(k) \tag{17.6}$$

where

$$\Omega(\mathcal{L}, \mathcal{K}, \mathcal{N}_\Delta) = \begin{bmatrix} A + BK & | & \Upsilon(\mathcal{K}) \\ - - - - & - - & - - - - \\ 0 & | & \Gamma(\mathcal{L}, \mathcal{K}, \mathcal{N}_\Delta) \end{bmatrix},$$

herein

$$\Upsilon(\mathcal{K}) = \begin{bmatrix} -B_1K_1 & -B_2K_2 & \ldots & -B_pK_p \end{bmatrix},$$

$$\Gamma(\mathcal{L}, \mathcal{K}, \mathcal{N}_\Delta) = (\lceil A - L_i C_i \rceil) + (\lceil BK \rceil + \mathbf{1}_p \otimes \Upsilon(\mathcal{K})) - L \otimes I_n.$$

Therefore the cost function (17.4) can be rewritten as

$$J = \sum_{k=0}^{\infty} \xi^T(k)(Q + \bar{K}^T R \bar{K})\xi(k), \tag{17.7}$$

where

$$Q = \begin{bmatrix} Q_x & 0 \\ 0 & \lceil Q_i \rceil \end{bmatrix}, R = \lceil R_i \rceil, \bar{K} = \begin{bmatrix} K & \lceil K_i \rceil \end{bmatrix}.$$

17.4.2 Sub-optimisation Solution

With Schur complement method and Lyapunov stability analysis, the control optimisation problem (17.5) can be reformulated as follows (see [15] for more details):

$$\begin{aligned}
&\underset{P,\mathcal{L},\mathcal{K},\mathcal{N}_\Delta}{\text{minimise}} \quad \alpha \\
&\text{subjectto} \quad \alpha > 0, \\
&\qquad\qquad P = P^T \succ 0, \\
&\qquad\qquad P \prec \alpha I, \\
&\qquad\qquad \begin{bmatrix} -P & \Omega^T & I & \bar{K}^T \\ * & -P^{-1} & 0 & 0 \\ * & * & -Q^{-1} & 0 \\ * & * & * & -R^{-1} \end{bmatrix} \prec 0.
\end{aligned} \tag{17.8}$$

The last constraint is a nonlinear matrix inequality (NLMI) due to the existence of P^{-1}. At the cost of reducing feasible set, the NLMI can be replaced with an additional given scalar variable β_0

$$\alpha < \beta_0, \begin{bmatrix} -P & \Omega^T & I & \bar{K}^T \\ * & -\frac{1}{\beta_0} I & 0 & 0 \\ * & * & -Q^{-1} & 0 \\ * & * & * & -R^{-1} \end{bmatrix} \prec 0.$$

With the convex optimisation solver CVX [21], the optimisation problem can be solved, giving rise to sub-optimal sets $\mathcal{L}, \mathcal{K}, \mathcal{N}_\Delta$.

17.5 Simulations

Simulation is run under the MATLAB/SIMULINK environment. For simulation, three agents with the strongly connected state estimation communication topology are assumed, as shown in Fig. 17.2. The convex optimisation solver yields the following communication gain: $N_{12} = 0.2444, N_{13} = 0.2806, N_{21} = 0.2478, N_{23} = 0.3401, N_{31} = 0.2726, N_{32} = 0.1791$. An external white noise is exerted to the beam model. The accelerations of all three channels in time domain are shown in Fig. 17.3a in contrast with the open-loop system. For evaluation, the FRFs from voltage-input Channel 1 to acceleration-output Channel 1 are extrated based on Welch's averaged periodogram method [22] and shown in Fig. 17.4. As is shown, the distributed controllers added effective damping on the second to fifth mode. The damping effect on the first mode is not obvious, this is possibly due to the small acceleration-output/voltage-input gain at lower frequencies, note that the first vibration mode is around 3 Hz.

17.6 Conclusions

In this paper, an observer-based distributed cooperative control scheme is adopted to realize vibration damping for a beam model coupled with piezoelectric actuators and accelerometers. Due to the acceleration feedback, a feed-through term is existent in the system. Via an extra diffusion of exact control actions among all the agents, the control optimisation problem can be solved without introducing additional computational load compared with strictly proper cases. A convex optimisation solver is used to transform NLMIs to LMIs, at the cost of losing possible optimal solutions. The controlled beam is simulated and the control algorithm has effective damping for the FE beam model.

In terms of future work, a better way to solve the NLMI constraint shall be investigated, aiming to give better solution sets. Also the distributed control scheme has not been implemented in the real physical setup, the damping performance is expected to be limited due to spill-over effects [23]. How to mitigate this issue will be considered in the near future.

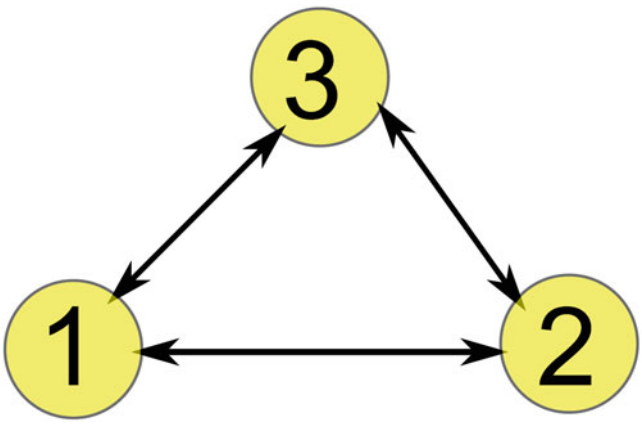

Fig. 17.2 State estimation communication topology: strongly connected graph

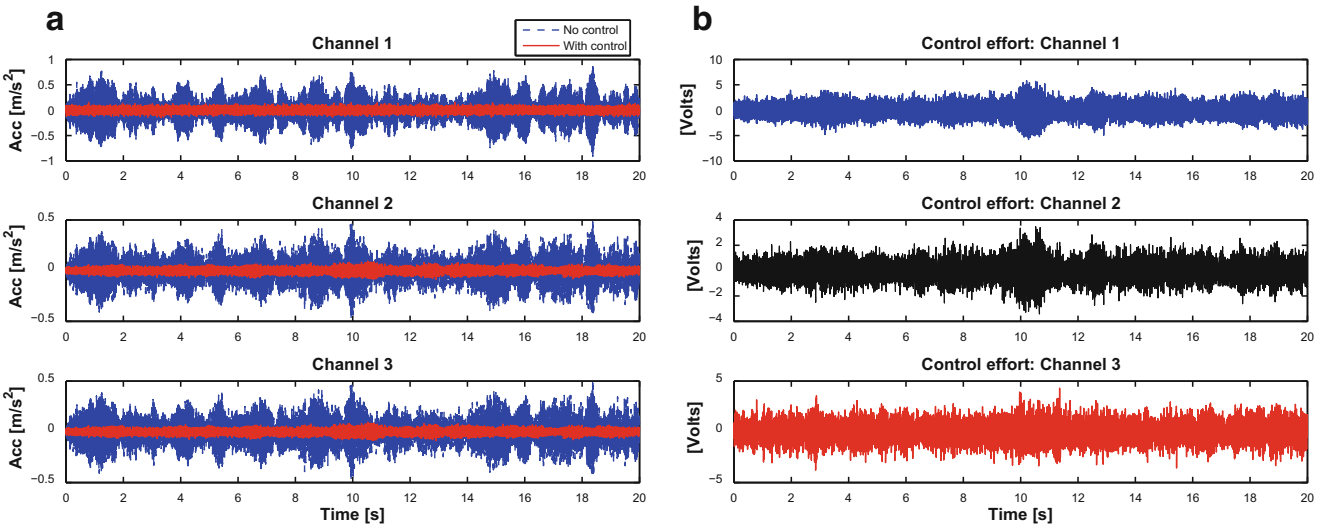

Fig. 17.3 Control performance in time domain. (**a**) Simulated measurements of accelerometers. (**b**) Voltages applied on the piezoelectric elements

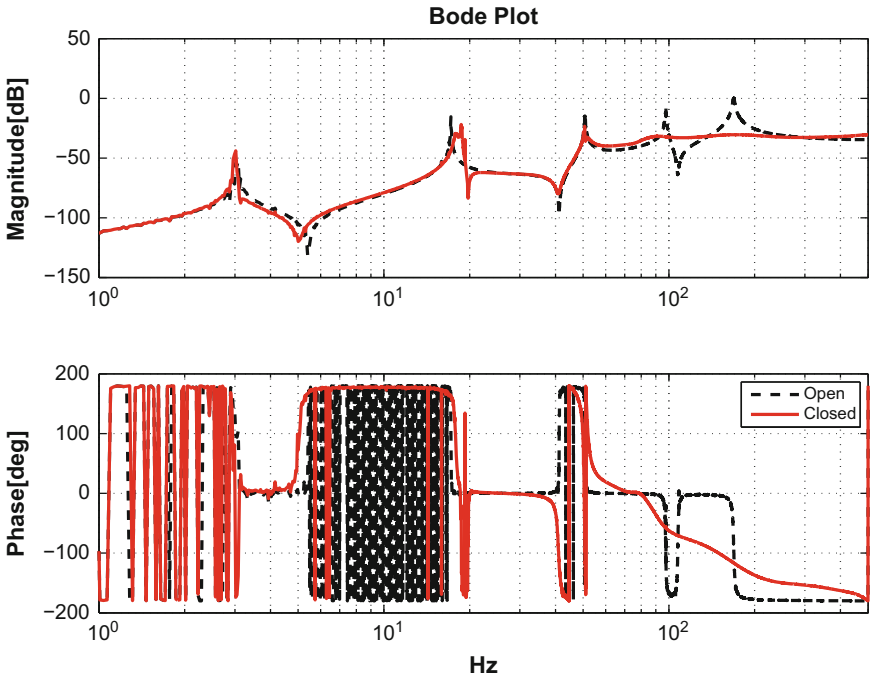

Fig. 17.4 Control performance in frequency domain

Acknowledgements This work is supported by the European Commission under the framework of FP7-PEOPLE-2013-ITN—Marie-Curie Action: "Innovative Training Networks": ARRAYCON—applications of distributed control on smart structures, with project reference 605087.

References

1. Li, K.: Structural vibration damping with synchronized energy transfer between piezoelectric patches. Ph.D. dissertation, INSA de Lyon (2012)
2. Halim, D.: Vibration analysis and control of smart structures. Ph.D. dissertation, The University of Newcastle (2002)
3. Cavallo, A., De Maria, G., Natale, C., Pirozzi, S.: Robust control of flexible structures with stable bandpass controllers. Automatica **44**(5), 1251–1260 (2008)
4. Hu, Y.-R., Ng, A.: Active robust vibration control of flexible structures. J. Sound Vib. **288**(1), 43–56 (2005)

5. Balas, G.J., Doyle, J.C.: Robustness and performance trade-offs in control design for flexible structures. IEEE Trans. Control Syst. Technol. **2**(4), 352–361 (1994)
6. Raji, R.S.: Smart networks for control. IEEE, Spectrum **31**(6), 49–55 (1994)
7. McCammon, I.D., Jacobsen, S.C.: Communication and control for distributed microsystems. IEEE Control Syst. Mag. **10**(2), 48–50 (1990)
8. Ayres, G., Paganini, F.: Convex method for localized control design in spatially invariant systems. In: Proceedings of the IEEE Conference on Decision and Control, pp. 3751–3756 (2000)
9. Engels, W.P., Baumann, O.N., Elliott, S.J., Fraanje, R.: Centralized and decentralized control of structural vibration and sound radiation. J. Acoust. Soc. Am. **119**(3), 1487–1495 (2006)
10. Elliott, S.J., Gardonio, P., Sors, T.C., Brennan, M.J.: Active vibroacoustic control with multiple local feedback loops. J. Acoust. Soc. Am. **111**(2), 908–915 (2002)
11. Spencer, B.F., Ruiz-Sandoval, M.E., Kurata, N.: Smart sensing technology: opportunities and challenges. Struct. Control Health Monit. **11**(4), 349–368 (2004)
12. Frampton, K.D.: Vibro-acoustic control with a distributed sensor network. J. Acoust. Soc. Am. **119**(4), 2170–2177 (2006)
13. Frampton, K.D., Baumann, O.N., Gardonio, P.: A comparison of decentralized, distributed, and centralized vibro-acoustic control. J. Acoust. Soc. Am. **128**(5), 2798–2806 (2010)
14. Lewis, F.L., Zhang, H., Hengster-Movric, K., Das, A.: Cooperative Control of Multi-Agent Systems, Communications and Control Engineering. Springer, London (2014)
15. Orihuela, L., Millan, P., Vivas, C., Rubio, F.R.: Distributed control and estimation scheme with applications to process control. IEEE Trans. Control Syst. Technol. **23**(4), 1563–1570 (2015)
16. Hassan, H., Yves, B., Razek, A.: Finite element model of a beam structure with piezoelectric patches using RL shunt circuits. In: AC2011, 14th International Conference on Active Systems for Dynamics Markets, pp. 124–131 (2011)
17. De Marqui Junior, C., Erturk, A., Inman, D.J.: An electromechanical finite element model for piezoelectric energy harvester plates. J. Sound Vib. **327**(1), 9–25 (2009)
18. Gawronski, W.K.: Advanced Structural Dynamics and Active Control of Structures. Mechanical Engineering Series. Springer, New York (2004)
19. Hespanha, J.P.: Linear Systems Theory. Princeton University Press, Princeton (2009)
20. Olfati-Saber, R., Fax, J.A., Murray, R.M.: Consensus and cooperation in networked multi-agent systems. Proc. IEEE **95**(1), 215–233 (2007)
21. CVX Research, I.: CVX: Matlab Software for Disciplined Convex Programming, Version 2.0 (2012)
22. Welch, P.D.: The use of fast Fourier transform for the estimation of power spectra: a method based on time averaging over short, modified periodograms. IEEE Trans. Audio Electroacoust. AU-**15**(2), 70–73 (1967)
23. Bontsema, J., Curtain, R.F.: A note on spillover and robustness for flexible systems. IEEE Trans. Autom. Control **33**(6), 567–569 (1988)

Chapter 18
Experimental Characterization of a Tuned Vibration Absorber

Tuğrul Aksoy, Gökhan O. Özgen, Bülent Acar, and Caner Gençoğlu

Abstract In this paper, experimental characterization studies conducted for a tuned vibration absorber is presented. The tuned vibration absorber has been particularly designed to reduce transverse resonant vibration response of a supported cylinder structure at its dominant two modes. Various testing configurations and techniques have been used such as transmissibility measurements, frequency response measurements, sweep sine testing, impact testing, and random testing. Different testing approaches were needed to explain the differences between actual TVA characteristics and the initial design objectives. Finally, structure and tuned vibration absorber are tested together to check the actual vibration reduction performance of the tuned vibration absorber.

Keywords Tuned vibration absorbers • Magnetic damping • Sine-sweep testing • Random testing • Experimental characterization

18.1 Introduction

Tuned vibration absorbers (TVA) are frequently used systems in order to suppress the oscillations of structures and machines. They can be used for not only forced vibration problems but also resonant vibration problems. The first TVA system was invented by Frahm in 1909 and basic theory of tuned vibration absorber was developed by Den Hartog [1]. TVA systems basically consist of mass [M] and stiffness [K] elements. Damping [C] may be added to the TVA system if the vibration reduction is desired to be distributed to a wider frequency range.

There are many types of TVA designs reported in the literature. Some of the commonly used types of TVAs are the spring-mass type, resonant beam type, pendulum type and dogbone type TVAs [2–4]. In order to characterize TVA systems, engineers have chosen various types of experimental methods. For instance, impact testing method was employed by Kathe and Littlefield to measure a vibration absorber's performance [5]. On the other hand, harmonic testing method was used in several studies in order to characterize TVA systems in a certain frequency range [6, 7]. However, experimental studies examining the TVA systems as a standalone system are rare in the literature.

In this study, a TVA system, which is designed to suppress the resonant vibratory motion of a hollow cylindrical structure, is experimentally characterized. This TVA system is parametrically designed by targeting the two dominant modes of the structure. The design work for this TVA system has not yet been published. In this paper however, experimental characterization of the prototype TVA system is presented. In this study, various types of experiments are carried out on the TVA system standalone in order to verify the design parameters of the TVA and assess the nonlinearity of the system. The prototype TVA system is also mounted on the main structure and the two systems are tested together to observe the vibration reduction performance of the prototype TVA system.

In the second section of this study, the prototype TVA system is described. In the third section, the experiments performed on the TVA system in order to characterize the TVA parameters and asses any nonlinear characteristics of the system are

T. Aksoy (✉)
Department of Mechanical Engineering, Middle East Technical University, Ankara, Turkey

Roketsan Inc., PO Box 30, Elmadağ, 06780 Ankara, Turkey
e-mail: e162808@metu.edu.tr

G.O. Özgen
Department of Mechanical Engineering, Middle East Technical University, Ankara, Turkey

B. Acar • C. Gençoğlu
Roketsan Inc., PO Box 30, Elmadağ, 06780 Ankara, Turkey

E. Wee Sit (ed.), *Sensors and Instrumentation, Volume 5*, Conference Proceedings of the Society for Experimental Mechanics Series, DOI 10.1007/978-3-319-29859-7_18

explained. In the same section, experiments carried out on the main system in order to investigate the vibration reduction performance of the TVA are also described. In the final and fourth section, concluding remarks about the study are presented.

18.2 Description of the TVA System

The TVA system under consideration in this study is a magnetically damped spring-mass system. Fabricated prototype of the TVA system is presented in Fig. 18.1. As observed from this figure, TVA system comprises an aluminum block and two copper plates constituting the mass of TVA and two helical springs as stiffness elements. Two shafts are passed through the helical springs and the linear bearings fixed to the aluminum block in order to constrain the TVA mass element to have only one degree of freedom. Two rare-earth magnets are also placed as parallel to the copper plates so that the magnetic (eddy-current) damping is introduced to the TVA system. These magnets are attached to thin magnet plates which are fixed to the TVA interface by means of bolts via slots opened on the plates. By this way, the distance between copper plates and magnets can be changed; thus, the magnetic damping coefficient can be altered. Magnetic damping coefficient can be estimated from the following relation [8]:

$$c = k\frac{B^2\vartheta}{\rho} \tag{18.1}$$

where B denotes the magnetic flux density, ρ represents the conductor resistivity, ϑ is the conductor volume and k is a dimensionless constant.

Since the TVA system includes shafts and linear bearings, sliding motion between them results in a certain amount of nonlinearity caused by friction forces. This nonlinearity may adversely affect the functioning of the TVA; thus, it should be characterized. On the other hand, damping and tuning frequency parameters of the TVA must be verified, i.e. checked if target design values are achieved with the fabricated prototype.

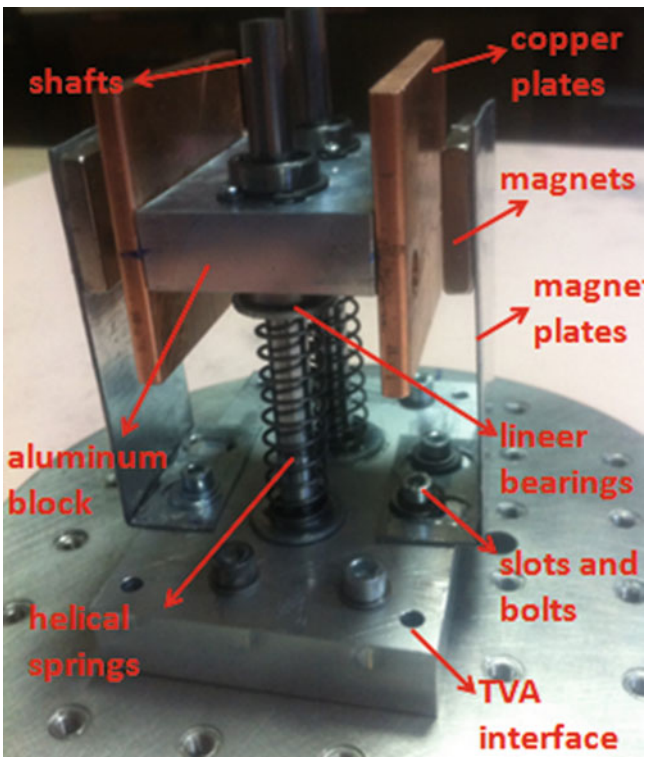

Fig. 18.1 TVA assembly and components

18.3 Characterization of the TVA System

18.3.1 Investigation of Nonlinear Effects on the TVA System

In order to characterize the nonlinearity within the TVA system, firstly random tests are carried out on the TVA prototype at four different input acceleration levels defined in terms of root mean square (RMS) values. After that, sine-sweep tests are performed at four different input acceleration amplitudes. Experiments are performed by using a vibration shaker which is shown in Fig. 18.2. As observed from this figure, two accelerometers are located on the TVA (points 1 and 2) and transmissibility frequency response functions (FRFs) are extracted from these accelerometers by selecting the accelerometer at point 1 as the input signal. Note that the shaker is positioned at an angle w.r.t. to horizontal plane in order to simulate the actual orientation of the TVA system when mounted on the target structure. This inclined orientation is expected to be the main source of nonlinearity since an inclined orientation creates non-zero normal forces at the linear bearings in turn creating non-zero friction forces at the same locations. It is expected that as the response amplitudes increase for the TVA mass, frictional forces at the linear bearings become less significant thus the nonlinear characteristics of the TVA will also be less significant. Tests are performed to find the level of input to be applied to the TVA base such that it behaves as a dominantly linear structure. The design validation tests are then conducted at these input levels where the TVA shows linear behavior. It is assumed that during the operational use of the TVA, response levels in the TVA mass ensures a dominantly linear behavior of the TVA system.

18.3.1.1 Random Vibration Tests

Random vibration tests are applied on the TVA system with no magnetic damping by applying a white noise spectrum profile between 1 and 20 Hz frequency range at the TVA base. Four tests are performed which are for acceleration RMS values of 0.1gRMS, 0.2gRMS, 0.3gRMS and 0.5gRMS, where g is the gravitational acceleration. Transmissibility FRFs obtained during random tests are presented in Fig. 18.3. From this figure, it can be said that the FRFs are dominated by the frictional forces at bearing locations for low input acceleration levels since TVA system seems to be highly damped while no intentional damping is present in the system other than the frictional forces at bearing locations. As the input amplitude is increased, apparent damping in the TVA system is decreased since order-of-magnitude of frictional forces are expected to be independent of the input level. It should also be noted that the FRF data has significant variance error even for high amplitude levels. Use of higher sensitivity accelerometers may improve the signal-to-noise ratio characteristics of the FRF measurements.

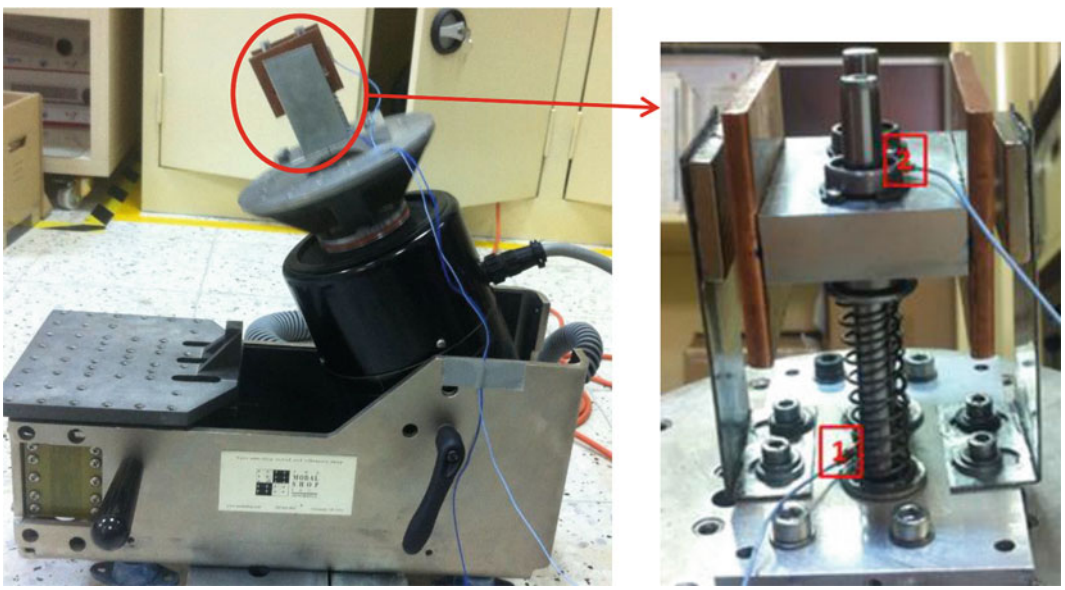

Fig. 18.2 Modal shaker and TVA system

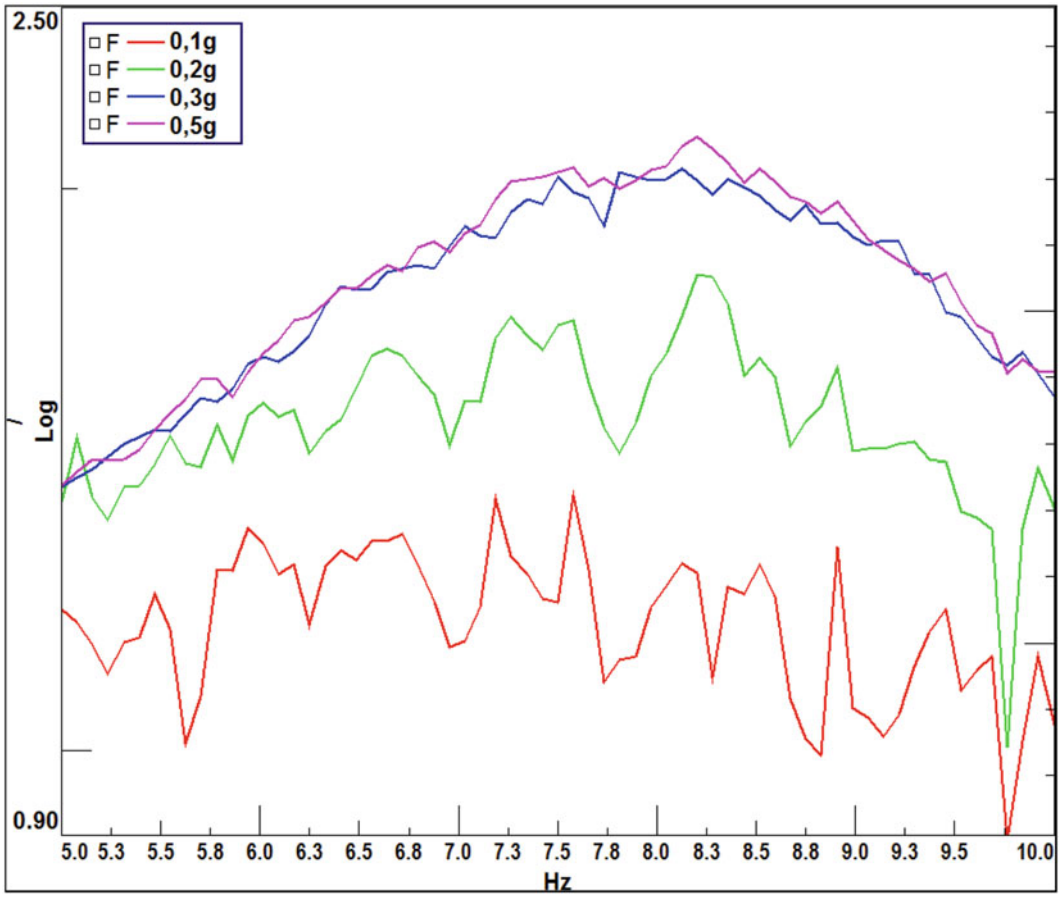

Fig. 18.3 Transmissibility FRFs of the TVA prototype obtained from random tests at different amplitudes

18.3.1.2 Sine-Sweep Tests

Sine-sweep tests are performed in a certain frequency range with a predefined sweep rate [9]. In this study, sine-sweep tests are performed in a frequency range in 5–10 Hz which includes the target tuning frequency of the TVA system. A sweep rate of 0.01 Hz/s is used in linear sweep mode. As in the case of random tests, sine-sweep tests are also carried out for four different acceleration magnitudes, which are of 0.1g, 0.2g, 0.3g and 0.5g. Transmissibility FRFs obtained from these sine-sweep tests are shown in Fig. 18.4. By observing this figure, it can be said that the FRFs converge as the excitation magnitudes increase as in the case of random tests. However, the FRF data obtained from the sine-sweep tests are less susceptible to variance error compared to random test data.

18.3.2 Verification of TVA Parameters

In order to verify the target tuning frequency and damping parameter of the TVA, sine-sweep tests are performed at 0.5g which is the magnitude where the nonlinear effects seem to be less significant, a conclusion made based on random and sine-sweep transmissibility FRF test results. Since in the design stage damping parameter of the TVA was not accurately estimated analytically, sine-sweep tests are repeated by altering the distance between copper plates and magnets in order to find the actual TVA configuration that will produce the desired damping ratio (the target value of the damping ratio for the TVA system). Two averages are taken for each test condition.

Transmissibility FRF results obtained from the sine-sweep tests which are performed for various magnet-copper plate distance configurations are presented in Fig. 18.5. From these FRFs, the tuning frequency of TVA is found as 8.35 Hz.

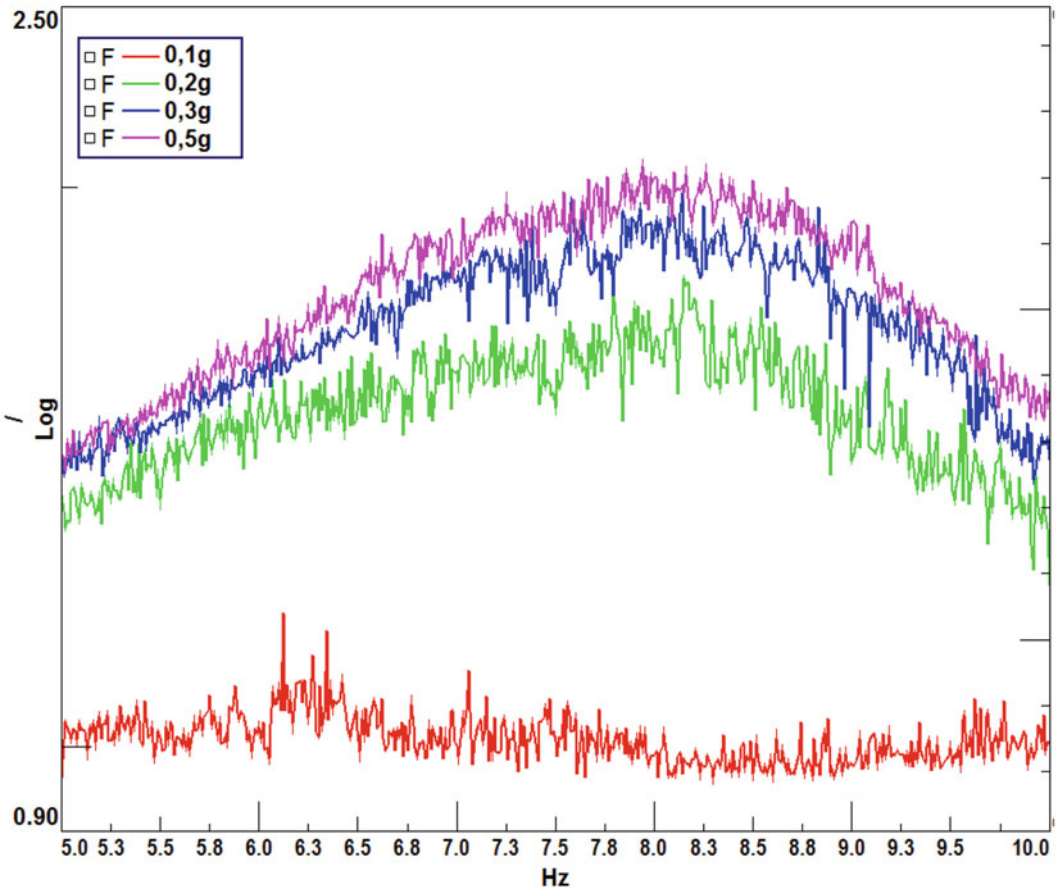

Fig. 18.4 Transmissibility FRFs of the TVA prototype obtained from sine-sweep tests at different amplitudes

In addition, target damping ratio of 0.34 for the designed TVA system is reached when the distance between the copper plates and the magnets is 3 mm. Damping ratios are calculated by using the following transmissibility expression [10]:

$$\frac{X}{Y} = \frac{\sqrt{1 + (2\zeta r)^2}}{\sqrt{\left(1 - (r)^2\right)^2 + (2\zeta r)^2}} \tag{18.2}$$

where ζ represents the damping ratio and r denotes the frequency ratio (ω/ω_n).

18.3.3 Characterization of TVA Vibration Reduction Performance

Impact test method is used on the main structure in order to assess the vibration reduction performance of the prototype TVA system. The main structure, for which the vibrations are tried to be reduced, is a supported cylindrical structure [11] as demonstrated in Fig. 18.6. As observed from this figure, prototype TVA system is attached to the end of the cylinder where the vibration levels are expected to be the highest. The system is excited from the tip by means of a modal impact hammer and FRFs are extracted from the accelerometer located at the tip of the cylinder as shown in Fig. 18.7.

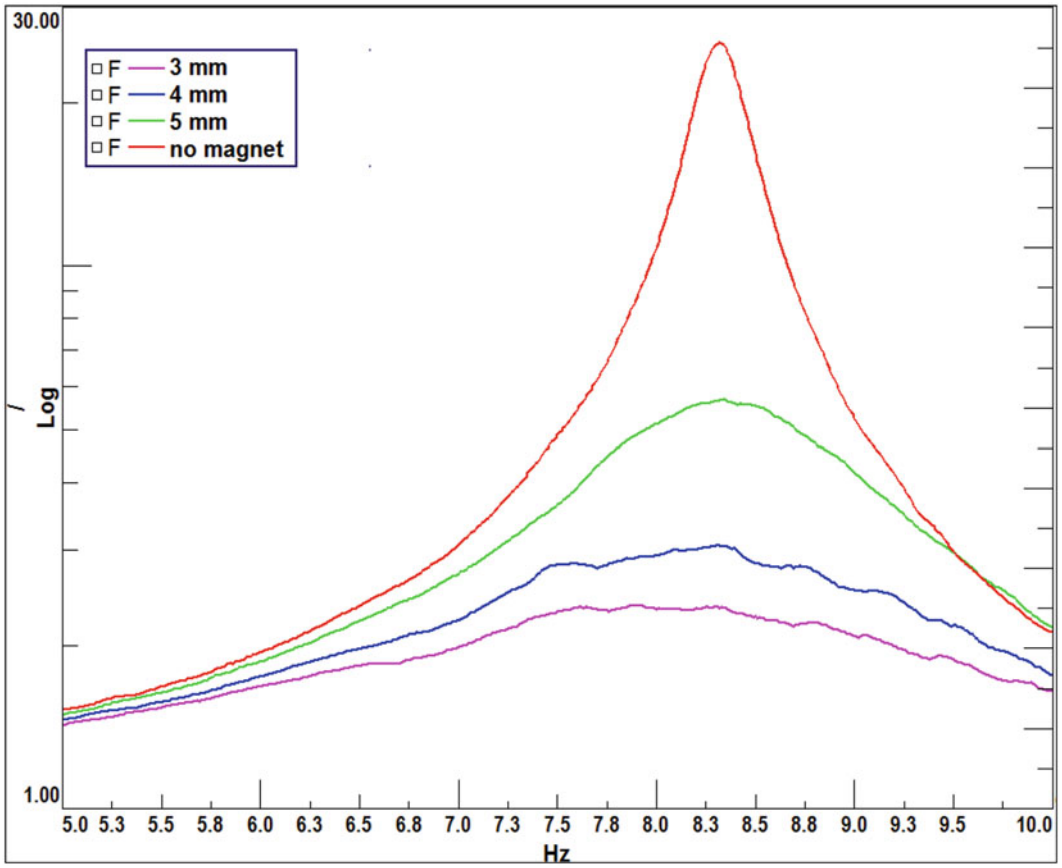

Fig. 18.5 Sine-sweep test results for different magnet-copper plate distances

Fig. 18.6 Main structure and TVA mounting location on the structure

As a result of the modal tests, accelerance FRFs are obtained for with TVA (modified) and without TVA (unmodified) cases along the three axes of the accelerometer shown in Fig. 18.7. These FRF results are presented in Figs. 18.8, 18.9 and 18.10 for the modified and unmodified cases. From these figures, it can be observed that the vibration levels of the main structure are effectively suppressed with TVA addition.

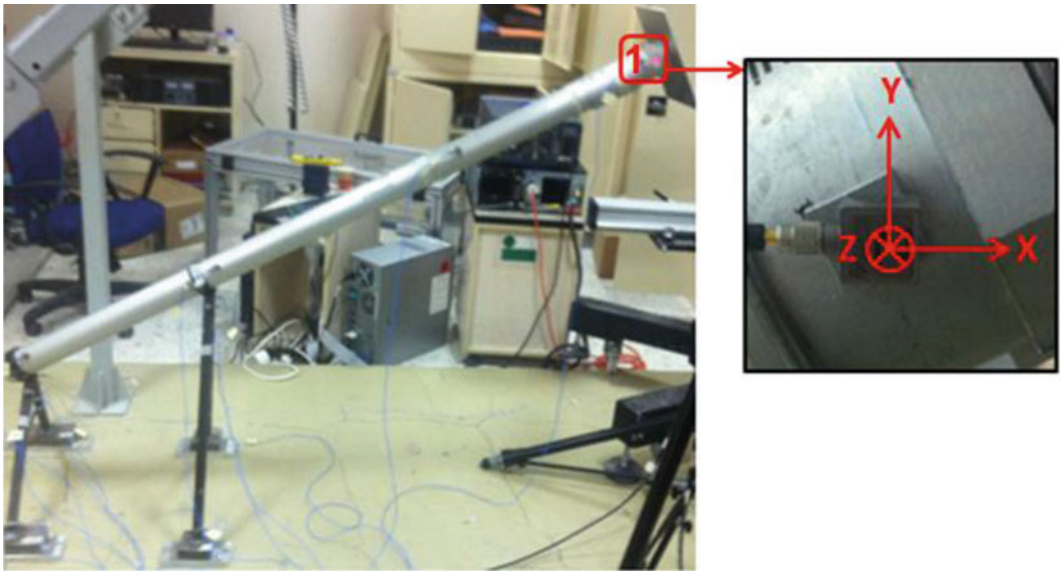

Fig. 18.7 Orientation of the accelerometer used for tip response FRF measurement

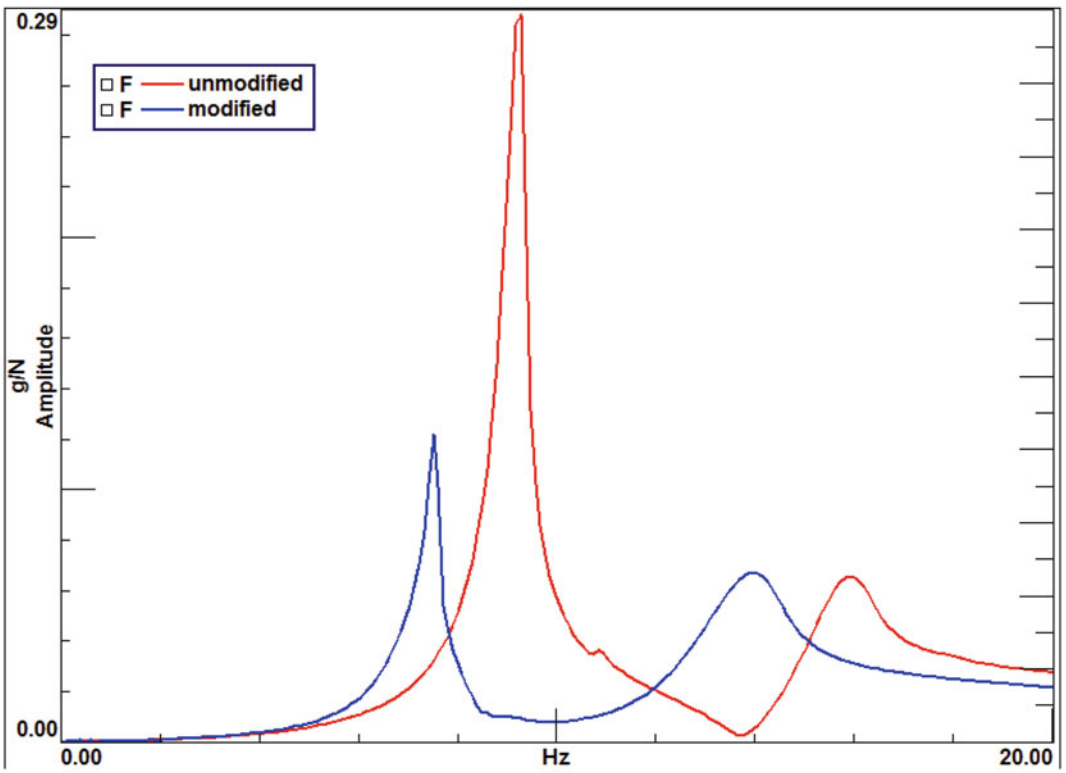

Fig. 18.8 Comparison of accelerance FRFs in x-direction

18.4 Conclusion

A tuned vibration absorber system which is designed to reduce the vibrations of a supported cylindrical structure is considered in this study. Firstly, TVA system is experimentally characterized as a standalone system. For that purpose, nonlinear characteristic of the TVA system is explored by means of random and sine-sweep tests. Then the target parameters of TVA are verified through sine-sweep tests which are performed at various damping configurations. Finally, TVA system is attached to the main structure and the vibration reduction performance of the TVA is measured by modal impact tests. It is observed that the TVA system is able to reduce the vibrations of the structure to the desired levels.

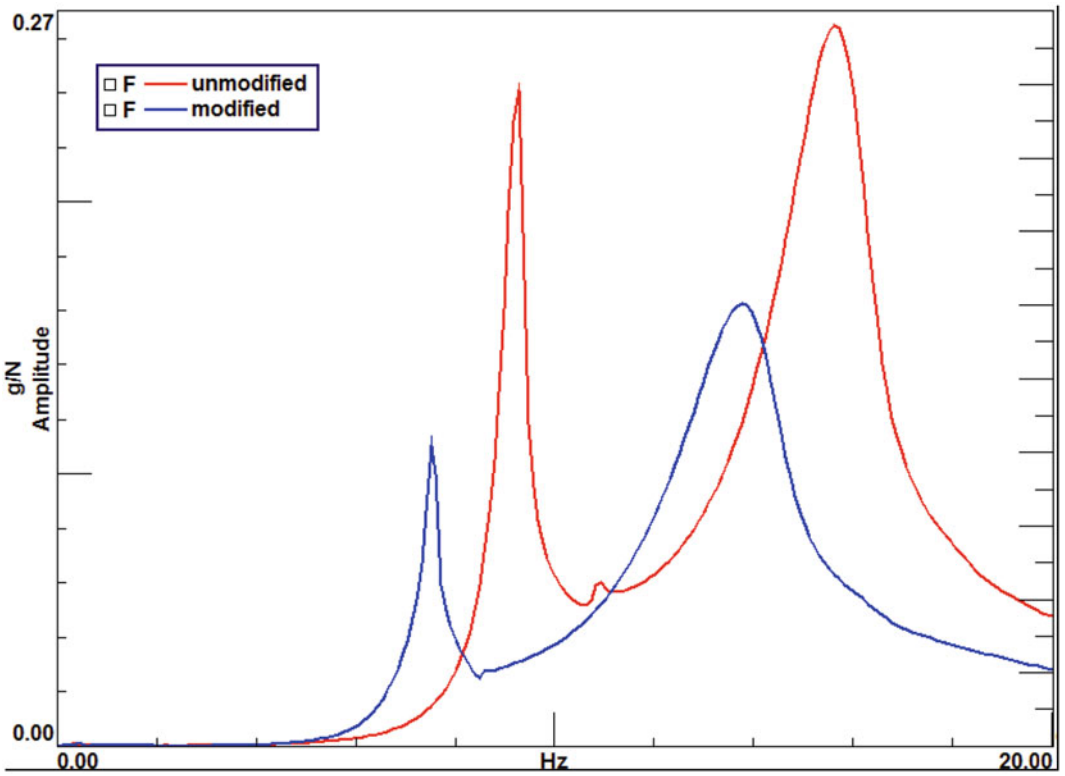

Fig. 18.9 Comparison of accelerance FRFs in y-direction

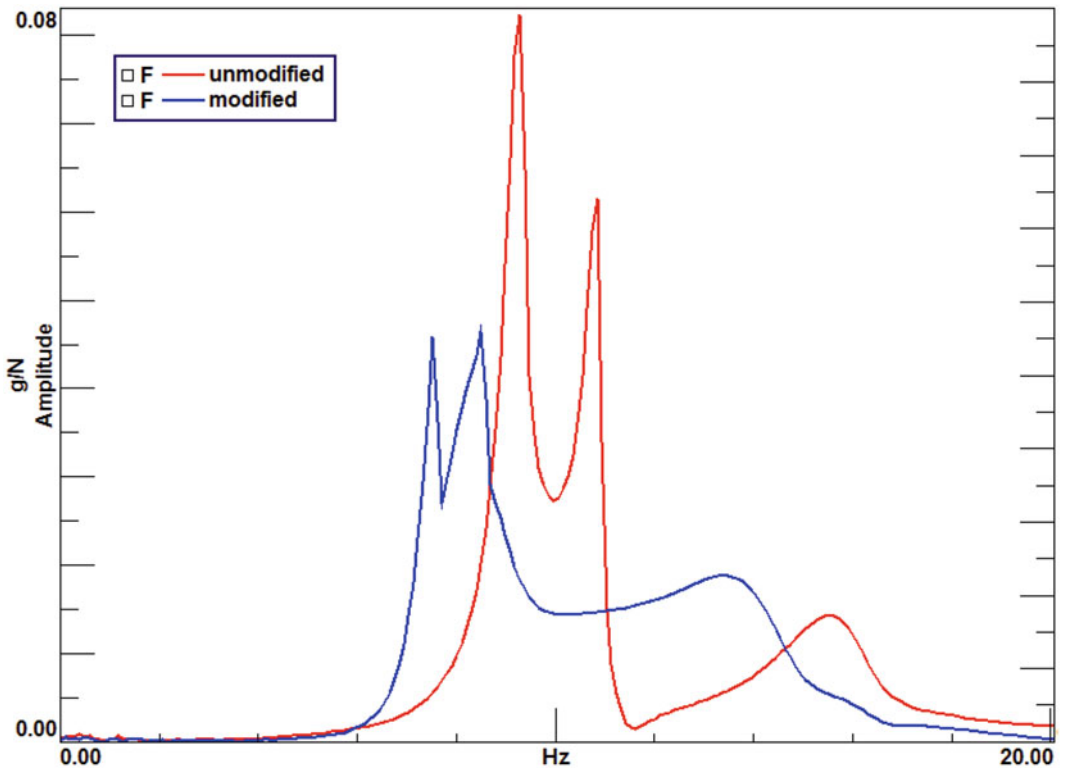

Fig. 18.10 Comparison of accelerance FRFs in z-direction

References

1. Den Hartog, J.P.: Mechanical Vibrations, 4th edn. McGraw-Hill Book Company Inc., New York (1956)
2. Kathe, E.L.: Gun barrel vibration absorber. U.S. Patent No. 6,167,794 B1 (1998)
3. Hill, S., Synder, S., Cazzolato, B.: An adaptive vibration absorber. Acoustics 2002 - Innovation in Acoustics and Vibration (2002)
4. Lourenco, R.: Design, construction and testing of an adaptive pendulum tuned mass damper. M.S. thesis, University of Waterloo (2011)
5. Littlefield, A., Kathe, E.: Adaptive gun barrel vibration absorber. US Army Armament Research, Development and Engineering Center (2002)
6. Bonsel, J., Fey, R., Nijmeijer, H.: Application of a dynamic vibration absorber to a piecewise linear beam system. Nonlinear Dynam. **37**, 227–243 (2004)
7. Harris, A.: Multi-degree of freedom passive and active vibration absorbers for the control of structural vibration. M.S. thesis, Faculty of the Virginia Polytechnic Institute and State University (2003)
8. Kienholtz, D., Pendleton, S.: Demonstration of solar array vibration suppression. Smart Structures and Materials, 2193 (1994)
9. LMS Test Lab12A Documentation. Leuven, Belgium (2012)
10. Kelly, S.G.: Response due to harmonic excitation of support. Mechanical Vibrations Theory and Applications, SI ed., pp. 228–234. Cengage Learning, Stamford, USA (2012)
11. Aksoy, T.: Tuned vibration absorber design for a supported hollow cylindrical structure. M.S. thesis, Middle East Technical University (2015)